Quantum Optics with Trapped Calcium Ions

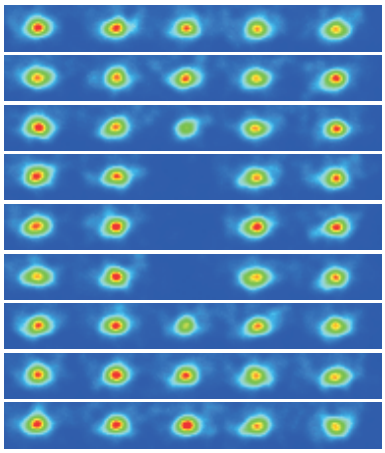

Peter Staanum

Danish National Research Foundation
Center for Quantum Optics – QUANTOP
Institute of Physics and Astronomy
University of Aarhus, Denmark

PhD thesis
February 2004

Quantum Optics with Trapped Calcium Ions

Peter Staanum

Danish National Research Foundation
Center for Quantum Optics – QUANTOP
Institute of Physics and Astronomy
University of Aarhus, Denmark

PhD thesis
February 2004

This thesis is submitted to the Faculty of Science at the University of Aarhus, Denmark, in order to fulfill the requirements for obtaining the PhD degree in Physics. The studies have been carried out under the supervision of Ass. Prof. Michael Drewsen in the Ion Trap Group at the Institute of Physics and Astronomy, University of Aarhus from August 1999 to February 2004.

Contents

Preface vii

List of publications ix

1 Introduction 1
- 1.1 Quantum optics with cold trapped ions . . . 1
- 1.2 Quantum optics with Ca^+ ions in Aarhus . . . 3
- 1.3 Outline of the thesis . . . 4

2 Atom-light interactions 5
- 2.1 A free two-level atom . . . 5
  - 2.1.1 Interaction with a travelling-wave light-field . . . 6
  - 2.1.2 Inclusion of spontaneous emission . . . 9
- 2.2 Trapped two-level atoms interacting with a light-field . . . 10
  - 2.2.1 A single trapped atom . . . 11
  - 2.2.2 Multiple ions . . . 13

3 Laser cooling of trapped ions 15
- 3.1 Doppler cooling of trapped ions . . . 16
  - 3.1.1 Doppler cooling of a free two-level ion . . . 16
  - 3.1.2 The $^{40}Ca^+$ ion . . . 18
  - 3.1.3 Doppler cooling of the $^{40}Ca^+$ ion . . . 19
- 3.2 Ion strings in a three-dimensional harmonic potential . . . 20
- 3.3 Sideband cooling . . . 21
  - 3.3.1 Rate equation description in the Lamb-Dicke limit . . . 22
  - 3.3.2 Rate equation with second-order contributions . . . 26
- 3.4 Sideband cooling of the $^{40}Ca^+$ ion . . . 28
  - 3.4.1 The sideband-cooling scheme . . . 28
  - 3.4.2 Discussion . . . 33
- 3.5 Quantum Monte Carlo simulations of the sideband-cooling scheme . . . 34
  - 3.5.1 Theory . . . 34
  - 3.5.2 Simulation results . . . 35
  - 3.5.3 Comparison to a rate equation model . . . 39
  - 3.5.4 Conclusion . . . 44
- 3.6 Measuring the population of motional states . . . 45

4 Internal state detection **47**
4.1 Internal state detection using shelving . . . 47
4.2 State-selective shelving using STIRAP . . . 48
4.2.1 STIRAP – general theory . . . 48
4.2.2 State-selective shelving in $^{40}Ca^{+}$ using STIRAP . . . 50
4.2.3 STIRAP in a five-level system . . . 53
4.3 State-selective shelving in $^{40}Ca^{+}$ using a Raman transition . . . 55
4.4 Conclusion . . . 56

5 Quantum logic with trapped ions **57**
5.1 Quantum gates . . . 57
5.1.1 Single-qubit gates . . . 58
5.1.2 Two-qubit gates . . . 58
5.2 Quantum gates using trapped ions . . . 59
5.2.1 The Cirac-Zoller proposal . . . 60
5.2.2 The Mølmer-Sørensen proposal . . . 61
5.2.3 Other gate proposals . . . 62
5.2.4 Practical large-scale quantum computation with trapped ions? . 63
5.3 Quantum logic operations in the $^{40}Ca^{+}$ ion . . . 64

6 Applications of optical dipole potentials in trapped-ion quantum logic **65**
6.1 Trapped ions and optical dipole potentials . . . 65
6.2 A geometric Controlled-Z gate using optical dipole forces . . . 67
6.2.1 Implementation in alkaline earth ions . . . 70
6.2.2 Error sources . . . 78
6.2.3 Discussion . . . 81
6.3 Individual addressing of trapped ions . . . 82
6.3.1 Trapped-ion quantum logic utilizing position-dependent ac Stark shifts . . . 83
6.3.2 Discussion . . . 88

7 The linear Paul trap **91**
7.1 Linear Paul trap theory . . . 91
7.2 Trap design and construction . . . 94
7.2.1 Design considerations . . . 94
7.2.2 Electrode shape and dimensions . . . 96
7.2.3 Trap construction . . . 99

8 Experimental equipment and methods **101**
8.1 Vacuum chamber . . . 101
8.2 Trap voltage supplies . . . 103
8.2.1 RF-supplies . . . 104
8.2.2 DC-supply . . . 106
8.3 Magnetic field coils . . . 106
8.4 Laser light sources for Ca^{+} ions . . . 108
8.4.1 397 nm sources . . . 108
8.4.2 Infrared sources . . . 109
8.5 Laser light control . . . 109
8.5.1 397 nm sources . . . 110

8.5.2 Infrared sources . . . 111
8.6 Ion production . . . 113
8.7 Imaging system . . . 114

9 Trap characterization and ion mass measurements 117
9.1 Measuring the trap parameters . . . 117
9.1.1 Experimental setup . . . 118
9.1.2 Theory: The driven damped harmonic oscillator . . . 121
9.1.3 Axial trap frequencies . . . 121
9.1.4 Radial trap frequencies . . . 123
9.2 Micromotion . . . 138
9.3 Ion mass measurements . . . 139
9.3.1 Theory . . . 140
9.3.2 Experiment . . . 145

10 Shelving in the metastable $3d\,^2D_{5/2}$ state 151
10.1 Lifetime measurement of the $3d\,^2D_{5/2}$ state . . . 151
10.1.1 Experimental setup . . . 152
10.1.2 Data analysis . . . 153
10.1.3 Result and conclusion . . . 164
10.2 Internal state detection revisited . . . 165

11 Summary and outlook 167

A Derivations 169
A.1 Sideband cooling with second-order contributions to the rate equation . 169
A.1.1 Solution to the second-order rate equation . . . 169
A.1.2 Derivation of Eqs. (3.3.26) and (3.3.27) . . . 170
A.2 Displacements and phases in the geometric Controlled-Z gate . . . 171
A.3 The coupled motion of two trapped ions . . . 172

B The Ca^+ ion 175
B.1 Abundance of Ca-isotopes . . . 175
B.2 Transitions in the $^{40}Ca^+$ ion . . . 175
B.3 Zeeman-splitting in the $^{40}Ca^+$ ion . . . 177

C Sideband cooling – quantum Monte Carlo simulations 179
C.1 The simulation program . . . 179
C.2 Time evolution of coefficients . . . 180

Bibliography 183

Preface

The present thesis is based on my work during the last four and a half years in the Ion Trap Group at the Institute of Physics and Astronomy, University of Aarhus, under the supervision of Michael Drewsen. The work has given me the opportunity to explore the fascinating field of quantum optics with trapped ions, to work with lasers, vacuum technology and electronics as well as doing earth bound things like drilling a hole in a piece of metal. All these aspects has made the work very varied and exciting.

Based on the previous work and experience in the Ion Trap Group, the work has focussed on setting up an experiment for quantum optics studies involving few trapped ions. There are many different parts in the experimental setup and many people has given their contribution to the project. We have now seen the first results of this work, but there is more work to do and hopefully many more results to come.

In the thesis I attempt to give an overview of the project as a whole. Some sections may be very basic knowledge for the experienced ion trap physicist or quantum optician. These parts will hopefully be appreciated by students who will work on the project in the future. Other chapters are very detailed, reflecting which parts of the project the author mainly has been involved in.

During my years at the institute I have met and co-operated with several people, who deserves a few words.

First of all, Michael Drewsen is acknowledged for initiating this very interesting project, for competently guiding the work, teaching me ion trap physics and much more, and for interesting physics discussions. In the Ion Trap Group, I also had the pleasure of working with several other persons. In the first years, I enjoyed working with Liv Hornekær, Niels Kjærgaard, Anne Marie Thommesen and Kristian Mølhave, who all helped me find my way in the lab, and with Zelinda Videsen, Kristian Støchkel and Andy Brøner. More recently, I have had the pleasure of working together with fellow PhD student Anders Mortensen, who is acknowledged for proof-reading this thesis, and with Randi Martinussen, Inger Jensen, Jens Lindballe, Frank Jensen and Niels Nissen. Dirk Voigt spend two years with us as a PostDoc and deserves credit for his important contributions to the project, especially for building lasers. More recently, Jens Lykke Sørensen has joined the group and contributed to the present work. Randi, Inger and Jens are all acknowledged for keeping the good mood during the numerous late night hours in the lab. Finally, I would like to thank Grete Flarup for proof-reading this thesis.

The technical staff at the Institute has been very important for this project. The people in the workshop managed by Uffe Simonsen are acknowledged for their contributions and Torben Thomsen is acknowledged for his invaluable advice when I was trying to

handle the machines myself. Thanks to the 'vacuum-guys', Karsten Rasmussen and Jens Vestergaard, for their assistance and to Folmer Lyckegaard in the chemistry lab. A special thanks to Robert Stensgaard, Erik Søndergaard, Helge Wahlgreen, Frank Mikkelsen, Michael Jensen and Tonny Korsbjerg in the electronics department for building all the possible and almost impossible electronics devices which allow us to do experiments, and for always being approachable. From the scientific staff, I would like to thank Klaus Mølmer for answering my questions when the theory became too tough and for a fruitful collaboration on some of the work presented in Chap. 6. Thanks also to Erik Lægsgaard for revealing his secrets about all sorts of ultrahigh vacuum compatible materials.

During all the years I have also met many friendly people at the institute with whom I have talked about everything but physics (and physics of course) – thank you all! Especially though, I should mention Peter Arnborg, Thomas Laustsen, Brian Julsgaard and Kjartan Kinch, with whom I have spend many enjoyable days during the last more than 8 years.

Finally, a very big thank you to my parents and sister for their support during all my years of studying physics and to Astrid for proof-reading this thesis and for her support and understanding during these last months of writing.

Financial support from QUANTOP, the Danish National Research Foundation Center for Quantum Optics, and from ACAP, the Aarhus Center for Atomic Physics, funded by the Danish National Research Foundation, is gratefully acknowledged.

Aarhus, Denmark Peter Staanum
February, 2004

List of Publications

[I] P. Staanum, and M. Drewsen, *Trapped-ion quantum logic utilizing position-dependent ac Stark shifts*, Phys. Rev. A **66**, 040302(R) (2002).

[II] M. Drewsen, I. Jensen, J. Lindballe, N. Nissen, R. Martinussen, A. Mortensen, P. Staanum, and D. Voigt, *Ion Coulomb crystals: a tool for studying ion processes*, Int. J. Mass. Spect. **229**, 83 (2003).

[III] P. Staanum, I. S. Jensen, R. Martinussen, D. Voigt, and M. Drewsen, *Lifetime measurement of the metastable* $3d\ ^2D_{5/2}$ *state in the* $^{40}Ca^+$ *ion using the shelving technique on a few-ion string*, Phys. Rev. A **69**, 032503 (2004).

[IV] A. Mortensen, J. J. T. Lindballe, I. S. Jensen, P. Staanum, D. Voigt, and M. Drewsen, *Isotope shifts of the* $4s^2\ ^1S_0 \rightarrow 4s5p\ ^1P_1$ *transition and hyperfine splitting of the* $4s5p\ ^1P_1$ *state in calcium*, Phys. Rev. A **69**, 042502 (2004).

[V] M. Drewsen, A. Mortensen, R. Martinussen, P. Staanum, and J. L. Sørensen, *Non-destructive identification of cold and extremely localized single molecular ions.* Submitted for publication.

[VI] P. Staanum, M. Drewsen, and K. Mølmer, *A geometric quantum gate for ions based on optical dipole forces induced by Gaussian beams.* Manuscript in preparation.

Chapter 1

Introduction

1.1 Quantum optics with cold trapped ions

One of the fathers of quantum mechanics, Erwin Schrödinger, once said [1]

" ... *we never experiment with just one electron or atom or (small) molecule.*"

-E. Schrödinger, 1952.

Today the situation is, however, quite different, because single or several ions or atoms can be trapped, e.g., by various combinations of electric and/or magnetic fields, and used in experiments. Moreover, the development of so-called laser cooling methods, which started about 30 years ago, has enabled experimentalists to routinely cool trapped ions or atoms to temperatures only a fraction of a degree above absolute zero. Owing to this level of experimental control, cold and trapped ions and atoms have become unique test cases for the study of many effects within the field of quantum optics.

In parallel with the development in laser cooling and in quantum optics in general, computer chips have become smaller and smaller and faster and faster. Despite this, one never finds them fast enough! This is particularly true for computer simulations of large quantum systems, because the size of the computational task, i.e., the number of variables to keep track of, grows *exponentially* with the number of particles in the quantum system.

To overcome this problem, Richard Feynman put forward the idea of performing such simulations by the use of another quantum system - or a *quantum simulator*. This was in 1982 and only a few years later, in 1985, David Deutsch came up with the notion of a *quantum computer*, i.e., a computing device based on quantum mechanical principles, which can simulate any physical system in a time which only grows *polynomially* with the size of the system. In addition to simulating quantum systems, a quantum computer can also solve computational tasks, which are intractable on a classical computer. This was demonstrated by the quantum algorithms constructed by Peter Shor [2] and Lov

[1] As quoted in Ref. [1].

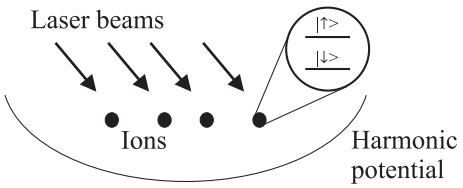

Figure 1.1: Simple illustration of the Cirac-Zoller proposal [4]. A string of ions trapped in a harmonic potential is illuminated by laser beams which can address the ions individually. Internal states of the ions define the qubit states $|\downarrow\rangle$ and $|\uparrow\rangle$.

Grover [3], which can factorize large numbers and search an unordered database [2], respectively, faster than any classical algorithm.

Now, what does a quantum computer look like? Recall first, that a classical computer performs logic operations on binary numbers, where each binary digit, a bit, can assume the value 0 or 1. In quantum logic the basic unit is the quantum bit, or *qubit*, i.e., a two-level quantum system, which can be in a superposition of states, $|\downarrow\rangle$ and $|\uparrow\rangle$, representing the values 0 and 1. A physical realization of a quantum computer consists of several qubits, on which elementary quantum logic operations, so-called quantum gates, can be performed. Owing to the high degree of experimental control over trapped and laser-cooled ions, they are very attractive candidates for implementation of quantum logic. Specifically, it was proposed by Ignacio Cirac and Peter Zoller in 1995 [4] to use a string of trapped ions, cooled to their motional ground-state in the trap, as a physical system, on which quantum gates can be performed by manipulating the quantum states of the ions with laser pulses (see Fig. 1.1). Although many studies involving cold trapped ions had already been done before the Cirac-Zoller proposal, it is probably fair to say that there has been a growing interest in the field of quantum optics with cold trapped ions ever since. In addition to the relevance for quantum computation, this interest is motivated by the fact that a string of cold trapped ions is highly relevant for the creation of so-called *entangled states*, which are interesting for fundamental studies of quantum mechanics, but also useful in connection with spectroscopy [5] and in quantum information [6].

An entangled state can be defined as a quantum state of two or more quantum systems, whose common wavefunction cannot be separated into a product of wavefunctions for any subset of the systems [3]. One example of an entangled state of two two-level quantum systems with internal states $|\downarrow\rangle$ and $|\uparrow\rangle$, e.g., two ions, is the following:

$$\Phi = \frac{|\downarrow\rangle|\downarrow\rangle + |\uparrow\rangle|\uparrow\rangle}{\sqrt{2}}. \tag{1.1.1}$$

According to the probability interpretation of quantum mechanics, this state has the property that if we measure the state of one particle to be $|\downarrow\rangle$ ($|\uparrow\rangle$), then the quantum state of the other particle will collapse onto $|\downarrow\rangle$ ($|\uparrow\rangle$), even if the particles are

[2] An example of an unordered database is the phone-numbers in a phone book. Suppose a hot-looking girl gives a young man her phone number, but he doesn't know her name and desperately wants to find out by searching through the phone numbers in his phone book. If there are N entries in the phone book, it would on average take him $N/2$ steps. With Grovers algorithm he can do it in a number of steps proportional to $\sqrt{N}$ - if only he had a quantum computer.

[3] This definition is appropriate for a pure state, not for a mixed state [7].

non-interacting and arbitrarily far apart! In their famous paper from 1935, Einstein, Podolsky and Rosen (EPR) [8] considered this to be a paradox and concluded that the theory of quantum mechanics was incomplete. To determine from experiments if quantum mechanics really was incomplete or not, was considered impossible until John Bell proved a certain inequality, which relates a set of quantum mechanical observables. This inequality (and a class of other so-called Bell inequalities) can be violated by an entangled state if quantum mechanics is complete but will be obeyed by the so-called 'hidden variable' theories, which originated from the EPR-paper. This fact has triggered the fundamental interest in entangled states, which today have been created of trapped ions [9] as well as photons [10], atoms [11] and even macroscopic samples of atoms [12].

The possibilities of implementing quantum logic and creating entangled states with trapped ions, make quantum optics with trapped ions a very interesting field of physics. It is also a rapidly evolving field where impressive experimental achievements have been reached in the past few years, especially by the groups of Dave Wineland at NIST in Boulder, USA, and of Rainer Blatt in Innsbruck, Austria, with the first demonstrations of two-ion quantum gates [13, 14], a quantum algorithm [15], creation of entangled states of two and four particles [9, 16] and violation of a Bell inequality [17]. The possibilities within the field are, however, by no means exhausted and other groups are also working hard to explore these possibilities.

More information about quantum computing and quantum optics with trapped ions can, e.g., be found in Refs. [1, 18, 19] [4] and - of course - the rest of this thesis.

1.2 Quantum optics with Ca^+ ions in Aarhus

The project presented in this thesis is aiming at the creation of entangled states and demonstration of quantum gates along the lines of the Cirac-Zoller proposal. In the project we have chosen to work with the alkaline earth Ca^+ ion, or more specifically $^{40}Ca^+$, since this is the naturally most abundant of the calcium isotopes. The $^{40}Ca^+$ ion is well suited for quantum optics studies because it has only a single optically active electron outside a closed shell, which makes the level scheme sufficiently simple that the ion can be laser-cooled using only a few laser sources. Yet, it has metastable states which are useful, e.g., for quantum state detection. The ground state is a $^2S_{1/2}$ state, and we define our qubit by the two Zeeman sublevels of the ground state as

$$|\downarrow\rangle = {}^2S_{1/2}(m_J = -1/2) \tag{1.2.1}$$

$$|\uparrow\rangle = {}^2S_{1/2}(m_J = +1/2). \tag{1.2.2}$$

Most alkaline earth ions have properties similar to Ca^+, and the specific choice of Ca^+ was mainly motivated by practical reasons. First, laser light at the relevant wavelengths is available, e.g., using standard infrared diode lasers and a frequency doubled Titanium-Sapphire laser. Second, a Titanium-Sapphire laser, which is the most expensive of the mentioned laser sources, was already present in the lab at the start-up of the project. When the author of this thesis entered the group, lasers for so-called Doppler laser cooling were running and the first laser-cooling experiments with

[4] Ref. [18] was used as a reference for some of the history above.

Ca^+ were started. Furthermore, there was a large expertise in building and running so-called linear Paul traps.

For the work presented in this thesis, we started out by designing and building a relatively small linear Paul trap, suitable for trapped-ion quantum logic experiments. Other crucial ingredients in the project are the ability to detect the internal state of an ion and to cool ions to near their motional ground state in the trap. A ground state cooling scheme has been studied theoretically and is discussed in the thesis. In order to eventually demonstrate this cooling scheme, demonstrate internal state detection and to perform quantum logic operations, additional diode laser systems have been introduced, and improvements of the level of laser-control have been necessary, both in terms of power-stability, frequency-stability and the shaping of laser-pulses.

1.3 Outline of the thesis

The thesis is organized as follows. Chapters 2–6 are mainly theoretical, describing the theoretical background for the project, some general issues in trapped-ion quantum logic and some further theoretical work. Chapters 7–10 are mainly experimental, presenting the experimental details of the project and experimental results. Chap. 11 gives a summary and an outlook.

Chapter 2: An introduction to the basic concepts of light-atom (or light-ion) interactions for free as well as trapped atoms.

Chapter 3: A short introduction to the Doppler laser cooling technique is followed by a more detailed description of the sideband-cooling technique to be used for cooling $^{40}Ca^+$ ions to (near) their motional ground state and a presentation of the results of a numerical study using quantum Monte Carlo simulations.

Chapter 4: Here, detection of the internal state of a $^{40}Ca^+$ ion is discussed, particularly for a scheme based on two so-called Stimulated Raman Adiabatic Passage (STIRAP) processes.

Chapter 5: This chapter gives a general discussion of quantum gates and of some of the many proposals for performing quantum gates with cold trapped ions.

Chapter 6: This chapter contains two theoretical proposals involving optical dipole potentials, one for performing a two-ion quantum gate and one for individual addressing of trapped ions on a string. The gate proposal will be published in Ref. [VI] and the individual addressing proposal has been published in Ref. [I].

Chapter 7: In this chapter the theory of confinement of charged particles in a linear Paul trap is described, and the design and construction of the new trap is presented.

Chapter 8: Here the additional experimental equipment and experimental methods are described.

Chapter 9: This chapter concerns a series of experiments performed in order to characterize the trap. Furthermore, some preliminary experiments on ion mass measurements are presented. Results from the latter experiments will be published in Ref. [V].

Chapter 10: In this chapter a lifetime measurement of a metastable state in the $^{40}Ca^+$ ion is presented, and its relevance for the detection scheme presented in Chap. 4 is discussed. The lifetime measurement is published in Ref.[III].

Chapter 11: Summary and outlook.

Chapter 2

Atom-light interactions

In this chapter some basic concepts in the description of a two-level atom interacting with a monochromatic travelling-wave light-field are introduced, since they will be necessary for understanding the following chapters. The case of a free two-level atom is considered in Sec. 2.1 [1], where important notions, such as Rabi-frequency, Rabi-oscillations, saturation intensity, power broadening and pulse-area are introduced. In Sec. 2.2, we consider first a single two-level atom confined in a harmonic potential and describe the atom-light interaction in the so-called Lamb-Dicke limit. Following that, the treatment is extended to multiple mutually interacting ions and described in terms of the motional eigenmodes of the ions.

2.1 A free two-level atom

In this section we consider the two-level atom illustrated in Fig. 2.1, with ground state $|g\rangle$ and excited state $|e\rangle$, which are eigenstates of the atomic Hamiltonian H_{atom}, i.e.,

$$H_{atom}\,|g\rangle = E_g\,|g\rangle \quad \text{and} \quad H_{atom}\,|e\rangle = E_e\,|e\rangle\,, \tag{2.1.1}$$

where E_g and E_e are the eigenenergies of the two states. In general the atomic wavefunction ψ can be written as a superposition of the two eigenstates,

$$\Psi(\boldsymbol{r},t) = c_g\,|g\rangle + c_e\,|e\rangle\,, \tag{2.1.2}$$

where the coefficients c_g and c_e in general are complex numbers. The transition frequency between $|g\rangle$ and $|e\rangle$ is

$$\omega_{eg} = \frac{E_e - E_g}{\hbar}, \tag{2.1.3}$$

and the natural decay rate from the exited state to the ground state is denoted by Γ.

In the following we consider the time-evolution of the atomic wavefunction when the atom interacts with a travelling-wave light-field which is monochromatic and near-resonant with the atomic transition. In Sec. 2.1.1, we consider only the interaction with the light-field, neglecting spontaneous emission. In Sec. 2.1.2 spontaneous emission is included in the description.

[1] The given treatment is somewhat linked to Refs. [20, 21].

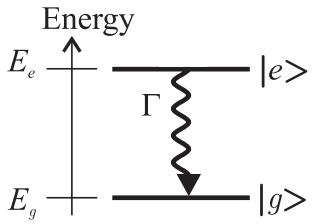

Figure 2.1: A two-level atom with ground state $|g\rangle$ and excited state $|e\rangle$ at energies E_g and E_e, respectively. The natural decay rate from the excited state to the ground state is denoted by Γ.

2.1.1 Interaction with a travelling-wave light-field

We consider a monochromatic travelling-wave light-field characterized by the electric field

$$\boldsymbol{E}(\boldsymbol{r},t) = E_0\hat{\boldsymbol{\epsilon}}\cos(\boldsymbol{k}\cdot\boldsymbol{r} - \omega_L t + \phi) \tag{2.1.4}$$

having amplitude E_0, wave-vector $\boldsymbol{k}$, frequency ω_L, a constant phase ϕ and where $\hat{\boldsymbol{\epsilon}}$ is a unit vector describing the polarization of the light-field. The interaction with the two-level atom is described by the Hamiltonian [22]

$$H' = -e\boldsymbol{E}(\boldsymbol{r},t)\cdot\boldsymbol{r}, \tag{2.1.5}$$

and the time evolution of the atomic wavefunction ψ is governed by the time-dependent Schrödinger equation

$$i\hbar\frac{\partial\Psi}{\partial t} = (H_{atom} + H')\Psi. \tag{2.1.6}$$

Introducing the wavefunction in the form of Eq. (2.1.2), the Schrödinger equation translates to the following coupled differential equation for the coefficients c_g and c_e:

$$i\hbar\dot{c_g} = H'_{ge}c_e \qquad (E_g \equiv 0) \tag{2.1.7}$$

$$i\hbar\dot{c_e} = \hbar\omega_{eg}c_e + H'_{eg}c_g, \tag{2.1.8}$$

where

$$H'_{eg} = \langle e|\, H' \,|g\rangle = (H'_{ge})^* \tag{2.1.9}$$

and dots denote derivatives with respect to time. By introducing $\tilde{c_e} = c_e e^{i\omega_{eg}t}$, Eqs. (2.1.7) and (2.1.8) can be transformed into

$$i\hbar\dot{c_g} = H'_{ge}\tilde{c_e}e^{-i\omega_{eg}t} \tag{2.1.10}$$

$$i\hbar\dot{\tilde{c_e}} = H'_{eg}c_g e^{i\omega_{eg}t}, \tag{2.1.11}$$

which will be solved in the following. If we make the so-called dipole approximation, i.e., we neglect the spatial variation of the light-field over the atomic wavefunction, and

use Eqs. (2.1.4) and (2.1.5), the matrix elements in Eqs. (2.1.10) and (2.1.11) can be written as

$$\begin{aligned} H'_{eg} &= -eE_0 \langle e| \hat{\boldsymbol{\epsilon}} \cdot \boldsymbol{r} \cos(\boldsymbol{k} \cdot \boldsymbol{r} - \omega_L t + \phi) |g\rangle \qquad (2.1.12) \\ &= -eE_0 \langle e| r |g\rangle \cos(\boldsymbol{k} \cdot \boldsymbol{r} - \omega_L t + \phi) = \hbar\Omega \cos(\boldsymbol{k} \cdot \boldsymbol{r} - \omega_L t + \phi) \\ H'_{ge} &= \hbar\Omega^* \cos(\boldsymbol{k} \cdot \boldsymbol{r} - \omega_L t + \phi), \qquad (2.1.13) \end{aligned}$$

where

$$\Omega = -\frac{eE_0 \langle e| r |g\rangle}{\hbar} \qquad (2.1.14)$$

is the so-called *Rabi-frequency* and $r = \hat{\boldsymbol{\epsilon}} \cdot \boldsymbol{r}$.

Inserting Eqs. (2.1.12) and (2.1.13) into Eqs. (2.1.10) and (2.1.11), introducing the detuning $\delta = \omega_L - \omega_{eg}$ and assuming $|\delta| \ll \omega_{eg}$, it can be found that

$$i\hbar\dot{c_g} = \frac{\hbar\Omega^*}{2}\tilde{c_e}\left[e^{i(\boldsymbol{k}\cdot\boldsymbol{r}-\delta t-2\omega_{eg}t+\phi)} + e^{-(\boldsymbol{k}\cdot\boldsymbol{r}-\delta t+\phi)}\right] \approx \frac{\hbar\Omega^*}{2}\tilde{c_e}e^{-i(\boldsymbol{k}\cdot\boldsymbol{r}-\delta t+\phi)} \qquad (2.1.15)$$

$$i\hbar\dot{\tilde{c_e}} = \frac{\hbar\Omega}{2}c_g\left[e^{i(\boldsymbol{k}\cdot\boldsymbol{r}-\delta t+\phi)} + e^{-i(\boldsymbol{k}\cdot\boldsymbol{r}-\delta t-2\omega_{eg}t+\phi)}\right] \approx \frac{\hbar\Omega}{2}c_g e^{i(\boldsymbol{k}\cdot\boldsymbol{r}-\delta t+\phi)}, \qquad (2.1.16)$$

where we have made the *rotating-wave approximation* (RWA) in neglecting the quickly oscillating terms. For later application we note that the approximate expressions on the right hand side (r.h.s.) could have been derived by using the Hamiltonian

$$H_{RWA} = \frac{\hbar\Omega}{2}e^{i(\boldsymbol{k}\boldsymbol{r}-\omega_L t+\phi)}|e\rangle\langle g| + \frac{\hbar\Omega^*}{2}e^{-i(\boldsymbol{k}\boldsymbol{r}-\omega_L t+\phi)}|g\rangle\langle e| \qquad (2.1.17)$$

instead of H'.

Eqs. (2.1.15) and (2.1.16) can be transformed into two uncoupled second-order differential equations for c_g and $\tilde{c_e}$, which readily can be solved. With initial conditions $c_g(t=0) = 1$ and $\tilde{c_e}(t=0) = 0$, and choosing $\boldsymbol{r} = \boldsymbol{0}$, the solutions are

$$c_g(t) = \left[\cos\left(\frac{\chi t}{2}\right) - \frac{i\delta}{\chi}\sin\left(\frac{\chi t}{2}\right)\right]e^{i\delta t/2} \qquad (2.1.18)$$

$$\tilde{c_e}(t) = -\frac{i\Omega}{\chi}\sin\left(\frac{\chi t}{2}\right)e^{-i(\delta t/2-\phi)}, \qquad (2.1.19)$$

where $\chi = \sqrt{|\Omega|^2 + \delta^2}$ will be called the off-resonant Rabi-frequency. From these equations, it follows that the population in the ground state and in the excited state oscillates at the off-resonant Rabi-frequency according to the following equations:

$$|c_g(t)|^2 = \cos^2\left(\frac{\chi t}{2}\right) + \frac{\delta^2}{\chi^2}\sin^2\left(\frac{\chi t}{2}\right) \qquad (2.1.20)$$

$$|c_e(t)|^2 = 1 - |c_g(t)|^2 = \frac{|\Omega|^2}{\chi^2}\sin^2\left(\frac{\chi t}{2}\right). \qquad (2.1.21)$$

The oscillations, which are called *Rabi-oscillations*, are illustrated for the excited state population in Fig. 2.2 for different values of δ.

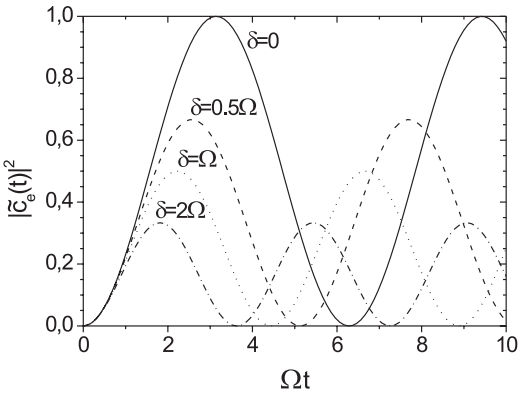

Figure 2.2: Rabi-oscillations of the excited state population for a two-level atom interacting with a travelling-wave light-field [see Eq. (2.1.21)].

In the following chapters we shall consider the time evolution of general superposition states as in Eq. (2.1.2) in the presence of a resonant light-field ($\delta = 0$). In this case the evolution from time zero of the ground state part of the wave-function can be found from Eqs. (2.1.18) and (2.1.19) by setting $\delta = 0$. Since a phase factor on Ω can be absorbed in the coefficients, we assume Ω to be real and positive, and hence it follows that $\chi = \Omega$. Thus, $|g\rangle$ evolves as

$$|g\rangle \mapsto \cos\left(\frac{\Omega t}{2}\right)|g\rangle - ie^{i\phi}\sin\left(\frac{\Omega t}{2}\right)|e\rangle\,, \tag{2.1.22}$$

and similarly it can be found that $|e\rangle$ evolves as

$$|e\rangle \mapsto -ie^{-i\phi}\sin\left(\frac{\Omega t}{2}\right)|g\rangle + \cos\left(\frac{\Omega t}{2}\right)|e\rangle\,. \tag{2.1.23}$$

In the following chapters we shall also consider light *pulses*, meaning that Ω varies in time. Until now we have tacitly assumed that Ω is constant, but the time-dependence can be incorporated as follows. If the light pulse is resonant with the atomic transition ($\delta = 0$), and Ω varies so slowly that the rotating wave approximation still can be made, then the evolution of the system is the same as in Eqs. (2.1.22) and (2.1.23) above, but with Ωt replaced by the *rotation-angle* [21, 23]

$$\Theta(t) = \int_{-\infty}^{t} |\Omega(t')|\,dt'. \tag{2.1.24}$$

For a (finite) pulse, the area under the function $|\Omega(t)|$ is finite and equal to $\Theta(\infty)$. This so-called *pulse-area* names some special pulses according to their pulse-area, namely $\pi/2$-pulses, π-pulses and 2π-pulses. A 2π-pulse, having $\Theta(\infty) = 2\pi$, changes the sign of the coefficients c_g and c_e, but it has no effect on the population in the states $|g\rangle$ and $|e\rangle$. A π-pulse makes a population inversion, taking all population in $|g\rangle$ to $|e\rangle$ and vice versa. A $\pi/2$-pulse will, e.g., starting from the ground state $|g\rangle$ create an equal superposition of the ground state and the excited state.

2.1.2 Inclusion of spontaneous emission

In order to include spontaneous emission in the description of a two-level atom interacting with a travelling-wave light-field, we turn to a density-matrix description. The density matrix $\underline{\underline{\rho}}$ for the two-level atom is given by

$$\underline{\underline{\rho}} = \begin{bmatrix} \rho_{ee} & \rho_{eg} \\ \rho_{ge} & \rho_{gg} \end{bmatrix} = \begin{bmatrix} c_e c_e^* & c_e c_g^* \\ c_g c_e^* & c_g c_g^* \end{bmatrix}, \tag{2.1.25}$$

where the time evolution of the matrix elements is given by the optical Bloch equations [20]:

$$\begin{aligned} \frac{d\rho_{gg}}{dt} &= \Gamma\rho_{ee} + \frac{i}{2}(\Omega^* e^{-i\delta t}\rho_{eg} - \Omega e^{i\delta t}\rho_{ge}) \\ \frac{d\rho_{ee}}{dt} &= -\Gamma\rho_{ee} - \frac{i}{2}(\Omega^* e^{-i\delta t}\rho_{eg} - \Omega e^{i\delta t}\rho_{ge}) \\ \frac{d\rho_{ge}}{dt} &= -\left(\frac{\Gamma}{2} + i\delta\right)\rho_{ge} + \frac{i}{2}\Omega^* e^{-i\delta t}(\rho_{ee} - \rho_{gg}) \\ \frac{d\rho_{eg}}{dt} &= -\left(\frac{\Gamma}{2} - i\delta\right)\rho_{eg} - \frac{i}{2}\Omega e^{i\delta t}(\rho_{ee} - \rho_{gg}). \end{aligned} \tag{2.1.26}$$

The optical Bloch equations can be solved numerically [20]. Qualitatively, one finds that the ground and excited state populations, ρ_{gg} and ρ_{ee}, perform damped Rabi-oscillations with damping coefficient Γ (see, e.g., Ref. [21] p. 206). In the limit $t \gg 1/\Gamma$ the populations reach their steady-state values, which can be found analytically from the steady-state equations [time-derivatives equal to zero in Eq. (2.1.26)] [20]. In steady state the population in the excited state is

$$\rho_{ee} = \frac{|\Omega|^2/4}{\delta^2 + |\Omega|^2/2 + \Gamma^2/4} = \frac{1}{2}\frac{s}{1+s}, \tag{2.1.27}$$

where

$$s = \frac{|\Omega|^2/2}{\delta^2 + \Gamma^2/4} \tag{2.1.28}$$

is the so-called *saturation parameter*. Thus, the excited state population is at most 1/2, which is only approached in the saturation limit ($s \gg 1$). From Eq. (2.1.28) we can introduce the on-resonance saturation parameter

$$s_0 = s(\delta = 0) = 2\frac{|\Omega|^2}{\Gamma^2} = \frac{I}{I_{sat}}, \tag{2.1.29}$$

where

$$I_{sat} = \frac{\hbar\Gamma\omega_{eg}^3}{12\pi c^2} \tag{2.1.30}$$

is the *saturation intensity*, $I = \varepsilon_0 E_0^2/2$ is the intensity of the travelling-wave light-field, and $\Gamma = \omega_{eg}^3 e^2 |\langle g| r |e\rangle|^2 / (3\pi\varepsilon_0\hbar c^3)$ [22].

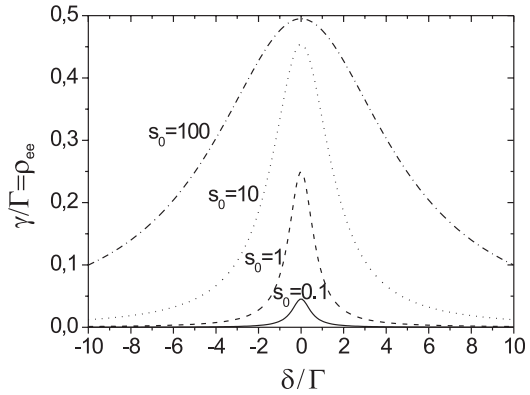

Figure 2.3: Scattering rate γ in units of Γ (steady-state population ρ_{ee} of the excited state $|e\rangle$) versus detuning for different on-resonance saturation parameters s_0.

In the steady state, the decay rate from the excited state, $\Gamma\rho_{ee}$, is equal to the excitation rate from the ground state, which is called the scattering rate and denoted by γ:

$$\gamma = \Gamma\rho_{ee} = \Gamma\frac{|\Omega|^2/4}{\delta^2 + |\Omega|^2/2 + \Gamma^2/4}, \tag{2.1.31}$$

which is plotted in Fig 2.3 for different values of s_0. The curves are Lorentzian [2] in shape with *power-broadened* width $\sqrt{2|\Omega|^2 + \Gamma^2}$.

2.2 Trapped two-level atoms interacting with a light-field

The confining potential in a linear Paul trap is to a good approximation harmonic in all three spatial dimensions. For an atom confined in a harmonic potential, the interaction with light is in general quite different from that for a free atom. To describe the light-atom interaction in this case, we consider an atom moving in one dimension, confined in a harmonic potential of the form

$$U_{1d-harm} = \frac{1}{2}m\omega_z^2 z^2, \tag{2.2.1}$$

where m is the atom mass, ω_z is the (angular) oscillation frequency of an atom in the harmonic potential and z is the position coordinate.

In the following, we consider first a single atom and extend the treatment to multiple (interacting) ions after that.

[2] Formally, a normalized Lorentz distribution function L with width Γ is given by $L = \Gamma/[2\pi(\delta^2 + \Gamma^2/4)]$.

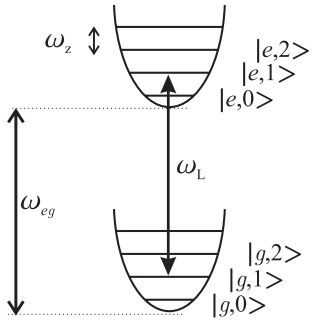

Figure 2.4: Energy-levels of a two-level atom trapped in a 1-dimensional harmonic potential interacting with a light-field of frequency ω_L.

2.2.1 A single trapped atom

In order to give a quantum mechanical description, we introduce the Hamiltonian H_{trap} for the harmonically confining potential of the trap,

$$H_{trap} = \hbar\omega_z \left(a^\dagger a + \frac{1}{2} \right), \tag{2.2.2}$$

where $a^\dagger$ and a are the harmonic oscillator creation and annihilation operators, respectively. The corresponding motional eigenstates of the atom are denoted by $|n\rangle$, where n is the vibrational quantum number. The total Hamiltonian for the atom in the harmonic potential is

$$H = H_{trap} + H_{atom}, \tag{2.2.3}$$

and the atomic eigenstates are combined eigenstates of the form $|g\rangle \otimes |n\rangle \equiv |g, n\rangle$ and $|e\rangle \otimes |n\rangle \equiv |e, n\rangle$. The corresponding energy levels are illustrated in Fig. 2.4.

In the rotating wave approximation, the interaction with a travelling-wave light-field is described by H_{RWA} in Eq. (2.1.17) with $\boldsymbol{r}$ replaced by $\boldsymbol{z}$ in this one-dimensional case. The matrix element for a transition between the states $|g, n\rangle$ and $|e, n'\rangle$ is

$$\langle e, n'| H_{RWA} |g, n\rangle = \frac{\hbar\Omega}{2} e^{-i\omega_{eg}t} \langle n'| e^{i\boldsymbol{k}\cdot\boldsymbol{z}} |n\rangle . \tag{2.2.4}$$

Introducing $\boldsymbol{z} = \boldsymbol{z}_0(a + a^\dagger)$, where $\boldsymbol{z}_0 = z_0\hat{\boldsymbol{z}}$ with $z_0 = \sqrt{\hbar/(2m\omega_z)}$ being the size of the harmonic oscillator ground state, the z-dependent matrix element in the equation above can be written as

$$\langle n'| e^{i\boldsymbol{k}\cdot\boldsymbol{z}} |n\rangle = \langle n'| e^{i\eta_{eg}(a+a^\dagger)} |n\rangle \equiv U_{n'n}(\eta_{eg}), \tag{2.2.5}$$

where $\eta_{eg} = \boldsymbol{k} \cdot \boldsymbol{z}_0$ is the so-called *Lamb-Dicke parameter*. η_{eg} determines the transition probability between the harmonic oscillator eigenstates. From Eq. (2.2.4) it can be seen that the effective Rabi-frequency $\Omega_{n'n}$ for a $|g, n\rangle \rightarrow |e, n'\rangle$ transition is

$$\Omega_{n'n} = \Omega U_{n'n}(\eta_{eg}). \tag{2.2.6}$$

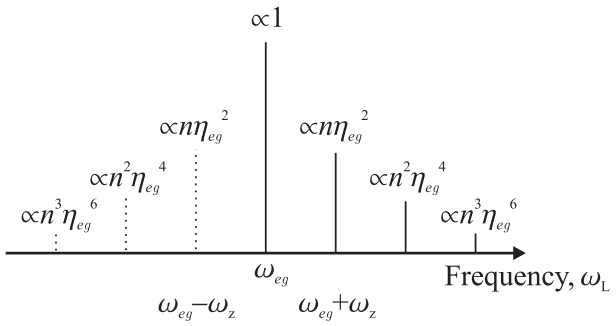

Figure 2.5: Absorption spectrum of a two-level atom trapped in a one-dimensional harmonic potential interacting with a light-field of frequency ω_L in the Lamb-Dicke limit.

If the states $|g,n\rangle$ and $|e,n'\rangle$ are coupled by a resonant light-field, we can therefore write the time evolution of the states as

$$\begin{aligned} |g,n\rangle &\mapsto \cos(\Omega_{n'n}t)\,|g,n\rangle - ie^{i\phi}\sin(\Omega_{n'n}t)\,|e,n'\rangle \\ |e,n'\rangle &\mapsto -ie^{-i\phi}\sin(\Omega_{n'n}t)\,|g,n\rangle + \cos(\Omega_{n'n}t)\,|e,n'\rangle\,, \end{aligned} \tag{2.2.7}$$

in analogy with Eqs. (2.1.22) and (2.1.23).

The matrix element $U_{n'n}(\eta_{eg})$ can be evaluated in terms of generalized Laguerre polynomials L_n^α [24]:

$$U_{n'n}(\eta_{eg}) = e^{-\eta_{eg}^2/2}\sqrt{\frac{n_<!}{n_>!}}\eta_{eg}^{|n'-n|}L_{n_<}^{|n'-n|}(\eta_{eg}^2), \tag{2.2.8}$$

where $n_< = \min(n,n')$ and $n_> = \max(n,n')$. Thus, $\Omega_{n'n}$ is generally n-dependent and different from Ω, even for an $|n\rangle \to |n\rangle$ transition, where $\Omega_{nn} = e^{-\eta_{eg}^2/2}L_n^0(\eta_{eg}^2)\Omega$.

In the following chapters we shall focus on the so-called *Lamb-Dicke limit* where $\sqrt{n+1}\,\eta_{eg} \ll 1$. In this limit $U_{n'n}(\eta_{eg})$ can be expanded as follows:

$$\begin{aligned} &U_{n'n}(\eta_{eg}) \\ &= \langle n'|\,1 - \eta_{eg}^2\left(a^\dagger a + 1/2\right) + i\eta_{eg}\left(a + a^\dagger\right) - \eta_{eg}^2\left(a^2 + {a^\dagger}^2\right)/2\,|n\rangle + \mathcal{O}\left[(\sqrt{n}\eta_{eg})^3\right] \\ &= \left[1 - \eta_{eg}^2\left(n + 1/2\right)\right]\delta_{n',n} + i\eta_{eg}\left[\sqrt{n}\delta_{n',n+1} + \sqrt{n+1}\delta_{n',n-1}\right] \\ &\quad - \eta_{eg}^2/2\left[\sqrt{n(n-1)}\delta_{n',n+2} + \sqrt{(n+1)(n+2)}\delta_{n',n-2}\right] + \mathcal{O}\left[(\sqrt{n}\eta_{eg})^3\right]. \end{aligned} \tag{2.2.9}$$

Hence in the Lamb-Dicke limit, the transition strength for a $|g,n\rangle \to |e,n'\rangle$ transition is roughly proportional to $(n\eta_{eg}^2)^{|n'-n|}$, which is illustrated in Fig. 2.5. The central transition at $\omega_L = \omega_{eg}$, where $\Delta n = n' - n = 0$, is usually referred to as the *carrier-transition*. Transitions with $\Delta n > 0$ are called *blue sideband transitions*, and transitions with $\Delta n < 0$ are called *red sideband transitions*. Since $n' \geq 0$, there is only a finite number of red sideband transitions from a given state $|n\rangle$.

2.2.2 Multiple ions

Until now we have not distinguished between (neutral) atoms or ions since the charge of the ion was irrelevant. In this section we shall consider multiple ions which are interacting via the Coulomb interaction, so from here on we must specialize to ions.

Looking at the special case of two singly-charged ions trapped in a one-dimensional harmonic potential, the potential energy is

$$U(z_1, z_2) = \frac{1}{2} m\omega_z^2 (z_1^2 + z_2^2) + \frac{e^2}{4\pi\varepsilon_0 (z_2 - z_1)} \qquad (z_2 > z_1), \tag{2.2.10}$$

where z_1 and z_2 denote the position of the ions along the z-axis. The equilibrium positions of the ions are given by the analytical expression

$$z_{2,eq} = -z_{1,eq} = \left(\frac{e^2}{16\pi\varepsilon_0 m\omega_z^2} \right)^{1/3} = 4^{-1/3} l, \tag{2.2.11}$$

where

$$l = \left(\frac{e^2}{4\pi\varepsilon_0 m\omega_z^2} \right)^{1/3} \tag{2.2.12}$$

is chosen as a length unit. The equilibrium distance is $\Delta z = z_{2,eq} - z_{1,eq} = 2^{1/3} l$. For three ions the equilibrium positions can also be found analytically, but for more than three ions the problem must be solved numerically. For up to ten ions the equilibrium positions are given in the work by James [25] and depicted in Fig. 2.6(a).

It is well known, e.g., from solid-state and molecular physics, that a system of interacting particles has a set of motional eigenmodes with corresponding eigenfrequencies, and that the motion of the particles can be described in terms of these eigenmodes. The same holds for a string of N ions in a harmonic potential, which in the one-dimensional case has N mutually perpendicular motional modes with distinct eigenfrequencies. These eigenmodes and eigenfrequencies are also calculated in Ref. [25] for up to ten ions. The eigenfrequencies are depicted in Fig. 2.6(b) and given for two and three ions in Table 2.1. All the eigenmodes for two and three ions are illustrated in Fig. 2.7. The first mode [3] is the so-called center-of-mass mode, where the ions move together at the trap frequency ω_z as a rigid body. The second mode is the so-called breathing mode at frequency $\sqrt{3}\omega_z$, where the ions move with an amplitude proportional to their equilibrium distance from the center, and where ions on either side of the center move with opposite phase. In general the N eigenmodes for an N ion string can be described by normalized eigenvectors $\boldsymbol{b}^{(p)}$ ($p = 1-N$), where the m'th coordinate $b_m^{(p)}$ ($m = 1-N$) in $\boldsymbol{b}^{(p)}$ is the relative oscillation amplitude of the m'th ion in the string and the sign of the coordinates indicates their relative phase. The vectors $\boldsymbol{b}^{(p)}$ are given in the third column in Table 2.1 for $N = 2$ and 3.

The theory for a single ion in a harmonic potential interacting with a travelling-wave light-field, which was presented in the previous section, can be generalized to describe the interaction with a single ion in an N-ion string in a given motional mode. This can

[3] With modes numbered in order of increasing eigenfrequency.

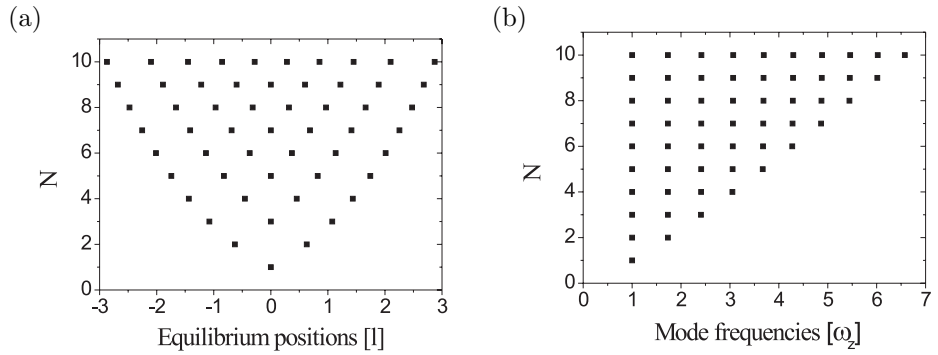

Figure 2.6: (a) Equilibrium positions in units of l [see Eq. (2.2.12)] for $N = 1-10$ ions. (b) Mode frequencies in units of ω_z for $N = 1-10$ ions.

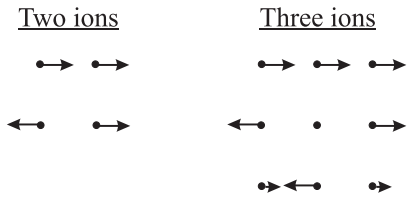

Figure 2.7: Eigenmodes for two and three ions. The uppermost mode is the center-of-mass mode and the mode illustrated below is the breathing mode.

be done by introducing an effective Lamb-Dicke parameter $\eta_{eff,m}$ $(m = 1-N)$ for each of the N ions, which according to James [25] is given by

$$\eta_{eff,m} = \eta_{eg} \frac{b_m^{(p)}}{\sqrt{\omega^{(p)}/\omega_z}}, \tag{2.2.13}$$

where $\omega^{(p)}$ is the eigenfrequency for the mode. In Table 2.1 the vector $\boldsymbol{\eta_{eff}}$ is given for all modes of two and three ions.

N	p	$\boldsymbol{b}^p$	$\omega^{(p)}/\omega_z$	$\boldsymbol{\eta_{eff}}/\eta_{eg}$
2	1	$\frac{1}{\sqrt{2}}(1,1)$	1	$\frac{1}{\sqrt{2}}(1,1)$
	2	$\frac{1}{\sqrt{2}}(-1,1)$	$\sqrt{3}$	$\frac{1}{\sqrt[4]{12}}(-1,1)$
3	1	$\frac{1}{\sqrt{3}}(1,1,1)$	1	$\frac{1}{\sqrt{3}}(1,1,1)$
	2	$\frac{1}{\sqrt{2}}(-1,0,1)$	$\sqrt{3}$	$\frac{1}{\sqrt[4]{12}}(-1,0,1)$
	3	$\frac{1}{\sqrt{6}}(1,-2,1)$	$\sqrt{29/5}$	$\sqrt[4]{\frac{5}{1044}}(1,-2,1)$

Table 2.1: Normalized mode eigenvectors $\boldsymbol{b}^{(p)}$, mode frequencies $\omega^{(p)}$ in units of ω_z and effective Lamb-Dicke parameter vectors with coordinates given in units of η_{eg} for 2 and 3 ions.

Chapter 3

Laser cooling of trapped ions

For more than a decade, laser cooling has played a very significant role in physics [1], and laser cooling techniques are today widely used, for example in the production and study of Bose-Einstein condensates of atomic gases [2]. Here we shall focus on laser cooling of trapped ions, where it is possible to cool a single ion or a string of ions to the motional ground state of the trapping potential with a very large probability. In all schemes for performing quantum gates and creating entangled states with trapped ions (see Chap. 5), the starting point is indeed a string of ions cooled to near its motional ground state and hence obtaining this is a crucial step for the present project.

Laser cooling of ions to their motional ground state starts with the most frequently encountered type of laser cooling, namely Doppler cooling, which was first proposed by Hänsch and Schawlow [27]. Doppler cooling brings the ions to a temperature of about 1 mK, which only for very strongly confining traps corresponds to the ion being near the motional ground state. In the trap relevant for the present work, an additional cooling step is necessary to cool the ions to their motional ground state. This cooling step uses the so-called sideband-cooling technique, as first proposed by Wineland and Dehmelt in 1975 [28].

For the specific sideband-cooling scheme, which we intend to use, a numerical study has been performed in order to investigate how well the scheme performs, at least theoretically, and to determine suitable values for the relevant parameters, e.g., laser intensities.

The chapter is organized as follows. In Sec. 3.1, we first consider Doppler cooling of a two-level ion in order to introduce some general concepts, then the internal levels of the $^{40}Ca^{+}$ ion is presented and Doppler cooling of the $^{40}Ca^{+}$ ion is described. Sec. 3.2 is a small digression, where motional modes and stability of ion strings in a three-dimensional harmonic potential briefly are discussed before we come to the general theory of sideband cooling in Sec. 3.3, where a rate equation description of sideband cooling is given. In Sec. 3.4 our sideband-cooling scheme is described. In Sec. 3.5, the results of the numerical study using quantum Monte Carlo simulations are presented

[1] The Nobel Prize in Physics for 1997 was awarded to Claude Cohen-Tannoudji, Steven Chu and William D. Phillips *"for development of methods to cool and trap atoms with laser light"* [26].

[2] The Nobel Prize in Physics for 2001 was awarded to Eric A. Cornell, Wolfgang Ketterlee and Carl E. Wieman *"for the achievement of Bose-Einstein condensation in dilute gases of alkali atoms, and for early fundamental studies of the properties of the condensates"* [26].

and compared to a simple rate equation model. Finally, a discussion of how to actually measure the distribution of population in the motional quantum states of the trapping potential is given in Sec. 3.6.

3.1 Doppler cooling of trapped ions

In Doppler cooling of atoms or ions, the Doppler effect is exploited together with momentum conservation in the absorption of photons to cool a sample of atoms or ions. In the cooling process scattering of photons is an essential part, which for a two-level ion in a harmonic potential can be described by the same formalism as for a free ion, provided that the oscillation frequency ω_z is much smaller than the transition linewidth Γ [29]. Intuitively, this is understandable since, at least for a saturated transition, scattering of photons takes place on a timescale of Γ^{-1}, which is much faster than the timescale on which an ion changes its potential energy (ω_z^{-1}), i.e., the ion appears to be free. One may also think of it as the linewidth being much larger than the spacing between the vibrational sidebands in Fig. 2.5, such that the sidebands which result from the oscillation in the trapping potential are unresolved. For the present work, the natural linewidth of the (dipole-allowed) transition relevant for Doppler cooling of the $^{40}Ca^{+}$ ion is $2\pi \times 22\,\mathrm{MHz}$, which should be compared to a typical trap frequency of the order of $2\pi \times 1\,\mathrm{MHz}$, thus making it sufficient to treat Doppler cooling of free ions.

3.1.1 Doppler cooling of a free two-level ion

Consider a two-level ion moving in one dimension irradiated by two counter-propagating laser-beams, both having frequency $\omega_L < \omega_{eg}$. When the ion moves towards (away from) one laser, the light appears to be shifted into (out of) resonance due to the Doppler effect, and hence the atom preferentially scatters photons, which slows down the atom (see Fig. 3.1). Since the photon momentum typically is much smaller than the ion momentum, an equilibrium state can only be reached after many scattering events. Therefore, Doppler cooling requires a closed system of internal levels, as for the two-level ion considered here. The equilibrium kinetic energy of the ion has a lower bound, the so-called Doppler cooling limit, which is set by 'recoil-kicks' due to the continuous absorption and spontaneous emission of photons.

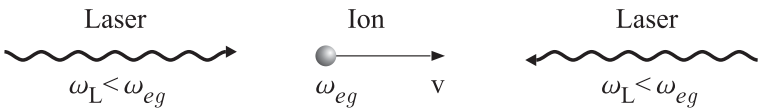

Figure 3.1: Doppler cooling in one dimension of a free ion.

In the following, Doppler cooling in one spatial dimension (z) is described quantitatively. Consider first the force F_+ exerted by a travelling-wave laser beam, propagating in the direction of positive z and having wave-number k_z, on an ion moving with velocity v_z. Recoil-kicks due to spontaneous emission are neglected for the time being since, owing to the spatial symmetry of the radiation pattern, the corresponding net force averaged over many scattering events is zero. The force due to absorption of photons is equal to the photon momentum $\hbar k_z$ times the scattering rate γ defined in Eq. (2.1.31),

with δ replaced by $(\delta - k_z v_z)$ in order to take the Doppler effect into account. Using the notation of Chap. 2, F_+ can be written as

$$F_+ = \hbar k_z \Gamma \frac{|\Omega|^2/4}{(\delta - k_z v_z)^2 + |\Omega|^2/2 + \Gamma^2/4}. \tag{3.1.1}$$

In order to counteract the radiation pressure from this laser and hence to cool the ion along the z-axis, a counter-propagating laser beam must be introduced, as illustrated in Fig. 3.1. Provided that the saturation parameter s is small, the forces from the two laser beams can be added [30] yielding a total force, F_z, which can be written as

$$\begin{aligned} F_z =& F_+ + F_- \\ =& \frac{\hbar k_z \Gamma |\Omega|^2}{4} \left[\frac{1}{(\delta - k_z v_z)^2 + |\Omega|^2/2 + \Gamma^2/4} - \frac{1}{(\delta + k_z v_z)^2 + |\Omega|^2/2 + \Gamma^2/4} \right]. \end{aligned} \tag{3.1.2}$$

F_+, F_- and F_z are illustrated in Fig. 3.2 for $\delta = -\Gamma/2$ and $s = 0.1$. F_z is zero when $v_z = 0$ and varies linearly with a negative slope (for $\delta < 0$) near $v_z = 0$, which means that it acts as a frictional force for small v_z. Expanding F_z, we find indeed that

$$F_z = -\alpha v_z + \mathcal{O}(v_z^3), \tag{3.1.3}$$

where

$$\begin{aligned} \alpha =& -\frac{\partial F_z}{\partial v_z}(v_z = 0) = -\hbar k_z^2 \frac{\delta \Gamma |\Omega|^2}{[\delta^2 + |\Omega|^2/2 + \Gamma^2/4]^2} \\ =& -2\hbar k_z^2 \frac{s}{(1+s)^2} \frac{\delta \Gamma}{\delta^2 + \Gamma^2/4} \end{aligned} \tag{3.1.4}$$

is the friction coefficient. The friction coefficient is positive for $\delta < 0$ and negative for $\delta > 0$, in which case the force is not a frictional force, but rather a heating force which speeds up the ion. By maximizing α with respect to δ, it can easily be found that the friction coefficient is maximal (and positive) for $\delta = -\Gamma/2$ with a maximal value of

$$\alpha_{max} = \frac{2s}{(1+s)^2} \hbar k_z^2. \tag{3.1.5}$$

In Fig. 3.2, where the optimal detuning $\delta = -\Gamma/2$ is used, the straight dash-dotted line is the linear approximation of the cooling force with slope α_{max} for $s = 0.1$.

The frictional cooling force gives rise to a decrease in the kinetic energy of the ion with the cooling rate $R_{cool} = - < F_z v_z > = \alpha < v_z^2 >$. As already mentioned, the ultimate temperature is, however, limited by heating processes due to absorption and spontaneous emission of photons.

Let us consider heating due to spontaneous emission first. The average of the recoil momenta, $< \boldsymbol{p}_{recoil} >$, is zero, however, since the direction of each recoil is random, the ion makes a random walk in momentum space, which means that $< \boldsymbol{p}_{recoil}^2 >$ increases linearly with the number of scattered photons, due to momentum diffusion [20]. The exact value of the heating rate depends on the transition and the laser configuration in question, but it is of the order of $R_{heat} = \gamma(\hbar k_z)^2/m$, where m is the ion mass [20]. In absorption of photons, there is essentially no preferred direction of absorption, when

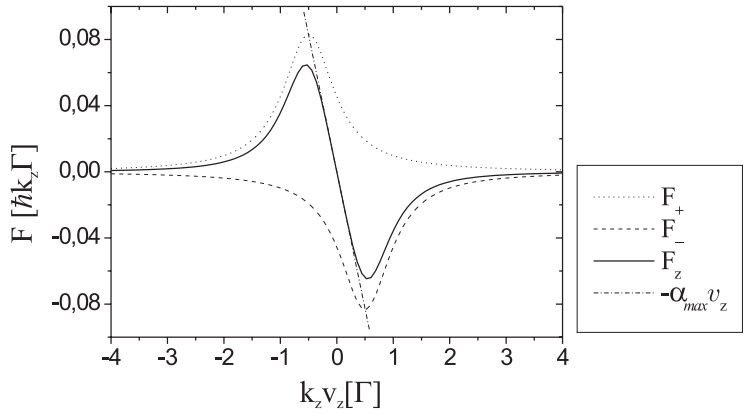

Figure 3.2: Forces exerted by two counter-propagating laser beams, with detuning $-\Gamma/2$ and saturation parameter $s = 0.1$, on an ion moving with velocity v_z. The various curves are discussed in the text.

the ion speed is small ($k_z v_z \ll \Gamma$). Hence each time a photon is absorbed, the ion gets a random momentum kick along the z-axis, which leads to momentum diffusion along the z-axis. The associated heating rate is also of the order of R_{heat} [20]. In equilibrium $R_{cool} = 2R_{heat}$, which for the optimal choice of detuning, $\delta = -\Gamma/2$, yields an equilibrium kinetic energy of $\hbar\Gamma/4$. Defining the temperature T of an ion through its kinetic energy, using the relation $k_B T/2 = m < v_z^2 > /2$, where k_B is Boltzmann's constant, we find that the equilibrium kinetic energy corresponds to the so-called Doppler temperature

$$T_D \equiv \frac{\hbar\Gamma}{2k_B}, \tag{3.1.6}$$

which characterizes the Doppler cooling limit.

Cooling of a free particle in three dimensions would require six pairwise counter-propagating laser beams. In an ion trap it is not strictly necessary to use counter-propagating laser beams since the radiation pressure exerted by a laser beam is counteracted by the trapping potential. Furthermore, cooling in three dimensions can be accomplished using only a single cooling laser beam if it has a component of its wave-vector along each of three principal axes, which is defined by the trapping potential, as discussed in more detail in Chap. 7. In the experiments with single ions or strings of ions described in this thesis, the ions were normally Doppler laser cooled using two beams counter-propagating parallel to the ion string and one laser beam propagating perpendicular to the ion string.

3.1.2 The $^{40}Ca^{+}$ ion

Before a description of Doppler cooling of the $^{40}Ca^{+}$ ion, the relevant internal levels has to be introduced, which is done in the following.

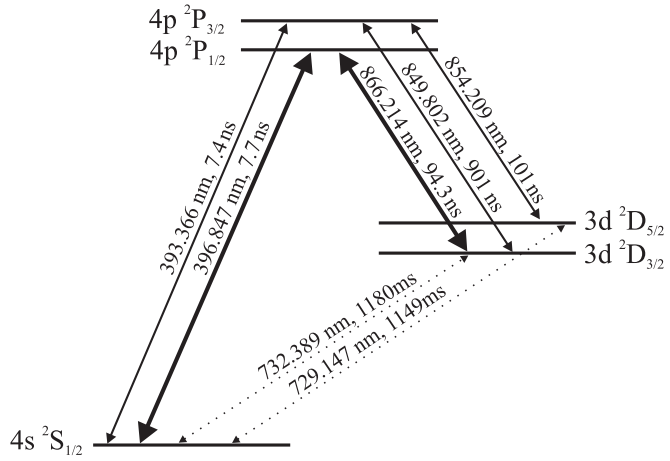

Figure 3.3: Partial level scheme for the $^{40}Ca^+$ ion, showing the five lowest lying energy levels. Solid arrows indicate dipole-allowed transitions, with the fat arrows indicating the Doppler cooling transitions discussed in the text. Dotted arrows indicate electric quadrupole transitions. Transition wavelengths are given together with the inverse of the respective transition rates.

The $^{40}Ca^+$ ion has only a single optically active electron outside a closed shell, and hence for most purposes it can be considered as a one-electron atom. The lowest lying energy levels of the $^{40}Ca^+$ ion are shown in Fig. 3.3. The $4s\,^2S_{1/2}$ ground state is coupled to the $4p\,^2P_{1/2}$ state and the $4p\,^2P_{3/2}$ state by dipole-allowed transitions at 397 nm and 393 nm, respectively, as indicated by the arrows. These P-states are in turn coupled by dipole-allowed transitions at 850 nm, 854 nm and 866 nm to the $3d\,^2D_{3/2}$ state and the $3d\,^2D_{5/2}$ state. The D-states are metastable, with a natural lifetime of a little more than a second, since they are only coupled to the ground state by an electric quadrupole transition.

Apart from the wavelengths, the inverse of the transition rate has been indicated for each transition in Fig. 3.3. The transition rates from the P-states to the D-states will be denoted by Γ_{850}, Γ_{854} and Γ_{866}, where the indices are the transition wavelength in nanometers. The transition rates from the $^2P_{1/2}$ state and the $^2P_{3/2}$ state to the ground state will be denoted $\Gamma_{1/2}$ and $\Gamma_{3/2}$, respectively. The natural lifetime of the $^2P_{1/2}$ state is equal to $(\Gamma_{1/2}+\Gamma_{866})^{-1} = 7.1\,\text{ns}$, and the natural linewidth of the $^2P_{3/2}$ state is equal to $(\Gamma_{3/2}+\Gamma_{850}+\Gamma_{854})^{-1} = 6.8\,\text{ns}$.

Saturation parameters and saturation intensities for each transition can be defined as in Eq. (2.1.29) and Eq. (2.1.30) using the relevant transition strength and frequency instead of Γ and ω_{eg}.

An overview of the transition wavelengths, transition rates and saturation intensities for the S–P and D–P transitions in $^{40}Ca^+$ is given in App. B.

3.1.3 Doppler cooling of the $^{40}Ca^+$ ion

From the level scheme in Fig. 3.3, it is clear that the $^{40}Ca^+$ ion does not contain a closed transition between two levels, for which Doppler cooling was described above.

Nevertheless, Doppler cooling of the $^{40}Ca^+$ ion is possible, e.g., using a laser at 397 nm and one at 866 nm [3]. The main cooling transition for this configuration is the 397 nm $4s\,^2S_{1/2}$–$4p\,^2P_{1/2}$ transition. From the $^2P_{1/2}$ state the ion will not always decay back to the $^2S_{1/2}$ state, but sometimes decay to the $^2D_{3/2}$ state, from which it is pumped back to the $^2P_{1/2}$ state by the laser at 866 nm.

Since the described Doppler cooling process involves three levels and two laser sources, we cannot immediately use the theory for a two-level system. However, since $\Gamma_{1/2}/\Gamma_{866} \approx 12$, and the momentum of a 397 nm photon is about twice as large as that of a 866 nm photon, the cooling limit is expected to be given by the Doppler cooling limit for the 397 nm transition, assuming that the $^2D_{3/2}$–$^2P_{1/2}$ transition is saturated. The Doppler cooling limit for the 397 nm transition is

$$T_D = 0.5\,\mathrm{mK}. \tag{3.1.7}$$

This intuitive argument is supported by a numerical study of laser cooling of $^{138}Ba^+$ [31], which has a level structure similar to $^{40}Ca^+$, showing that the cooling limit mainly is set by the laser parameters for the $^2S_{1/2}$–$^2P_{1/2}$ transition and is of the order of the Doppler cooling limit, although the picture is more complicated than for a simple two-level system.

In practice, the magnetic sublevels of the states involved in the Doppler cooling process have to be considered. For the blue cooling transition, optical pumping into one of the magnetic sublevels of the $^2S_{1/2}$ state has to be avoided, which can be done using light which is linearly polarized (π) with respect to a quantization axis defined by an applied magnetic bias field, or using any combination of π-, σ^+- and σ^--polarized light. For the $^2D_{3/2}$–$^2P_{1/2}$ transition, optical pumping into dark states [32] or magnetic sublevels of the $^2D_{3/2}$ state has to be avoided, which can be done by choosing the red cooling laser light to be linearly polarized perpendicular to the magnetic bias field. This method has been employed in the experiments described in this thesis, however, usage of a (large) magnetic field introduces an unwanted Zeeman-splitting, which will be a drawback in later experiments. Using a small magnetic field, the repumping rate would be limited by the corresponding Larmor frequency, but this limitation can fortunately be circumvented by (fast) rotation of the red cooling laser light polarization using an electrooptic modulator (see Chap. 8).

Finally, we note that the 397 nm photons emitted during the Doppler cooling process are very important since they allow us to observe the ions using an imaging system, which is described in Chap. 8.

3.2 Ion strings in a three-dimensional harmonic potential

When a few ions are Doppler laser-cooled to a sufficiently low temperature and trapped in a linear Paul trap with appropriate trap parameters, they can form a string of ions, having the properties discussed in Sec. 2.2.2. In the following, we first consider the requirements on the trapping parameters for obtaining a string of N ions, assuming

[3] In the following, the cooling lasers driving the 397 nm transition and the 866 nm transition will often be referred to as *the blue cooling laser* and *the red cooling laser* or the *repumper laser*, respectively.

that the Doppler cooling process described above makes the ions sufficiently cold. Then we briefly discuss motional modes in a three-dimensional harmonic potential.

The three-dimensional trapping potential of a linear Paul trap is to a good approximation harmonic of the form

$$U_{3d-harm} = \frac{1}{2}m(\omega_x^2 x^2 + \omega_y^2 y^2 + \omega_z^2 z^2), \tag{3.2.1}$$

where ω_z is called the *axial trap frequency*, and ω_x and ω_y are called the *radial trap frequencies*. Normally, we have $\omega_x \approx \omega_y > \omega_z$. For simplicity we assume in the following that $\omega_x = \omega_y \equiv \omega_r$. If ω_r/ω_z is sufficiently large, the N ions will be squeezed onto a string along the z-axis. More quantitatively, the inequality $2\omega_r^2 + \omega_z^2 > (\omega_{max}^N)^2$, where ω_{max}^N is the highest modefrequency for the N-ion string, must be fulfilled [33], which can be expressed as

$$\left(\frac{\omega_r}{\omega_z}\right)^2 > (\mu_N - 1)/2, \tag{3.2.2}$$

where $\mu_N = (\omega_{max}^N/\omega_z)^2$. To find an approximate expression for $(\mu_N - 1)/2$ as a function of N, the numerically calculated values [25] of $(\mu_N - 1)/2$ are fitted to the expression aN^b over the range $N = 2 - 10$, which roughly is the relevant range in the context of this thesis. Using Eq. (3.2.2) and the fitted values of a and b, the following requirement for obtaining an N-ion string is found:

$$\frac{\omega_r}{\omega_z} > 0.60N^{0.89}. \tag{3.2.3}$$

In general, this inequality must be fulfilled separately by ω_x and ω_y, instead of ω_r, for an ion string to be stable.

For an N-ion string in a three-dimensional potential, there are $3N$ motional modes. N of these modes are the axial modes described in Chap. 2. In addition there are radial center-of-mass modes at frequency ω_x and ω_y and modes at eigenfrequencies which are combinations of ω_x, ω_y and ω_z [34]. All modes can in principle be cooled to near the motional ground state by sideband cooling, but only one axial mode is relevant for quantum logic operations.

3.3 Sideband cooling

In the regime where the linewidth Γ of an internal transition in a trapped ion is much smaller than the trap frequencies, i.e. $\Gamma \ll \omega_x, \omega_y, \omega_z$, the absorption profile for the transition exhibits well-resolved sidebands. This regime is known as the *strong-binding regime* or the *resolved-sideband limit*. For a dipole-transition, Γ is typically several MHz, and getting into the resolved-sideband limit in this case requires a very strongly confining trap. What is more feasible in order to get into the resolved-sideband limit, is to utilize a narrow transition, such as a Raman transition [35] or an electric quadrupole-transition [36, 37] in combination with trap frequencies around a few MHz. In this case it becomes possible to resolve the sideband transitions, which is exploited in *sideband cooling* to cool a single ion or several ions to near their motional ground state in the trap.

As mentioned, sideband cooling of trapped ions was first suggested by Wineland and Dehmelt in 1975 [28]. The first experimental demonstration was reported for a single ion in 1989 by Diedrich *et al.* [36] and has been followed by other demonstrations [35, 37, 38], also for multiple ions (up to four) [9, 34, 39]. The sideband-cooling technique has also been used for cooling of atoms in optical lattices [40, 41, 42] and in an optical dipole-trap [43].

The principle of sideband cooling of a two-level ion is illustrated in Fig. 3.4(a). A laser resonant with a red sideband transition excites the ion from $|g,n\rangle \rightarrow |e,n-1\rangle$, which reduces the vibrational quantum number by one. In the Lamb-Dicke limit, the spontaneous decay from $|e\rangle$ back to $|g\rangle$ is preferentially on the carrier, which completes a cooling cycle, $|g,n\rangle \rightarrow |e,n-1\rangle \rightarrow |g,n-1\rangle$, removing one vibrational quantum from the system but leaving it in its initial internal state. After additional cooling cycles, the ion eventually ends up in the ground state $|g,0\rangle$, where no more excitations can occur.

Note that the Lamb-Dicke parameter must be non-zero since vibrational state changing transitions has to be allowed. On the other hand, it should be sufficiently small that the Lamb-Dicke limit is fulfilled, such that spontaneous decay preferentially happens on the carrier-transition. For this work a Lamb-Dicke parameter of $\eta = 0.2$ is a typical value. Note also that in order to remain in the resolved-sideband limit, the power-broadened linewidth of the sideband-cooling transition should also be much smaller than the trap frequency, which requires that the Rabi-frequency of the sideband-cooling laser is much smaller than ω_x, ω_y and ω_z.

Before going on with a more detailed description of sideband cooling, we should mention the so-called electromagnetically induced transparency (EIT) cooling technique which also allows cooling to near the motional ground state. The technique was proposed by Morigi *et al.* in Ref. [44] and demonstrated by the Innsbruck group for $^{40}Ca^{+}$ [45, 46].

3.3.1 Rate equation description in the Lamb-Dicke limit

In the following, we give a rate equation description of sideband cooling of a two-level ion, which will be useful for describing the scheme we intend to use in $^{40}Ca^{+}$ (Sec. 3.4), and in connection with the quantum Monte Carlo simulations of this cooling scheme (Sec. 3.5).

Here we consider for simplicity only sideband cooling of the axial motion of a single two-level ion. Sideband cooling of a two-level ion can conveniently be described in terms of transitions within the ground state manifold of vibrational levels $\{|g,n\rangle\}$, i.e., transitions from $|g,n\rangle$ to $|g,n''\rangle$ via an excited state $|e,n'\rangle$. Here we assume the Lamb-Dicke limit, considering only the cases where $n' = n, n \pm 1$ and $n'' = n \pm 1$. The corresponding ground state manifold transitions which involve $|g,n\rangle$ are illustrated in Fig. 3.4(b). The transition rate for a $|g,n\rangle \rightarrow |g,n-1\rangle$ (cooling) transition can be written as $\eta_{eg}^2 n A_-$, where the factor of $\eta_{eg}^2 n$ originates from the transition between vibrational levels [see Eq. (2.2.9)], and A_- is a rate which accounts for the internal dynamics of the ion due to the interaction with the sideband-cooling laser. Similarly, the transition rate for a $|g,n\rangle \rightarrow |g,n+1\rangle$ (heating) transition can be written as $\eta_{eg}^2(n+1)A_+$. Expressions for $A_\pm$ will be given below. These transition rates lead to the following rate equation for the occupation probability $P(n)$ of the state $|g,n\rangle$ [47]:

$$\dot{P}(n) = \eta_{eg}^2 \Big[(n+1)\, A_- P(n+1) - [(n+1)\, A_+ + n A_-]\, P(n) + n A_+ P(n-1) \Big]. \quad (3.3.1)$$

From this equation, a differential equation for the average population $\overline{n}$ can be derived:

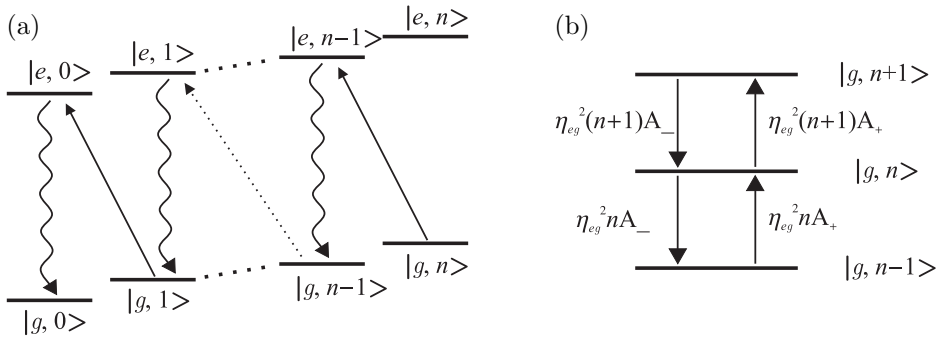

Figure 3.4: (a) Sideband cooling of a two-level ion. Through successive red sideband excitations and spontaneous emission events, the ion ends up in its motional ground state $|g, 0\rangle$. (b) Cooling and heating transitions within the ground state manifold of vibrational levels.

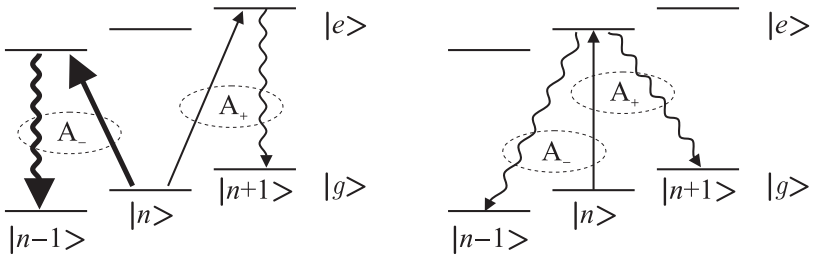

Figure 3.5: Illustration of the terms contained in A_- and A_+. n can change in the optical excitation process (left) or in the spontaneous emission process (right). The fat arrows indicate the intended sideband-cooling cycle, also shown in Fig. 3.4(a).

$$\dot{\overline{n}} = \sum_{n=0}^{\infty} n\dot{P}(n) = -\eta_{eg}^2(A_- - A_+)\overline{n} + \eta_{eg}^2 A_+, \tag{3.3.2}$$

which has the solution

$$\overline{n}(t) = \left(\overline{n}_0 - \overline{n}_{SS}^{(1)}\right) e^{-W^{(1)}t} + \overline{n}_{SS}^{(1)}, \tag{3.3.3}$$

where

$$W^{(1)} = \eta_{eg}^2 \left(A_- - A_+\right) \tag{3.3.4}$$

is the cooling rate,

$$\overline{n}_{SS}^{(1)} = \frac{A_+}{A_- - A_+} \tag{3.3.5}$$

is the steady-state value $\overline{n}(t \to \infty)$ and $\overline{n}_0 = \overline{n}(t = 0)$. The superscript (1) indicates that the expressions are valid to first order in η_{eg}^2. The solution to $\overline{n}(t)$ is only stable when the cooling rate is positive, i.e., when $A_- > A_+$, which also was anticipated from Fig. 3.4(b).

When the Rabi-frequency Ω of the sideband-cooling laser is much less than the transition linewidth Γ, the rates $A_\pm$ have two contributions each, which are illustrated in Fig. 3.5 [48]. Each rate has a contribution from events where n changes in the optical excitation process, $|g, n\rangle \to |e, n \pm 1\rangle \to |g, n \pm 1\rangle$, and one from events where n changes in the spontaneous emission process, $|g, n\rangle \to |e, n\rangle \to |g, n \pm 1\rangle$. In particular, A_- contains a term for the cooling cycle $|g, n\rangle \to |e, n-1\rangle \to |g, n-1\rangle$, where the optical excitation is driven resonantly on the red sideband, whereas A_+ only contains terms from off-resonant excitations due to the cooling laser. When the cooling laser is tuned to the red sideband, $A_\pm$ can be expressed quantitatively in the following way [47, 48]

$$A_\pm = \Gamma[\alpha R(\omega_z) + R(\omega_z \pm \omega_z)], \tag{3.3.6}$$

where

$$R(\delta) = \frac{\Omega^2/4}{\delta^2 + \Gamma^2/4}. \tag{3.3.7}$$

α is a factor of the order of unity, which accounts for the direction of the spontaneously emitted photon and is given by

$$\alpha = \int_0^\pi \sin\theta \, d\theta \cos^2\theta \, W(\theta), \tag{3.3.8}$$

where θ is the angle between the emitted photon and the z-axis, and $W(\theta)$ is a normalized distribution-function for the radiation pattern of the transition. Using $\Gamma \ll \omega_z$ (resolved sideband-limit), the following simple expressions for A_- and A_+ can be found:

$$A_- \approx \Omega^2/\Gamma \quad \text{and} \quad A_+ \approx \frac{\Gamma\Omega^2}{4\omega_z^2}\,(\alpha + 1/4)\,. \tag{3.3.9}$$

Inserting $A_\pm$ into the expressions for $W^{(1)}$ and $\overline{n}_{SS}^{(1)}$, we find

$$W^{(1)} \approx \eta_{eg}^2 \Omega^2/\Gamma \tag{3.3.10}$$

and

$$\overline{n}_{SS}^{(1)} \approx \left(\frac{\Gamma}{2\omega_z}\right)^2 (\alpha + 1/4). \tag{3.3.11}$$

Note that since a change of vibrational state is necessary for cooling, $W^{(1)}$ is proportional to η_{eg}^2. The steady-state value, $\overline{n}_{SS}^{(1)}$, is limited by off-resonant carrier or blue sideband excitations and approaches zero when they become negligible, i.e., when $\Gamma/\omega_z \to 0$.

In Eq. (3.3.6) it was assumed that $\Omega \ll \Gamma$. This restriction can be circumvented in a more detailed calculation (still assuming Ω, $\Gamma \ll \omega_z$) of the rates $A_\pm$, using a density

matrix approach. This has been done in Ref. [49] and yields the following multi-line formula

$$A_-(\omega_z) = -\frac{2\Gamma\Gamma_{coh}R_{coh}(\delta)(1-\alpha)}{\Gamma+4\Gamma_{coh}R_{coh}(\delta)} + \frac{\Omega^2/2}{\Gamma+4\Gamma_{coh}R_{coh}(\delta)} \tag{3.3.12}$$
$$\times \mathrm{Re}\left\{(\omega_z+i\Gamma)\left[\omega_z+i\Gamma+\frac{\Omega^2}{2}\left(\frac{1}{\delta-\omega_z-i\Gamma_{coh}}-\frac{1}{\delta+\omega_z+i\Gamma_{coh}}\right)\right]^{-1}\right.$$
$$\times i\left[\Gamma\left(\frac{1}{\delta+i\Gamma_{coh}}-\frac{1}{\delta-\omega_z-i\Gamma_{coh}}\right)\right.$$
$$\left.\left.-2(1+i\Gamma/\omega_z)\Gamma_{coh}R_{coh}(\delta)\left(\frac{1}{\delta-\omega_z-i\Gamma_{coh}}-\frac{1}{\delta+\omega_z+i\Gamma_{coh}}\right)\right]\right\}$$

and

$$A_+(\omega_z) = A_-(-\omega_z), \tag{3.3.13}$$

where

$$R_{coh}(\delta) = \frac{\Omega^2/4}{\delta^2+\Gamma_{coh}^2}. \tag{3.3.14}$$

Tuning to the red sideband for optimal sideband-cooling conditions corresponds to $\delta = \omega_z$. A coherence decay rate, Γ_{coh}, has been introduced, which is equal to $\Gamma/2$ for a true two-level ion if external decoherence effects are neglected [4], but in general it may deviate from $\Gamma/2$. Using the expressions for $A_\pm$ above with $\delta = \omega_z$, it has been shown that the more general expression for $\overline{n}_{SS}^{(1)}$ is [50, 51]

$$\overline{n}_{SS}^{(1)} = \left(\frac{\Gamma_{coh}}{\omega_z}\right)^2(\alpha+1/4) + \left(\frac{\Omega}{2\omega_z}\right)^2\left(\frac{2\Gamma_{coh}}{\Gamma}-1\right) + \mathcal{O}\left[(\Gamma_{coh}/\omega_z)^4, (\Omega/\omega_z)^4\right]. \tag{3.3.15}$$

When $\Gamma_{coh} = \Gamma/2$, the result in Eq. (3.3.5) is recovered since the second term above cancels exactly.

For the cooling rate, we find from Eq. (3.3.12) to zeroth order in Γ/ω_z, Γ_{coh}/ω_z and Ω/ω_z that

$$W^{(1)} = \eta_{eg}^2\left[A_-(\omega_z) - A_+(\omega_z)\right] = \eta_{eg}^2\frac{\Omega^2}{2\Gamma_{coh}}, \tag{3.3.16}$$

again using $\delta = \omega_z$ in $A_\pm$. For $\Gamma_{coh} = \Gamma/2$ this expression for the cooling rate is identical to Eq. (3.3.10).

The theory above was described with the axial motion of a single ion in mind, but it applies equally well to motion along the x-axis or the y-axis if the axial frequency ω_z is replaced by the corresponding radial frequency ω_x or ω_y. Furthermore, cooling of the various motional modes of an N-ion string is described by the same theory, if ω_z is replaced by the relevant mode frequency, although an effective Lamb-Dicke parameter, as given in Eq. (2.2.13) for the one-dimensional case, should be taken into account.

[4] Corresponding to the decay rate $\Gamma/2$ of ρ_{ge} and ρ_{eg} in Eq. (2.1.26).

3.3.2 Rate equation with second-order contributions

Since Doppler cooling normally is performed prior to sideband cooling, the temperature reached after Doppler cooling defines the starting point for the sideband-cooling process. By equating $k_B T_D$ with $(\overline{n} + 1/2)\hbar\omega_z$, it follows that the average axial vibrational quantum number after Doppler cooling is $\overline{n} \approx 10$ for $\omega_z = 2\pi \times 1.0\,\mathrm{MHz}$, assuming that the Doppler cooling limit of $T_D \approx 0.5\,\mathrm{mK}$ for $^{40}Ca^+$ is reached. Hence, for this experimentally relevant case, there is initially an appreciable population over a large range of vibrational levels. With a Lamb-Dicke parameter of the order of 0.2, the Lamb-Dicke criterion $\sqrt{n+1}\eta_{eg} \ll 1$ is not well fulfilled, and even the Lamb-Dicke parameter itself cannot be said to be *much* smaller than one. These facts suggest that contributions of second order in η_{eg}^2 could be important in describing $\overline{n}(t)$ in sideband cooling. In order to investigate this in the limit where $\sqrt{n+1}\eta_{eg} < 1$, we have extended the rate equation in Eq. (3.3.1) to contain second-order cooling and heating terms due to transitions of the type $|g,n\rangle \rightarrow |g,n\pm 2\rangle$ within the ground state manifold of vibrational levels. There are three types of events which can give rise to such a transition, namely events where (i) n changes by ± 2 in the spontaneous decay ($|g,n\rangle \rightarrow |e,n\rangle \rightarrow |g,n\pm 2\rangle$), (ii) n changes by ± 2 in the optical excitation process ($|g,n\rangle \rightarrow |e,n\pm 2\rangle \rightarrow |g,n\pm 2\rangle$) or (iii) n changes by ± 1 in each of these processes ($|g,n\rangle \rightarrow |e,n\pm 1\rangle \rightarrow |g,n\pm 2\rangle$). In order to describe the internal dynamics by rates analogous to $A_\pm$, we introduce rates A_{++} and A_{--} for the second-order heating and cooling transitions, respectively. Similar to Eq. (3.3.6), $A_{\pm\pm}$ is written as follows in the limit $\Omega \ll \omega_z$:

$$A_{\pm\pm} = \tilde{\alpha} R(\omega_z) + R(\omega_z \pm 2\omega_z) + \alpha R(\omega_z \pm \omega_z), \tag{3.3.17}$$

where

$$\tilde{\alpha} = \int_0^\pi \sin\theta\, d\theta\, \cos^4\theta\, W(\theta) \tag{3.3.18}$$

and the first, second and third terms in $A_{\pm\pm}$ correspond to the events (i), (ii) and (iii), respectively. The total transition probabilities for the second-order cooling and heating transitions are proportional to A_{--} and A_{++}, respectively, to η_{eg}^4 and to an n-dependent factor originating from transitions between the harmonic oscillator eigenstates, which appears from the following extended rate equation [5]:

$$\begin{aligned}\dot{P}(n) =& \eta_{eg}^4 (n+1)(n+2) A_{--} P(n+2) + \eta_{eg}^2 (n+1) A_- P(n+1) \\ &- \eta_{eg}^2 \Big[(n+1)A_+ + nA_- + \eta_{eg}^2 (n+1)(n+2)A_{++} + \eta_{eg}^2 n(n-1)A_{--} \Big] P(n) \\ &+ \eta_{eg}^2 n A_+ P(n-1) + \eta_{eg}^4 n(n-1) A_{++} P(n-2).\end{aligned} \tag{3.3.19}$$

From this rate equation, the following differential equation, which involves both $\overline{n}$ and $\overline{n^2}$, can be found:

$$\begin{aligned}\dot{\overline{n}} = \sum_{n=0}^{\infty} n\dot{P}(n) =& -2\eta_{eg}^4 (A_{--} - A_{++})\overline{n^2} - \eta_{eg}^2 \left[A_- - A_+ - 2\eta_{eg}^2 (A_{--} + 3A_{++}) \right] \overline{n} \\ &+ \eta_{eg}^2 (A_+ + 4\eta_{eg}^2 A_{++}).\end{aligned} \tag{3.3.20}$$

[5] The restriction $\Omega \ll \Gamma \ll \omega_z$ concerns only the rates $A_{\pm\pm}$ and not the rate equation itself. Therefore, the rate equation should be valid for $\Omega, \Gamma \ll \omega_z$ with properly calculated rates $A_{\pm\pm}$.

In order to get rid of the $\overline{n^2}$-term, we make the reasonable assumption that the distribution over the vibrational levels is a thermal distribution [6] such that $\overline{n^2}$ can be replaced by $2\overline{n}^2 + \overline{n}$ (see App. A.1). The resulting non-linear differential equation in $\overline{n}$ is solved in App. A.1. The solution is

$$\overline{n}(t) = \frac{W^{(2)}}{W'}\left[e^{W^{(2)}t}\left(1 + \frac{W^{(2)}}{W'(\overline{n}_0 - \overline{n}^{(2)}_{SS})}\right) - 1\right]^{-1} + \overline{n}^{(2)}_{SS}, \tag{3.3.21}$$

where

$$W' = 4\eta^4_{eg}(A_{--} - A_{++}), \tag{3.3.22}$$

$$W^{(2)} = \sqrt{(W^{(1)} - 8\eta^4_{eg}A_{++})^2 + 4\eta^2_{eg}W'(A_+ + 4\eta^2_{eg}A_{++})} \tag{3.3.23}$$

and

$$\overline{n}^{(2)}_{SS} = \frac{W^{(2)} - W^{(1)}}{2W'} + \frac{A_{++}}{A_{--} - A_{++}}. \tag{3.3.24}$$

In the limit $\eta_{eg} \to 0$, $\overline{n}^{(2)}_{SS}$ approaches $\overline{n}^{(1)}_{SS}$, $W^{(2)}$ approaches $W^{(1)}$, and it can be verified that the exponential decay law in Eq. (3.3.3) is recovered from Eq. (3.3.21). When $e^{W^{(2)}t} \gg 1$, which is fulfilled for all but small t, we find

$$\overline{n}(t) \approx \frac{\overline{n}_0 - \overline{n}^{(2)}_{SS}}{1 + W'(\overline{n}_0 - \overline{n}^{(2)}_{SS})/W^{(2)}} e^{-W^{(2)}t} + \overline{n}^{(2)}_{SS} \qquad \left(e^{W^{(2)}t} \gg 1\right). \tag{3.3.25}$$

Again the decay is exponential, however with a modified cooling rate and steady-state value as compared to the solution in Eq. (3.3.3). Using the expressions for $A_{\pm\pm}$ in Eq. (3.3.17), assuming $\Omega, \Gamma \ll \omega_z$ and expanding $W^{(2)}$ and $\overline{n}^{(2)}_{SS}$ to first order in $(\Gamma/\omega_z)^2$, it can be found that (see App. A.1)

$$W^{(2)} = W^{(1)}\left[1 + 2\eta^2_{eg}\left(\frac{\Gamma}{\omega_z}\right)^2\left[\alpha^2 - \tilde{\alpha} - 1/9 + \eta^2_{eg}\alpha\,(4\tilde{\alpha} + \alpha + 4/9)\right]\right] \tag{3.3.26}$$

$$\overline{n}^{(2)}_{SS} = \overline{n}^{(1)}_{SS}\left[1 + \eta^2_{eg}\frac{4\tilde{\alpha} + \alpha + 4/9}{\alpha + 1/4}\right]. \tag{3.3.27}$$

Note that no expansion in the Lamb-Dicke parameter was made. The relative deviation of $W^{(2)}$ from $W^{(1)}$ and of $\overline{n}^{(2)}_{SS}$ from $\overline{n}^{(1)}_{SS}$ scales as η^2_{eg}. For the cooling rate the deviation is very small due to the presence of the factor $(\Gamma/\omega_z)^2$. To estimate the relative deviation of $\overline{n}^{(2)}_{SS}$ from $\overline{n}^{(1)}_{SS}$, i.e., the second term in the parentheses in Eq. (3.3.27), we have to calculate α and $\tilde{\alpha}$. Using $W(\theta) = 3(1 + \cos^2\theta)/8$, which is relevant for a $\sigma^{\pm}$ transition between the $^2S_{1/2}$ and $^2P_{1/2}$ state in $^{40}Ca^+$ [52], we find $\alpha = 2/5$ and $\tilde{\alpha} = 9/35$. This yields a relative deviation of $2360\eta^2_{eg}/819 \sim 3\eta^2_{eg}$, which equals 11% when $\eta_{eg} = 0.2$.

[6] After the Doppler cooling process, the distribution over vibrational levels is expected to be a thermal distribution. At least to first order in η^2_{eg}, it can then be shown that a thermal distribution is maintained during the sideband-cooling process [48].

From an experimental point of view, it is comforting that for a reasonable value of $\eta = 0.2$, the second-order contribution to the steady-state excitation is only of the order of 10%, which is likely to be small in comparison with 'experimental heating sources'. On the other hand, the effect is not negligible and should be taken into account, e.g., in a comparison between careful numerical studies and the rate equation theory.

3.4 Sideband cooling of the $^{40}Ca^{+}$ ion

In this section the sideband-cooling scheme, which will be implemented using the $^{40}Ca^{+}$ ion, is described.

3.4.1 The sideband-cooling scheme

The three internal levels involved in the sideband-cooling scheme are the two ground state sublevels $^2S_{1/2}(\pm 1/2)$ (the qubit levels) and one of the sublevels of the $^2P_{1/2}$ state. The cooling scheme is illustrated in Fig. 3.6, where the notation $|1\rangle = {}^2S_{1/2}(-1/2)$, $|2_-\rangle = {}^2P_{1/2}(-1/2)$, $|2_+\rangle = {}^2P_{1/2}(+1/2)$ and $|3\rangle = {}^2S_{1/2}(+1/2)$ has been introduced (i.e., $|1\rangle$=$|\downarrow\rangle$, $|3\rangle$=$|\uparrow\rangle$), and the involved sublevel of the $^2P_{1/2}$ state is $|2_-\rangle$ ($|2_+\rangle$ could also have been chosen as discussed below). The intended cooling cycle is the following

$$|1, n\rangle \longrightarrow |3, n-1\rangle \longrightarrow |2_-, n-1\rangle \longrightarrow |1, n-1\rangle\,. \tag{3.4.1}$$

The first step is a resolved sideband two-photon Raman transition driven by the lasers with indices '12' and '32' (Raman lasers in the following) on the red sideband of the $|1\rangle$–$|3\rangle$ transition (assuming $\delta = 0$ in Fig. 3.6). In the second step, a pumping laser (index 'pump') excites the ion from $|3\rangle$ to $|2_-\rangle$ on the carrier (the sidebands are unresolved, but in the Lamb-Dicke limit the transition is mainly via the carrier). A spontaneous decay on the carrier from $|2_-\rangle$ to $|1\rangle$ completes the cooling cycle (in the Lamb-Dicke limit the spontaneous decay is also mainly on the carrier).

From the excited state $|2_-\rangle$ the ion may also decay back to $|3\rangle$ or to the $^2D_{3/2}$ state (dashed wavy arrows in Fig. 3.6). In the former case, the ion will eventually be pumped back to $|2_-\rangle$, whereas the latter possibility necessitates a repumper laser on the 866 nm $^2D_{3/2}$–$^2P_{1/2}$ transition as in Doppler cooling. The scheme works in principle the same way if $|2_+\rangle$ is chosen as the excited state, however, there are some differences for the two choices, which will be discussed below. When the specific excited state is irrelevant for the discussion, we will use the notation $|2\rangle$, meaning either $|2_-\rangle$ or $|2_+\rangle$.

The lasers are supposed to be applied continuously to the ion, so the picture one should have in mind is that the population is making Rabi-oscillations within the family of states $\{|1, n\rangle,\ |3, n-1\rangle,\ |2, n-1\rangle\}$ rather than being transferred stepwise from one state to the next. Occasionally, a change of family takes place, mainly by spontaneous decay from $|2, n-1\rangle$ to the state $|1, n-1\rangle$ in the family $\{|1, n-1\rangle,\ |3, n-2\rangle,\ |2, n-2\rangle\}$. Eventually, the ion ends up in $|1, 0\rangle$ which ideally is a dark state. Only due to excitations on the carrier or a blue sideband of the Raman transition, a fraction of the total population will be found outside the $|1, 0\rangle$ state, mainly oscillating within the $\{|1, 1\rangle,\ |3, 0\rangle,\ |2, 0\rangle\}$ family.

In the following, the Raman transition, the pumping transition and the spontaneous decay are discussed in a little more detail together with the Zeeman-splitting of the ground state sublevels indicated in Fig. 3.6, which turns out to be necessary.

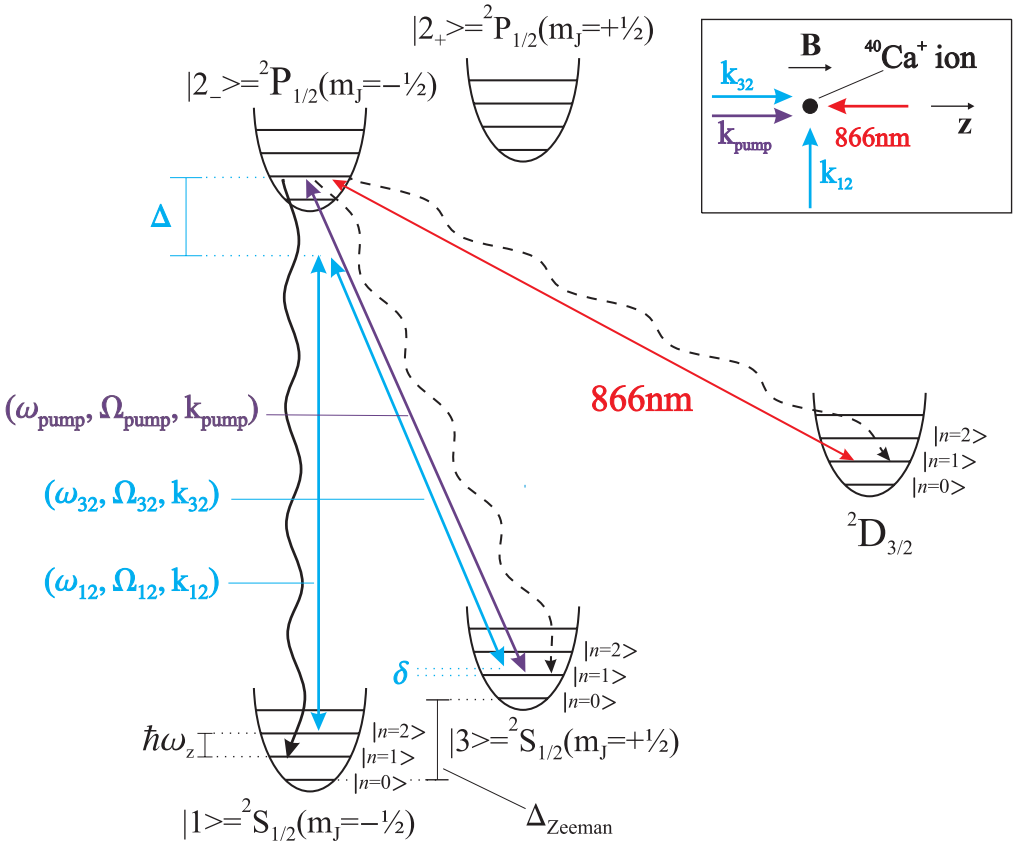

Figure 3.6: The sideband-cooling scheme, illustrated here for a $|1,2\rangle \rightarrow |3,1\rangle \rightarrow |2_-,1\rangle \rightarrow |1,1\rangle$ cooling cycle. For the respective laser beams, ω denotes laser frequencies, Ω denotes Rabi-frequencies, and k denotes wave-numbers. Δ and δ are the one- and two-photon detunings defined in Eq. (3.4.2) and Eq. (3.4.3), Δ_{Zeeman} is the Zeeman-splitting of the ground state sublevels, and $\Delta \gg \Delta_{Zeeman}, \omega_z$ is assumed. In a cooling cycle the Raman lasers (blue) drive red sideband transitions from $|1,n\rangle$ to $|3,n-1\rangle$, ideally with $\delta = 0$. The pumping laser (violet) pumps population from $|3,n-1\rangle$ to $|2_-,n-1\rangle$, and a subsequent spontaneous decay to $|1,n-1\rangle$ completes the cooling cycle. Spontaneous decays back to $|3\rangle$ or to the $^2D_{3/2}$ state (dashed wavy arrows) are also allowed, which in the latter case necessitates a repumper laser (red). The top right inset shows the geometry for implementing the sideband-cooling scheme. The magnetic field **B** defines the quantization axis of the ion.

Raman transition: $|1,n\rangle \rightarrow |3,n''\rangle$

The Raman transition is a two-photon transition between the two ground state sublevels, $|1\rangle$ and $|3\rangle$, with one (both) of the excited states $|2\pm\rangle$ as intermediate state(s). The sidebands on the $|1,n\rangle$–$|3,n''\rangle$ transition are resolved. Referring to Fig. 3.6, the Raman laser beams are characterized by frequency ω_{i2}, Rabi-frequency Ω_{i2} and wave-number

k_{i2} (i=1,3). The one-photon detuning, Δ, and the two-photon detuning, δ, are defined as

$$\Delta = (E_2 - E_1)/\hbar - \omega_{12} - \omega_z, \tag{3.4.2}$$

$$\delta = \Delta_{Zeeman} + \omega_z + (\omega_{12} - \omega_{32}), \tag{3.4.3}$$

where E_1, E_2 and E_3 are the energies of the states $|1\rangle$, $|2\rangle$ and $|3\rangle$, respectively, in the presence of the magnetic field **B**, which gives rise to a Zeeman-splitting of the two ground state sublevels of $\Delta_{Zeeman} = (E_3 - E_1)/\hbar$.

The effective Rabi-frequency for the Raman transition is given by

$$\Omega_{Raman} = \frac{\Omega_{12}\Omega_{32}^*}{\Delta}. \tag{3.4.4}$$

In order to avoid excitation on a one-photon transition from $|1\rangle$ or $|3\rangle$ to $|2\rangle$, Δ is supposed to be much larger than the natural transition linewidth $\Gamma_{1/2}$. In this case the scattering rate on the $|i\rangle$–$|2\rangle$ transition ($i = 1, 3$) is of the order of $\Gamma_{12}\Omega_{i2}^2/\Delta^2$. Since this rate scales as Δ^{-2} and $\Omega_{Raman} \propto \Delta^{-1}$, we can essentially avoid one-photon scattering events by choosing Δ large enough ($\Delta/\Gamma_{1/2} \simeq 50 - 100$) and with the accessible laser-power still obtain an appreciable Raman Rabi-frequency [7].

For driving sideband transitions between $|1\rangle$ and $|3\rangle$, the individual laser frequencies ω_{12} and ω_{32} are in principle irrelevant (assuming $\Delta \gg \Gamma_{1/2}$); the relevant parameter is the frequency *difference* $\omega_{12} - \omega_{32}$. This fact is exploited in reaching the resolved sideband limit for the Raman transition by deriving the two beams from the same laser, such that fluctuations in the laser frequency, which are responsible for the laser linewidth, cancel out in taking the frequency difference. A frequency difference between the Raman beams will be generated and changed in a controlled way using two acousto-optic modulators (AOM's). The effective linewidth of the Raman transition has a contribution from the width and stability of the AOM-drivers ($\sim 20\,\mathrm{kHz}$, full width at $-40\,\mathrm{dB}$). The effective linewidth also has contributions from magnetic field fluctuations leading to fluctuations in Δ_{Zeeman} and from drifts/fluctuations of the trap frequencies.

Finally, we note that for the Raman transition the relevant wave-vector, which, e.g., enters in the Lamb-Dicke parameter, is the difference between the wave-vectors of the Raman beams. Thus the geometry shown in the inset of Fig. 3.6 allows cooling along the trap axis as well as in the radial plane (along both principal axes in the radial plane, although it is not seen from Fig. 3.6).

Pumping-transition: $|3, n''\rangle \rightarrow |2\pm, n'\rangle$

The pumping laser with frequency ω_{pump}, Rabi-frequency Ω_{pump} and wave-number k_{pump} is supposed to couple the state $|3\rangle$ to the excited state $|2_-\rangle$, as indicated in Fig. 3.6, or alternatively to $|2_+\rangle$. Sidebands are unresolved for the pumping transition. $|2_-\rangle$ or $|2_+\rangle$ can be selected as the excited state by choosing the pumping laser to be σ^-- or π-polarized, respectively, with respect to the quantization axis defined by the magnetic field **B** shown in Fig. 3.6.

As for the optimal choice of excited state, we note that if we choose $|2\rangle$=$|2_+\rangle$ (π-polarized pumping beam), excitation from the state $|1\rangle$ to $|2_-\rangle$ would be possible due

[7] Δ should not be much larger than the fine-structure splitting of the P-states, since that would almost cancel the total transition-amplitude [53]. With $\Delta/\Gamma_{1/2} \simeq 50 - 100$ this is no problem.

to the pumping laser, which would lead to heating as illustrated in Fig. 3.7(a). The $|1\rangle$–$|2_-\rangle$ transition can be suppressed as compared to the $|3\rangle$–$|2_+\rangle$ transition if a Zeeman-splitting much larger than $\Gamma_{1/2}$ can be obtained. By choosing $|2\rangle = |2_-\rangle$ instead (σ^--polarized pumping beam), excitation from $|1\rangle$ would be avoided (to the extent that the polarization is pure σ^-).

Finally, we note that when the pumping laser propagates parallel to the z-axis as in Fig. 3.6 (for σ^--polarization), it can induce changes in the state of the axial motion, which gives rise to a small heating contribution. If the pumping beam propagates perpendicular to the z-axis (for π-polarization), it cannot change the vibrational state along the z-axis.

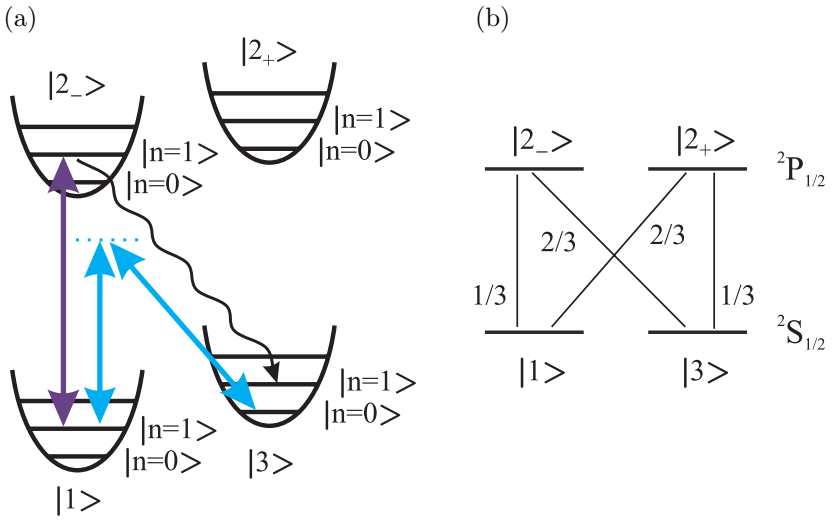

Figure 3.7: The excited state for the pumping transition can be selected through polarization of the pumping beam. (a) Selecting $|2\rangle$=$|2_+\rangle$ by using a π-polarized pumping beam, a heating cycle is introduced due to excitations from $|1\rangle$ to $|2_-\rangle$. Here the $|3, n=0\rangle \rightarrow |1, n=1\rangle \rightarrow |2_-, n=1\rangle \rightarrow |3, n=1\rangle$ heating cycle is shown. (b) Branching ratios for spontaneous decay from sublevels of the $^2P_{1/2}$ state to sublevels of the $^2S_{1/2}$ ground state.

Spontaneous decay: $|2\pm, n'\rangle \rightarrow |1, n\rangle, |3, n''\rangle$

If decay to the $^2D_{3/2}$ state is neglected, the spontaneous decay from the $^2P_{1/2}(\pm 1/2)$ states can happen to either of the ground state sublevels with the probabilities shown in Fig. 3.7(b). A decay (on the carrier) to the state $|1\rangle$ is good in terms of cooling, since it completes a cooling cycle. A decay back to the state $|3\rangle$ is bad, since it introduces an extra step of pumping and decay before a cooling cycle can be completed, which hence slows down the cooling process and gives rise to additional possibilities for heating events to take place. Hence, from that point of view, it would be desirable to optimize the probability for a decay to $|1\rangle$ by choosing $|2\rangle$=$|2_+\rangle$ [see Fig. 3.7(b)]. Unfortunately, this choice introduces the heating cycle in Fig. 3.7(a), and therefore we have to be content

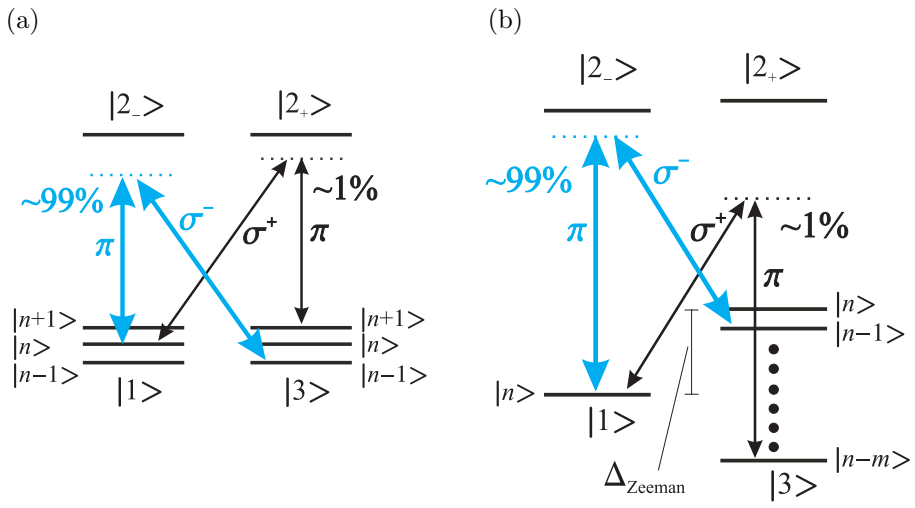

Figure 3.8: Non-perfect polarization of the Raman beams gives rise to unwanted Raman transitions (black thin arrows) which can be suppressed, using a Zeeman-splitting of the ground state sublevels. (a) Without Zeeman-splitting, $\Delta n = 1$ for the unwanted transitions, so that the transition strength is proportional to η^2. (b) With the Zeeman-splitting $\Delta_{Zeeman} \gg \omega_z$, we have $|\Delta n| = m \approx 2\Delta_{Zeeman}/\omega_z - 1 \gg 1$ for the unwanted transitions, such that the transition strength is suppressed by the factor $\eta^{2m} \ll 1$.

with the choice $|2\rangle$=$|2_-\rangle$, unless a very large Zeeman-splitting, $\Delta_{Zeeman} \gg \Gamma_{1/2}$, can be obtained.

Zeeman-splitting

Finally, we shall argue that the Zeeman-splitting is necessary even for a σ^--polarized pumping beam, where the heating cycle in Fig. 3.7(a) would be absent.

Consider the situation in Fig. 3.6, where the $|3\rangle$–$|2\rangle$ Raman beam is σ^--polarized, and the $|1\rangle$–$|2\rangle$ Raman beam is π-polarized, such that $|2_-\rangle$ is the intermediate level for the Raman transition. If $\Delta_{Zeeman} = 0$, and the Raman beams are non-perfectly polarized such that the $|3\rangle$–$|2\rangle$ Raman beam contains a component of σ^+-polarized light ($\sim 1\%$ is not unlikely), then the $|1, n\rangle$–$|3, n+1\rangle$ blue sideband transition illustrated in Fig. 3.8(a) would be driven, which leads to heating.

By using a Zeeman-splitting, $\Delta_{Zeeman} \gg \omega_z$ [see Fig. 3.8(b)], the unwanted Raman transitions due to the σ^+-polarized light will be of the type $|1, n\rangle - |3, n-m\rangle$, where $m \approx 2\Delta_{Zeeman}/\omega_z - 1 \gg 1$ (if $n - m \geq 0$). Hence there will be no such transitions from $|1, 0\rangle$, and in the Lamb-Dicke limit any allowed transitions would be suppressed by the factor $\eta^{2m} \ll 1$.

An alternative possibility would be to choose $\Delta_{Zeeman} = \omega_z$, such that the states $|1, n\rangle$ and $|3, n-1\rangle$ are degenerate [42]. In this case ω_{12}=ω_{32} for red sideband transitions, meaning that the previously 'unwanted' transitions would be red sideband transitions as well. However, when we later on shall be concerned with carrier and blue sideband transitions for performing gate operations, there would be some unwanted

transitions again.

3.4.2 Discussion

In order to achieve a good starting point for performing quantum logic operations, we are aiming at a steady-state value of $\overline{n}_{SS} \lesssim 1\%$ in all 3 spatial dimensions using the sideband-cooling scheme described above. Moreover, the duration of the sideband-cooling process should not be longer than a few milliseconds in order to compete with external heating mechanisms. Thus, assuming a starting point of $\overline{n}_0 \approx 10$, the cooling rate W should be a few kHz or more.

In the description of the sideband-cooling scheme given above, we made the qualitative observations that some heating effects can be avoided by choosing a σ^--polarized pumping beam, i.e., choosing $|2_-\rangle$ as the excited state for the pumping transition. On the other hand, choosing $|2_+\rangle$ could potentially speed up the cooling process, as discussed in connection with the spontaneous decay. Furthermore, it is experimentally advantageous to employ a Zeeman-splitting much larger than the trap frequency in order to avoid heating due to non-perfect polarization of the Raman beams.

Before initiating any experiments, it would, however, be desirable to obtain more quantitative knowledge. Particularly, it would be useful to know if reasonable values for W and $\overline{n}_{SS}$ can be obtained at all, and if so, what an appropriate choice of Rabi-frequencies, Ω_{Raman} and Ω_{pump}, would be. Furthermore, since the two-photon detuning δ experimentally only can be controlled to a certain extent, quantitative knowledge about the influence of a non-zero two-photon detuning on W and $\overline{n}_{SS}$ would be valuable. Finally, differences between the two choices of pumping laser polarization are also relevant.

Although some knowledge can be gained from the literature, as discussed below, none of the studies in the literature, which are known to the author, are directly applicable or sufficiently general to answer the questions about all the above-mentioned parameters. In order to investigate these questions, the study presented in the next section has therefore been carried out using quantum Monte Carlo simulations.

A few theoretical discussions of sideband-cooling schemes for three-level ions can be found in the literature. Marzoli *et al.* [54] describe some special cases of sideband cooling of a three-level ion, of which one case is equivalent to our scheme, however, the description is only valid under the assumption of a low-intensity pumping laser, a small two-photon detuning δ and the Lamb-Dicke limit. Lindberg and Javanainen [55] discuss a scheme in which the cooling mechanism in principle is the same as for our scheme presented above. In their scheme, a pair of Raman beams is also utilized for driving a red sideband transition, but no pumping laser is used. The necessary pumping of population is instead mediated by off-resonant one-photon excitations due to one of the Raman lasers. This requires a rather small one-photon detuning, which unfortunately gives rise to excitation out of the otherwise dark state $|1,0\rangle$, and hence leads to a quite high steady-state temperature. The scheme has been tested experimentally in Innsbruck, showing a ground state occupation probability of $\sim 85\%$ [56]. Finally, Cirac *et al.* discuss laser cooling of a trapped three-level ion in a standing wave light-field in Ref. [57].

Experimentally, the sideband-cooling scheme presented in the previous section has been shown to work using cesium atoms in optical lattices and optical dipole traps [40, 41, 42, 43, 58]. Values of $\overline{n}$ down to 0.024 have been obtained in 2 dimensions with

Lamb-Dicke parameter ~ 0.2 and trap frequencies $\sim 2\pi \times 40\,\mathrm{kHz}$ [40]. In the optical lattice/dipole trap experiments, the trap frequency is generally of the order of $2\pi \times 100\,\mathrm{kHz}$ in one or two dimensions but much weaker ($\sim 2\pi \times 100\,\mathrm{Hz}$) in at least one dimension. Only in the work by Vuletic *et al.* [42] was the trap frequency as high as $2\pi \times 3.2\,\mathrm{MHz}$ in one dimension. These results are, however, hard to transfer or scale to our case with a different atomic system in a linear Paul trap, where trap frequencies of 1 MHz or more can be achieved in all three spatial dimensions. Owing to the high trap frequencies in ion traps, the sideband-cooling scheme should work even better here than in optical lattices or dipole traps.

3.5 Quantum Monte Carlo simulations of the sideband-cooling scheme

The simulations of the sideband-cooling scheme presented in this section are based on the Monte Carlo wavefunction method developed by Mølmer, Castin and Dalibard [59, 60].

In the simulations three internal levels and the vibrational levels from $n = 0$ up to an upper limit, n_{max}, are included. Vibrational state changing transitions with $\Delta n = 0, \pm 1 \pm 2$ are allowed. The one-photon detuning, Δ, is assumed to be so large that the excited state, $|2\rangle$, can be adiabatically eliminated with respect to the Raman transition. Decay and repumping involving the $^2D_{3/2}$ state are neglected. No assumption is made about the intensity of the pumping laser.

3.5.1 Theory

The wavefunction of a three-level ion (internal states $|1\rangle$, $|2\rangle$ and $|3\rangle$) confined in a harmonic potential, is written as

$$|\psi(t)\rangle = \sum_{i=1}^{3} \sum_{n=0}^{n_{max}} C_i^n(t)\,|i,n\rangle\,. \tag{3.5.1}$$

Following the Monte Carlo wavefunction method, this wavefunction is evolved in time according to a set of equations [Eqs. (3.5.6)–(3.5.8) below], interrupted by collapses of the wavefunction at times chosen stochastically according to a probability-distribution for a collapse given by the current wavefunction. One such stochastic evolution of the wavefunction is called a 'history'. A true description of the time-evolution of the system is obtained by averaging over a (large) number of histories.

The wavefunction, or rather the coefficients C_i^n, are evolved using the computer program described in App. C. The included coefficients C_i^n ($n = 0 - n_{max}$) are initialized such that $C_2^n = 0$ and $C_1^n = C_3^n = \sqrt{P(n)/2}$, where $P(n) = \sum_i |C_i^n|^2$ is the population in the vibrational level $|n\rangle$, which is chosen to follow a thermal distribution with average excitation $\overline{n}_0$, i.e., $P(n) = \overline{n_0}^n/(\overline{n_0}+1)^{n+1}$. Since the coefficients C_i^n in this case become small for large n and $P(n)$ is expected to follow a thermal distribution during the cooling process [48], it is a good approximation to neglect coefficients with n larger than some appropriately chosen number n_{max}. In the simulations $\overline{n}_0 \sim 1$ was chosen, meaning that only the final part of the cooling process is simulated, which is sufficient to extract a cooling rate W and a steady-state value $\overline{n}_{SS}$. In most simulations it was sufficient to choose $n_{max} = 5$, but in some cases, where $\overline{n}_{SS}$ was high $n_{max} = 20$ was used.

The time-evolution of the coefficients is governed by the Hamiltonian for the trapped three-level ion interacting with the Raman lasers and the pumping laser, which is

$$H = H_{trap} + H_{ion} + H_{Raman} + H_{pump}, \tag{3.5.2}$$

where

$$H_{trap} + H_{ion} = \hbar\omega_z a^\dagger a + E_2 \left|2\right\rangle \left\langle 2\right| + E_3 \left|3\right\rangle \left\langle 3\right| \quad \left(\frac{1}{2}\hbar\omega_z + E_1 \equiv 0\right) \tag{3.5.3}$$

and, in the rotating-wave approximation,

$$H_{Raman} = \hbar\Omega_{12} e^{i(\boldsymbol{k}_{12}\boldsymbol{z} - \omega_{12}t)} \left|2\right\rangle \left\langle 1\right| + \hbar\Omega_{32} e^{i(\boldsymbol{k}_{32}\boldsymbol{z} - \omega_{32}t)} \left|2\right\rangle \left\langle 3\right| + h.c. \tag{3.5.4}$$

$$H_{pump} = \hbar\Omega_{pump} e^{i(\boldsymbol{k}_{pump}\boldsymbol{z} - \omega_{pump}t)} \left|2\right\rangle \left\langle 3\right| + h.c., \tag{3.5.5}$$

where any constant phases of the laser-fields are assumed to be included in the definition of the Rabi-frequencies. In the simulation-program, the coefficients have to be propagated in timesteps which are smaller than any relevant timescale for the evolution of the system. Due to the large one-photon detuning Δ for the Raman transition, the fastest evolution happens on a timescale of Δ^{-1}, which is much faster than any other process. In order to allow timesteps larger than Δ^{-1}, the state $|2\rangle$ is therefore adiabatically eliminated with respect to the Raman transition. The details of the adiabatic elimination are given in App. C, where it turns out to be useful to define a new set of coefficients, $\widetilde{C}_1^n = C_1^n e^{i\delta t}$, $\widetilde{C}_2^{n'} = C_2^{n'} e^{i(E_2/\hbar+\delta)t}$ and $\widetilde{C}_3^{n''} = C_3^{n''} e^{i(E_3/\hbar+\omega_z)t}$, which obey the following 'equations of motion':

$$\dot{\widetilde{C}}_1^n = -i\left[(n-1)\omega_z - \frac{|\Omega_{12}|^2}{4\Delta}\right]\widetilde{C}_1^n + i\frac{\Omega_{Raman}^*}{4}\sum_{n''}\widetilde{C}_3^{n''}U_{nn''}(-\eta) \tag{3.5.6}$$

$$\dot{\widetilde{C}}_2^{n'} = -i\left(n'\omega_z - \delta\right)\widetilde{C}_2^{n'} - \frac{\Gamma_{1/2}}{2}\widetilde{C}_2^{n'} - i\frac{\Omega_{pump}}{2}\sum_{n''}\widetilde{C}_3^{n''}U_{n'n''}(\eta_{pump}) \tag{3.5.7}$$

$$\begin{aligned}\dot{\widetilde{C}}_3^{n''} = &-i\left[n''\omega_z - \frac{|\Omega_{32}|^2}{4\Delta} - \delta\right]\widetilde{C}_3^{n''} - i\frac{\Omega_{pump}^*}{2}\sum_{n'}\widetilde{C}_2^{n'}U_{n''n'}(-\eta_{pump}) \\ &+ i\frac{\Omega_{Raman}}{4}\sum_{n}\widetilde{C}_1^{n}U_{n''n}(\eta).\end{aligned} \tag{3.5.8}$$

Here $\eta_{pump} = \boldsymbol{k_{pump}} \cdot \boldsymbol{z}_0$ is the Lamb-Dicke parameter for the pumping transition, $\omega = \omega_{12} - \omega_{32}$ and $\eta = (\boldsymbol{k}_{12} - \boldsymbol{k}_{32}) \cdot \boldsymbol{z}_0 = \eta_{12} - \eta_{32}$ is the Lamb-Dicke parameter for the Raman transition, which depends on the difference wave vector of the Raman beams. The Raman Rabi-frequency defined in Eq. (3.4.4) enters naturally in the terms which couple $\widetilde{C}_1^n$ and $\widetilde{C}_3^{n''}$. The terms $|\Omega_{i2}|^2/(4\Delta)$ $(i = 1, 3)$ in Eqs. (3.5.6) and (3.5.8) correspond to the Stark shift of $|1\rangle$ and $|3\rangle$ induced by the respective Raman beams, however, these shifts are unimportant here since they can be removed by redefining E_1 and E_3. The non-Hermitian term, $-\Gamma_{1/2}\widetilde{C}_2^{n'}/2$, in Eq. (3.5.7) accounts for the spontaneous decay from $|2\rangle$ [59, 60].

3.5.2 Simulation results

For all simulations presented below we consider cooling of the axial motion and take $\omega_z = 2\pi \times 0.8\,\mathrm{MHz}$ (and $\Gamma_{1/2} = 2\pi \times 20.7\,\mathrm{MHz}$ for $^{40}Ca^+$). Ω_{Raman}, Ω_{pump} and δ can

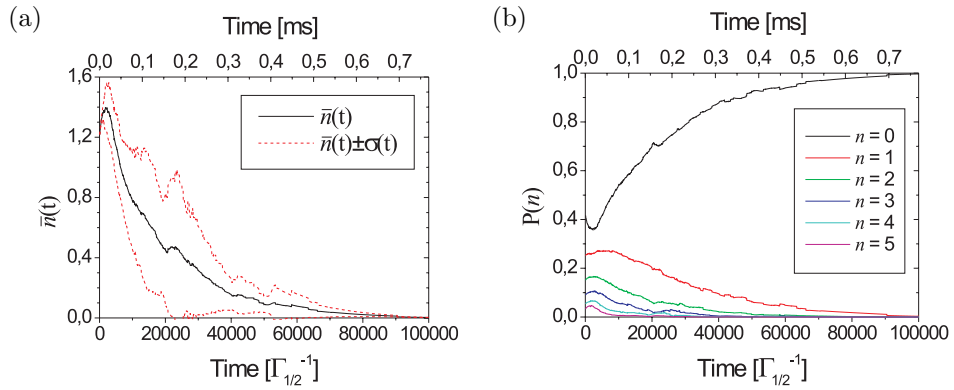

Figure 3.9: Time-evolution of the vibrational state population in a 'typical' quantum Monte Carlo-simulation, averaged over 100 histories with $n_{max} = 5$. σ^--polarized pumping laser, $\Omega_{Raman} = 0.004\Gamma_{1/2} = 0.104\omega_z$, $\Omega_{pump} = 0.04\Gamma_{1/2} = 1.04\omega_z$ and $\delta = 0$. (a) Solid line: $\overline{n}(t)$. Dashed lines: $\overline{n}(t)\pm\sigma(t)$, where $\sigma(t)$ is the standard deviation of $n(t)$ found from the 100 histories. (b) Time-evolution of the population in the vibrational levels, illustrating how the system is driven towards $|n = 0\rangle$.

be varied freely. For the Raman transition the laser configuration shown in Fig. 3.6 is assumed, which means that $|\eta| = k_{32}z_0 = 0.199$. The excited state $|2_-\rangle$ or $|2_+\rangle$ is chosen by the polarization of the pumping laser. For σ^--polarization ($|2_-\rangle$) the pumping laser is assumed to propagate parallel to the z-axis, as in Fig. 3.6 such that $\eta_{pump} = k_{pump}z_0 = 0.199$. For π-polarization ($|2_+\rangle$) the pumping laser is assumed to propagate perpendicular to the z-axis, such that $\eta_{pump} = 0$. The technical details of evolving the wavefunction according to the Monte Carlo wavefunction method are discussed in App. C.

A typical result from a simulation is shown in Fig. 3.9, where $\overline{n}(t)$ and $P(n)$ are obtained from averaging over 100 histories. The increase in $\overline{n}(t)$ seen in Fig. 3.9(a) for times $t \lesssim 3000\Gamma_{1/2}^{-1}$ originates from a coherent transfer of population from $|3, n\rangle$ to $|1, n+1\rangle$ on the Raman transition. For times later than $t \sim 3000\Gamma_{1/2}^{-1}$, the coherence appears to be lost, and $\overline{n}(t)$ can be fitted by an exponential decay law as in Eq. (3.3.3) or Eq. (3.3.20), which yields an estimate of the cooling rate W and the steady-state value $\overline{n}_{SS}$ [8]. Alternatively, the steady-state value can be estimated by averaging over $\overline{n}(t)$ in the steady-state limit of a single history, which provides a more accurate determination of $\overline{n}_{SS}$ than the value obtained from a fit to $\overline{n}(t)$ since only relatively few histories were simulated. Fig. 3.9(b) clearly shows how the population initially distributed over six vibrational levels is driven towards $|n = 0\rangle$ during the sideband-cooling process.

From several simulations of this kind for different values of the pump Rabi-frequency and the Raman Rabi-frequency, both for a σ^--polarized pumping beam ($|2\rangle$=$|2_-\rangle$) and a π-polarized pumping beam ($|2\rangle$=$|2_+\rangle$), we have obtained the results for the cooling rate and the steady-state population plotted in Figs. 3.10 and 3.11 (plotted as symbols, the curves are discussed below). The simulations are quite time-consuming, so in scanning

[8] Even though three internal levels are involved in the present scheme, a rate equation description of $\overline{n}(t)$ is still valid and leads in general to a well-defined cooling rate and steady-state value [57].

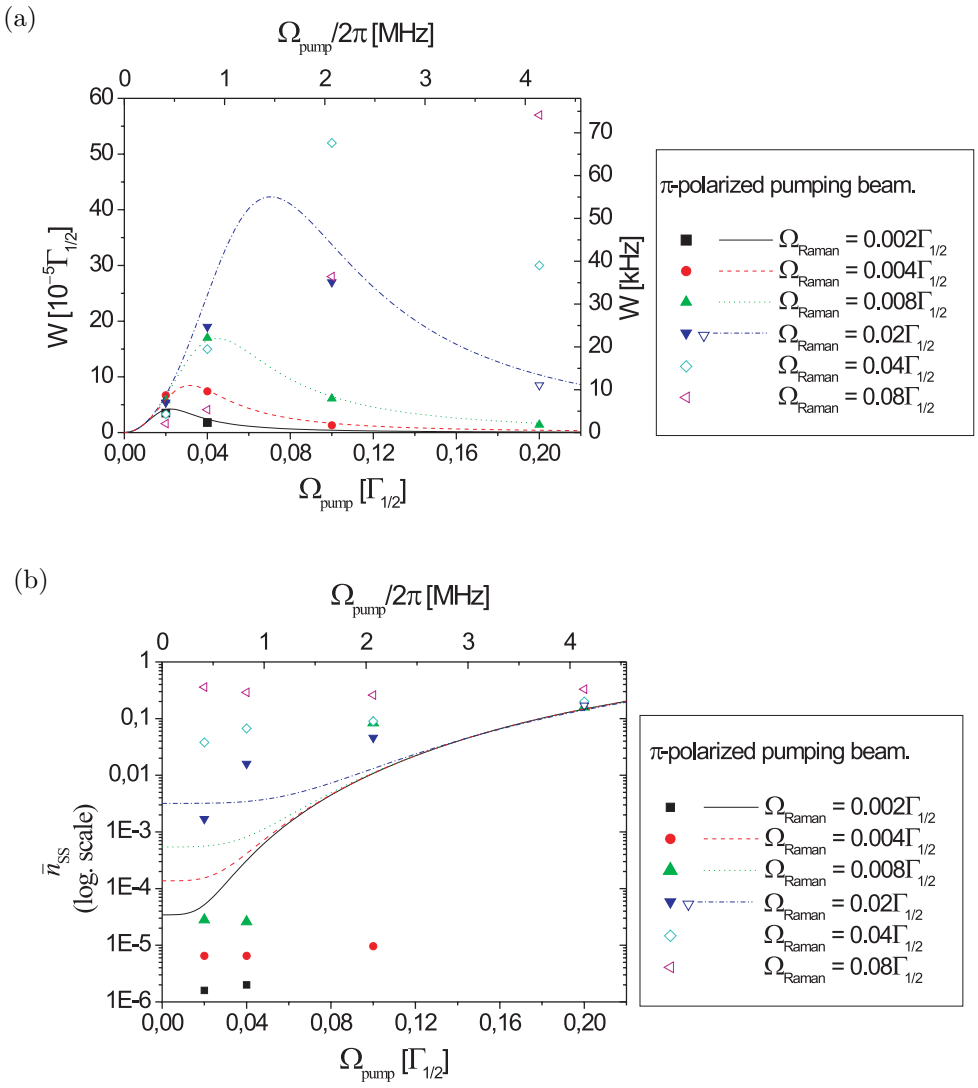

Figure 3.10: Monte Carlo simulation results for a π-polarized pumping beam ($|2\rangle$=$|2_+\rangle$). Solid (open) symbols are based on an average over 100 (25) histories with $n_{max} = 5\,(20)$. The curves are based on the rate equation model described in Sec. 3.5.3. (a) W_π. The green dotted curve is a fit to Eq. (3.5.17). All other curves are plotted according to Eq. (3.5.17) with a and b scaled by Ω^2_{Raman}. (b) $\overline{n}_{SS,\pi}$. The curves are plotted according to Eq. (3.5.26).

over a large parameter space, only relatively few histories were simulated for each set of parameters. Due to the statistical nature of the Monte Carlo wavefunction method and the low number of simulations, the cooling rates are only true within a factor of two, whereas the uncertainties of the steady-state values are below 10%. The results plotted as solid symbols are based on an average over 100 histories with $n_{max} = 5$.

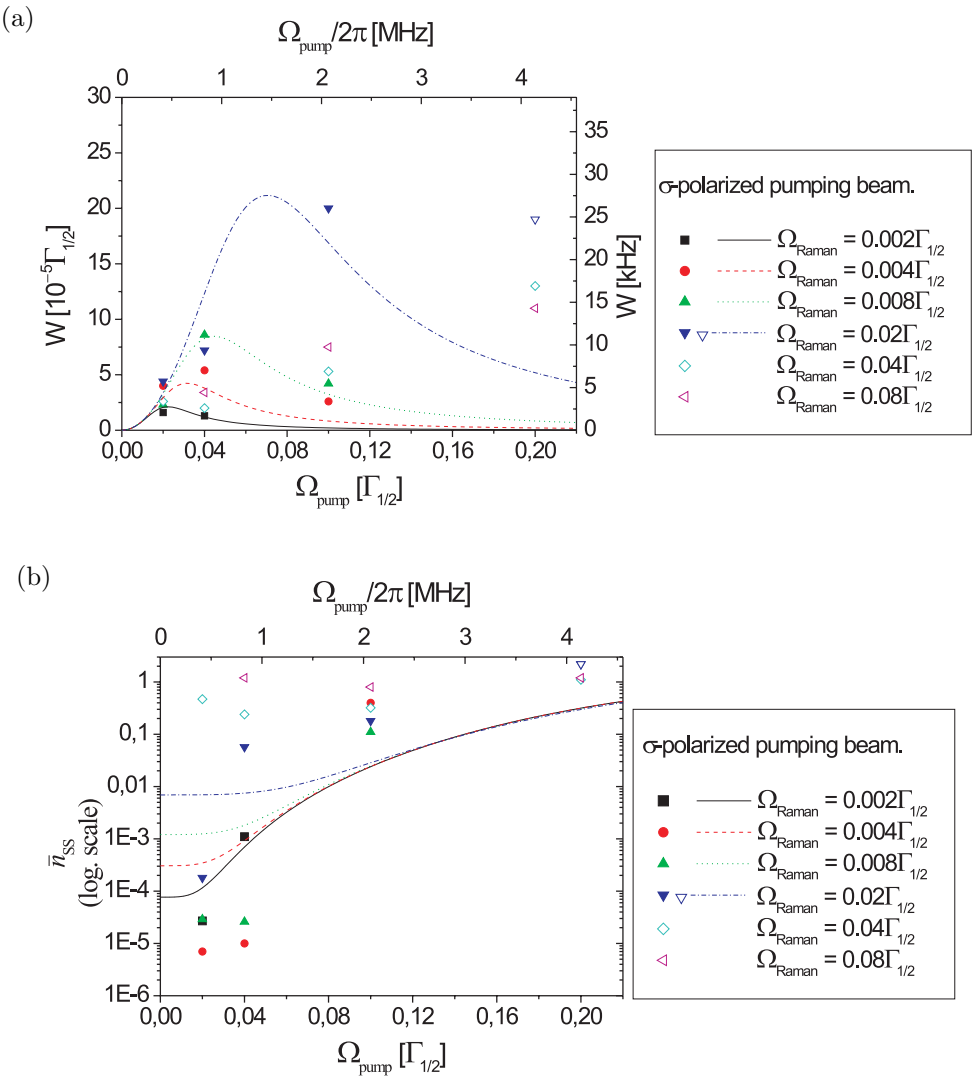

Figure 3.11: Same as Fig. 3.10, but for a σ^--polarized pumping beam ($|2\rangle$=$|2_-\rangle$). (a) W_σ. All curves are plots of $W_\sigma = W_\pi/2$, with W_π given by Eq. (3.5.17) using a and b from Eqs. (3.5.18) and (3.5.19) scaled by Ω^2_{Raman}. (b) $\overline{n}_{SS,\sigma}$. The curves are plotted according to Eq. (3.5.26) with α_π replaced by $1+\alpha_\sigma$.

The results plotted as open symbols are based on an average over 25 histories with $n_{max} = 20$. Except for the simulations with $\Omega_{Raman} = 0.08\Gamma_{1/2}$ or $\Omega_{pump} = 0.2\Gamma_{1/2}$, $\overline{n}_{SS}$ was obtained by averaging over $\overline{n}(t)$ in the steady-state of a single history.

From the cooling rate results in Fig. 3.10(a) and Fig. 3.11(a), we first observe (perhaps with the eye guided by the curves) that the cooling rate approaches zero in the limits of small and large Ω_{pump}. Consequently, for a given Rabi-frequency there is a value of Ω_{pump} for which the cooling rate is maximized. Furthermore, the higher the

Raman Rabi-frequency, the higher is the maximal cooling rate, which could be anticipated, since high Rabi-frequencies imply a fast evolution towards steady-state. On the other hand, high Rabi-frequencies give rise to relatively high values of $\overline{n}_{SS}$, as it can be observed from Fig. 3.10(b) and Fig. 3.11(b), which is due to increased heating from off-resonant excitations on the carrier and the blue sideband. For a π-polarized pumping laser, the cooling rates are generally larger and the steady-state values lower than for a σ-polarized pumping laser. This was anticipated from the discussion of the spontaneous decay in Sec. 3.4.1. However, since a π-polarized pumping laser gives rise to the heating cycle illustrated in Fig. 3.7(a), which is unaccounted for in the simulations, the results for a π-polarized pumping laser are only valid when $\Delta_{Zeeman} \gg \Gamma_{1/2}$. If this is not the case, the results should be considered as upper and lower limits for W_π and $\overline{n}_{SS,\pi}$, respectively.

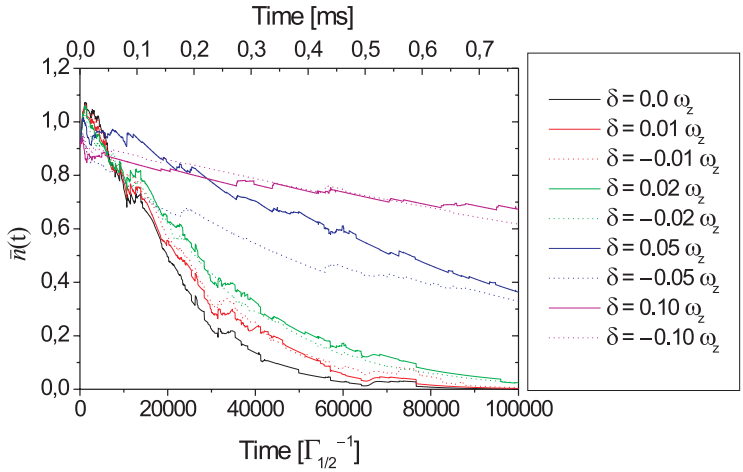

Figure 3.12: Sideband cooling for different values of the two-photon detuning δ using a σ^--polarized pumping laser, $\Omega_{Raman} = 0.004\Gamma_{1/2} = 0.104\omega_z$ and $\Omega_{pump} = 0.04\Gamma_{1/2} = 1.04\omega_z$ as in Fig. 3.9. All curves represent averages over 100 histories with $n_{max} = 5$.

Finally, a few simulations have been carried out in order to investigate the influence of the two-photon detuning, δ. The time-evolution of $\overline{n}(t)$ is shown in Fig. 3.12 for various values of $|\delta|$ in the range $[0.01\omega_z; 0.1\omega_z]$, using a σ^--polarized pumping laser, $\Omega_{pump} = 0.04\Gamma_{1/2}$ and $\Omega_{Raman} = 0.004\Gamma_{1/2}$ as in Fig. 3.9. Simulations with even smaller detunings, $\delta = \pm 0.0005\omega_z, \pm 0.002\omega_z, \pm 0.005\omega_z$, were also carried out, but the curves (not shown) were essentially coincident with the curve where $\delta = 0$. For the considered relatively small Rabi-frequencies, the cooling rate is significantly smaller for $|\delta| \geq 0.05\omega_z$ ($\geq 2\pi \times 40\,\mathrm{kHz}$) than for the case with $\delta = 0$. Presumably, $\overline{n}_{SS,\sigma}$ is also larger. For larger Rabi-frequencies, δ is expected to be less critical due to power broadening effects.

3.5.3 Comparison to a rate equation model

In the following, the results of the Monte Carlo simulations will be compared to a rate equation model. There are two reasons for doing this: First, to check if the results of the

Monte Carlo simulations are reasonable. Second, because some simple formulas which describe the main features of W and $\overline{n}_{SS}$ versus Ω_{pump} and Ω_{Raman} would be very useful for making a quick estimate of the performance of the sideband-cooling scheme for a given set of parameters. Especially, a formula predicting a relation between Ω_{pump} and Ω_{Raman} for which the cooling rate is maximized would be useful. The model will be kept simple since having done the simulations, it would be somewhat redundant to develop a detailed model. In trying to grasp the main behaviour of the cooling rate W and the state value $\overline{n}_{SS}$, some approximations will be made, which make the model more or less empirical.

As a first model, it would be tempting to apply the (first-order) rate equation theory for a two-level system, presented in Sec. 3.3 above, by describing the three-level $^{40}Ca^{+}$ ion in terms of parameters for a two-level ion. As illustrated in Fig. 3.13, we can think of the state $|1\rangle$ as the ground state of a two-level ion with $|3\rangle$ being the excited state. Transitions between these states are driven by the Raman lasers, while 'spontaneous decay' is mediated by pumping from $|3\rangle$ to $|2\rangle$ followed by a real spontaneous decay to $|1\rangle$. Intuitively, it would be reasonable to assume that the 'spontaneous decay rate' is equal to the steady-state population in $|2\rangle$, resulting from driving of the pumping transition, times the real spontaneous decay rate from $|2\rangle$ to $|1\rangle$. Indeed this is the result obtained in Ref. [54] in the limit where $\Omega_{pump} \ll \Gamma_{1/2}$. For an on-resonance pumping laser, we find in our case the 'spontaneous decay rates'

$$\Gamma_{\pi} = \frac{2\Omega_{pump}^2}{3\Gamma_{1/2}} \quad \text{and} \quad \Gamma_{\sigma} = \frac{\Omega_{pump}^2}{3\Gamma_{1/2}} \tag{3.5.9}$$

for a π-polarized pumping laser ($|2\rangle$=$|2_{+}\rangle$) and a σ^{-}-polarized pumping laser ($|2\rangle$=$|2_{-}\rangle$), respectively. The coherence decay rate, which appears in Eq. (3.3.15) and Eq. (3.3.16), is given by [54]

$$\Gamma_{coh} = \frac{\Omega_{pump}^2}{2\Gamma_{1/2}}. \tag{3.5.10}$$

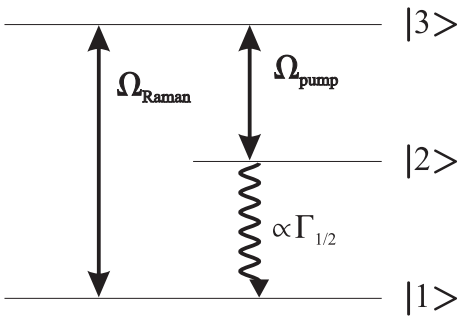

Figure 3.13: The three-level system $\{|1\rangle,|2\rangle,|3\rangle\}$ represented as a two-level system with ground state $|1\rangle$ and excited state $|3\rangle$.

Having established these decay rates, we can immediately obtain expressions for W and $\overline{n}_{SS}$ from the rate equation theory for a two-level system by inserting $\Omega = \Omega_{Raman}$,

$\Gamma = \Gamma_\pi$ or $\Gamma = \Gamma_\sigma$ and the above expression for Γ_{coh}. In the rate equation theory, the resolved sideband limit was assumed, which translates to $\Omega_{Raman}, \Gamma_{\pi,\sigma} \ll \omega_z$ in this model and is reasonably fulfilled in all the simulations. The low-intensity requirement $\Omega_{Raman} \ll \Gamma_{\pi,\sigma}$ is, however, only fulfilled for very few of the simulations, i.e., for the cooling rate we have to use Eq. (3.3.16) (essentially identical to the low-intensity result). For $\overline{n}_{SS}$ we would have to use Eq. (3.3.15). Using Eq. (3.3.16), we find that the cooling rate is given by

$$W = \eta^2 \left(\frac{\Omega_{Raman}}{\Omega_{pump}} \right)^2 \Gamma_{1/2}, \tag{3.5.11}$$

from which we realize that the cooling rate becomes infinitely large when $\Omega_{pump} \to 0$. This is unphysical! Instead, we expect the cooling rate to approach zero when $\Omega_{pump} \to 0$ (as we also found in the simulations) because if there is no pumping to the excited state, cooling cannot take place. We note that the divergence is not just a result of keeping only the lowest order term in Eq. (3.3.16). It appears in this artificial two-level ion because the excitation and the spontaneous decay go via different paths such that it is possible to keep Ω^2 (Ω^2_{Raman}) fixed while decreasing Γ ($\sim \Omega^2_{pump}\Gamma^{-1}_{1/2}$), which is impossible in a real two-level ion, where Ω^2 is proportional to Γ. The divergence would disappear if a 'power-broadening term' proportional to Ω^2 and independent of Γ and Γ_{coh}, was inserted in the denominator of $R_{coh}(\delta)$ [see Eq. (3.3.14)]. There is, however, no justification for inserting such a term since the result quoted in Eq. (3.3.12) [49] is sufficiently general (no restriction on Ω with respect to Γ; $\Omega \ll \omega_z$ still required) that such a 'power-broadening' term already should have appeared if it should be present.

Now, instead of directly applying the two-level rate equation theory as above, we shall try to develop a model which takes more of the three-level features into account [9]. To this end, we divide a cooling or heating cycle of the type $|1, n\rangle \to |3, n''\rangle \to |2, n'\rangle \to |1, n'''\rangle$ into two steps: (i) $|1, n\rangle \to |3, n''\rangle$ and (ii) $|3, n''\rangle \to |2, n'\rangle \to |1, n'''\rangle$, of which step (ii) already has been discussed/solved above in the limit where $\Omega_{pump} \ll \Gamma_{1/2}$. Step (i) is in the following considered as a two-level transition with linewidth $2\Gamma_{coh}$, driven by the Raman lasers with Rabi-frequency $\Omega_{n''n} = \Omega_{Raman}\,|U_{n''n}(\eta)|$. In this case the steady-state population of the 'excited' state $|3, n''\rangle$, which will be denoted $\rho_3(n \to n'')$, is [compare Eq. (2.1.27)]

$$\rho_3(n \to n'') = \frac{\Omega^2_{n''n}/4}{\Gamma^2_{coh} + \delta^2_{n'',n} + \Omega^2_{n''n}/2}, \tag{3.5.12}$$

where

$$\delta_{n'',n} = (n - n'' - 1)\omega_z \tag{3.5.13}$$

when the Raman lasers are tuned to the red sideband of the transition.

To describe steps (i) and (ii) by independent rates, i.e., to neglect any coherent effects in this three-level system, we have to assume that the Rabi-frequencies are small. For step (i), this means $\Omega_{Raman} \ll \Gamma_{coh} \sim \Omega^2_{pump}/\Gamma_{1/2}$. For step (ii), we have already made the assumption $\Omega_{pump} \ll \Gamma_{1/2}$, and hence the relation $\Omega_{Raman} \ll \Omega^2_{pump}/\Gamma_{1/2} \ll \Gamma_{1/2}$ should be fulfilled for the model to be valid. Under these assumptions, the rate by

[9] Klaus Mølmer is acknowledged for fruitful discussions about this model.

which we run through the above cycle is approximately the steady-state population of $|3, n''\rangle$ times the 'decay rate' from $|3, n''\rangle$ to $|1, n'''\rangle$, i.e., $\rho_3(n \to n'')\Gamma_{\pi,\sigma}$.

To estimate the cooling rate, we note that the cooling cycle $|1, n\rangle \to |3, n-1\rangle \to |2, n-1\rangle \to |1, n-1\rangle$ by far is stronger than any other cooling or heating cycles, and we shall therefore only consider this cycle. The rate by which we run through this cooling cycle is given by $\rho_3(n \to n-1)\Gamma_{\pi,\sigma}$ such that the population $P(n)$ in a vibrational state $|n\rangle$ changes as follows

$$\dot{P}(n) = [\rho_3(n+1 \to n)P(n+1) - \rho_3(n \to n-1)P(n)]\,\Gamma_{\pi,\sigma}, \tag{3.5.14}$$

which in the Lamb-Dicke limit yields

$$\dot{\overline{n}} = \sum_{n=0}^{\infty} n\dot{P}(n) = -\frac{\eta^2\Gamma_{\pi,\sigma}\Omega_{Raman}^2}{4} \sum_{n=0}^{\infty} \frac{nP(n)}{\Gamma_{coh}^2 + n\eta^2\Omega_{Raman}^2/2}. \tag{3.5.15}$$

If the denominator in the sum was n-independent, $\overline{n}(t)$ would be described by an exponential decay law with a well-defined cooling rate. Since this is not the case, we assume instead that we can use some sort of (constant) average value for the n in the denominator. This value is denoted by $\tilde{n}$. Under this assumption, the cooling rate for a π-polarized pumping beam is

$$W_\pi = \frac{1}{4}\frac{\eta^2\Omega_{Raman}^2}{\Gamma_{coh}^2 + \tilde{n}\eta^2\Omega_{Raman}^2/2}\Gamma_\pi = \frac{2}{3}\frac{\eta^2(\frac{\Omega_{Raman}}{\Gamma_{1/2}})^2(\frac{\Omega_{pump}}{\Gamma_{1/2}})^2}{(\frac{\Omega_{pump}}{\Gamma_{1/2}})^4 + 2\tilde{n}\eta^2(\frac{\Omega_{Raman}}{\Gamma_{1/2}})^2}\Gamma_{1/2} \tag{3.5.16}$$

and for a σ^--polarized pumping beam $W_\sigma = W_\pi/2$, since $\Gamma_\sigma = \Gamma_\pi/2$. These expressions for the cooling rate are finite when $\Omega_{pump} \to 0$. Even better, the functions approach zero both for small and large values of Ω_{pump}, which also is the case for the Monte Carlo simulation results in Fig. 3.10(a) and Fig. 3.11(a). Comparing with these results, we find indeed a reasonable agreement for $\tilde{n} \sim 1$ which is a typical value of $\overline{n}$ in the simulations. To describe the results even better, we replace $2\eta^2(\Omega_{Raman}/\Gamma_{1/2})^2/3$ and $2\tilde{n}\eta^2(\Omega_{Raman}/\Gamma_{1/2})^2$ in Eq. (3.5.16) by two free parameters a and b, respectively, which yields the following empirical formula:

$$W_\pi = \frac{a(\frac{\Omega_{pump}}{\Gamma_{1/2}})^2}{(\frac{\Omega_{pump}}{\Gamma_{1/2}})^4 + b}\Gamma_{1/2}, \tag{3.5.17}$$

and again $W_\sigma = W_\pi/2$.

Using this expression the results for W_π with $\Omega_{Raman} = 0.008\Gamma_{1/2}$ have been fitted [green dotted line in Fig. 3.10(a)], which yields the following values for a and b

$$a = 6.7 \cdot 10^{-7} = 1.0 \cdot 10^{-2}\left(\frac{\Omega_{Raman}}{\Gamma_{1/2}}\right)^2 \tag{3.5.18}$$

and

$$b = 4.0 \cdot 10^{-6} = 6.3 \cdot 10^{-2}\left(\frac{\Omega_{Raman}}{\Gamma_{1/2}}\right)^2. \tag{3.5.19}$$

These numbers should be compared to the quantities which were replaced by a and b, i.e., $2\eta^2(\Omega_{Raman}/\Gamma_{1/2})^2/3 = 1.7\cdot 10^{-6}$ and $2\tilde{n}\eta^2(\Omega_{Raman}/\Gamma_{1/2})^2 = 5.1\cdot 10^{-6}\tilde{n}$, respectively, which agree with the fitted values of a and b within a factor of 3 (for $\tilde{n}\approx 1$). The other curves in Fig. 3.10(a) are *not* fitted [10]; they are plotted according to Eq. (3.5.17) with the values for a and b given above scaled by Ω^2_{Raman}. For $\Omega_{Raman} = 0.04\Gamma_{1/2}$ and $\Omega_{Raman} = 0.08\Gamma_{1/2}$ no curves are plotted since the model breaks down for large values of Ω_{Raman}. Taking the crudeness of the model into account and the fact that the criterion $\Omega_{Raman} \ll \Omega^2_{pump}/\Gamma_{1/2} \ll \Gamma_{1/2}$ only is fulfilled for the largest values of Ω_{pump}, all the curves fit the cooling rates fairly well. In order to compare to the results for W_σ, the curves in Fig. 3.11(a) are plotted using $W_\sigma = W_\pi/2$ and the values of a and b given above scaled by Ω^2_{Raman}. Again the model agrees reasonably well with the simulations [11]. From Eq. (3.5.17) and the fitted value of b, we find that the cooling rate is maximized for

$$\Omega_{pump} = 0.4\sqrt{\Omega_{Raman}\Gamma_{1/2}}, \tag{3.5.20}$$

for which $W_\pi = 2W_\sigma \approx 0.02\Omega_{Raman}$.

In order to estimate $\overline{n}_{SS}$ from our simple model, we consider only the two lowest vibrational levels where $n = 0, 1$. This is a valid approximation if $\overline{n}_{SS}$ is so low that all population essentially is piled up in the state $|n = 0\rangle$. In the following the cooling rate for going through steps (i) and (ii) above, starting from $|1, 1\rangle$ and ending in $|1, 0\rangle$, is denoted by $\gamma(1 \to 0)$. Similarly, the heating rate for going from $|1, 0\rangle$ to $|1, 1\rangle$ is denoted by $\gamma(0 \to 1)$. In equilibrium $\gamma(1 \to 0)P(1) = \gamma(0 \to 1)P(0)$, which yields $\overline{n}_{SS} \approx P(1) \approx \gamma(0 \to 1)/\gamma(1 \to 0)$ when $\overline{n}_{SS} \ll 1$. The dominating contribution to the cooling rate originates from the cycle $|1, 1\rangle \to |3, 0\rangle \to |2, 0\rangle \to |1, 0\rangle$, which yields the cooling rate

$$\gamma(1 \to 0)_{\pi,\sigma} = \rho_3(1 \to 0)\Gamma_{\pi,\sigma}. \tag{3.5.21}$$

The heating rate $\gamma(0 \to 1)$ has three contributions, namely from events where the vibrational quantum number increases in one of the three transitions in the cycle $|1, 0\rangle \to |3, n''\rangle \to |2, n'\rangle \to |1, 1\rangle$. Heating on the Raman transition gives the contribution $\rho_3(0 \to 1)\Gamma_{\pi,\sigma}$. For a π-polarized pumping beam, the pumping step does not give rise to heating since $\eta_{pump} = 0$ is assumed in this case. For a σ^--polarized pumping beam, the contribution from the pumping transition to the heating rate is $\rho_3(0 \to 0)\eta^2\Gamma_\sigma$. The heating contribution due to the spontaneous decay is $\rho_3(0 \to 0)\eta^2\alpha_{\pi,\sigma}\Gamma_{\pi,\sigma}$, where the values of $\alpha_{\pi,\sigma}$ are given by

$$\alpha_\pi = 2/5 \quad \text{and} \quad \alpha_\sigma = 1/5, \tag{3.5.22}$$

which follows from Eq. (3.3.8) and the distribution-functions [52]

$$W_\pi = \frac{3}{8}(1 + \cos^2\theta) \quad \text{and} \quad W_\sigma = \frac{3}{4}(1 - \cos^2\theta), \tag{3.5.23}$$

[10] Above, the data with $\Omega_{Raman} = 0.008\Gamma_{1/2}$ were used for the fit since these are the data with the smallest Raman Rabi-frequency where the number of simulated data points is maximal (four), thus optimizing the validity of the model and the number of data points.

[11] A fit to Eq. (3.5.17) with a new set of parameters, a and b, does not give a significantly better agreement for W_σ.

where the indices π and σ still denote the polarization of the pumping laser (not the polarization of the emitted photon). In total we find

$$\gamma(0 \to 1)_\pi = \rho_3(0 \to 1)\Gamma_\pi + \rho_3(0 \to 0)\eta^2\alpha_\pi\Gamma_\pi \tag{3.5.24}$$

and

$$\gamma(0 \to 1)_\sigma = \rho_3(0 \to 1)\Gamma_\sigma + \rho_3(0 \to 0)\eta^2(\alpha_\sigma + 1)\Gamma_\sigma. \tag{3.5.25}$$

Thus, we find for a π-polarized pumping beam the steady-state population

$$\begin{aligned}\overline{n}_{SS,\pi} =& \frac{\gamma(0 \to 1)_\pi}{\gamma(1 \to 0)_\pi} \\ =& \frac{\alpha_\pi \left[\Omega_{pump}^4 + 2\eta^2\Omega_{Raman}^2\Gamma_{1/2}^2\right]}{\Omega_{pump}^4 + 4\omega_z^2\Gamma_{1/2}^2 + 2\Omega_{Raman}^2\Gamma_{1/2}^2} + \frac{\Omega_{pump}^4 + 2\eta^2\Omega_{Raman}^2\Gamma_{1/2}^2}{\Omega_{pump}^4 + 16\omega_z^2\Gamma_{1/2}^2 + 2\eta^2\Omega_{Raman}^2\Gamma_{1/2}^2}.\end{aligned} \tag{3.5.26}$$

$\overline{n}_{SS,\sigma}$ can be obtained from $\overline{n}_{SS,\pi}$ by replacing α_π with $1+\alpha_\sigma$. The curves in Fig. 3.10(b) and Fig. 3.11(b) are plotted according to these expressions for the steady-state values. Clearly, the quantitative agreement with the simulations is poor, and fitting the results of the simulations to an empirical expression, with the same dependence on Ω_{pump} as in Eq. (3.5.26), does not lead to a significantly better agreement. We note, however, that the model, strictly speaking, is only valid for the largest values of Ω_{pump}, where the assumption $\overline{n}_{SS} \ll 1$ is only poorly fulfilled. Taking this into account and the fact that the simulated steady-state values vary by as much as six orders of magnitude over the considered range of Ω_{pump}, it is not surprising that the quantitative agreement with the model is doubtful. Qualitatively, the simulations and the rate equation model agree in the sense that $\overline{n}_{SS}$ increases with increasing Ω_{pump} and Ω_{Raman} and that the variation of $\overline{n}_{SS}$ with Ω_{pump} is largest for small values of Ω_{Raman}. Going into more detail, it is furthermore found that in the limit $\Omega_{pump} \to 0$, both the simulation results and the curves based on the rate equation model level off to constant values. For the rate equation model, it follows from Eq. (3.5.26), when $\Omega_{Raman} \ll \omega_z$, that the limiting value for $\overline{n}_{SS}$ when $\Omega_{pump} \to 0$ is proportional to Ω_{Raman}^2. This proportionality is well fulfilled by the simulated values of W_π and W_σ at the lowest used value of $\Omega_{pump} = 0.02\Gamma_{1/2}$ for values of Ω_{Raman} up to $\Omega_{Raman} = 0.02\Gamma_{1/2} = 0.52\omega_z$ (with the exception of W_σ at $\Omega_{Raman} = 0.002\Gamma_{1/2}$).

Now, instead of trying to obtain a better agreement with the simulations by improving the rate equation model for $\overline{n}_{SS}$, we shall take a practical standpoint: It is quite clear that a low value of $\overline{n}_{SS}$ only can be obtained for low values of the Rabi-frequencies. Whether the theoretical value is 10^{-4} or 10^{-5} does not matter too much since experimentally this is anyway very hard to reach and to measure. The cooling rates are well described by Eq. (3.5.17) for small values of Ω_{Raman}, and in this case we have a good rule of thumb [Eq. (3.5.20)] for obtaining the maximal possible cooling rate. Time will show what the corresponding steady-state value turns out to be in experiments.

3.5.4 Conclusion

In conclusion, the simulations show that cooling to near the motional ground state is feasible. Values of $\overline{n}_{SS}$ below 1% are attainable in theory. Cooling rates of some tens

of kHz can be obtained, which is acceptable, since heating from external sources is expected to take place on a time-scale of $\sim 100\,\mathrm{ms}$ (see the discussion in Chap. 7). The cooling rates and $\overline{n}_{SS}$ vary significantly with the Rabi-frequencies, generally with high Rabi-frequencies yielding high cooling rates and large steady-state values. Thus, the fastest way to reach a low steady-state value is to start out with large Rabi-frequencies and lower the Rabi-frequencies according to Eq. (3.5.20), until a sufficiently low steady-state value can be reached. These conclusions hold for both polarizations of the pumping beam, although cooling is more efficient for a π-polarized pumping beam, when $\Delta_{Zeeman} \gg \Gamma_{1/2}$ is fulfilled. To avoid creating the large magnetic field needed to fulfill this criterion, we will use a σ^--polarized pumping in the experiments, but keep in mind that the performance of the scheme can be improved.

Finally, from the results in Fig. 3.12, we learned that the frequency of the Raman transition must be precisely controlled on the level of a few tens of kHz at least for relatively low Rabi-frequencies.

3.6 Measuring the population of motional states

In order to experimentally characterize the performance of the sideband-cooling scheme, i.e., to measure W and $\overline{n}_{SS}$, we need to be able to measure the average vibrational excitation $\overline{n}$ or, even better, the population $P(n)$ in a range of vibrational levels.

Here we describe two well-known methods, one for measuring $\overline{n}$ [35, 37] and one method for determining $P(n)$ over a range of vibrational levels [61]. We assume that it can be determined with 100% efficiency, if the ion is in the internal state $|1\rangle$ or $|3\rangle$. Furthermore, we assume that all population initially is in the internal state $|1\rangle$. Most of the population should already be in $|1,0\rangle$ after sideband cooling, and the rest can be optically pumped to $|1\rangle$ without significantly changing the distribution over vibrational levels, by leaving a σ^--polarized pumping laser on for a period after the sideband-cooling process.

Now, for measuring $\overline{n}$, assume that the distribution over the vibrational levels is a thermal distribution. Starting out with all population in $|1\rangle$ and applying the Raman lasers for a time T on the blue sideband (BSB), the population in $|3\rangle$ will be

$$P^{BSB} = \sum_{n=1}^{\infty} \frac{\overline{n}^{(n-1)}}{(\overline{n}+1)^n} \sin^2\left(|\Omega_{n,n-1}|\, T/2\right), \tag{3.6.1}$$

where $\Omega_{n'n} = \Omega_{Raman} U_{n'n}(\eta)$. By applying several such BSB-pulses and detecting the internal state (starting with all population in $|1\rangle$ before each pulse), P^{BSB} can be measured as the probability for a transfer to $|3\rangle$. A pulse of the same duration on the red sideband (RSB) will result in a population in state $|3\rangle$ of

$$P^{RSB} = \sum_{n=0}^{\infty} \frac{\overline{n}^{(n+1)}}{(\overline{n}+1)^{n+2}} \sin^2\left(|\Omega_{n,n+1}|\, T/2\right), \tag{3.6.2}$$

which can be measured similarly. From Eqs. (3.6.1) and (3.6.2), it follows that

$$\frac{P^{RSB}}{P^{BSB}} = \frac{\overline{n}}{\overline{n}+1} \quad \Longleftrightarrow \quad \overline{n} = \frac{P^{RSB}}{P^{BSB} - P^{RSB}}. \tag{3.6.3}$$

In practice, $T \approx \pi/(\eta\Omega_{Raman})$ should be chosen since this choice maximizes the values of P^{BSB} and P^{RSB} when $\overline{n} \ll 1$, and hence it minimizes the uncertainty on $\overline{n}$. To avoid errors from being slightly off-resonant with the RSB or the BSB, one should measure sideband absorption spectra as in Refs. [35, 37], by varying the two-photon detuning δ around the sideband frequencies.

More detailed information about the population of the vibrational states can be obtained, e.g., by applying a BSB-pulse for a time T and measuring the population in $|3\rangle$ versus T, i.e., measuring Rabi-oscillations of the population. Since the effective BSB Rabi-frequency is n-dependent, the oscillation of the population in $|3\rangle$ will contain many n-dependent frequency components, each with weight $P(n)$. The weight functions $P(n)$ can then be determined from a fit to the measured data (or a Fourier transform), possibly assuming some relation between the weight functions, e.g., that of a thermal state [37, 61].

Chapter 4

Internal state detection

In this chapter we turn to the issue of detection of the internal state of an ion, i.e., discrimination between the qubit states $|\downarrow\rangle = {}^2S_{1/2}(m_J = -1/2)$ and $|\uparrow\rangle = {}^2S_{1/2}(m_J = +1/2)$. As discussed in the previous chapter (where we used the notation $|1\rangle$=$|\downarrow\rangle$and $|3\rangle$=$|\uparrow\rangle$), discrimination between these two states is a prerequisite for gaining knowledge about the vibrational state of the ions. Furthermore, it is necessary for determining the outcome of a quantum logic operation.

The chapter is organized as follows. In Sec. 4.1, we discuss in general terms how to detect the internal state of an ion. In Sec. 4.2 we present the scheme we are pursuing, which is based on two so-called *stimulated Raman adiabatic passage* (STIRAP) processes [62]. The theory behind STIRAP is presented in Sec. 4.2.1, some realistic parameters for the process to work in $^{40}Ca^+$ is given in Sec. 4.2.2, and in Sec. 4.2.3 it is shown how the two STIRAP processes can be turned into a single (fast) process. In Sec. 4.3 an alternative scheme is briefly discussed. A conclusion is given in Sec. 4.4.

4.1 Internal state detection using shelving

To discriminate between the two qubit states, we want to obtain a situation where the ion scatters light only if it initially is in $|\uparrow\rangle$, and not if it initially is in $|\downarrow\rangle$. As mentioned in the description of Doppler cooling, a $^{40}Ca^+$ ion can be observed by detecting 397 nm light emitted during Doppler cooling. If we somehow could take the ion from $|\downarrow\rangle$ to a state where it does not scatter light, while leaving it untouched if it is in $|\uparrow\rangle$, and subsequently apply the cooling lasers and detect fluorescence light, the desired situation will be achieved. From the $^{40}Ca^+$-level scheme in Fig. 3.3, it appears that the non-scattering state of choice is the metastable ${}^2D_{5/2}$ state. When the ion is in the ${}^2D_{5/2}$ state, the optically active electron of the ion is said to be *shelved* [63] and remains in this state until it decays to the ground state by an electric quadrupole transition. Owing to the lifetime of the ${}^2D_{5/2}$ state of more than a second, it is possible to apply the cooling lasers and collect fluorescence light in a sufficiently long period that an unequivocal distinction between the ion being initially in $|\downarrow\rangle$ or $|\uparrow\rangle$ can be made. This is demonstrated in Chap. 10.

The states $|\downarrow\rangle$ and $|\uparrow\rangle$ only differ with respect to the projection of the ions' total spin on the quantization axis ($m_J = \pm 1/2$). Hence a method which state-selectively

takes the ion to the $^2D_{5/2}$ state must exploit this difference. One possible method is to break the degeneracy of the energy levels by applying a (large) magnetic field, followed by a resonant excitation from $|\downarrow\rangle$ to the $^2D_{5/2}$ state, the last step being off-resonant with respect to $|\uparrow\rangle$ [64, 65]. We shall not discuss this possibility any further, but instead turn to the possibility of discriminating between $|\downarrow\rangle$ and $|\uparrow\rangle$ by exploiting the fact that the interaction between the ion and circularly polarized light depends on the internal state $|\downarrow\rangle$ or $|\uparrow\rangle$.

4.2 State-selective shelving using STIRAP

One method for transferring population between two quantum states is by adiabatic population transfer using STIRAP. In STIRAP, population transfer is achieved through the interaction of two laser-pulses with an atomic or molecular quantum system. Experimentally STIRAP has been demonstrated by several groups (see the review article by *Bergmann et al.* [62] and references therein). In most experiments, the laser pulses have effectively been created by letting atomic or molecular beams pass through two displaced laser beams with constant intensity. With cold trapped ions the laser pulses can instead be created using acoustooptic modulators (see Chap. 8).

4.2.1 STIRAP – general theory

In its simplest form, STIRAP takes place in a three-level Λ-system as illustrated in Fig. 4.1(a), with the levels denoted by $|1\rangle$, $|2\rangle$ and $|3\rangle$. Adiabatic population transfer is supposed to take place from $|1\rangle$ to $|3\rangle$, which both are assumed to be long-lived on the timescale of the entire STIRAP process. The three-level system interacts with two laser-fields, which act on the $|1\rangle$–$|2\rangle$ and the $|2\rangle$–$|3\rangle$ transition, respectively, having detunings Δ_{i2} $(i = 1, 3)$ with respect to the transition frequencies and time-dependent Rabi-frequencies $\Omega_{i2}(t)$ as indicated in Fig. 4.1(a). From the excited state $|2\rangle$, coherence can be lost by spontaneous decay to $|1\rangle$ or $|3\rangle$, or population can be lost from the three-level system by spontaneous decay to states outside the system.

The pulse sequence used for STIRAP is shown in Fig. 4.1(b). It is often referred to as being *counter-intuitive* in the sense that the *first* applied pulse, $\Omega_{32}(t)$, couples the *final* state $|3\rangle$ and the intermediate state $|2\rangle$. This coupling creates, however, a new set of eigenstates of the system in such a way that by applying a second pulse, $\Omega_{12}(t)$, on the $|1\rangle$–$|2\rangle$ transition which partly overlaps in time with the first pulse, it is possible to transfer all population from $|1\rangle$ to $|3\rangle$.

In the rotating-wave approximation and assuming real Rabi-frequencies (without loss of generality), the interaction of the laser-fields with the three-level system is described by the Hamiltonian [62]

$$H = \frac{\hbar}{2}\begin{bmatrix} 0 & \Omega_{12}(t) & 0 \\ \Omega_{12}(t) & 2\Delta_{12} & \Omega_{32}(t) \\ 0 & \Omega_{32}(t) & 2(\Delta_{12}-\Delta_{32}) \end{bmatrix} \tag{4.2.1}$$

in the basis $\{|1\rangle, |2\rangle, |3\rangle\}$. When $\Delta_{12} - \Delta_{32} = 0$, the (time-dependent) eigenstates

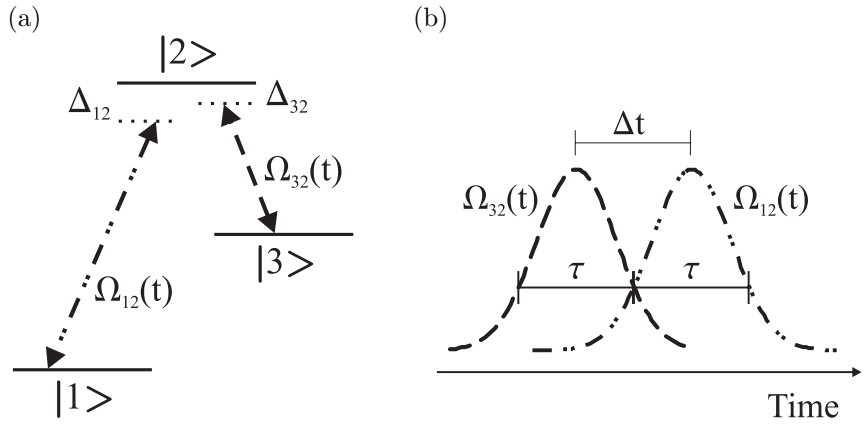

Figure 4.1: STIRAP in a three-level system. (a) The three levels, $|1\rangle$, $|2\rangle$ and $|3\rangle$, and lasers with detuning Δ_{12} and Δ_{32} and time-dependent Rabi-frequencies $\Omega_{12}(t)$ and $\Omega_{32}(t)$. (b) The counter-intuitive pulse sequence, here a set of Gaussian pulses which transfers all population from $|1\rangle$ to $|3\rangle$.

belonging to this Hamiltonian are [66]

$$|\psi_+\rangle = \sin\Theta\sin\Phi\,|1\rangle + \cos\Phi\,|2\rangle + \cos\Theta\sin\Phi\,|3\rangle \tag{4.2.2}$$

$$|\psi_0\rangle = \cos\Theta\,|1\rangle - \sin\Theta\,|3\rangle \tag{4.2.3}$$

$$|\psi_-\rangle = \sin\Theta\cos\Phi\,|1\rangle - \sin\Phi\,|2\rangle + \cos\Theta\cos\Phi\,|3\rangle\,, \tag{4.2.4}$$

where

$$\tan\Theta = \frac{\Omega_{12}}{\Omega_{32}} \quad \text{and} \quad \tan\Phi = \frac{\sqrt{\Omega_{12}^2+\Omega_{32}^2}}{\Delta_{12}+\sqrt{\Delta_{12}^2+\Omega_{12}^2+\Omega_{32}^2}} = \sqrt{-\frac{\omega_-}{\omega_+}}, \tag{4.2.5}$$

with $\omega_\pm$ being defined by the energy eigenvalues

$$\hbar\omega_\pm = \hbar\left(\Delta_{12} \pm \sqrt{\Delta_{12}^2+\Omega_{12}^2+\Omega_{32}^2}\right) \quad \text{and} \quad \hbar\omega_0 = 0. \tag{4.2.6}$$

In order to transfer population from $|1\rangle$ to $|3\rangle$ in a coherent way and without population loss due to spontaneous decay, it is desirable not to excite state $|2\rangle$. Of the three eigenstates above, the state $|\psi_0\rangle$ is therefore particularly interesting, since it is a coherent superposition of only state $|1\rangle$ and $|3\rangle$. Starting out with all population in $|1\rangle$ and assuming $\Omega_{32} \gg \Omega_{12}$ ($\Theta = 0$), it can be observed that $|\langle\psi_0|1\rangle| = 1$, and $|\langle\psi_\pm|1\rangle| = 0$, i.e., in terms of the new eigenstates, the system is in the state $|\psi_0\rangle$. Then, by lowering Ω_{32} while increasing Ω_{12} until $\Omega_{12} \gg \Omega_{32}$, the angle Θ changes from 0 to $\pi/2$, i.e., the state $|\psi_0\rangle$ is rotated from $|1\rangle$ to $|3\rangle$. At the same time $|\psi_\pm\rangle$ is being rotated as well. Now, if this change of Rabi-frequencies is performed in such a way that the quantum state of the system adiabatically follows $|\psi_0\rangle$, while all three eigenstates are being rotated, then population will be transferred from $|1\rangle$ to $|3\rangle$. Adiabatic following

requires that [67]

$$\left|\frac{d\Theta}{dt}\right| = \left|\frac{\dot{\Omega}_{12}\Omega_{32} - \Omega_{12}\dot{\Omega}_{32}}{\Omega_{12}^2 + \Omega_{32}^2}\right| \ll |\omega_\pm - \omega_0| \,. \tag{4.2.7}$$

For the r.h.s of this inequality always to be large, we have to assume that $\Delta_{12} = \Delta_{32} \ll \Omega_{12}, \Omega_{32}$, which implies $|\omega_\pm - \omega_0| = \sqrt{\Omega_{12}^2 + \Omega_{32}^2}$. If the Rabi-frequencies vary smoothly in time over the duration T of the STIRAP process, then, since Θ changes by $\pi/2$, the average value of $|d\Theta/dt|$ is $\pi/(2T)$. Inserting this average value in the adiabaticity criterion Eq. (4.2.7) the condition

$$\sqrt{\Omega_{12}^2 + \Omega_{32}^2}\, T \gg 1 \tag{4.2.8}$$

is obtained.

The Rabi-frequencies can be varied in many different ways, while fulfilling the adiabaticity criterion [68], however, the most frequently encountered time-dependence of the Rabi-frequencies is a Gaussian pulse, having its origin in the beam-experiments where the time-dependence is defined by the usual Gaussian profile of the laser-beams. In the following it is assumed that the pulses are Gaussian, as shown in Fig. 4.1(b), of the form

$$\Omega_{12}(t) = \Omega_{12}^0 \exp\left[-\left(\frac{t - \Delta t/2}{\tau}\right)^2\right] \tag{4.2.9}$$

$$\Omega_{32}(t) = \Omega_{32}^0 \exp\left[-\left(\frac{t + \Delta t/2}{\tau}\right)^2\right], \tag{4.2.10}$$

with a characteristic width τ and a delay Δt between the pulses. With this choice of pulses, it can be shown that the optimal choice of delay with respect to the adiabaticity criterion is $\Delta t = \tau \equiv \Delta t_{ad}$ [67]. In practice, the pulses are truncated at positive and negative times where the value of the exponential functions is negligible.

4.2.2 State-selective shelving in $^{40}Ca^+$ using STIRAP

A state-selective transfer of population from $|\downarrow\rangle$ to the $^2D_{5/2}$ state can be achieved using two STIRAP processes as illustrated in Fig. 4.2. The first STIRAP process takes population from the $^2S_{1/2}$ state to the $^2D_{3/2}$ state, using the $^2P_{1/2}$ state as the excited state in the STIRAP process. By using a σ^+-polarized laser, $|\downarrow\rangle$ is coupled to the $^2P_{1/2}(m_J = +1/2)$ level, while $|\uparrow\rangle$ is unaffected, thus making this STIRAP process state-selective. By a second STIRAP process, population is transferred from the $^2D_{3/2}$ state to the $^2D_{5/2}$ state [1]. This step need not take place between any particular sublevels, however, in order to optimize the coupling between the various sublevels and hence to obtain the largest Rabi-frequencies at a given laser-intensity, the entire STIRAP process should take place as follows: $|\downarrow\rangle$–$^2P_{1/2}(m_J = +1/2)$–$^2D_{3/2}(m_J = +3/2)$–$^2P_{3/2}(m_J = +3/2)$–$^2D_{5/2}(m_J = +5/2)$.

In the theory described above, STIRAP works with 100% efficiency if the adiabaticity criterion is fulfilled. In real life there are of course a range of practical problems, which will be addressed in the following.

[1] Note that a single STIRAP process from the ground state to the $^2D_{5/2}$ state with the $^2P_{3/2}$ state as the excited state cannot be state-selective.

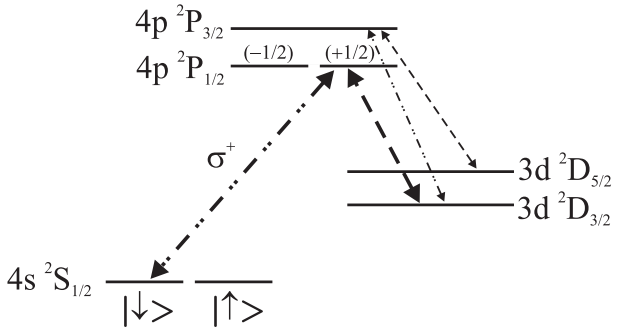

Figure 4.2: The double STIRAP-process in $^{40}Ca^{+}$. The first STIRAP process (thick arrows) from $|\downarrow\rangle$ to the $^2D_{3/2}$ state is state-selective since $|\uparrow\rangle$ is unaffected by the σ^+-polarized beam on the $^2S_{1/2}$-$^2P_{1/2}$ transition. The second STIRAP process (thin arrows) goes from the $^2D_{3/2}$ state to the $^2D_{5/2}$ state.

Non-zero two-photon detuning

To what extent can we keep the two-photon detuning $\delta \equiv \Delta_{12} - \Delta_{32}$ equal to zero, and what are the implications if it is non-zero? The answer to the first part of the question is 'a few MHz', having its origin in laser frequency drifts (see Chap. 8). The implications of a non-zero two-photon detuning are discussed in Refs. [69, 70], where it is shown that a non-zero two-photon detuning results in an admixture of the excited state $|2\rangle$ in ψ_0. In particular, the loss mechanism presented by spontaneous decay from $|2\rangle$ and out of the system is considered. In the limit where $|\delta|\,, |\Delta_{i2}| \ll \Omega^0 \equiv \Omega^0_{12} = \Omega^0_{32}$ $(i = 1, 3)$ the transfer efficiency, i.e., the probability by which population is transferred from $|1\rangle$ to $|3\rangle$, is roughly equal to $\exp[-C\Gamma_2\tau\delta^2/(\Omega^0)^2]$, where C is a constant which depends on the specific pulse sequence and Γ_2 is the decay rate from $|2\rangle$ [70].

In order to determine suitable parameters for the Rabi-frequency Ω^0, the pulse width τ, the delay Δt and an average one-photon detuning $\Delta = (\Delta_{12} + \Delta_{32})/2$ for a realistic non-zero two-photon detuning, some numerical simulations have been performed by Frank K. Jensen [71] using the formalism of Ref. [70]. The simulations were performed with the $^2D_{3/2}$-$^2P_{3/2}$-$^2D_{5/2}$ STIRAP process in mind, using $\Gamma_2 = \Gamma_{3/2} = 2\pi \times 21.5\,\mathrm{MHz}$, i.e., the spontaneous decay rate from the $^2P_{3/2}$ state to the ground state, but, as discussed below, the results can almost directly be applied to the other STIRAP process. First we consider the variation in transfer efficiency with the delay Δt. With the Rabi-frequency varied in the range $\Omega^0/2\pi = 80 - 800\,\mathrm{MHz}$, and with fixed $\Delta = 2\pi \times 5\,\mathrm{MHz}$ and $\delta = 2\pi \times 5\,\mathrm{MHz}$, which is believed to be a worst-case scenario for the two-photon detuning, it was found that the transfer efficiency only varied weakly with the delay, but having a maximum around $\Delta t = 1.3\tau \equiv \Delta t_{sp}$. Although the optimum with respect to non-adiabatic losses (which is not taken into account in the simulations) is $\Delta t_{ad} = \tau$, it should be easy to keep both types of losses small, since the dependence on Δt was found to be weak in the simulations. In all further simulations $\Delta t = 1.3\tau$ was used. It was then found that the transfer efficiency is relatively insensitive to the one-photon detuning over the range $\Delta/2\pi = 0 - 500\,\mathrm{MHz}$, when $|\delta|\,/2\pi < 10\,\mathrm{MHz}$ and with the Rabi-frequency $\Omega^0/2\pi = 150\,\mathrm{MHz}$ and the pulse width $\tau = 5\,\mu\mathrm{s}$ fixed. In accordance with the expression $\exp[-C\Gamma_2\tau\delta^2/(\Omega^0)^2]$ for the

transfer efficiency, the simulations also showed that large Rabi-frequencies, small τ and, of course, a small two-photon detuning gave a high transfer efficiency. With a realistic set of parameters of

$$\tau = 5\,\mu\text{s}, \qquad \Delta t = 6.5\,\mu\text{s}, \qquad \Omega^0 = 2\pi \times 300\,\text{MHz} \tag{4.2.11}$$

and, say, $\Delta = 2\pi \times 20\,\text{MHz}$, the transfer efficiency is $\sim 97\%$ for the worst-case two-photon detuning of $|\delta|/2\pi = 5\,\text{MHz}$. If the two-photon detuning is halved to $|\delta|/2\pi = 2.5\,\text{MHz}$, the transfer efficiency would be $\sim 99\%$. The adiabaticity criterion is well fulfilled by the parameters above. The stated Rabi-frequency requires intensities of about $3 \cdot 10^5\,\text{mW/cm}^2$ and $3 \cdot 10^4\,\text{mW/cm}^2$ for the 850 nm $^2D_{3/2}$-$^2P_{3/2}$ transition and the 854 nm $^2D_{5/2}$-$^2P_{3/2}$ transition, respectively, which in both cases is realistic.

To a large extent the results of the simulations also apply to the $|\downarrow\rangle$–$^2P_{1/2}(m_J = +1/2)$–$^2D_{3/2}$ STIRAP process since the spontaneous decay rate from the $^2P_{1/2}$ state is almost the same as for the $^2P_{3/2}$ state. The transfer efficiency may even be larger for this first STIRAP process since the spontaneous decay from $^2P_{1/2}(m_J = +1/2)$ goes back to $|\downarrow\rangle$ in $\sim 2/3$ of the cases. Thus population remains within the three-level system and has another chance of being transferred to the $^2D_{3/2}$ state. Using $\Omega^0 = 2\pi \times 300\,\text{MHz}$ again, intensities of $3 \cdot 10^4\,\text{mW/cm}^2$ are required on both transitions, which once again is realistic.

Finite ion-velocity

The initial tests of the STIRAP-scheme will be performed on a Doppler laser-cooled ion. Since the effective power-broadened linewidths of the transitions are larger than the trap frequency, the ion can to a good approximation be treated as a free particle with respect to both two-photon STIRAP transitions. If the Doppler cooling limit is reached, the root-mean-square velocity is $v_{\text{rms}} \approx 0.6\,\text{m/s}$, which results in a Doppler-shift of $2\pi \times 0.7\,\text{MHz}$ of the 850 nm and the 854 nm D–P transitions and in general a non-zero two-photon detuning in the STIRAP process. If the 850 nm and the 854 nm beams are co-propagating, the first-order Doppler-shift cancels to within 0.5% and hence it is not expected to cause any problems. For the $|\downarrow\rangle$–$^2P_{1/2}(m_J = +1/2)$–$^2D_{3/2}$ STIRAP process involving the 397 nm transition and the 866 nm transition, the same trick does not work very well due to the larger wavelength difference, and we end up with a Doppler-shift of $2\pi \times 0.8\,\text{MHz}$ using co-propagating beams and the same value for v_{rms} as above. According to the simulations discussed above, a two-photon detuning of this order of magnitude would still allow population transfer with $> 99\%$ probability, however, since the ion sometimes moves faster than v_{rms} and the Doppler cooling limit is not necessarily reached, a larger two-photon detuning cannot be ruled out. If the two-photon detuning turns out to be critical for this STIRAP process, it can be made less sensitive to the two-photon detuning by increasing the Rabi-frequency on one or both of the transitions.

After sideband cooling the Doppler-shift is not expected to present any problem.

Other effects

In the theory section we considered a pure three-level system, however, both STIRAP processes in $^{40}Ca^+$ could in principle involve several Zeeman sublevels, for example up to 14 magnetic sublevels for the $^2D_{3/2}$-$^2P_{3/2}$-$^2D_{5/2}$ STIRAP process. If the polarization

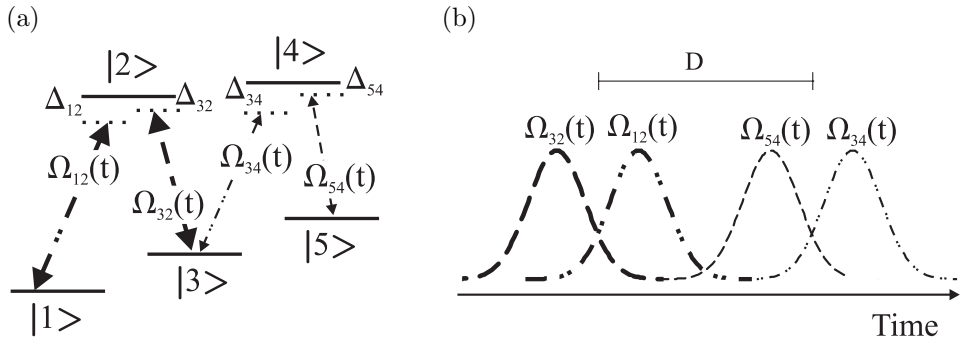

Figure 4.3: STIRAP in a five-level system. (a) The five levels and lasers with detunings Δ_{12}, Δ_{32}, Δ_{34}, and Δ_{54} and Rabi-frequencies $\Omega_{12}(t)$, $\Omega_{32}(t)$, $\Omega_{34}(t)$ and $\Omega_{54}(t)$. (b) Two STIRAP pulse sequences, with delay D between them, which transfer all population from $|1\rangle$ to $|5\rangle$.

of the laser-fields is chosen right, it all comes down to three relevant levels again. If not, one may end up with a very rich multi-level system, where adiabatic transfer in some cases is blocked. This is discussed further in Ref. [62] and in a series of papers on STIRAP in multi-level systems [72, 73, 74].

Varying Zeeman-shifts induced by fluctuating magnetic fields will contribute to a non-zero two-photon detuning, hence any such fields should be shielded to the necessary extent.

Furthermore, any residual so-called micromotion, which is a fast quiver motion at the same frequency as the oscillation frequency of a voltage applied to the trap electrodes (see Chap. 7 and Chap. 9), will contribute to the two-photon detuning. Hence micromotion must be minimized.

Since the STIRAP process relies on maintaining a coherence between two internal states of the ion, the laser sources should have a coherence time longer than the duration of the STIRAP process, and jumps of the laser light phase should be avoided.

4.2.3 STIRAP in a five-level system

To be able to consider the two STIRAP processes as separate processes, as we did above, the two sets of pulses need to be separated in time. One might wonder if it is possible to describe the two processes as one and possibly also reduce the duration of the double STIRAP process by overlapping the two sets of STIRAP pulses in time instead of running them as individual processes.

In order to describe this situation, we consider the five-level system shown in Fig. 4.3(a) interacting with four laser beams having the indicated Rabi-frequencies and one-photon detunings. For each of the two three-level systems, $|1\rangle$-$|2\rangle$-$|3\rangle$ and $|3\rangle$-$|4\rangle$-$|5\rangle$, we can write down a Hamiltonian as in Eq. (4.2.1). The full Hamiltonian for the five-level system is the sum of the two three-level Hamiltonians in the basis $\{|1\rangle,|2\rangle,|3\rangle,|4\rangle,|5\rangle\}$

and looks as follows:

$$H = \frac{\hbar}{2}\begin{bmatrix} 0 & \Omega_{12} & 0 & 0 & 0 \\ \Omega_{12} & 2\Delta_{12} & \Omega_{32} & 0 & 0 \\ 0 & \Omega_{32} & 2(\Delta_{12}-\Delta_{32}) & \Omega_{34} & 0 \\ 0 & 0 & \Omega_{34} & 2\Delta_{34} & \Omega \\ 0 & 0 & 0 & \Omega_{54} & 2(\Delta_{34}-\Delta_{54}) \end{bmatrix}. \tag{4.2.12}$$

Assuming two-photon resonance in each of the three-level systems, i.e., $\Delta_{12} - \Delta_{32} = \Delta_{34} - \Delta_{54} = 0$, we find an eigenstate $|\Psi\rangle = \sum_{i=1}^{5} c_i |i\rangle$ with eigenvalue 0 if and only if $c_2 = c_4 = 0$, namely

$$|\Psi_0\rangle = N[\cos\phi\cos\Theta\,|1\rangle - \cos\phi\sin\Theta\,|3\rangle + \sin\phi\sin\Theta\,|5\rangle], \tag{4.2.13}$$

where N is a normalization factor, Θ is defined as before and

$$\tan\phi = \frac{\Omega_{34}}{\Omega_{54}}. \tag{4.2.14}$$

In this case it is possible to adiabatically transfer population from $|1\rangle$ to $|5\rangle$ by changing both Θ and ϕ from 0 to $\pi/2$. Consider Gaussian pulses as shown in Fig. 4.3(b), with $\Omega_{12}(t)$ and $\Omega_{32}(t)$ defined by Eqs. (4.2.9)–(4.2.10), and

$$\Omega_{34}(t) = \Omega_{34}^0 \exp\left[-\left(\frac{t-\Delta t/2-D}{\tau}\right)^2\right] \tag{4.2.15}$$

$$\Omega_{54}(t) = \Omega_{54}^0 \exp\left[-\left(\frac{t+\Delta t/2-D}{\tau}\right)^2\right], \tag{4.2.16}$$

i.e, $\Omega_{34}(t)$ and $\Omega_{54}(t)$ are delayed by D with respect to $\Omega_{12}(t)$ and $\Omega_{32}(t)$, respectively. For $D \gg \tau$ population is transferred step-wise, first from $|1\rangle$ to $|3\rangle$ and then to $|5\rangle$, as in the previously considered situation of two independent sets of pulses. The interesting regime in this context is therefore $|D| \lesssim \tau$. In Fig. 4.4 the population P_i in state $|i\rangle$ $(i = 1, 3, 5)$ is plotted for delays $D = \tau$ and $D = -\tau$. In both cases the transfer from $|1\rangle$ to $|5\rangle$ is completed in a time which is of the order of the pulse width τ. In fact, the process is faster with a negative delay - a *double counter-intuitive pulse sequence*. Similar ideas of population transfer in a multi-level system were put forward in Ref. [62], and in Ref. [75] where the particular case $D = 0$ was considered, and demonstrated experimentally in Ref. [76].

From Fig. 4.4 we also note that the state $|3\rangle$ is not fully populated before the population is transferred further on to $|5\rangle$; especially for $D = -\tau$, very little population is found in state $|3\rangle$. In our case the states $|3\rangle$ and $|5\rangle$, which corresponds to the $^2D_{3/2}$ state and the $^2D_{5/2}$ state, respectively, have almost equal natural lifetimes of more than a second. Thus, we do not suffer from any appreciable decay from the intermediate state $|3\rangle$. However, one could imagine a similar double STIRAP process in another atomic or molecular system, where the initial and final states ($|1\rangle$ and $|5\rangle$) have a long lifetime of, say, a second, but the intermediate state $|3\rangle$ has a lifetime of only, say, 100 μs. In this case there can be a non-negligible probability of spontaneous decay from $|3\rangle$ during a double STIRAP process of some microseconds duration. Denoting the spontaneous decay rate from $|3\rangle$ by Γ_3 and defining $I_3 = \int_{-\infty}^{\infty} P_3(t/\tau)d(t/\tau)$, the decay probability

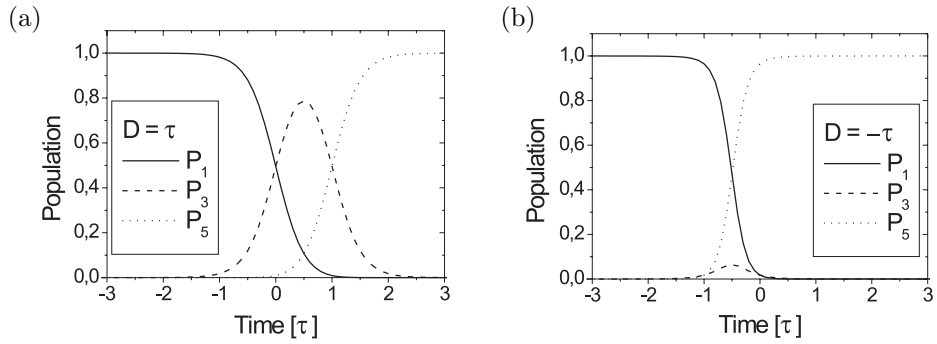

Figure 4.4: (a) Population transfer in a five-level system with delay $D = \tau$ between the two sets of STIRAP pulses. (b) Same as (a), but with negative delay $D = -\tau$.

from $|3\rangle$ is given by $[1 - \exp(-\Gamma_3 \tau I_3)] \approx \Gamma_3 \tau I_3$, when $\Gamma_3 \tau I_3 \ll 1$. In Fig. 4.5, the value of the integral I_3 is plotted as a function of the delay, showing that a negative delay reduces the decay probability significantly.

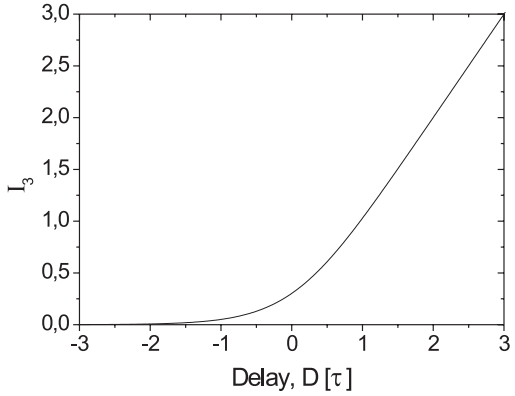

Figure 4.5: Value of $I_3 = \int_{-\infty}^{\infty} P_3(t/\tau)d(t/\tau)$ versus delay D. For $\Gamma\tau I_3 \ll 1$, I_3 is equal to the probability of a decay from state $|3\rangle$ in units of $\Gamma\tau$.

4.3 State-selective shelving in $^{40}Ca^{+}$ using a Raman transition

Transfer of population from the ground state to the $^2D_{5/2}$ state can also take place using a Raman transition between the two states via the $^2P_{3/2}$ state. State-selectivity can be obtained as described in the following.

For a given laser polarization on the $^2S_{1/2}$–$^2P_{3/2}$ and the $^2D_{5/2}$–$^2P_{3/2}$ transitions, the Raman transition will involve certain Zeeman sublevels of the three states. The Rabi-frequency depends on the coupling strengths between these Zeeman sublevels (see

the tabulated Clebsch-Gordan coefficients in App. B). By choosing appropriate polarizations of the two laser beams, it is possible to obtain different Raman Rabi-frequencies, $\Omega_\downarrow$ and $\Omega_\uparrow$, for a Raman transition from $|\downarrow\rangle$ and $|\uparrow\rangle$, respectively, to the $^2D_{5/2}$ state. Thus, by driving the Raman transition for a time T, such that $\Omega_\downarrow T/2 = m\pi$, where m is (close to) an odd integer, and $\Omega_\uparrow T/2 = n\pi$, where n is (close to) an even integer, population initially in $|\downarrow\rangle$ will effectively experience a π-pulse and end up in the $^2D_{5/2}$ state, whereas population in $|\uparrow\rangle$ will experience multiple 2π-pulses and end up in $|\uparrow\rangle$, where it started [2]. By going through Table B.3 and B.5 in App. B, it can be found that there exist two non-equivalent polarization configurations, where $\Omega_\uparrow$ and $\Omega_\downarrow$ are different. One configuration is a σ^-–π configuration, meaning that the $^2S_{1/2}$–$^2P_{3/2}$ ($^2D_{5/2}$–$^2P_{3/2}$) laser is σ^--polarized (π-polarized), for which the ratio $\Omega_\downarrow/\Omega_\uparrow = \sqrt{2}$. Noting that $12\sqrt{2} = 16.97... \approx 17$, we can use $m = 17$ and $n = 12$ to obtain the desired effective π- and 2π-pulses to a good precision, or similarly exploit that $70\sqrt{2} = 98.995... \approx 99$. The other configuration is a σ^-–σ^+ configuration for which $\Omega_\downarrow/\Omega_\uparrow = \sqrt{5}$, in which case we, for example, can exploit that $17\sqrt{5} = 38.013... \approx 38$ or $72\sqrt{5} = 160.996... \approx 161$. If requested, the ratio $\Omega_\downarrow/\Omega_\uparrow$ can be changed to $1/\sqrt{2}$ and $1/\sqrt{5}$ in the two cases by using a $\sigma^+ - \pi$ configuration and a $\sigma^+ - \sigma^-$ configuration, respectively, instead.

4.4 Conclusion

Each of the two methods for state-selective shelving presented above has its own advantages and drawbacks.

The STIRAP technique has the advantage of being quite robust with respect to the pulse-area of the applied laser pulses [62]. It has the drawback of involving four different laser wavelengths. Fortunately, two of them (397 nm and 866 nm) are the same as for Doppler cooling and the other two (850 nm and 854 nm) can be supplied in a relatively cheap and easy way by diode lasers.

The technique based on the Raman transition is attractive in the sense that it requires only a single step involving only two laser sources. Unfortunately, the technique requires good control of the pulse-area and furthermore the requirement of a 393 nm laser is a bit unattractive [3].

As stated in the introduction of this chapter, the scheme we are pursuing is the STIRAP based scheme mainly due to the robustness of the STIRAP technique and the good availability of laser sources. Furthermore, we saw that although the scheme in principle involves two STIRAP processes, they can be turned into a single five-level STIRAP process, which in itself will be interesting to study. The experimental equipment and setup for implementing the STIRAP processes are presented in Chap. 8. Some progress towards a demonstration of STIRAP is presented and discussed in Chap. 10.

[2] For m even and n odd, the roles of $|\downarrow\rangle$ and $|\uparrow\rangle$ are just interchanged.

[3] It could, e.g., be supplied by a blue laser diode, which can be hard to get, or by a frequency-doubled Ti:Sa laser, which is expensive.

Chapter 5

Quantum logic with trapped ions

In continuation of the general introduction to quantum computation and quantum optics with trapped ions given in Chap. 1, we shall here give a short overview of quantum gates and discuss their implementation in a system of cold trapped ions. Furthermore, we shall establish the relation to our choice of qubit states in $^{40}Ca^{+}$, using Raman transitions for quantum logic operations.

Quantum gates are briefly discussed in Sec. 5.1. Sec. 5.2 is devoted to the discussion of specific proposals involving strings of cold trapped ions with focus on the original proposal by Cirac and Zoller [4] and a proposal by Klaus Mølmer and Anders Sørensen [77, 78]. Furthermore, a short discussion of large-scale quantum computation is given. In Sec. 5.3 we discuss the relation to our own choice of qubit states.

5.1 Quantum gates

As mentioned in Chap. 1, a quantum bit, or qubit, is a two-level quantum system. Denoting the two levels by $|\downarrow\rangle$ and $|\uparrow\rangle$, a superposition of these states can in general be written as

$$\cos(\theta/2)\,|\downarrow\rangle + e^{i\phi}\sin(\theta/2)\,|\uparrow\rangle\,, \tag{5.1.1}$$

where the angles θ and ϕ are real numbers. Any global phase factor is irrelevant and therefore ignored. The potential strength of a quantum computer partly has its origin in the fact that a qubit, as opposed to a classical bit, can be in a superposition state. To illustrate the strength in this, we suppose we have N qubits, each in the superposition state $(|\downarrow\rangle + |\uparrow\rangle)/\sqrt{2}$. Then the product state made up of the N superposition states is

$$\frac{1}{2^{N/2}}[|\downarrow\rangle + |\uparrow\rangle]_1 \otimes [|\downarrow\rangle + |\uparrow\rangle]_2 \otimes \cdots \otimes [|\downarrow\rangle + |\uparrow\rangle]_N = \frac{1}{2^{N/2}} \sum_{i=0}^{2^N-1} |i\rangle\,, \tag{5.1.2}$$

where i is understood to be the binary representation of the number i with 0's and 1's represented by $|\downarrow\rangle$ and $|\uparrow\rangle$, respectively. Thus, with N qubits we can have a quantum

register containing 2^N numbers *at the same time*, on which quantum logic operations can be performed [1].

Any quantum logic operation on such a quantum register is a unitary operation, which can be constructed from a specific set of unitary operations, often referred to as a *a universal set of gate operations* [79]. This set simply consists of all unitary operations on single qubits and a so-called Controlled-NOT (CNOT) gate. The CNOT gate is a gate between two qubits, and it must be possible to perform this gate between *any two* qubits in a quantum register [79]. In practical applications one may, of course, wish to make use of a larger set of gate operations.

5.1.1 Single-qubit gates

Any single-qubit gate corresponds to a transformation of the type

$$\cos(\theta/2)\,|\downarrow\rangle + e^{i\phi}\sin(\theta/2)\,|\uparrow\rangle \longmapsto \cos(\theta'/2)\,|\downarrow\rangle + e^{i\phi'}\sin(\theta'/2)\,|\uparrow\rangle\,. \tag{5.1.3}$$

Recalling the discussion in Chap. 2 of the time evolution of a trapped two-level atom interacting with a light-field, especially Eq. (2.2.7), it is clear that for a trapped ion θ can be changed in a controlled way by applying laser-pulses with a suitable pulse-area, and the relative phase ϕ can conveniently be controlled by the phase of the light-field. Thus single-qubit gates can readily be implemented if individual access to the qubits is available.

One example of a single qubit gate-operation, which will be used below, is a 'rotation gate' given by the matrix representation

$$R(\delta\theta) = \begin{bmatrix} \cos(\delta\theta/2) & -\sin(\delta\theta/2) \\ \sin(\delta\theta/2) & \cos(\delta\theta/2) \end{bmatrix} \tag{5.1.4}$$

in the basis $\{|\downarrow\rangle, |\uparrow\rangle\}$.

5.1.2 Two-qubit gates

The CNOT gate involves two qubits, and hence it acts in general on a superposition state of the form

$$\alpha\,|\downarrow\rangle\,|\downarrow\rangle + \beta\,|\downarrow\rangle\,|\uparrow\rangle + \gamma\,|\uparrow\rangle\,|\downarrow\rangle + \delta\,|\uparrow\rangle\,|\uparrow\rangle\,, \qquad \alpha,\,\beta,\,\gamma,\,\delta\,\epsilon\,\mathbb{C}. \tag{5.1.5}$$

In Table 5.1 the truth table of the CNOT gate is given with the two qubits named the 'control' qubit and the 'target' qubit, respectively. The gate flips the state (a NOT operation) of the target qubit only if the control qubit is in state $|\uparrow\rangle$. Thus, applying the CNOT gate to the superposition state above would swap γ and δ. Sometimes it is more convenient to consider the so-called Controlled-Z gate [18], which changes the sign of the coefficient on $|\uparrow\rangle\,|\uparrow\rangle$, but does nothing to the other three coefficients. The CNOT-gate and the Controlled-Z gate are equivalent up to two rotations of the target

[1] The state in Eq. (5.1.2) is in fact the starting point in Grovers algorithm for searching an unordered database [3].

Input		Output	
Control	Target	Control	Target
↓	↓	↓	↓
↓	↑	↓	↑
↑	↓	↑	↑
↑	↑	↑	↓

Table 5.1: Truth table for CNOT gate.

qubit, as the following matrix identity shows

$$\underbrace{\left[\begin{array}{cc|c} 1 & 0 & \\ 0 & 1 & 0 \\ \hline & 0 & \begin{array}{cc} 0 & 1 \\ 1 & 0 \end{array} \end{array}\right]}_{\text{CNOT}} = \underbrace{\left[\begin{array}{cc|c} \frac{1}{\sqrt{2}} & \frac{-1}{\sqrt{2}} & \\ \frac{1}{\sqrt{2}} & \frac{1}{\sqrt{2}} & 0 \\ \hline & 0 & \begin{array}{cc} \frac{1}{\sqrt{2}} & \frac{-1}{\sqrt{2}} \\ \frac{1}{\sqrt{2}} & \frac{1}{\sqrt{2}} \end{array} \end{array}\right]}_{\text{R}(\frac{\pi}{2}),\ \text{target qubit}} \cdot \underbrace{\left[\begin{array}{cc|c} 1 & 0 & \\ 0 & 1 & 0 \\ \hline & 0 & \begin{array}{cc} 1 & 0 \\ 0 & -1 \end{array} \end{array}\right]}_{\text{Controlled-Z}} \cdot \underbrace{\left[\begin{array}{cc|c} \frac{1}{\sqrt{2}} & \frac{1}{\sqrt{2}} & \\ \frac{-1}{\sqrt{2}} & \frac{1}{\sqrt{2}} & 0 \\ \hline & 0 & \begin{array}{cc} \frac{1}{\sqrt{2}} & \frac{1}{\sqrt{2}} \\ \frac{-1}{\sqrt{2}} & \frac{1}{\sqrt{2}} \end{array} \end{array}\right]}_{\text{R}(-\frac{\pi}{2}),\ \text{target qubit}} \tag{5.1.6}$$

where the matrix representations of the gates are written in the basis $\{|{\downarrow\downarrow}\rangle, |{\downarrow\uparrow}\rangle, |{\uparrow\downarrow}\rangle, |{\uparrow\uparrow}\rangle\}$.

In the introduction in Chap. 1, the importance of entangled states was underlined [2]. Quantum gates and the preparation of entangled states are related issues since, with the ability to make a CNOT gate, one is also able to prepare entangled states from a product state. For example

$$\text{CNOT}\Big\{ \left[\cos(\theta/2)\,|{\downarrow}\rangle + e^{i\phi}\sin(\theta/2)\,|{\uparrow}\rangle\right] \otimes |{\downarrow}\rangle \Big\} = \cos(\theta/2)\,|{\downarrow}\rangle\,|{\downarrow}\rangle + e^{i\phi}\sin(\theta/2)\,|{\uparrow}\rangle\,|{\uparrow}\rangle \tag{5.1.7}$$

is an entangled state for a suitably chosen θ. Preparation of entangled states of trapped ions is discussed a little further in the following section.

5.2 Quantum gates using trapped ions

There are numerous proposals for implementation of quantum gates using a string of cold trapped ions, and a detailed discussion of all of them would be to go too far. The Cirac-Zoller proposal [4], which was the first of these proposals, is discussed in some detail below since it nicely illustrates some general ideas and problems and has been demonstrated successfully by the Innsbruck group [13]. The so-called Mølmer-Sørensen gate proposal [77, 78] is also discussed in some detail since, unlike the Cirac-Zoller proposal, it does not require ground state cooling, and individual addressing of ions is not necessary for two-qubit gate operations. Moreover, the proposal was successfully used in the demonstration by the NIST group of two- and four-particle entangled states of trapped ions [9], and it is possible that our first experiments on entangled states and

[2] Recall that an entangled state of two or more particles is a quantum state whose common wavefunction cannot be separated into a product of wavefunctions for any subset of the system.

quantum gates will use this approach as well (some other gate proposal). The present section concludes with a short overview of a few other gate proposals, each with their own advantages and disadvantages, followed by an outlook towards large-scale ion trap computing.

5.2.1 The Cirac-Zoller proposal

In the Cirac-Zoller proposal a string of ions confined in the harmonic potential of a linear Paul trap as illustrated by the simple illustration in Fig. 1.1. The ions are assumed to be cooled to their motional ground state in the trap, and can be addressed individually by laser beams with a spectral resolution much better than the trap frequency ω_z. The Lamb-Dicke limit is assumed, and hence the most relevant transitions for performing gate operations are carrier transitions and transitions on the first red sideband (RSB) and the first blue sideband (BSB).

To get a feeling for such gate operations, consider the following example, which creates an entangled state starting from two ions being in the internal state $|\downarrow\rangle$ and in the motional ground state $|0\rangle$:

$$|\downarrow\rangle\,|\downarrow\rangle\,|0\rangle \tag{5.2.1}$$

$$\Downarrow \quad \text{BSB } \pi/2\text{-pulse, Ion 2}$$

$$|\downarrow\rangle \underbrace{\left[\,|\downarrow\rangle\,|0\rangle - i\,|\uparrow\rangle\,|1\rangle\,\right]}_{\text{entangled state}}$$

$$\Downarrow \quad \text{RSB } \pi\text{-pulse, Ion 1}$$

$$\underbrace{\left[\,|\downarrow\rangle\,|\downarrow\rangle - |\uparrow\rangle\,|\uparrow\rangle\,\right]}_{\text{entangled state}}|0\rangle\,.$$

First, a BSB $\pi/2$-pulse on Ion 2 [compare Eq. (2.2.7) with $\phi = 0$] creates an entangled state between the internal state of Ion 2 and the common motional state of the ions. Then a RSB π-pulse on Ion 1, which has no effect on the $|\downarrow\rangle|\downarrow\rangle|0\rangle$ part of the wavefunction, rotates the $|\downarrow\rangle\,|\uparrow\rangle|1\rangle$ part such that the entangled state is mapped onto the internal states of the ions. In this example excitation and de-excitation of the motional state on the BSB and the RSB, respectively, provide a way of 'communicating' between the qubits. This sort of communication is also required for a two-qubit gate, which therefore also involves sideband-pulses. Two essential points in the example were individual addressing of the ions and the assumption that the ions were cooled to their motional ground state (any other Fock state would also work).

The Rabi-frequencies applied on sideband transitions and hence the duration T of a two-qubit gate operation must be limited if off-resonant excitations on the carrier are to be avoided. In other words, the power-broadened linewidth should be much smaller than the spacing, ω_z, between the vibrational levels. In the resolved-sideband limit, the power-broadened linewidth is essentially given by the Rabi-frequency, and hence the

following restriction on the duration T of a $\pi/2$ sideband-pulse applies

$$T = \frac{\pi}{\eta\Omega} \gg \frac{\pi}{\eta\omega_z}, \tag{5.2.2}$$

where η is the Lamb-Dicke parameter, and Ω is the free-ion Rabi-frequency. For single-qubit gates there is no need to excite the motional state, and hence they can be implemented by a carrier pulse for which the restriction on the duration of a $\pi/2$-pulse is $T \gg \pi/\omega_z$. Thus single-ion gates are not only relatively easy to implement, they are also much faster than two-qubit gates.

In the original proposal of Cirac and Zoller for making a CNOT-gate operation, the key step is a π phase-shift of one of the four combined eigenstates in Eq. (5.1.5), which is obtained by applying a 2π-pulse on an auxiliary transition. In $^{40}Ca^{+}$, as well as many other ion species, such an auxiliary transition is, however, not readily available. Fortunately, Childs and Chuang [80] have shown how to get around this requirement by using so-called composite pulses, which indeed was the technique used by the Innsbruck group in their demonstration of the Cirac-Zoller CNOT-gate [13].

5.2.2 The Mølmer-Sørensen proposal

The Mølmer-Sørensen proposal is illustrated for two ions in Fig. 5.1 [77, 78]. Here, the ions are illuminated by two laser-fields characterized by the same Rabi-frequency Ω and frequencies $\omega_{\pm} = \omega_{\uparrow\downarrow} \pm \delta$, where $\pm\delta$ is the detuning from the carrier resonance frequency $\omega_{\uparrow\downarrow}$. The Lamb-Dicke limit, $\eta\sqrt{n+1} \ll 1$, is assumed. Now, if $0 < \delta < \omega_z$ and the applied fields are so weak that $\eta\Omega \ll \omega_z - \delta$, no one-photon transitions are allowed, however, two-photon transitions of the type $|\downarrow\rangle|\downarrow\rangle|n\rangle$–$|\uparrow\rangle|\uparrow\rangle|n\rangle$ via the intermediate states $|\downarrow\rangle|\uparrow\rangle|m\rangle$ and $|\uparrow\rangle|\downarrow\rangle|m\rangle$ ($m = n-1, n, n+1$) are perfectly allowed. By including the transition paths via the intermediate states in a second-order perturbation theory calculation, it can be found that the Rabi-frequency for the two-photon transitions is [78]

$$\tilde{\Omega} = -\frac{2\omega_z(\eta\Omega)^2}{\omega_z^2 - \delta^2}, \tag{5.2.3}$$

which remarkably enough is independent of n! The n-dependence of the effective Rabi-frequencies on the individual transition paths simply cancels out. Also $|\downarrow\rangle|\uparrow\rangle|n\rangle$–$|\uparrow\rangle|\downarrow\rangle|n\rangle$ two-photon transitions via the intermediate states $|\downarrow\rangle|\downarrow\rangle|m\rangle$ and $|\uparrow\rangle|\uparrow\rangle|m\rangle$ ($m = n-1, n, n+1$) are allowed, and the corresponding two-photon Rabi-frequency is $-\tilde{\Omega}$. Thus, using a bichromatic laser pulse, coherent dynamics involving all four combined eigenstates $|\downarrow\rangle|\downarrow\rangle$, $|\downarrow\rangle|\uparrow\rangle$, $|\uparrow\rangle|\downarrow\rangle$ and $|\uparrow\rangle|\uparrow\rangle$ is possible. Since the two-photon Rabi-frequency is n-independent, the dynamics is insensitive to heating during gate operations and ground state cooling is not required. Furthermore, since both ions are illuminated by the same laser beams, individual addressing is not required.

Using this scheme an entangled state can be created, for example the state $(|\downarrow\rangle|\downarrow\rangle + |\uparrow\rangle|\uparrow\rangle)/\sqrt{2}$, which can be created from the state $|\downarrow\rangle|\downarrow\rangle$ by applying a bichromatic $\pi/2$-pulse on the $|\downarrow\rangle|\downarrow\rangle$–$|\uparrow\rangle|\uparrow\rangle$ transition. A CNOT-gate can be implemented by combining suitable bichromatic pulses with single-qubit operations. The Mølmer-Sørensen scheme has been generalized to the case where $\eta\Omega \sim \omega_z - \delta$, under the assumption that $\Omega^2 \ll \omega_z^2$ and $\eta^2 \ll 1$ [81]. In this case the gate-operations are faster, however, the motional state is excited during the gate-operations and only at specific points in time it returns to its initial state, thus making the scheme sensitive to heating during the gate operations.

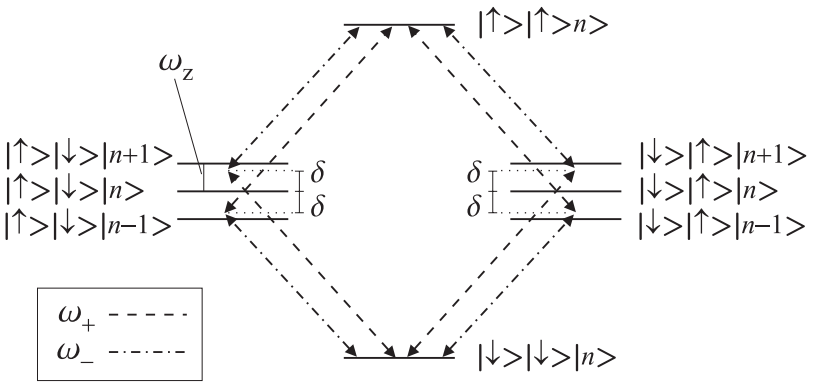

Figure 5.1: The Mølmer-Sørensen proposal. Two trapped ions are illuminated by two laser beams with frequency ω_+ and ω_-, respectively. The indicated transition paths interfere to give a n-independent two-photon Rabi-frequency $\tilde{\Omega}$, see Eq. (5.2.3).

5.2.3 Other gate proposals

Geometric quantum gates [81] is a class of gates, where the ions are motionally excited by a suitable driving force, which takes them on a round-trip in position-momentum phase space. If the driving force is internal-state dependent, then so is the phase acquired during the round trip, which in turn enables the implementation of a Controlled-Z gate, as demonstrated by the NIST group [14]. In geometric gates the internal states of the ions are unchanged during the gate-operations, which results in a fidelity superior to that of gates where the internal states are directly involved in the gate-operations [14]. Furthermore, ground state cooling is not required. Our own gate proposal, which is presented in Chap. 6, is one example of a geometric gate.

Mintert and Wunderlich [82] have proposed to use micro-wave radiation for quantum logic operations on qubits represented by ground state hyperfine levels or Zeeman-splitted sublevels of an ion, the advantage being that well known NMR pulse-techniques can be applied in making gate-operations. The Lamb-Dicke parameter is extremely small for micro-wave radiation, however, by applying a magnetic field gradient along an ion string, it is possible to obtain an effective Lamb-Dicke parameter of a suitable magnitude. Owing to the differential Zeeman shift of the individual ions imposed by the magnetic field gradient, the scheme also allows individual addressing of the ions in frequency-space. Currently, work is ongoing at Hamburg University to implement these ideas [83].

Monroe *et al.* have suggested a 'Magic Lamb-Dicke parameter' method for making a CNOT gate [84]. The method has been demonstrated experimentally on a single ion, with one qubit stored in the internal states of the ion ($|\downarrow\rangle$ and $|\uparrow\rangle$) and another qubit stored in two motional states ($|n=0\rangle$, $|n=2\rangle$) [85]. By using a 'magic' ratio of 4/3 between the two effective carrier Rabi-frequencies $\Omega_{0,0}$ and $\Omega_{2,2}$, which are governed by the Lamb-Dicke parameter, it was possible to flip the internal state of the ion dependent on its motional state. This is indeed a CNOT-operation. The method can be applied to two or more ions, if the motional state is mapped onto the internal state, as in the example given in Eq. (5.2.1).

Jonathan, Plenio and Knight have presented a scheme where the ac Stark shift

induced by a strong laser field [86] is utilized. When a strong laser field is applied to an ion, the system can conveniently be described in terms of combined eigenstates of the laser field and the internal states of the ion, i.e., the so-called dressed states [87]. The frequency splitting between the dressed states depends on the Rabi-frequency of the applied field. When the laser field is applied to a single ion in a string and the splitting between two relevant dressed states is equal to the trap frequency, coherent dynamics involving the motional state occurs in such a way that it is possible to perform a CNOT gate-operation between two ions. The gate time $T \sim \omega_z^{-1}$ is not limited by the condition in Eq. (5.2.2). The proposal was later combined with the Mølmer-Sørensen proposal [88], such that individual addressing is not required and the scheme becomes heating insensitive.

5.2.4 Practical large-scale quantum computation with trapped ions?

If problems intractable on classical computers have to be tackled by future large-scale quantum computation, it will involve very long sequences of quantum gates and hundreds or even thousands of qubits [19]. Whether this will become possible is, however, yet unknown. One thing is certain, large-scale quantum computation, with its longer gate operation times and more qubits (ions), will inevitably increase the importance of problems, which are small or even negligible in the demonstration of single quantum gates in smaller systems. In trying to get around these problems it is likely that some of the ideas, which briefly are discussed below, will be important.

Getting to the point of having hundreds of qubits simply by filling more ions into a linear Paul trap does not seem like a passable road, since keeping the ions on a string at reasonably high axial trap frequencies, requires very large radial trap frequencies [see Eq. (3.2.3)]. In contrast, large-scale quantum computation with trapped ions using the quantum computer architecture envisaged by Wineland and co-workers seems to be more viable [89]. Here, several ion traps are combined in a large array, where ions can be shuttled between the various trap regions. In some regions the actual gate operations are performed, while in other regions the ions are stored or sympathetically cooled by the Coulomb interaction with other laser cooled ion species. At NIST, the possibility of realizing such a large scale system is presently being explored, with the fabrication of micro-traps, demonstration of ion-transfer between two traps and of sympathetic cooling to be used for quantum computing purposes [90, 91, 92]. See also Refs. [34, 93, 94] for work concerning sympathetic cooling of trapped ions.

Longer pulse sequences and hence longer gate-operation times means, all other things being equal, more errors and decoherence than in the demonstrations of single quantum gates. Errors in the gate-operations can be reduced if NMR composite-pulse techniques [95] are used. Decoherence rates can be reduced by encoding the information stored in a single qubit, into a so-called decoherence-free subspace of two qubits, which is less sensitive to perturbations from the environment than a single qubit [96]. If (or when) errors after all do occur, they can be corrected using quantum error correction techniques [97, 98]. With these techniques, the information stored in a single qubit can be encoded into several qubits, such that if an error occurs within one of these qubits, it can be corrected from a measurement of the state of the other qubits. It can be shown, that once the 'error' per qubit per quantum gate during a gate operation (see Ref. [98] for a precise definition) is below a certain threshold value, then arbitrarily long

quantum computations can be made robust [98]. This threshold value is of the order of 10^{-4} [98].

5.3 Quantum logic operations in the $^{40}Ca^{+}$ ion

In our envisaged implementation of quantum logic operations in the $^{40}Ca^{+}$ ion, gate operations involving the qubit states $|\downarrow\rangle = {}^2S_{1/2}(m_J = -1/2)$ and $|\uparrow\rangle = {}^2S_{1/2}(m_J = +1/2)$ are performed on the Raman transition which was used in the sideband-cooling scheme. The requirements for using the Raman transition for quantum logic operations are the same as for sideband cooling, except that the Raman lasers have to be intensity modulated in order to create laser pulses.

After sideband cooling, population is mainly in the state $|\downarrow, 0\rangle$ (should be more than 99%), which hence defines the starting point for quantum logic operations. For the two-photon Raman transition, the relevant Rabi-frequency is the Raman Rabi-frequency Ω_{Raman} [see Eq. (3.4.4)], the relevant Lamb-Dicke parameter is $\eta = \eta_{12} - \eta_{32}$ and the relative phase ϕ between the qubit states can be controlled by the phase-difference $\phi_{12} - \phi_{32}$ between the Raman beams.

The apparatus for making laser pulses and controlling the phase is described in Chap. 8.

Chapter 6

Applications of optical dipole potentials in trapped-ion quantum logic

In this chapter we consider the possibilities which arise when ions on a string are subject to a potential whose strength depends on the internal state of the ions. The potential to be considered is the optical dipole potential, or the ac Stark shift, due to a laser beam which is far-off resonant with respect to all internal transitions in the ions. If the beam is propagating perpendicular to the ion-string and its transverse intensity-profile varies over the ion-string, the dipole potential for each ion will be position-dependent and a force will in general be exerted on the ions. Both of these aspects will be exploited in the following.

The chapter starts out with a short introduction to optical dipole potentials in Sec. 6.1. In Sec. 6.2 follows a proposal for realizing a Controlled-Z gate, using the force which originates from a spatial variation in the dipole potential. This work will be published as Ref. [VI]. Finally, in Sec. 6.3 the difficulties of individual addressing of single ions on a string are discussed and a proposal for achieving individual addressing, as well as selective addressing of any pair of ions, which utilizes the position dependence of the optical dipole potential, is presented. The bulk of the work presented in Sec. 6.3 has been published in Ref. [I].

6.1 Trapped ions and optical dipole potentials

When an atom or ion is irradiated by a laser beam, the electric field $\boldsymbol{E}$ of the laser beam induces an atomic dipole moment $\boldsymbol{p}$, which oscillates at the laser frequency ω_L. The interaction potential of the induced dipole moment in the electric field, time-averaged over quickly oscillating terms, is given by [99]

$$U_{dip} = -\frac{1}{2} < \boldsymbol{pE} >_{time}, \tag{6.1.1}$$

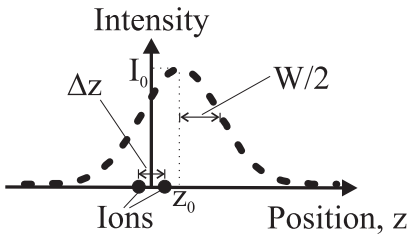

Figure 6.1: Intensity distribution for a Gaussian dipole beam [see Eq. (6.1.4)] with respect to the position of a two-ion string centered at $z = 0$.

which will be referred to as the (optical) dipole potential in the following. For the two-level atom considered in Sec. 2.1, the dipole potential at a position $\boldsymbol{r}$ is given by [99]

$$U_{dip}(\boldsymbol{r}) = -\frac{3\pi c^2}{2\omega_{eg}^3}\left(\frac{\Gamma}{\omega_{eg}-\omega_L}+\frac{\Gamma}{\omega_{eg}+\omega_L}\right) I(\boldsymbol{r}) \tag{6.1.2}$$

in the regime where the detuning $\Delta = \omega_L - \omega_{eg}$ is much larger than the linewidth Γ. The dipole potential is proportional to the intensity $I(\boldsymbol{r})$, since the induced dipole moment $\boldsymbol{p}$ is proportional to $\boldsymbol{E}$ and $I \propto |E|^2$.

The oscillating dipole can absorb power from the electric field and reemit it as dipole radiation, which in a photon-atom picture corresponds to photons being scattered by the atom. For the two-level atom the scattering rate is given by [99]

$$\Gamma_{sc}(\boldsymbol{r}) = \frac{3\pi c^2}{2\hbar\omega_{eg}^3}\left(\frac{\omega_L}{\omega_{eg}}\right)^3\left(\frac{\Gamma}{\omega_{eg}-\omega_L}+\frac{\Gamma}{\omega_{eg}+\omega_L}\right)^2 I(\boldsymbol{r}), \tag{6.1.3}$$

which is proportional to the intensity for the same reasons as for the dipole potential. Note that when the detuning fulfills $|\Delta| \ll \omega_{eg}+\omega_L = \Delta + 2\omega_{eg}$, the scattering rate drops off as Δ^{-2}, whereas the dipole potential only drops off as Δ^{-1}. Note also that for negative detuning, the scattering rate drops off as $(\omega_L/\omega_{eg})^3$. In the following we consider a string of trapped ions illuminated by a far-off resonant laser beam, called the dipole beam, which propagates perpendicular to the ion-string. The axis defined by the ion-string is the z-axis and $z = 0$ is chosen to be at the center of the ion-string. The transverse intensity distribution of the dipole beam, which is denoted by $I(z)$, could, e.g., be Gaussian, such that

$$I(z) = I_0 e^{-2(z-z_0)^2/W^2}, \tag{6.1.4}$$

where z_0 is the center of the dipole beam, W is the beam waist and I_0 is the peak intensity. This situation is illustrated in Fig. 6.1. Since the dipole potential is proportional to the intensity, it has the same variation along the z-axis as the intensity of the dipole beam. If the length scale over which the intensity varies [i.e., W in Eq. (6.1.4)] is much larger than the excursion of an ion from its equilibrium position, z_{eq}, it is meaningful to linearize the dipole potential around this equilibrium position:

$$U_{dip}(z) = U_{dip}(z_{eq}) - F_{dip}(z_{eq})(z - z_{eq}), \tag{6.1.5}$$

where

$$F_{dip}(z_{eq}) = -\frac{\partial U_{dip}(z)}{\partial z}\bigg|_{z=z_{eq}} \tag{6.1.6}$$

is the dipole force exerted on the ion along the trap axis due to the spatial variation of the dipole potential.

In the context of this thesis, where we generally consider multilevel ions, with two of the levels being the qubit states $|\downarrow\rangle$ and $|\uparrow\rangle$, the dipole potential and the scattering rate are not simply given by Eqs. (6.1.2) and (6.1.3), rather they are a sum over such terms originating from all relevant transitions. Since the strength of transitions from $|\downarrow\rangle$ and $|\uparrow\rangle$ to other internal levels depends on the polarization and the wavelength of the dipole beam, the dipole potential in general differs for the two qubit states.

For an ion-string illuminated by a dipole beam its potential energy, U, is the sum of the dipole potential for each ion, the potential energy of the ions in the trap and their Coulomb energy. Specifically for two ions, numbered by indices 1 and 2, we have

$$\begin{aligned} U(z_1, z_2, \alpha_1, \alpha_2) =& \frac{1}{2} m\omega_z^2 (z_1^2 + z_2^2) + \frac{e^2}{4\pi\epsilon_0 (z_2 - z_1)} + U_{dip}(z_{1,eq}, \alpha_1) + U_{dip}(z_{2,eq}, \alpha_2) \\ & - F_{dip}(z_{1,eq}, \alpha_1)(z_1 - z_{1,eq}) - F_{dip}(z_{2,eq}, \alpha_2)(z_2 - z_{2,eq}), \end{aligned} \tag{6.1.7}$$

if the linear expansion of the dipole potential is valid. α_1 and α_2 denote the internal states of the two ions and $z_2 > z_1$ is assumed.

This equation exhibits the mentioned properties of the optical dipole potential, which will be exploited in the following. The terms $U_{dip}(z_{1,eq}, \alpha_1)$ and $U_{dip}(z_{2,eq}, \alpha_2)$ contains the position-dependence to be utilized for achieving individual and selective addressing of ions on a string. The other four terms enables implementation of a geometric Controlled-Z gate, as we shall see now.

6.2 A geometric Controlled-Z gate using optical dipole forces

We consider two trapped ions having qubit levels $|\downarrow\rangle$ and $|\uparrow\rangle$ in the situation described above, where the potential energy is given by Eq. (6.1.7). The implementation of a geometric Controlled-Z gate between the two ions relies on the fact that the dipole force is internal state dependent. The idea is that when the ions are subject to a dipole force, which takes them away from their equilibrium positions, the resulting change in Coulomb energy gives rise to a phase-shift, which depends on the internal states of the ions. By choosing a suitable temporal and spatial profile of the dipole beam, the obtained phaseshifts of $|\downarrow\rangle|\downarrow\rangle$, $|\downarrow\rangle|\uparrow\rangle$, $|\uparrow\rangle|\downarrow\rangle$ and $|\uparrow\rangle|\uparrow\rangle$ can be made equivalent to a Controlled-Z gate. In the following, the displacement of the ions and the acquired phase are calculated for these combinations of the internal states in a full quantum mechanical description of the motion of the ions. Using these results, we shall then discuss a specific implementation in alkaline earth ions and find suitable parameters for the dipole beam intensity, its waist and position with respect to the ion-string and for the trap frequency ω_z.

To describe the motion of the ions, we first rewrite Eq. (6.1.7) as follows

$$\begin{aligned} U(z_{1,eq}, z_{2,eq}, \alpha_1, \alpha_2, t) = &\frac{3}{4} m\omega_z^2 \Delta z^2 + \frac{1}{2} m\omega_z^2 \left(z_+^2 + 3z_-^2\right) + U_{dip}(z_{1,eq}, \alpha_1, t) \\ &+ U_{dip}(z_{2,eq}, \alpha_2, t) - \frac{1}{\sqrt{2}} \left[F_{dip}(z_{1,eq}, \alpha_1, t) + F_{dip}(z_{2,eq}, \alpha_2, t)\right] z_+ \\ &- \frac{1}{\sqrt{2}} \left[F_{dip}(z_{2,eq}, \alpha_2, t) - F_{dip}(z_{1,eq}, \alpha_1, t)\right] z_- \end{aligned} \tag{6.2.1}$$

where

$$z_+ = \frac{1}{\sqrt{2}}(z_2 + z_1) \quad \text{and} \quad z_- = \frac{1}{\sqrt{2}}(z_2 - z_1 - \Delta z) \tag{6.2.2}$$

are the motional mode coordinates for the center-of-mass mode and the breathing mode, respectively, and $\Delta z = z_{2,eq} - z_{1,eq}$ denotes the equilibrium distance between the ions. Since the dipole beam intensity is supposed to vary over time, the dipole potentials and dipole forces are now explicitly time-dependent. Turning to a quantum mechanical description, we introduce lowering (raising) operators a ($a^\dagger$) and b ($b^\dagger$) for the mode coordinates, i.e., $z_+ = \sqrt{\hbar/(4m\omega_z)}(a + a^\dagger)$ and $z_- = \sqrt{\hbar/(4m\sqrt{3}\omega_z)}(b + b^\dagger)$. Inserting z_+ and z_- in the above expression for U, yields the Hamiltonian

$$\begin{aligned} H = &\hbar\omega_z a^\dagger a + \sqrt{3}\hbar\omega_z b^\dagger b + U_{dip}(z_{1,eq}, \alpha_1, t) + U_{dip}(z_{2,eq}, \alpha_2, t) \\ &+ f_+(\alpha_1, \alpha_2, t)(a + a^\dagger) + f_-(\alpha_1, \alpha_2, t)(b + b^\dagger), \end{aligned} \tag{6.2.3}$$

where

$$f_+(\alpha_1, \alpha_2, t) = -\sqrt{\frac{\hbar}{8m\omega_z}} [F_{dip}(z_{1,eq}, \alpha_1, t) + F_{dip}(z_{2,eq}, \alpha_2, t)] \tag{6.2.4}$$

and

$$f_-(\alpha_1, \alpha_2, t) = -\sqrt{\frac{\hbar}{8m\sqrt{3}\omega_z}} [F_{dip}(z_{2,eq}, \alpha_2, t) - F_{dip}(z_{1,eq}, \alpha_1, t)] \tag{6.2.5}$$

are responsible for excitation of the center-of-mass mode and the breathing mode, respectively. The time-evolution of the system can be described by a unitary time-evolution operator $\mathcal{U}$ which fulfills the time-dependent Schrödinger equation and evolves a wave-function Ψ in time according to $\Psi(t) = \mathcal{U}\Psi(t = 0)$ [100] [1]. For the Hamiltonian above, $\mathcal{U}$ can be expressed as a product

$$\mathcal{U} = \exp\left[-\frac{i}{\hbar}\int dt \left[U_{dip}(z_{1,eq}, \alpha_1, t) + U_{dip}(z_{2,eq}, \alpha_2, t)\right]\right] \mathcal{U}_+ \mathcal{U}_-, \tag{6.2.6}$$

where $\mathcal{U}_+$ and $\mathcal{U}_-$ are time-evolution operators corresponding to the Hamiltonians

$$H_+ = \hbar\omega_z a^\dagger a + f_+(\alpha_1, \alpha_2, t)(a + a^\dagger) \tag{6.2.7}$$

[1] The time-evolution operator also describes the time evolution of a density-matrix ρ: $\rho(t) = \mathcal{U}\rho(t = 0)\mathcal{U}^\dagger$.

and

$$H_- = \sqrt{3}\hbar\omega_z b^\dagger b + f_-(\alpha_1, \alpha_2, t)(b + b^\dagger), \tag{6.2.8}$$

respectively. Since H_+ and H_- have an identical structure, the solutions $\mathcal{U}_+$ and $\mathcal{U}_-$ can be found in an identical way. Furthermore, if more than two ions were considered, the resulting additional modes would just give rise to additional terms in the Hamiltonian H and hence to additional factors in the time-evolution operator $\mathcal{U}$, which would be of the same form as $\mathcal{U}_+$ and $\mathcal{U}_-$. Thus, the generalization to an arbitrary number of ions is in principle straightforward. In the following we solve for $\mathcal{U}_+$ with the understanding that the solution $\mathcal{U}_-$ can be obtained from $\mathcal{U}_+$ simply by replacing f_+ with f_- and ω_z with $\sqrt{3}\omega_z$. To this end, we switch to the interaction picture with respect to the Hamiltonian of the free harmonic oscillator [100, 101]

$$H_{int,+} = e^{i\omega_z t a^\dagger a} f_+(\alpha_1, \alpha_2, t)(a^\dagger + a) e^{-i\omega_z t a^\dagger a} = f_+(\alpha_1, \alpha_2, t)(a e^{-i\omega_z t} + a^\dagger e^{i\omega_z t}) \tag{6.2.9}$$

and make the Ansatz that

$$\mathcal{U}_{int,+} = e^{i\omega_z t a^\dagger a}\mathcal{U}_+ = e^{-|\beta_+|^2/2} e^{i\phi_+} e^{i\beta_+^* a^\dagger} e^{i\beta_+ a}, \tag{6.2.10}$$

where $\beta_+ = \beta_+(\alpha_1, \alpha_2, t) = p_+/\sqrt{m\hbar\omega_z} - iz_+/\sqrt{\hbar/(m\omega_z)}$ is a displacement in the harmonic oscillator phase space, and where p_+ is the center-of-mass mode momentum. $\phi_+ = \phi_+(\alpha_1, \alpha_2, t)$ is the phase acquired due to excitation by the force term f_+. From the time-dependent Schrödinger equation for $\mathcal{U}_{int,+}$ it can then be shown that

$$\beta_+(\alpha_1, \alpha_2, t) = -\frac{1}{\hbar}\int_0^t dt' f_+(\alpha_1, \alpha_2, t') e^{-i\omega_z t'} \tag{6.2.11}$$

and

$$\phi_+(\alpha_1, \alpha_2, t) = -\frac{1}{\hbar^2}\,\mathrm{Im}\left[\int_0^t dt' f_+(\alpha_1, \alpha_2, t') e^{-i\omega_z t'} \underbrace{\left(\int_0^{t'} dt'' f_+(\alpha_1, \alpha_2, t'') e^{i\omega_z t''}\right)}_{-\hbar\beta_+^*(\alpha_1, \alpha_2, t')}\right]. \tag{6.2.12}$$

The displacement of the ions is in general internal state dependent, which leads to coupling (or entanglement) between the internal and the motional states. For the gate operation, this is an undesired effect and we shall therefore request the displacement to be zero at the end of the gate operation, such that $\mathcal{U}_{int,+} = e^{i\phi_+}$. In the implementation of the Controlled-Z gate described below, we will take the dipole-potential to be of the form $U_{dip}(z_{i,eq}, \alpha_i, t) = U_{const}(z_{i,eq}) + U_{osc}(z_{i,eq}, \alpha_i)g(t)$ $(i = 1, 2)$ in a time interval $[0, T]$ and zero otherwise. Mathematically, we assume below that $g(t)$ and f_{const} vanish outside $[0, T]$. From this specific form of the dipole potential, it follows that f_+ can be written as $f_+(\alpha_1, \alpha_2, t) = f_{const}(z_{1,eq}, z_{2,eq}) + f_{osc}(z_{1,eq}, z_{2,eq}, \alpha_1, \alpha_2)g(t)$, which together with Eq. (6.2.11) implies that the center-of-mass mode displacement at the end of the gate operation is

$$\beta_+(T) = i\frac{f_{const}}{\hbar\omega_z}(1 - e^{-i\omega_z T}) - i\frac{f_{osc}}{\hbar}\int_0^T dt g(t) e^{-i\omega_z t}. \tag{6.2.13}$$

For this expression to be zero, T should be equal to an integer number, n, of oscillation periods, $T = 2\pi n/\omega_z$, and the integral in the last term should be zero, which in fact is equivalent to saying that the Fourier transform of $g(t)$, $\tilde{g}(\omega)$, is zero at $\omega = \omega_z$, since, using that $g(t)$ is zero outside $[0, T]$, it follows that

$$\frac{1}{\sqrt{2\pi}} \int_0^T dt g(t) e^{-i\omega_z t} = \frac{1}{\sqrt{2\pi}} \int_{-\infty}^{\infty} dt g(t) e^{-i\omega_z t} = \tilde{g}(\omega_z). \tag{6.2.14}$$

The phase ϕ_+ in Eq. (6.2.12), which is equal to the area of the (z_+, p_+) phase-space trajectory in units of $\hbar$, depends on the internal state of both ions, as needed for the Controlled-Z gate. From Eq. (6.2.12) it can be shown that the phase acquired during the gate operation can be expressed as

$$\phi_+(T) = \frac{1}{\hbar^2} \int_{-\infty}^{\infty} d\omega' \frac{\left|\tilde{f_+}(\omega')\right|^2}{\omega' - \omega_z} = C_1 f_{const}^2 + C_2 f_{const} f_{osc} \tilde{g}(0) + \frac{1}{\hbar^2} \int_{-\infty}^{\infty} d\omega' \frac{|\tilde{g}(\omega')|^2}{\omega' - \omega_z}, \tag{6.2.15}$$

where $\tilde{f_+}(\omega)$ is the Fourier transform of $f_+(t)$ and C_1 and C_2 are constants. The first term on the r.h.s. is irrelevant, since it is independent of the internal state of the ions and the second term disappears if we require $\tilde{g}(0) = 0$, which we shall do for reasons discussed below. Thus, the only interesting term is the last one, from which we observe that the closer the characteristic frequencies of the function $g(t)$ are to the oscillation frequency ω_z (or $\sqrt{3}\omega_z$ for the breathing mode), the larger is the accumulated phase.

The total phase acquired during the gate operation, however, also has a contribution from the internal state dependent Stark shifts appearing in the first factor in Eq. (6.2.6). This contribution can totally scramble the desired gate operation, since it is of first order in the dipole beam intensity, whereas ϕ_+ only is of second order in the intensity. With the specific form of the dipole potential assumed above, the first term, $U_{const}(z_{i,eq})$, gives rise to a Stark-shift induced phase-shift, which is independent of the internal state and hence uncritical to the gate operation. The Stark-shift induced phase-shift due to the term $U_{osc} g(t)$ cancels if $\int_0^T g(t)dt = 0$, or equivalently if $\tilde{g}(0) = 0$.

For the displacement of the breathing mode to be zero at the end of the gate operation, $\tilde{g}(\sqrt{3}\omega_z) = 0$ and $T = 2\pi m/(\sqrt{3}\omega_z)$ with m integer, should be fulfilled. Thus we have in total three conditions on $\tilde{g}(\omega)$: $\tilde{g}(0) = \tilde{g}(\omega_z) = \tilde{g}(\sqrt{3}\omega_z) = 0$. These conditions can be fulfilled by a proper choice of $g(t)$. Conversely, a function $\tilde{g}(\omega)$ which vanishes at 0, ω_z and $\sqrt{3}\omega_z$ can be constructed and Fourier-transformed to yield $g(t)$. The conditions on T can be fulfilled approximately for special values of n; for example we have $\left(n, m, \left|\sqrt{3}n - m\right|\right) = (15, 26, 2\%); (56, 97, 0.5\%); (209, 362, 0.1\%)$.

6.2.1 Implementation in alkaline earth ions

An experimental realization of the Controlled-Z gate is possible using the alkaline earth $^{40}Ca^+$, $^{88}Sr^+$ or $^{138}Ba^+$ ions, which all have a similar internal structure, making our 'favorite' choice of qubit states $|\downarrow\rangle = n\,^2S_{1/2}(-1/2)$ and $|\uparrow\rangle = n\,^2S_{1/2}(+1/2)$. Below, results are presented for $^{40}Ca^+$ and $^{138}Ba^+$. We assume in the following that the dipole beam frequency ω_L is close to or below the transition frequencies $\omega_{1/2}$ and $\omega_{3/2}$ of the $n\,^2S_{1/2}$–$n\,^2P_{1/2}$ and the $n\,^2S_{1/2}$–$n\,^2P_{3/2}$ transitions, respectively, such that we only need to consider contributions to the dipole potential from these two transitions (assuming

that ω_L is not in the immediate vicinity of the transition frequencies of the weak $n\,^2S_{1/2}$–$(n-1)\,^2D_{3/2,5/2}$ electric quadrupole transitions). We consider a dipole beam containing only σ^+- and σ^--polarized light components with respect to the quantization axis for the ions (the propagation direction of the dipole beam), in which case the contributions to the dipole potential in the two states $|\downarrow\rangle$ and $|\uparrow\rangle$ are illustrated in Fig. 6.2. The respective dipole potentials can therefore be written as

$$U_\downarrow = \psi_+ I_+ + \psi_- I_- \quad \text{and} \quad U_\uparrow = \psi_- I_+ + \psi_+ I_-, \tag{6.2.16}$$

where $I_\pm$ is the intensity of the σ^+- and σ^--polarized components, respectively, and where

$$\psi_+ = \frac{3\pi c^2}{2}\left[\frac{2\Gamma_{1/2}}{3\omega_{1/2}^3}\left(\frac{1}{\omega_{1/2}-\omega_L}+\frac{1}{\omega_{1/2}+\omega_L}\right)+\frac{\Gamma_{3/2}}{3\omega_{3/2}^3}\left(\frac{1}{\omega_{3/2}-\omega_L}+\frac{1}{\omega_{3/2}+\omega_L}\right)\right] \tag{6.2.17}$$

and

$$\psi_- = \frac{3\pi c^2}{2}\frac{\Gamma_{3/2}}{\omega_{3/2}^3}\left(\frac{1}{\omega_{3/2}-\omega_L}+\frac{1}{\omega_{3/2}+\omega_L}\right) \tag{6.2.18}$$

depend only on the properties of the ion and the dipole laser frequency. Here, $\Gamma_{1/2}$ and $\Gamma_{3/2}$ are the transition strengths of the $n\,^2S_{1/2}$–$n\,^2P_{1/2}$ and the $n\,^2S_{1/2}$–$n\,^2P_{3/2}$ transitions [2], respectively. Now, to make the force derived from the dipole potential depend upon the qubit state, the intensities of the two polarization components have to differ. This does, however, give rise to an internal state dependent Stark-shift induced phase. In order to get rid of the internal state dependence, we choose to vary the intensity of the polarization components in time, such that after the gate operation the integrated Stark-shift induced phase is equal for $|\downarrow\rangle$ and $|\uparrow\rangle$ in each ion. Meanwhile, the dipole force is still present to enable a non-trivial quantum logic operation. Choosing the intensity of the polarization components to vary sinusoidally with frequency Ω, the temporal variation of the intensity is given by

$$I_\pm(z,t) = \frac{1}{2}I(z)[1 \pm \sin(\Omega t)] \tag{6.2.19}$$

in the time interval $[0,T]$ and zero outside this interval. Such a variation in time can easily be realized using an electrooptic modulator. With the intensity given by Eq. (6.2.19) the dipole potential has the form asserted in the previous section, making the identification $g(t) = \sin(\Omega t)$. As for the choice of Ω, we recall the requirements $T = 2\pi n/\omega_z$ with n integer, $\tilde{g}(0) = \tilde{g}(\omega_z) = \tilde{g}(\sqrt{3}\omega_z) = 0$ and that the characteristic frequency of $g(t)$, i.e., Ω, should be close to ω_z. A good choice is therefore $\Omega = (1-1/n)\omega_z$ with $n \gg 1$, such that in the time interval $[0,T]$ the ions experience an integer number $(n-1)$ of polarization rotation periods and undergo an integer number (n) of oscillations in the trap. The Fourier transform of $g(t)$ on the interval $[0,T]$ [see Eq. (6.2.14)] contains two terms, which are proportional to $\sin[(\omega-\Omega)T/2]/(\omega-\Omega)$ and $\sin[(\omega+\Omega)T/2]/(\omega+\Omega)$, respectively. These sinc-functions peak at $\omega = \Omega$ and $\omega = -\Omega$, but they have exact zeros at $\omega = 0$ and $\omega = \omega_z$, are suppressed at $\omega = \sqrt{3}\omega_z$ and are even further suppressed if $\sqrt{3}n$ is close to an integer.

[2] The same notation was introduced in Chap. 3 for these quantities in $^{40}Ca^+$. In this chapter, the notation applies for the relevant ion species.

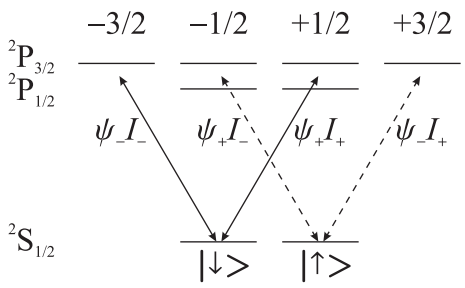

Figure 6.2: Relevant energy-levels and transitions in alkaline earth ions (e.g.,$^{40}Ca^+$, $^{88}Sr^+$, and $^{138}Ba^+$) for calculating the dipole potential for the qubit states $|\downarrow\rangle = {}^2S_{1/2}(-1/2)$ (solid lines) and $|\uparrow\rangle = {}^2S_{1/2}(+1/2)$ (dashed lines) due to a dipole beam containing σ^+– and σ^-–polarized components with intensities I_+ and I_-, respectively. ψ_+ and ψ_- are defined in the text.

In order to calculate the displacement and the acquired phase for the center-of-mass mode and the breathing mode for the specific intensity variation in Eq. (6.2.19), the f-function entering in the integrals in Eqs. (6.2.11) and (6.2.12) has to be determined using the definitions in Eqs. (6.2.4) or (6.2.5). For f_+, which is responsible for excitation of the center-of-mass mode, we find

$$f_+(\downarrow\downarrow) = -\left[f_{0+} + f_{1+}\sin(\Omega t)\right], \tag{6.2.20}$$
$$f_+(\downarrow\uparrow) = -\left[f_{0+} + f_{2+}\sin(\Omega t)\right], \tag{6.2.21}$$
$$f_+(\uparrow\downarrow) = -\left[f_{0+} - f_{2+}\sin(\Omega t)\right], \tag{6.2.22}$$
$$f_+(\uparrow\uparrow) = -\left[f_{0+} - f_{1+}\sin(\Omega t)\right], \tag{6.2.23}$$

where

$$f_{0+} = \sqrt{\frac{\hbar}{8m\omega_z}}(\tilde{F}_1 + \tilde{F}_2)(\psi_+ + \psi_-), \tag{6.2.24}$$
$$f_{1+} = \sqrt{\frac{\hbar}{8m\omega_z}}(\tilde{F}_1 + \tilde{F}_2)(\psi_+ - \psi_-), \tag{6.2.25}$$
$$f_{2+} = \sqrt{\frac{\hbar}{8m\omega_z}}(\tilde{F}_1 - \tilde{F}_2)(\psi_+ - \psi_-) \tag{6.2.26}$$

and

$$\tilde{F}_i = -\frac{1}{2}\frac{\partial I(z)}{\partial z}\bigg|_{z=z_{i,eq}} \qquad (i = 1, 2). \tag{6.2.27}$$

The full time-dependent expressions $\beta(t)$ and $\phi(t)$, which can be obtained by carrying out the integrals in Eqs. (6.2.11) and (6.2.12), are given in App. A, both for the center-of-mass mode and the breathing mode. Here we only state the acquired phases at the end of the gate operation, which for the center-of-mass mode are given by

$$\phi_+(\downarrow\downarrow, T) = \phi_+(\uparrow\uparrow, T) = \frac{f_{1+}^2}{(2\hbar)^2}\frac{2\omega_z T}{\omega_z^2 - \Omega^2} \approx \frac{f_{1+}^2}{(\hbar\omega_z)^2}\frac{n^2\pi}{2} \tag{6.2.28}$$

and

$$\phi_+(\downarrow\uparrow,T) = \phi_+(\uparrow\downarrow,T) = \frac{f_{2+}^2}{(2\hbar)^2}\frac{2\omega_z T}{\omega_z^2-\Omega^2} \approx \frac{f_{2+}^2}{(\hbar\omega_z)^2}\frac{n^2\pi}{2}, \tag{6.2.29}$$

where an internal state independent term has been neglected and the approximation is good for large n. These phases scale quadratically with n, with one factor of n originating from the gate time T and the other one originating from the denominator, owing to the fact that Ω was chosen to be near-resonant with ω_z. The phases acquired due to excitation of the breathing mode are given by the following expressions

$$\phi_-(\downarrow\downarrow,T) = \phi_-(\uparrow\uparrow,T) = \frac{f_{1-}^2}{(2\hbar)^2}\frac{2\sqrt{3}\omega_z T}{3\omega_z^2-\Omega^2} \approx \frac{f_{1-}^2}{(\hbar\omega_z)^2}\frac{\sqrt{3}n\pi}{2} \tag{6.2.30}$$

and

$$\phi_-(\downarrow\uparrow,T) = \phi_-(\uparrow\downarrow,T) = \frac{f_{2-}^2}{(2\hbar)^2}\frac{2\sqrt{3}\omega_z T}{3\omega_z^2-\Omega^2} \approx \frac{f_{2-}^2}{(\hbar\omega_z)^2}\frac{\sqrt{3}n\pi}{2}, \tag{6.2.31}$$

where

$$f_{1-} = f_{1+}\frac{\tilde{F}_2-\tilde{F}_1}{\sqrt[4]{3}(\tilde{F}_2+\tilde{F}_1)} \quad \text{and} \quad f_{2-} = f_{2+}\frac{\tilde{F}_2+\tilde{F}_1}{\sqrt[4]{3}(\tilde{F}_2-\tilde{F}_1)}. \tag{6.2.32}$$

These phases scale only linearly with n, since the rotation frequency Ω is off-resonant with the breathing mode frequency of $\sqrt{3}\omega_z$. In Eqs. (6.2.30) and (6.2.31) some terms have been neglected, which are smaller than the stated terms by a factor of n and further suppressed if $\sqrt{3}n$ is close to an integer.

The combined effect of the above phaseshifts is equivalent to a single phaseshift of $\phi_\pm = \phi_\pm(\downarrow\downarrow) - \phi_\pm(\downarrow\uparrow) - \phi_\pm(\uparrow\downarrow) + \phi_\pm(\uparrow\uparrow) = 2[\phi_\pm(\downarrow\downarrow) - \phi_\pm(\downarrow\uparrow)]$ for the $|\uparrow\rangle|\uparrow\rangle$ state [102]. Thus, to make a Controlled-Z gate, we require that

$$\begin{aligned}\pi =& 2\left[\phi_+(\downarrow\downarrow,T) + \phi_-(\downarrow\downarrow,T) - \phi_+(\downarrow\uparrow,T) - \phi_-(\downarrow\uparrow,T)\right] \\ \approx& \frac{\pi n^2}{(\hbar\omega_z)^2}\left[f_{1+}^2 - f_{2+}^2 + \frac{\sqrt{3}}{n}\left(f_{1-}^2 - f_{2-}^2\right)\right].\end{aligned} \tag{6.2.33}$$

For an experimental realization of the considered gate, two highly relevant parameters are the required peak intensity I_0 and the fidelity loss due to off-resonant scattering events. The required peak intensity enters in Eq. (6.2.33) through the f-functions. Once a choice of beam profile and position of the dipole beam with respect to the ion-string is made, the intensity can therefore be determined as a function of the dipole beam wavelength λ_L. Since the intensity is set by the requirement that an effective phaseshift of π should be obtained, an inherently small effect of the optical dipole forces will lead to the requirement of a large intensity. The intensity in turn sets the scattering rate [see Eq. (6.1.3)] and hence the probability for off-resonant scattering events during the gate operation time T. In the following we shall find these parameters for specific configurations of the dipole beam.

We consider first the configuration depicted in Fig. 6.1 choosing $z_0 = W/2$, i.e., the two ions are centered at a distance of $W/2$ from the center of the dipole beam, which is where the intensity gradient and hence the dipole force is maximal. The equilibrium distance between the ions is assumed to be much smaller than the waist, such that the linearization of the dipole potential in Eq. (6.1.5) is a good approximation and the dipole force is almost equal for the two ions. To find the required intensity, we first find the f-functions for the considered beam configuration using the definitions in Eqs. (6.2.25)–(6.2.27) and (6.2.32), which yields $\tilde{F}_1 \approx \tilde{F}_2 \approx e^{-1/2} I_0/W$, $f_{2+} \approx f_{1-} \approx 0$ and non-zero expressions for f_{1+} and f_{2-}. From the expressions for f_{1+} and f_{2-} and Eq. (6.2.33) it follows that the required peak intensity

$$I_0 \approx \sqrt{\frac{2e^1 \hbar \omega_z^3 m W^2}{n^2(\psi_+ - \psi_-)^2}}, \tag{6.2.34}$$

where only the leading term in n has been retained. We note that large n leads to a large phase pick-up and hence a low intensity requirement and the same holds for the difference $\psi_+ - \psi_-$, since it determines the dipole potential difference between $|\downarrow\rangle$ and $|\uparrow\rangle$. Furthermore, for a small waist the dipole force is large, which in turn reduces the required intensity. Note also that the required laser *power* ($\sim I_0 W^2$) is proportional to W^3, which makes a small waist very attractive.

Knowing the required intensity, we can now determine the scattering rate Γ_{sc} and hence the probability for a scattering event during the gate operation, which is equal to $1 - \exp[-\Gamma_{sc} T] \approx \Gamma_{sc} T$, if $\Gamma_{sc} T \ll 1$. In calculating Γ_{sc}, we sum the scattering contributions due to the coupling of $|\downarrow\rangle$ and $|\uparrow\rangle$ to the $n\,^2P_{1/2}$- and the $n\,^2P_{3/2}$-state for both ions. Assuming an equal average population in the two internal states and an intensity of $e^{-1/2} I_0$ at the position of the ions, we find

$$\Gamma_{sc} T \approx \frac{\tilde{\Gamma}_{sc}}{\psi_+ - \psi_-} \sqrt{8\pi^2 \hbar \omega_z m W^2}, \tag{6.2.35}$$

where

$$\begin{aligned} \tilde{\Gamma}_{sc} =& \frac{3\pi c^2 \omega_L^3}{2\hbar} \\ & \times \left[\frac{\Gamma_{1/2}^2}{\omega_{1/2}^6} \left(\frac{1}{\omega_{1/2} - \omega_L} + \frac{1}{\omega_{1/2} + \omega_L} \right)^2 + \frac{\Gamma_{3/2}^2}{\omega_{3/2}^6} \left(\frac{1}{\omega_{3/2} - \omega_L} + \frac{1}{\omega_{3/2} + \omega_L} \right)^2 \right]. \end{aligned} \tag{6.2.36}$$

The front factor of $\tilde{\Gamma}_{sc}/(\psi_+ - \psi_-)$ in Eq. (6.2.35) contains the entire dependence of $\Gamma_{sc} T$ on the internal structure of the ion and the wavelength of the dipole beam, showing that $\Gamma_{sc} T$ can be minimized either by making $\tilde{\Gamma}_{sc}$ small or $\psi_+ - \psi_-$ large. $\tilde{\Gamma}_{sc}$ becomes small in the limit $\omega_L \ll \omega_{1/2}, \omega_{3/2}$ due to the factor of ω_L^3, however, in the same limit $\psi_+ - \psi_-$ is proportional to the *difference* $\Gamma_{1/2}\omega_{1/2}^{-4} - \Gamma_{3/2}\omega_{3/2}^{-4}$, which also is small. Alternatively, if $\omega_{1/2} < \omega_L < \omega_{3/2}$, $\psi_+ - \psi_-$ can become a *sum* of two terms, however, for $\tilde{\Gamma}_{sc}$ to be small in this case, a large fine-structure splitting is required. Both in the far-off resonant case and when the dipole laser is tuned in between the fine-structure levels, the $^{138}Ba^+$ ion turns out to be more attractive than the $^{40}Ca^+$ and the $^{88}Sr^+$ ions.

Now, to get some numbers out for the intensity and the scattering probability, we take a typical trap frequency of $\omega_z = 2\pi \times 1\,\mathrm{MHz}$, for which the equilibrium distance is

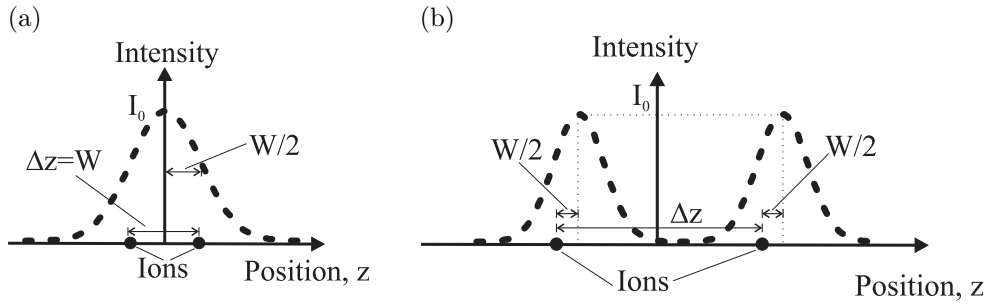

Figure 6.3: (a) Two ions positioned at a distance of $\pm W/2$ from the center of a Gaussian laser beam. (b) Two ions, each positioned at a distance of $W/2$ from the center of a tightly focussed Gaussian laser beam.

5.6 μm between two $^{40}Ca^+$ ions and 3.7 μm between two $^{138}Ba^+$ ions. The waist is taken to be 30 μm, which is larger than the equilibrium distance between the ions as assumed above. Finally, choosing $n = 15$ ($\sqrt{3}n \approx 26$) the intensity and the scattering rate can be calculated. For $^{40}Ca^+$ and $^{138}Ba^+$ with the dipole laser tuned in between the fine-structure levels or far red detuned (where ψ_+ and ψ_-, and hence the required power, approaches a constant), we find the following values for (Power, $\Gamma_{sc}T$, λ_L). $^{40}Ca^+$: (8 W, 30%, 395.1 nm) and ($\sim$0.5 MW, $<$ 4%, $>$1500 nm). $^{138}Ba^+$: (86 W, 6%, 474.5 nm) and ($\sim$33 kW, $<$ 1.2%, $>$1000 nm). Clearly, this is not very promising for an experimental realization. Since a smaller waist would decrease the required power as well as the scattering probability, it would be attractive to employ a beam configuration where the waist which is of the order of or smaller than Δz. In such cases the equations derived above are still valid, as long as the excursion of the ions from their equilibrium position is smaller than the waist. For example, one could choose $W = \Delta z$ and position the ions on either side of the center of the dipole beam ($z_0 = 0, z_{1,eq} = -W/2, z_{2,eq} = W/2$) as shown in Fig. 6.3(a). Taking $\omega_z = 2\pi \times 200$ kHz, it follows that $\Delta z = 16.4\,\mu$m for $^{40}Ca^+$ and $\Delta z = 10.9\,\mu$m for $^{138}Ba^+$. Using $n = 15$ ($T = 75\,\mu$s), the following values for (Power, $\Gamma_{sc}T$, λ_L) can be obtained. $^{40}Ca^+$: (120 mW, 8%, 395.1 nm) and ($\sim$6.5 kW, $<$ 0.9%, $>$1500 nm). $^{138}Ba^+$: (360 mW, 1%, 474.5 nm) and ($\sim$140 W, $<$ 0.2%, $>$1000 nm). The required power is relatively high, but it can be reduced, e.g., by a factor of 14 by choosing $n = 209$ ($\sqrt{3}n \approx 362$), which leaves the scattering probability unchanged but increases the gate time by a factor of 14 to 1 ms. Except for $^{40}Ca^+$ in the long wavelength limit, this would be realistic for a first demonstration of the present gate proposal, using one of the laser sources discussed below.

Before the discussion of laser sources, we consider a more favourable dipole beam configuration shown Fig. 6.3(b), where two tightly focussed beams with an equally large waist, which is smaller than the equilibrium distance between the ions, are directed onto one ion each and centered at a distance of $W/2$ from the ion, such that the dipole force is equal and maximal for both ions. Using Eqs. (6.2.34)–(6.2.36) above and choosing $\omega_z = 2\pi \times 200$ kHz and $W = 5\,\mu$m, we have plotted the required laser power and $\Gamma_{sc}T$ versus the dipole beam wavelength for $^{40}Ca^+$ and $^{138}Ba^+$ in Fig. 6.4, both in the far red detuned case [Fig. 6.4(a,c)] and in the case where the dipole beam is tuned in between the fine-structure levels [Fig. 6.4(b,d)]. In all cases $n = 15$, which yields a very reasonable gate time of $T = 75\,\mu$s. The plots in Fig. 6.4(a,c) extends to a wavelength

of 5 μm in order to show the long-wavelength behaviour, however, one should keep in mind that for wavelengths of the order of or larger than the waist of 5 μm, diffraction will be a limiting factor.

For $^{40}Ca^{+}$, we see from Fig. 6.4(a) that a high power of $\sim$ 200 W is required in the long wavelength limit for the considered parameters. By choosing $n = 209$ instead of 15, the required power drops by a factor of ~ 14, yielding a much more reasonable required power of $\sim$ 15 W in the long wavelength limit, i.e., roughly for wavelength above 2000 nm. When taking diffraction into account, a wavelength around 2000 nm therefore seems to be an optimal choice. At or near this wavelength, 15 W can easily be obtained from a commercially available Thulium Fiber Laser operating in the range 1750-2200 nm [3] and hence quantum gates for which $\Gamma_{sc}T \lesssim 10^{-3}$ should be feasible using $^{40}Ca^{+}$. In addition, a wavelength around 395 nm is attractive for $^{40}Ca^{+}$ [see Fig. 6.4(b)], since only 3 mW is required at this wavelength, which easily can be obtained. The scattering rate of a few percent is acceptable for a first demonstration, but not for implementation of error correcting schemes. By a reduction of the beam waist, e.g., using a dedicated lens system placed inside the vacuum chamber where the ion trap is situated, it should be possible to focus to below 1 μm [103] and hence reduce the scattering rate by a factor of 5–10.

Due to the larger fine-structure splitting of $^{138}Ba^{+}$, the scattering probability is already below 1% for a wavelength around 475 nm, i.e., between the fine-structure levels [see Fig. 6.4(d)]. The required power of $\sim$ 35 mW can easily be provided by frequency-doubled diode laser systems. Note also that light from an Argon-ion laser at a wavelength of 488 nm could be a reasonable possibility. However, as for $^{40}Ca^{+}$ a commercially available Thulium Fiber Laser operating around a wavelength of 2000 nm seems to be most ideal. In this case the scattering probability is as low as $\sim 10^{-4}$, which is comparable to the threshold value for fault-tolerant quantum computation [98]. In the long wavelength limit, the 1064 nm wavelength of a Nd:YAG laser would also be quite attractive with a scattering probability below 10^{-3} at a required power of $\sim$ 7 W.

Note that in all cases discussed above the required power, the scattering probability and the gate time can be adjusted by changing n, ω_z and W.

It should be noted, that the gate proposal is not limited to the case where $g(t) = \sin(\Omega t)$. It would for example also work with $g(t) = \sin[M \sin(\Omega t)]$, which occurs if a sinusoidally varying voltage is applied to an electrooptic modulator (modulation index M), with the polarization of the input beam oriented at 45° with respect to the principal axes of the modulator crystal. However, the calculations are more cumbersome than for the present case and will not be reproduced here.

Finally, in order to illustrate the time-development of the phase-space displacement and the acquired phase, we have plotted these quantities in Fig. 6.5. The plots are for $^{40}Ca^{+}$ with $\lambda_L = 395.1$ nm and $n = 15$. The trap frequency and the waist are irrelevant for these plots, when the intensity is set such that an effective phase-shift of π is obtained. Fig. 6.5(a) is a parametric plot of the real and imaginary parts of the displacement $\beta_+(t)$ of the center-of-mass mode, i.e., $p_+/\sqrt{\hbar m\omega_z}$ and $-z_+/\sqrt{\hbar/(m\omega_z)}$, respectively, when the ions are in the $|\downarrow\rangle|\downarrow\rangle$ state. Fig. 6.5(b) is a similar plot for the breathing mode, when the ions are in the $|\downarrow\rangle|\uparrow\rangle$ state. Note that the center-of-mass mode is more strongly excited than the breathing mode [the scale in Fig. 6.5(a) is about ten times larger than in Fig. 6.5(b)], since the driving force is near-resonant with the center-of-mass mode

[3] IPG Photonics, TLR-series, capable of delivering up to 150 W. `http://www.ipgphotonics.com`.

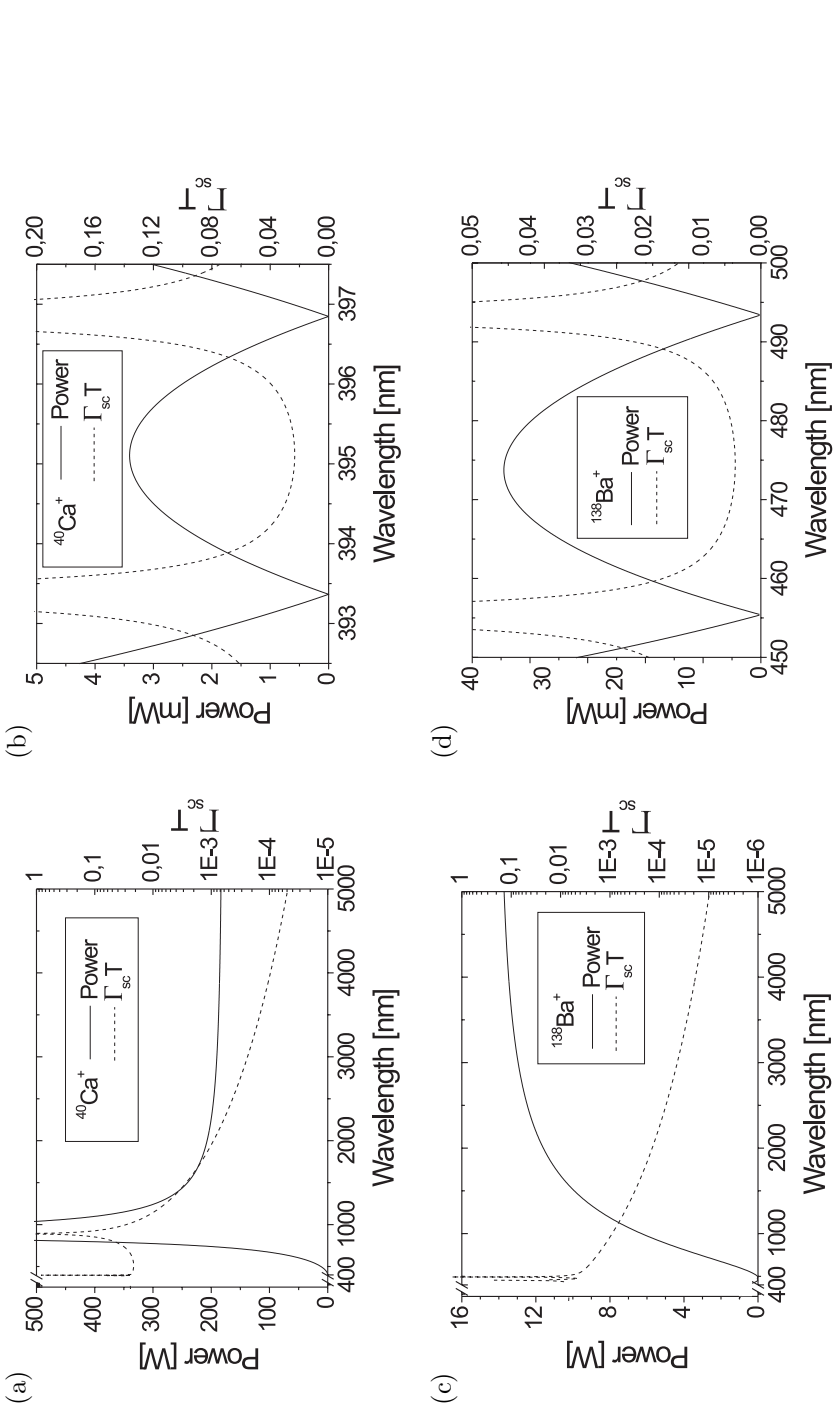

Figure 6.4: Required power and $\Gamma_{sc}T$ vs. dipole beam wavelength for $^{40}Ca^+$ and $^{138}Ba^+$. In all plots $\omega_z = 2\pi \times 200\,\mathrm{kHz}$, $W = 5\,\mu\mathrm{m}$, $n = 15$ and $T = 75\,\mu\mathrm{s}$. Note: In (a) and (c) diffraction is a limiting factor for long wavelengths. (a) $^{40}Ca^+$, far red detuned dipole laser. The divergences near 900 nm are due to a cancellation of $\psi_+ - \psi_-$. (b) $^{40}Ca^+$, dipole laser tuned in between the $n\,^2P_{1/2}$ and $n\,^2P_{3/2}$ fine-structure levels. (c) $^{138}Ba^+$, far red detuned dipole laser. (d) $^{138}Ba^+$, dipole laser tuned in between the $n\,^2P_{1/2}$ and $n\,^2P_{3/2}$ fine-structure levels.

frequency. The excitation of the center-of-mass mode at a frequency slightly below its eigenfrequency, leads to an increasing distance from the phase-space origin until the turning point near $\mathrm{Re}[\beta_+] \sim 1$, where the relative phase between the motion of the ions and the driving force makes the driving force have a damping effect on the motion of the ions, taking them back to the phase-space origin after 15 trap oscillation periods. For the breathing mode, the off-resonant driving force is unable to excite the ions to a large amplitude, so in this case the phase-space trajectory is in the vicinity of the phase-space origin, where it (almost) ends up right at the time, where the center-of-mass mode trajectory is back at the phase-space origin. The acquired phase, which is just the encircled phase-space area in units of $\hbar$, is plotted in Fig. 6.5(c). More precisely, the effective phase-shift of the $|\uparrow\rangle|\uparrow\rangle$ state, i.e., $2[\phi_+(\downarrow\downarrow,t) - \phi_-(\downarrow\uparrow,t)]$, is plotted together with the center-of-mass mode contribution of $2\phi_+(\downarrow\downarrow,t)$, showing that the breathing mode contribution is small. Note, that the acquired phase increases with the largest rate in the middle of the gate operation, corresponding to the part of the trajectory in Fig. 6.5(a) where $\mathrm{Re}[\beta_+] \sim 1$, where the area swept per unit time is largest. In contrast, at the beginning and at the end of the gate-operation, there are only small 'wiggles' on the curves, which to some extent makes the acquired phase robust against timing errors.

6.2.2 Error sources

Apart from the fidelity loss due to scattering induced by the dipole beam, there are many other potential error sources, which are relevant for the fidelity of the gate operation. A key element in the present gate proposal is the polarization rotation, which removes the internal state dependency of the Stark-shift induced phase. Since the Stark shift is of first order in intensity and the phase acquired by the change in Coulomb energy originates from second order effects, even small errors in the polarization rotation may be very critical to the actual gate operation. In the following, the influence on the polarization rotation from polarization errors, timing errors and power-, position- and frequency-fluctuations of the dipole laser is discussed.

Polarization errors

In case there is an imbalance of the intensity in the two polarization components, such that

$$I_\pm(z,t) = \frac{1}{2} I(z)(1 \pm \epsilon_p)[1 \pm \sin(\Omega t)], \tag{6.2.37}$$

where ϵ_p accounts for the imbalance, there will be two extra terms in the dipole potential. One term $[\propto \epsilon_p \sin(\Omega t)]$ enters with the same sign in $U_\downarrow$ and $U_\uparrow$ and hence it does not give rise to any Stark-shift induced phase-difference between $|\downarrow\rangle$ and $|\uparrow\rangle$. The other term, $\epsilon_p I(z)(\psi_+ - \psi_-)/2$, enters with a different sign in $U_\downarrow$ and $U_\uparrow$, which leads to a phase-difference of $\Delta\phi = \epsilon_p I(z)(\psi_+ - \psi_-)T/\hbar$ between $|\downarrow\rangle$ and $|\uparrow\rangle$ in each ion at the end of the gate operation. This difference should be much smaller than the desired phase-shift of π. Using the expression for $\Delta\phi$, Eqs. (6.1.4), (6.2.34) and $T = 2\pi n/\omega_z$, we obtain the condition

$$\epsilon_p \ll \sqrt{\frac{\hbar}{8\omega_z m W^2}}. \tag{6.2.38}$$

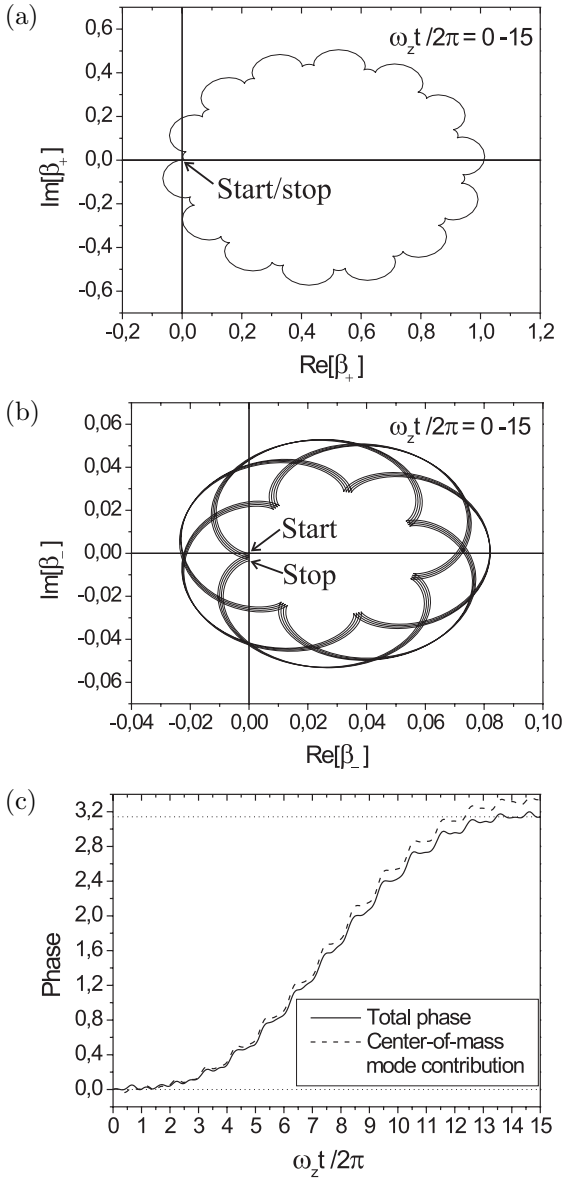

Figure 6.5: Real and imaginary parts of the center-of-mass mode and the breathing mode displacement $\beta_{\pm}(t)$ and the acquired phase for $^{40}Ca^{+}$ with $n = 15$ and a dipole beam wavelength of 395.1 nm. The trap frequency, the waist and the intensity are set to obtain an effective phaseshift equal to π of the $|\uparrow\rangle|\uparrow\rangle$ state. (a) Parametric plot showing $(\mathrm{Re}[\beta_+(t)], \mathrm{Im}[\beta_+(t)]) = (p_+/\sqrt{\hbar m\omega_z}, -z_+/\sqrt{\hbar/m\omega_z})$ for the center-of-mass mode, when the ions are in $|\downarrow\rangle|\downarrow\rangle$. (b) Parametric plot showing $(\mathrm{Re}[\beta_-(t)], \mathrm{Im}[\beta_-(t)]) = (p_-/\sqrt{\hbar m\sqrt{3}\omega_z}, -z_-/\sqrt{\hbar/m\sqrt{3}\omega_z})$ for the breathing mode, when the ions are in $|\downarrow\rangle|\uparrow\rangle$. In both (a) and (b) the phase-space trajectory starts out from the origin and goes clockwise as time elapses. (c) Acquired phase. The solid line is the total effective phase of $2[\phi_+(\downarrow\downarrow, t) - \phi_-(\downarrow\uparrow, t)]$. The dashed line is the center-of-mass mode contribution of $2\phi_+(\downarrow\downarrow, t)$. The dotted lines indicate phases of 0 and π.

In the situation considered above with $W = 5\,\mu$m and $\omega_z = 2\pi \times 200\,$kHz this means $\epsilon_p \ll 1/400$ for $^{40}Ca^+$ and $\epsilon_p \ll 1/700$ for $^{138}Ba^+$. Fulfilling these criteria is not very realistic, but fortunately the undesired phase-difference can be cancelled using the spin-echo technique [23]. Instead of generating the full effective phase-shift of π in a single operation, the gate-operation can be performed in four steps: (1) Run the gate at half the intensity, to get an effective phase-shift of $\pi/2$ on $|\uparrow\rangle|\uparrow\rangle$. (2) Swap the population between $|\downarrow\rangle$ and $|\uparrow\rangle$ by applying single-qubit π-pulses to both ions. (3) Same as (1). (4) Same as (2). The trick is that the undesired phase-differences due to an intensity imbalance, which are obtained in step (1) and (3), are of the same magnitude but have opposite signs (due to the population swapping) and therefore cancel out. The gate operations in (1) and (3) both give an effective phase-shift of $\pi/2$, even though the population is swapped in (2), because $\phi_\pm(\downarrow\downarrow, T) = \phi_\pm(\uparrow\uparrow, T)$ and $\phi_\pm(\downarrow\uparrow, T) = \phi_\pm(\uparrow\downarrow, T)$. The final π-pulse just swaps the population back. In making this spin-echo trick, the gate time is doubled (neglecting the duration of the relatively fast π-pulses) while the required intensity is halved. Since the required intensity is proportional to n^{-1} and the gate time $T \propto n$, these parameters can be re-adjusted if an appropriate value for n is available.

Finally, the imbalance also gives rise to errors in the gate operation, which the spin-echo trick does not cancel. These errors are of the order ϵ_p^2 or ϵ_p/n and hence they are suppressed to the 10^{-4} level at a small but realistic value of $\epsilon_p \sim 1\%$.

Timing errors

In case the gate time differs from the duration of a full number of polarization rotation periods, an undesired phase-difference will again build up. Assuming $T = \delta T + 2\pi(n-1)/\Omega$ and $\Omega\delta T \ll 1$, the phase-difference is equal to $\Delta\phi$ above, with the replacement $\epsilon_p \mapsto \delta T^2\Omega/(2T)$. Again using $W = 5\,\mu$m and $\omega_z = 2\pi \times 200\,$kHz and considering $^{40}Ca^+$ with $n = 15$, Eq. (6.2.38) translates to $\delta T \ll 0.5\,\mu$s, with a more relaxed limit for larger n (the limit is proportional to $\sqrt{n}$). Using electrooptic modulators to control the laser pulse length, this condition on δT is not very severe. Moreover, if step (1) and step (3) are subject to the same relative timing error as the entire gate operation, i.e., if they are of duration $[\delta T + 2\pi(n-1)/\Omega]/2$, the spin-echo trick will cancel the phase-difference.

Power fluctuations

If the total laser power fluctuates at a frequency ω_f, such that the total intensity is given by $I_0(t) = I_0[1+\epsilon_f \sin(\omega_f t)]$, then the resulting fluctuations in the dipole potential integrated over the gate time T will give rise to a phase difference between $|\downarrow\rangle$ and $|\uparrow\rangle$. If the intensity fluctuations are random, they can in general not be expected to cancel using the spin-echo trick. When $\omega_f \sim \Omega$ the phase difference $\Delta\phi \sim \epsilon_f I(z)(\psi_+ - \psi_-)/2$, i.e., the same phase-difference as above, just with ϵ_p replaced by ϵ_f, which means that $\epsilon_f \ll 1/400$ is required for $^{40}Ca^+$. When $\omega_f \ll \Omega$ the phase-difference is smaller by a factor of $2\pi n$ and even smaller if $\omega_f \gg \Omega$. Intensity stabilization fulfilling $\epsilon_f \ll 1/400$ should not be unrealistic, in fact a commercially available Laser Power Controller already offers a power-stability of $3 \cdot 10^{-4}$ within certain limits [4].

[4] Laser power controller from Brockton Electro Optics, `http://www.brocktoneo.com`. LPC-model: Power stability of $3 \cdot 10^{-4}$ over 8 hours, DC to 5 kHz, optical power up to 15 W, 425-1100 nm. LS-model: Same stability, DC to 2 MHz, optical power up to 4 W, 400-740 nm.

Position fluctuations

Fluctuations in the position of the dipole laser gives rise to intensity fluctuations, which leads to imperfect cancellation of the Stark-shift induced phase and an unwanted variation in the dipole force exerted on the ions. When ions are placed at a distance of $W/2$ from the center of a dipole beam, a displacement of the dipole beam along the trap axis of δz, will lead to a relative change in intensity and dipole force of the order of $(\delta z/W)^2$. Thus, for the errors associated with position fluctuations to be at the 10^{-4} level, the position fluctuations should be smaller than 1% of the waist size, which amounts to 50 nm in the case where $W = 5\,\mu$m. Although demanding, it is possible to reach this level of stability.

Frequency fluctuations

As for the power fluctuations, laser frequency fluctuations will lead to fluctuations in the dipole potential and hence to an imperfect cancellation of the Stark-shift induced phase. Since laser frequencies can be very accurately controlled and frequency fluctuations anyway are expected to be small as compared to the detuning from any of the two fine-structure levels, this is not expected to play any significant role.

6.2.3 Discussion

The gate proposal presented above has some similarities with the gate recently demonstrated by the NIST group [14]; in fact the physical mechanism which gives rise to the desired phase shift is the same. There are, however, also some essential differences between the two schemes.

In the NIST experiment, a dipole force along a given trap axis was provided by the intensity-gradient of a standing-wave light-field. The wavelength of the light-field and hence the period of the standing wave is set by the requirement that the Stark-shift induced phase shift of the two qubit levels is zero (corresponding to $\psi_+ + \psi_- = 0$ in our case), which can be fulfilled by tuning the laser in between two fine-structure levels. This can, however, give rise to a significant amount of scattering events. Moreover, since the spatial variation of the dipole force in a standing wave takes place on a length scale given by the wavelength of the light-field and since the ions must be well localized on this scale, the ions should be cooled to the Lamb-Dicke limit with respect to this wavelength. In Ref. [14] this is also the Lamb-Dicke limit for the qubit operations. Finally, in the NIST experiment, an equal dipole force on the two ions was obtained by adjusting their equilibrium distance to an integer number of standing wave periods, which may be difficult to generalize for performing a gate between any two ions in a multi-ion string.

In the proposal presented here, where the dipole force is provided by a variation in the beam-profile, the excursion of the ions from their equilibrium position should only be smaller than the beam waist, which is adjustable, but typically up to ten times larger than a relevant transition wavelength. This means that except for very tightly focussed laser beams, the Lamb-Dicke limit criterion need not be fulfilled. Furthermore, since the dipole beam propagates perpendicular to the ion-string in our proposal, addressing of specific ions for implementation of gates in a multi-ion string should be possible. A theoretical description of this situation should also be quite straightforward, as mentioned after Eq. (6.2.6). Finally, owing to the polarization rotation method, the dipole beam is

allowed to be far-off resonant with respect to the relevant internal transitions, such that a scattering probability below the asymptotic threshold value required for fault-tolerant quantum computation [98] in principle can be obtained in the long wavelength limit.

It should be mentioned, that quantum gates using optical dipole forces also was considered by Sasura and Steane [102] for an array of very small ion traps with a single ion in each trap.

In a very recent proposal, Garcia-Ripoll, Cirac and Zoller [104] present a geometric gate, where the momenta of the involved ions are controlled by absorption of photons from a discrete set of laser pulses. In this case requirements on the pulses naturally arise for having zero displacement and for obtaining the desired phase shift. It can be shown that these requirements are discrete versions of those expressed through $\tilde{g}(\omega)$ above.

6.3 Individual addressing of trapped ions

Apart from the ability to make gate-operations between any pair of ions, a key requirements for the implementation of a universal set of gate operations with trapped ions is individual addressing of ions for single-qubit operations, as discussed in Chap. 5. Individual addressing is, however, experimentally quite challenging due to the need for high trap frequencies, to ensure efficient sideband cooling and high gate-speeds, which leads to a small spatial separation of the ions (see also Ref. [24] for a discussion). For the present project as well as for the work in the Innsbruck group, a typical trap frequency is $\omega_z = 2\pi \times 1.0\,\mathrm{MHz}$, for which the equilibrium distance between two $^{40}Ca^{+}$ ions is $5.6\,\mu$m. At NIST, some of the more recent experiments have been conducted at roughly $2\pi \times 3\,\mathrm{MHz}$ trap-frequency [14], but previously trap frequencies as high as $\omega_z = 2\pi \times 10\,\mathrm{MHz}$ [105] have been used, in which case the spacing between two $^{9}Be^{+}$-ions is only $3.2\,\mu$m. For experiments with more than two ions the minimum ion separation becomes even smaller, decreasing as $N^{-0.56}$ in an N-ion string [25].

The most obvious method for individual addressing is simply to focus a laser beam onto a single ion, which for ion-ion distances of $\sim 5\,\mu$m typically requires waist sizes only a few times larger than the addressing beam wavelength, i.e., diffraction becomes a limiting factor. The method was demonstrated by the Innsbruck-group [106] and used in their demonstration of the Cirac-Zoller CNOT gate using a two-ion string [13]. In the latter experiment the ion-ion distance was $5.3\,\mu$m and the addressing laser of 729 nm wavelength was focussed to $2.5\,\mu$m (FWHM). When addressing one ion, the small fraction $(2.5 \cdot 10^{-3})$ of light incident on the second ion, gave rise to an estimated fidelity loss in the gate-operations of 3% [13]. With the stronger traps used at NIST or when more ions are involved, an even tighter focus is required to reduce the fidelity loss to a few percent, thus making the method even more demanding [24]. A possible solution to the problem is once again a dedicated lens system inside the vacuum chamber [103], but it seems nevertheless to be relevant to consider other methods.

Some alternative methods for individual addressing of ions have been presented, which use position-dependent micromotion [16, 107], but they are either hard to generalize beyond two ions or technically demanding. The gate-proposal by Mintert and Wunderlich [82] using a strong magnetic field-gradient also allows individual addressing of the ions, however, it is technically demanding to obtain the required field-gradient.

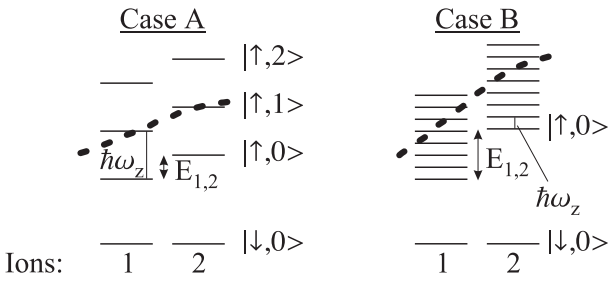

Figure 6.6: The basic idea of individual addressing. When a string of trapped ions is illuminated by a far-off resonant laser beam propagating perpendicular to the ion string, as in Fig. 6.1, the energy levels of the ions are ac Stark-shifted. The figure shows the qubit levels $|\downarrow\rangle$ and $|\uparrow\rangle$ of two ions confined in a harmonic trapping potential of oscillation frequency ω_z (external states $|0\rangle$, $|1\rangle$, etc..). Individual addressing is considered in two cases. Case A: $\hbar\omega_z > E_{1,2} \gg \hbar\gamma_{res}$, and Case B: $E_{1,2} \gg \hbar\omega_z \gg \hbar\gamma_{res}$. Note: For convenience, the energy-levels are shifted, such that the $|\downarrow\rangle$ state has the same energy for both ions.

6.3.1 Trapped-ion quantum logic utilizing position-dependent ac Stark shifts

We have proposed [I] to use a position-dependent optical dipole potential, or ac Stark shift, due to a far-off resonant laser beam to obtain a unique resonance-frequency of each ion, which allows individual addressing of ions on a string just by tuning the frequency of a laser beam illuminating the whole ion string. For the two-ion case the position-dependent dipole potential corresponds to the third and the fourth term in Eq. (6.1.7). In addition to individual addressing, the position-dependent ac Stark shift can be used for selecting any pair of ions in a multi-ion string for implementing a two-ion quantum gate, e.g., a Mølmer-Sørensen gate [78, 77], as we shall see below. With respect to focussing of the ac Stark-shifting laser beam, the scheme is technically not very demanding, since the beam is only supposed to be focussed to a spot size larger than the ion spacing, which makes the scheme applicable even in experiments with very tightly confining traps ($\omega_z/2\pi \sim 10\,\mathrm{MHz}$).

First, we consider the criteria for performing single qubit operations between states of the type $|\downarrow, n\rangle$ and $|\uparrow, n'\rangle$. To selectively manipulate such two states of a single ion in a string, the spectral resolution γ_{res} of the laser performing the qubit operation must first of all fulfill the criterion for the resolved sideband-limit, i.e., $\gamma_{res} \ll \omega_z$. Furthermore, the resolution must be sufficiently high that transitions in any other ion are prohibited. For simplicity, we consider in the following a two-ion string, with one motional mode having the oscillation frequency ω_z, and with the ac Stark shift induced energy difference between the two ions being $E_{1,2}$ (see Fig. 6.6). First, we treat the situation where $\hbar\omega_z > E_{1,2} \gg \hbar\gamma_{res}$ as sketched in Fig. 6.6 (Case A). In this case, $E_{1,2} = \hbar\omega_z/2$ is the optimum choice, since a laser resonant with a specific transition $|\downarrow, n\rangle$–$|\uparrow, n'\rangle$ in one ion, is maximally off-resonant with all the transitions of the type $|\downarrow, n\rangle$–$|\uparrow, n'\rangle$, $|\downarrow, n\rangle$–$|\uparrow, n'+1\rangle$, or $|\downarrow, n\rangle$–$|\uparrow, n'-1\rangle$ in the other ion, leading to the highest possible gate-speed. In the case $E_{1,2} \gg \hbar\omega_z \gg \hbar\gamma_{res}$ (Case B in Fig. 6.6), a laser

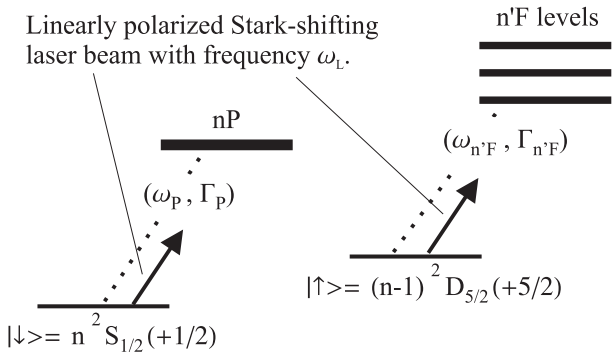

Figure 6.7: Relevant energy-levels and transitions in alkaline earth ions (e.g.,$^{40}Ca^+$, $^{88}Sr^+$, and $^{138}Ba^+$) for calculating the ac Stark-shifts of the qubit states [$|\downarrow\rangle = {}^2S_{1/2}(m_J = +1/2)$ and $|\uparrow\rangle = {}^2D_{5/2}(m_J = +5/2)$] in the case of a linearly polarized, far-off-resonant laser beam. The Stark-shifting laser beam is assumed to be so far red detuned that the fine-structure splitting of the P- and F-levels can be neglected.

resonant with a transition $|\downarrow, n\rangle$–$|\uparrow, n'\rangle$ in one ion, is only resonant (or near-resonant) with a transition $|\downarrow, n\rangle$–$|\uparrow, n' + m\rangle$ in the other ion, where $|m| \gg 1$. In the Lamb-Dicke limit such a transition is strongly suppressed. Case B is particularly interesting when more than two ions are present, since even in such cases the gate-time will only be limited by the vibrational frequency ω_z instead of a fraction thereof as in Case A.

An experimental realization of the above situation can be achieved, e.g., by using a string of two $^{40}Ca^+$-, $^{88}Sr^+$- or $^{138}Ba^+$-ions. The qubit states $|\downarrow\rangle$ and $|\uparrow\rangle$ can be represented by the two Zeeman sublevels of the $^2S_{1/2}$ ground state as we do in $^{40}Ca^+$, or for instance by one sublevel of the ground state and one sublevel of the metastable $^2D_{5/2}$ state, as the Innsbruck group does. Here, we postpone the discussion of our own choice of qubit states and discuss first the case where $|\downarrow\rangle = {}^2S_{1/2}(m_J = +1/2)$ and $|\uparrow\rangle = {}^2D_{5/2}(m_J = +5/2)$, since this turns out to be more favorable. The far-off-resonant Stark-shifting laser beam is assumed to propagate perpendicular to the ion string and its polarization is assumed to be linear along the axis defined by the ions. The relevant internal levels of the considered ions, with respect to the Stark-shifting laser beam, are shown in Fig. 6.7. For simplicity, we assume that the Stark-shifting laser beam is so far red detuned from any transition-frequency that fine-structure splitting can be neglected. The ac Stark shift $\varepsilon_\uparrow - \varepsilon_\downarrow$ of the $|\uparrow\rangle - |\downarrow\rangle$ transition of a single ion can be calculated by summing the contributions from all relevant dipole-allowed couplings. The dominant shift of $|\downarrow\rangle$ is from the $nS - nP$ coupling, whereas the shift of $|\uparrow\rangle$ is composed of contributions from a series of $(n-1)D - n'F$ couplings. This gives rise to the following approximate expression for the ac Stark shift:

$$\begin{aligned}\varepsilon_\uparrow - \varepsilon_\downarrow =& \frac{3\pi c^2}{2}\left[\frac{1}{\omega_P^3}\left(\frac{\Gamma_P}{\omega_P - \omega_L} + \frac{\Gamma_P}{\omega_P + \omega_L}\right)\right. \\ &\left. - \sum_{n'}\frac{1}{\omega_{n'F}^3}\left(\frac{\Gamma_{n'F}}{\omega_{n'F} - \omega_L} + \frac{\Gamma_{n'F}}{\omega_{n'F} + \omega_L}\right)\right] I_{ion} \equiv \psi \times I_{ion},\end{aligned} \tag{6.3.1}$$

where ω is the laser-frequency, ω_P and $\omega_{n'F}$ are the $nS - nP$ and $(n-1)D - n'F$

transition-frequencies, Γ_P and $\Gamma_{n'F}$ are the corresponding spontaneous decay rates, I_{ion} is the intensity of the Stark-shifting laser beam at the position of the ion and ψ accounts for the properties of the ion and the laser-frequency [99]. Assuming a Gaussian transverse intensity profile as given by Eq. (6.1.4), a maximum difference in the ac Stark shift of the ions is obtained by displacing the laser beam by $W/2$ with respect to the center of the ion string, i.e., with $z_0 = W/2$ in Fig. 6.1, $z_1 = -\Delta z/2$ and $z_2 = \Delta z/2$. In this case Eqs. (6.1.4) and (6.3.1) lead to the following difference in the transition-frequency of the ions:

$$E_{1,2} = \kappa\,(\varepsilon_\uparrow - \varepsilon_\downarrow) = \kappa\psi I_0, \tag{6.3.2}$$

where

$$\kappa = 2\sinh(\Delta z/W)\exp\left\{-\frac{1}{2}\left[1 + (\Delta z/W)^2\right]\right\}. \tag{6.3.3}$$

In Fig. 6.8(a), the laser power required to achieve an ac Stark shift difference $E_{1,2} = \hbar\omega_z/2$ in the case of $\omega_z = 2\pi \times 1\,\mathrm{MHz}$ is presented for $^{40}Ca^+$, $^{88}Sr^+$, and $^{138}Ba^+$ as a function of the laser wavelength [5]. The waist of the laser beam is taken to be $30\,\mu$m, which is much larger than the equilibrium spacing of $5.6\,\mu$m, $4.3\,\mu$m and $3.7\,\mu$m for the $^{40}Ca^+$-, $^{88}Sr^+$-, and $^{138}Ba^+$-ions, respectively. The required power, which approaches a constant in the long-wavelength limit, is well within reach of commercial lasers, e.g., a CO_2 laser ($\lambda = 10.6\,\mu$m), a Nd:YAG laser ($\lambda = 1064\,$nm), or a frequency-doubled Nd:YAG laser ($\lambda = 532\,$nm).

As in the gate-proposal in Sec. 6.2, an important parameter to consider is the spontaneous scattering rate, Γ_{sc}, of light from the Stark-shifting laser beam, since it will limit the ultimate coherence time. Under the assumptions made above in calculating the ac Stark shifts and assuming an equal average population in the two internal states, the sum of the scattering rates for both ions can be expressed as:

$$\Gamma_{sc} = \frac{E_{1,2}}{\kappa\psi}\frac{e^{-1/2}3\pi c^2\omega^3}{2\hbar} \times\left[\frac{1}{\omega_P^6}\left(\frac{\Gamma_P}{\omega_P-\omega_L}+\frac{\Gamma_P}{\omega_P+\omega_L}\right)^2+\sum_{n'}\frac{1}{\omega_{n'F}^6}\left(\frac{\Gamma_{n'F}}{\omega_{n'F}-\omega_L}+\frac{\Gamma_{n'F}}{\omega_{n'F}+\omega_L}\right)^2\right], \tag{6.3.4}$$

where $\Delta z/W \ll 1$, as obeyed by the parameters used in Fig. 6.8, is assumed.

In Fig. 6.8(b), the coherence time (or rather Γ_{sc}^{-1}) is plotted as a function of laser wavelength, and we see that in the long-wavelength limit, the coherence time grows as the wavelength to the third power, which is also readily deduced from Eq. (6.3.4). Hence, at first, a CO_2-laser seems to be favorable. However, since the lifetime of the $^2D_{5/2}$ level is only 1.1 s, 345 ms, and 47 s for $^{40}Ca^+$, $^{88}Sr^+$, and $^{138}Ba^+$, respectively, the use of the fundamental wavelength of a Nd:YAG laser might be more attractive, since this will be much easier to focus to the required spot size. Actually, since the maximal coherence time is limited by heating of the ions on a timescale of $1-100\,$ms in current experimental

[5] In Fig. 6.8 we do take the fine-structure splitting and the different couplings to the fine-structure levels into account. For the $(n-1)D - n'F$ transitions we sum over $n' = 4-10$. The data used are from Ref. [108] ($^{40}Ca^+$) and Refs. [109, 110, 111] ($^{88}Sr^+$ and $^{138}Ba^+$).

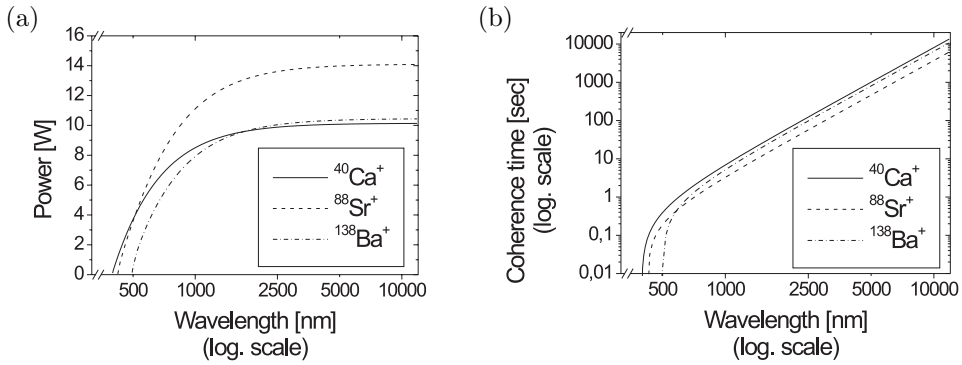

Figure 6.8: (a) The required laser power as a function of wavelength for obtaining an ac Stark shift difference $E_{1,2} = \hbar\omega_z/2$, when $\omega_z = 2\pi \times 1.0\,\mathrm{MHz}$ and $W = 30\,\mu\mathrm{m}$ for $^{40}Ca^+$, $^{88}Sr^+$, and $^{138}Ba^+$. (b) The corresponding coherence time (Γ_{sc}^{-1}).

setups [37, 92, 105] even a continuously operated frequency-doubled Nd:YAG laser can be used without introducing significant additional decoherence.

Once again, it is advantageous not to choose the waist W overly large as compared to Δz, since the power required to achieve a certain energy difference $E_{1,2}$ grows as W^3 and since the total scattering rate for a fixed $E_{1,2}$ also increases with W ($\Gamma_{sc} \propto W$). Furthermore, it should be noted that although a large $E_{1,2}$ implies a short coherence time, it also allows a high gate-speed.

The effect of the (internal state dependent) dipole-force exerted on the ions by the Stark-shifting laser beam has to be considered, since it is unwanted in this context of individual addressing. Fortunately, with the relatively large waist and the low intensity level used here (as compared to the gate proposal above), the effect of the dipole force is small, as the following estimate shows. The maximal optical dipole force will be on the order of $F_{dip} = -\partial\varepsilon_\downarrow/\partial z \approx E_{1,2}/\Delta z$. Taking the example of $^{40}Ca^+$, and using the same parameters as above, the maximal dipole force will be $\sim 10^5$ times smaller than the confining force exerted by the trap, and the associated change in the equilibrium distance between the ions, δz, is ~ 300 times smaller than the spread of the vibrational wavefunction. This displacement is totally negligible. Nevertheless, when the Stark-shifting laser beam is turned on, an ion obtains a speed $v \approx \delta z/t_{rise}$, where t_{rise} is the "rise-time" of the Stark-shifting laser beam. The associated kinetic energy must be much smaller than $\hbar\omega_z$, which is fulfilled if $t_{rise} \gg 1\,\mathrm{ns}$. In practice, this is no limitation.

The different ionic transition-frequencies, while applying the Stark-shifting laser beam, leads to a differential phase-development of the various ions, which in the case of two ions amounts to a phase-difference of $\Delta\phi = E_{1,2}T/\hbar$, when the Stark-shifting beam has been applied for a gate-time T. Since the frequency-differences are known, this can be accounted for by controlling the phase of the addressing light-field. Power fluctuations of the Stark-shifting beam will, however, also in this scheme give a contribution to the phase-difference which cannot easily be corrected for. To estimate this difference, suppose the intensity of the Stark shifting beam varies as $I(t) = I_0[1 + \epsilon_f \cos(\omega_f t + \varphi)]$. After a gate time T and having corrected by $\Delta\phi$, there will be a remaining phase-difference between two ions of $\epsilon_f E_{1,2}[\sin(\omega_f T + \varphi) - \sin(\varphi)]/(\hbar\omega_f)$. Thus, the most severe frequency components are those fulfilling $\omega_f T \ll 1$, for which the phase-difference

is $\sim \epsilon E_{1,2}T/\hbar$. Using $E_{1,2}/\hbar \sim \omega_z$, the condition $\epsilon\omega_z T \ll 1$ must therefore be fulfilled to keep the phase-difference small. Combining this with the condition $\omega_z T \gg 1$ for avoiding off-resonant sideband excitations, we find

$$\epsilon_f \omega_z T \ll 1 \ll \omega_z T, \tag{6.3.5}$$

which, e.g, can be fulfilled with $\epsilon_f = 10^{-4}$ and $\omega_z T = 100$. As mentioned in Sec. 6.2, $\epsilon_f = 10^{-4}$ can almost be provided by a commercially available Laser Power Controller [6].

Above, we considered in detail the simple case of two ions and one motional mode. If we take both motional modes, i.e., the center-of-mass mode at frequency ω_z and the stretch mode at frequency $\sqrt{3}\,\omega_z$, into account, the optimal value of $E_{1,2}$ is changed to $(\sqrt{3}-1)/2\hbar\omega_z = 0.366\hbar\omega_z$, but our conclusions remain valid. Further, we can generalize Case A and Case B of Fig. 6.6 up to at least five ions, which is sufficient for applying our proposal in combination with the proposal for large scale quantum computation in an array of ion traps mentioned in Chap. 5 [89]. To go much beyond five ions is difficult in Case A due to the additional energy levels, while in Case B the only limit is that $E_{1,2}/\hbar$ should not coincide with the frequency of one of the higher motional modes.

In addition to individual addressing, a Stark-shifting laser beam can be used for realizing two-ion quantum logic operations using the Mølmer-Sørensen scheme [77, 78], between *any* two ions in a string. As an example, we show in Fig. 6.9, how one can make two ions in a three-ion string have the same unique resonance-frequency, needed for making a Mølmer-Sørensen gate between these two ions. Two neighbouring ions, e.g., Ion 1 and Ion 2 in Fig. 6.9 can have the same resonance-frequency, if the center of the Stark-shifting beam is positioned halfway between Ion 1 and Ion 2.

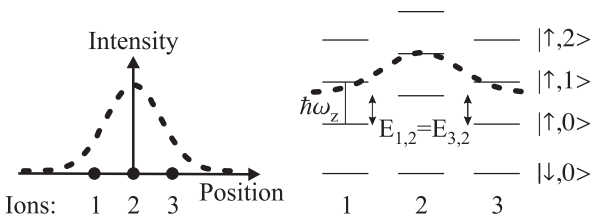

Figure 6.9: A Stark-shifting laser beam making two ions have the same unique resonance-frequency. This allows for selective addressing of any pair of ions for two-qubit operations.

Above we made the choice $|\uparrow\rangle = {}^2D_{5/2}(m_J = +5/2)$, but we could also have chosen $|\uparrow\rangle = {}^2D_{5/2}(m_J = +1/2)$, which has been used in the most recent experiments with $^{40}Ca^+$ by the Innsbruck group [13]. In this case there is an additional contribution to $\varepsilon_\uparrow - \varepsilon_\downarrow$ in Eq. (6.3.1) from the $3d\,^2D_{5/2}$–$4p\,^2P_{3/2}$ transition at 854 nm, which increases (decreases) $\varepsilon_\uparrow - \varepsilon_\downarrow$ for wavelengths above (below) 854 nm.

Now, turning to our own choice of qubit states in $^{40}Ca^+$, we consider the case where $|\downarrow\rangle = {}^2S_{1/2}(m_J = -1/2)$, $|\uparrow\rangle = {}^2S_{1/2}(m_J = +1/2)$, which also can be realized using $^{88}Sr^+$ or $^{138}Ba^+$. Here we present results for $^{40}Ca^+$ and $^{138}Ba^+$. An ac Stark shift can be induced by a circularly polarized Stark-shifting laser beam with wavelength λ_L tuned in between the two fine-structure levels of the P-states, as shown in Fig. 6.10. In this case

[6] Brockton Electro Optics.

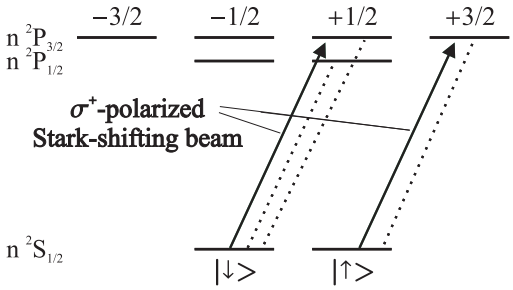

Figure 6.10: Relevant energy-levels and transitions (dashed lines) in alkaline earth ions (e.g.,$^{40}Ca^+$, $^{88}Sr^+$, and $^{138}Ba^+$) for calculating the ac Stark-shifts of the qubit states [$|\downarrow\rangle = {}^2S_{1/2}(m_J = -1/2)$ and $|\uparrow\rangle = {}^2S_{1/2}(m_J = +1/2)$] using a circularly polarized Stark-shifting laser beam.

the required power follows from Eq. (6.3.2) using $\psi_+ - \psi_-$ [see Eqs. (6.2.17) and (6.2.18)] for ψ and the off-resonant scattering rate is given by $e^{-1/2}E_{1,2}\tilde{\Gamma}_{sc}/[\kappa(\psi_+ - \psi_-)]$ [$\tilde{\Gamma}_{sc}$ is defined in Eq. (6.2.36)]. The required power and the scattering rate are plotted for $^{40}Ca^+$ in Fig. 6.11(a) using the same parameters as above, i.e., $\omega_z = 2\pi \times 1\,\text{MHz}$, $E_{1,2} = \hbar\omega_z/2$ and $W = 30\,\mu\text{m}$. For the optimal choice of laser parameters ($\lambda_L = 395.1\,\text{nm}$ and 64 mW laser power) the scattering rate is approximately 80 Hz. Unfortunately, this scattering rate allows only for a limited number of gate-operations, even if the Stark-shifting laser beam only is present during the quantum logic operations. For $^{88}Sr^+$ and $^{138}Ba^+$ somewhat lower scattering rates can be obtained, owing to their larger fine-structure splitting. Specifically for $^{138}Ba^+$ the graph in Fig. 6.11(b) shows a scattering rate of 8 Hz at the optimal choice of 474.5 nm wavelength and 540 mW laser power. Once again, an interesting alternative is a wavelength of 488 nm, which is directly available from an Argon-ion laser. Applying the same approach to $^{25}Mg^+$ or $^9Be^+$ (with hyperfine-levels of the ground state as qubit-levels [9]) is impracticable, due to their relatively small fine-structure splitting. Going to the long wavelength limit for $^{40}Ca^+$, $^{88}Sr^+$ or $^{138}Ba^+$ is not very feasible for $^{40}Ca^+$ and $^{88}Sr^+$ with the parameters used above, since the required laser power is about 960 W and 170 W, respectively. For $^{138}Ba^+$ the required power is about 30 W in the long wavelength limit, which is feasible, but maybe not very attractive.

6.3.2 Discussion

In conclusion, individual or selective addressing of trapped ions can be achieved by utilizing a Stark-shifting laser beam with modest focusing- and power-requirements. The performance of the scheme is good with the qubit states defined by sublevels of the ${}^2S_{1/2}$ ground state and the ${}^2D_{5/2}$ state, respectively, in $^{40}Ca^+$, $^{88}Sr^+$ or $^{138}Ba^+$, in which case decoherence due off-resonant scattering events can be made negligible. Furthermore, the possibility of selective addressing of two distant ions in a string seems to be very attractive. By combining our proposal with the NIST trap-array proposal Ref. [89], it should even be applicable in large scale quantum computation.

For the present project, where the qubit states are represented by the Zeeman sublevels of the ground state, the Stark-shifting method scheme gives rise to a relatively

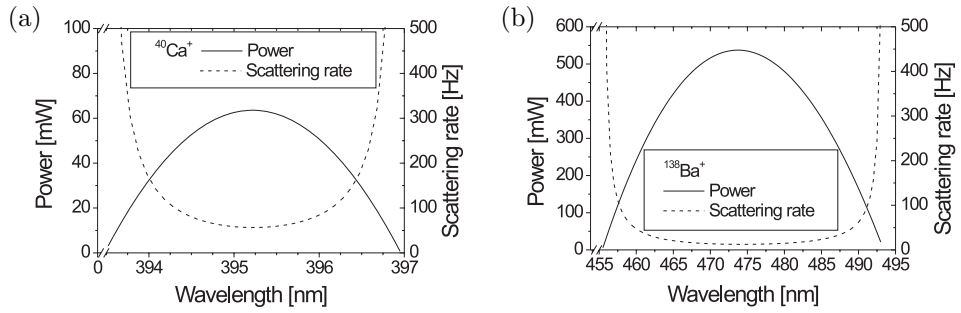

Figure 6.11: The required laser power and the scattering rate as a function of wavelength for obtaining an ac Stark shift difference $E_{1,2} = \hbar\omega_z/2$, when $\omega_z = 2\pi \times 1.0\,\mathrm{MHz}$ and $W = 30\,\mu\mathrm{m}$ with the choice $|\downarrow\rangle = {}^2S_{1/2}(m_J = -1/2)$ and $|\uparrow\rangle = {}^2S_{1/2}(m_J = +1/2)$ in (a) $^{40}\mathrm{Ca}^{+}$ and (b) $^{138}\mathrm{Ba}^{+}$.

high off-resonant scattering rate or requires a very large power in the long wavelength limit. Thus, in our case the most relevant method for individual addressing seems to be focussing of a laser beam onto a single ion. In combination with the relatively large ion-ion distances, which can be used in connection with the gate presented in Sec. 6.2, the focussing method would even be relatively simple to employ.

Chapter 7

The linear Paul trap

With the present chapter, we come to the experimental part of this thesis, which we shall enter encouraged by the following quotation [1]:

" *... quantum phenomena do not occur in a Hilbert space, they occur in a laboratory.*"

-Asher Peres.

To make quantum phenomena such as sideband cooling and quantum logic occur in our lab, a linear Paul trap suitable for such experiments has been designed and constructed. This trap is presented in the present chapter.

In Sec. 7.1 the theory of confinement of charged particles in a linear Paul trap is introduced. In Sec. 7.2, we present the trap and discuss the design considerations, which are based on the specific requirements to the trap frequencies discussed in previous chapters.

7.1 Linear Paul trap theory

The realization of a linear Paul trap, which we shall consider here, is illustrated in Fig. 7.1. It consists of four plate electrodes in a quadrupole configuration, where two diagonally opposite electrodes (dark blue in Fig. 7.1) each are sectioned into a center piece and two equally wide end-pieces. By applying a suitable combination of alternating and static voltages to the electrodes, it is possible to trap charged particles near the center of the trap, as indicated by the three ions (red dots) in a string configuration in Fig. 7.1. Confinement in the x–y plane (the radial plane) is obtained by applying a sinusoidally oscillating voltage (in the following named the RF-voltage) to two diagonally opposite electrodes while keeping the other two electrodes on ground with respect to the RF-voltage. This gives rise to an oscillating saddle potential, which, for a suitable RF-voltage and oscillation frequency, leads to an effectively confining potential in the radial plane. Axial confinement along the z-axis is obtained by applying a DC so-called endcap voltage, U_{end}, to the four electrode end-pieces.

For a quantitative description of the confinement of a charged particle, consider first the radial confinement due to an RF-voltage, $U_{RF}\cos(\Omega_{RF}t)$, applied to the two light

[1] As quoted in Ref. [18].

blue electrodes in the y–z plane in Fig. 7.1. In order to give a more general description, which will be useful later on, we also take into account a DC-voltage, U_a, applied to the six dark blue electrode pieces in the x–z plane in Fig. 7.1. The resulting electric potential in the radial plane is, to second order in the spatial coordinates, given by

$$\Phi(x,y,t) = \left[U_a - U_{RF}\cos(\Omega_{RF}t)\right]\frac{x^2-y^2}{2Lr_0^2} + \frac{1}{2L}\left[U_a + U_{RF}\cos(\Omega_{RF}t)\right], \qquad (7.1.1)$$

taking the origin of the coordinate system to be at the symmetry-center of the trap. r_0 denotes the distance from the trap center to the surface of the electrodes and L is a number of the order of unity. For electrodes of a hyperbolic cross-section $L = 1$, whereas for the plate electrodes shown in Fig. 7.1, the potential is comparatively weaker, meaning that $L > 1$. Therefore L is named 'the loss factor' in the following [112].

For a *single* charged particle, the equations of motion in the radial plane can be put onto the Mathieu form [113]:

$$\frac{\partial^2 x}{\partial\tau^2} + \left[a - 2q\cos(2\tau)\right]x = 0 \qquad (7.1.2)$$

$$\frac{\partial^2 y}{\partial\tau^2} + \left[-a + 2q\cos(2\tau)\right]y = 0, \qquad (7.1.3)$$

where we have introduced the dimensionless parameters

$$q = \frac{2QU_{RF}}{mLr_0^2\Omega_{RF}^2}, \quad a = \frac{4QU_a}{mLr_0^2\Omega_{RF}^2} \quad \text{and} \quad \tau = \frac{\Omega_{RF}t}{2}. \qquad (7.1.4)$$

Q and m are the charge and the mass of the trapped particle, respectively. Each of these so-called Mathieu equations has stable solutions in certain regions of the a–q plane, which implies that the radial motion of the charged particle is stable in certain *stability regions*, where *both* Mathieu equations have stable solutions. There are in principle an infinite number of such stability regions (see, e.g., Refs. [114] or [115]), but in practice the trap is only operated within the largest one, which is shown in Fig. 7.2. For $a, q \ll 1$, the radial motion is described by the equations [114, 115]

$$x(t) = x_0\left[1 - \frac{q}{2}\cos(\Omega_{RF}t)\right]\cos(\omega_{sec,x}t) \qquad (7.1.5)$$

$$y(t) = y_0\left[1 + \frac{q}{2}\cos(\Omega_{RF}t)\right]\cos(\omega_{sec,y}t), \qquad (7.1.6)$$

where

$$\omega_{sec,x} = \frac{1}{2}\sqrt{\frac{q^2}{2} + a}\,\Omega_{RF} \quad \text{and} \quad \omega_{sec,y} = \frac{1}{2}\sqrt{\frac{q^2}{2} - a}\,\Omega_{RF}. \qquad (7.1.7)$$

This means that the particle performs a so-called secular motion along the x-axis and the y-axis with amplitudes x_0 and y_0 at the secular frequencies $\omega_{sec,x}$ and $\omega_{sec,y}$, respectively. Superimposed on the secular motion is a fast, small-amplitude so-called *micromotion* at the RF-frequency, Ω_{RF}. Note, that the amplitude of the micromotion [i.e., $qx_0\cos(\omega_{sec,x}t)/2$ for the x-coordinate] is proportional to the distance from the trap center. Particularly, there is no micromotion on the trap axis, which is essential

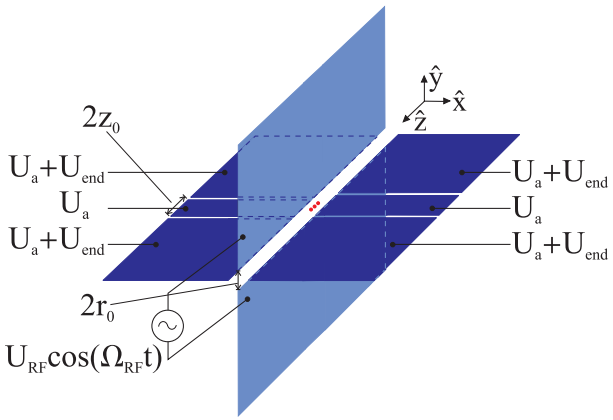

Figure 7.1: Geometry of the linear Paul trap presented in this chapter. An alternating voltage is applied to two diagonally opposite electrodes (light blue), which provides confinement in the x–y plane (the radial plane), as described in the text. U_a and the axially confining endcap voltage, U_{end}, are DC-voltages applied to the other electrodes as indicated.

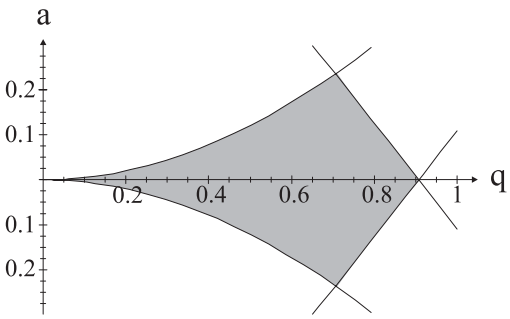

Figure 7.2: The largest stability region in the $a-q$ plane for a charged particle moving in the x–y plane subject to the potential of Eq. (7.1.1).

for the idea of using a string of trapped ions in a linear Paul trap for quantum logic operations. We shall return to the discussion of micromotion in Chap. 9.

Axial confinement of the charged particle is accomplished by applying the endcap voltage, U_{end}, to the four end-pieces of the dark blue electrodes in Fig. 7.1. Near the trap center this gives rise to the potential

$$\Phi_{end}(x,y,z) = \kappa U_{end}\left[z^2 - \frac{1}{2}(1-\chi)x^2 - \frac{1}{2}(1+\chi)y^2\right], \tag{7.1.8}$$

where κ is a geometrical factor of the order of $(2z_0)^{-2}$, where $2z_0$ is the width of the electrode center-pieces. The parameter χ accounts for the fact that the endcap voltage acts asymmetrically in the radial plane. From Eq. (7.1.8) it follows that the motion of

the charged particle along the z-axis is harmonic at frequency

$$\omega_z = \sqrt{\frac{2Q\kappa U_{end}}{m}}. \tag{7.1.9}$$

Since Φ_{end} contains x- and y-dependent terms (to fulfill the Laplace equation), the application of the endcap voltage gives rise to a modified set of Mathieu equations for the radial motion:

$$\frac{\partial^2 x}{\partial \tau^2} + [a + a_z(1-\chi) - 2q\cos(2\tau)]\, x = 0 \tag{7.1.10}$$

$$\frac{\partial^2 y}{\partial \tau^2} + [-a + a_z(1+\chi) + 2q\cos(2\tau)]\, y = 0, \tag{7.1.11}$$

where

$$a_z = -2\left(\frac{\omega_z}{\Omega_{RF}}\right)^2 \tag{7.1.12}$$

always is negative. This results in a modification of the stability regions in the a–q plane [116] and a change of the radial trap frequencies:

$$\omega_{sec,x} \mapsto \omega_x = \frac{1}{2}\sqrt{\frac{q^2}{2} + a + a_z(1-\chi)}\,\Omega_{RF} \tag{7.1.13}$$

$$\omega_{sec,y} \mapsto \omega_y = \frac{1}{2}\sqrt{\frac{q^2}{2} - a + a_z(1+\chi)}\,\Omega_{RF}. \tag{7.1.14}$$

Thus, for $\chi < 1$ the endcap voltage has a defocussing effect in the radial plane.

Neglecting micromotion, the potential energy of the ion can be written as that of a three-dimensional harmonic oscillator

$$U(x,y,z) = \frac{1}{2}m\left(\omega_x^2 x^2 + \omega_y^2 y^2 + \omega_z^2 z^2\right), \tag{7.1.15}$$

with the radial trap frequencies, ω_x and ω_y, and the axial, ω_z, determined by the trap geometry, the applied voltages and the charge and the mass of the ion.

7.2 Trap design and construction

7.2.1 Design considerations

In previous chapters we have seen that the different aspects of trapped-ion quantum logic experiments, e.g., sideband cooling and gate operations, only works efficiently, if the trapping potential meets certain criteria. First of all, the potential should be harmonic to a very good approximation, since the vibrational energy levels must be equidistantly spaced. Second, the trap frequencies should have a certain magnitude. Since quantum logic operations involves the axial modes, the magnitude of the axial oscillation frequency, ω_z, is subject to several conditions. ω_z sets in turn a lower bound on the radial trap frequencies due to the stability condition for an N-ion string given by Eq. (3.2.3). In the following, we consider first the most important conditions on ω_z and argue that the previously used 'typical' value of $\omega_z \sim 2\pi \times 1\,\mathrm{MHz}$ is a reasonable choice. After that we consider the implications for the radial trap frequencies.

The axial trap frequency is important in, at least, the following connections:

- It defines the frequency spacing between vibrational levels, which must be much larger than the spectral resolution of the Raman transition between the qubit states, in order to fulfill the condition for the resolved sideband-limit.
- In most schemes for quantum logic operations, the 'clock-frequency' of the gate-operations scales linearly with ω_z [see, e.g., Eq. (5.2.2)].
- The Lamb-Dicke parameter η ($\propto \sqrt{1/\omega_z}$) should be small enough to fulfill the condition of the Lamb-Dicke limit, i.e. $\eta\sqrt{n+1} \ll 1$. On the other hand it should be sufficiently large that first-order vibrational state changing transitions are not too strongly suppressed.
- To have a good starting point for sideband cooling, the average axial vibrational quantum number after Doppler cooling, $\overline{n} \sim k_B T_D/(\hbar\omega_z)$, should be small.
- For individual addressing of ions on a string, ω_z should not be too large, since the equilibrium distance between the ions scales as $\omega_z^{-2/3}$.

In addition to the items on this list, the size of the trap is an important parameter, both for practical reasons and due to heating of the ion motion as discussed below. The trap size is indirectly set by the desired trap frequencies, since if large trap frequencies, i.e., large electric field gradients, are needed, the trap must necessarily be small in order to avoid unreasonably large voltages. The size of the trap, or rather r_0, can be estimated as follows. For a given value of ω_z the string stability condition given by Eq. (3.2.3) puts a lower bound on ω_x and ω_y, which for small a and a_z roughly are equal to $q\Omega_{RF}/\sqrt{8} \equiv \omega_r$. With ω_r fixed to a value fulfilling the string stability condition and assuming q fixed (within the stability region in Fig. 7.2), Ω_{RF} is therefore fixed. Using $\omega_r = q\Omega_{RF}/\sqrt{8}$ and the definition of the q-parameter [Eq. 7.1.4], we find that

$$\frac{U_{RF}}{Lr_0^2} = \frac{4m\omega_r^2}{Qq}. \tag{7.2.1}$$

Taking $\omega_z = 2\pi \times 1\,\mathrm{MHz}$ and requiring four ions on a string as a reasonable benchmark, $\omega_r > 2\pi \times 2\,\mathrm{MHz}$ is required due to Eq. (3.2.3). Using $q = 0.3$ [2], we arrive at $\Omega_{RF} = \sqrt{8}\omega_r/q \approx 2\pi \times 20\,\mathrm{MHz}$ and

$$\frac{U_{RF}}{Lr_0^2} \sim 1\,\mathrm{kV/mm^2} \tag{7.2.2}$$

for $^{40}Ca^+$. Since we cannot expect U_{RF} to be much larger than 1 kV at $\Omega_{RF} \approx 2\pi \times 20\,\mathrm{MHz}$ without getting into technical difficulties, we arrive at a quantitative limit to the trap size of $r_0 \lesssim 1\,\mathrm{mm}$ for $L \simeq 1$.

Concerning heating of the motion of ions, there are at least two known relevant effects, namely the effect of thermal voltage fluctuations in the electrodes (Johnson noise) [105, 117] and fluctuations of so-called patch potentials [118], i.e., unwanted potentials which arise if regions on the surfaces of the electrodes are covered with some material, e.g., calcium in our case [105]. The heating rate due to Johnson noise is proportional to $R(\omega = \omega_z) r_0^{-2} \omega_z^{-1}$, where $R(\omega)$ is the frequency-dependent resistance

[2] Larger q is an option, but it does increase the effect of any micromotion, which in practice is present.

between two electrodes in a lumped-circuit model [117]. The heating rate due to fluctuating patch potentials is proportional to $S(\omega = \omega_z) r_0^{-4} \omega_z^{-1}$, where $S(\omega)$ is the power noise spectral density [105]. Experimentally, heating rates have been measured by the NIST group to be of the order of 1 phonon per 1–10 ms [92, 105] in traps of a few hundred μm size at trap frequencies of $\omega_z \sim 2\pi \times 3 - 10\,\mathrm{MHz}$. In Ref. [105], a survey of the heating rates in traps of various sizes shows consistency with a r_0^{-4}-scaling, thus suggesting that the major heating source is fluctuating patch potentials. In Refs. [34, 37] from the Innsbruck group, heating rates of the order of 1 phonon per 100 ms are quoted for trap sizes of $2r_0 \sim 1\,\mathrm{mm}$ with $\omega_z \sim 2\pi \times 1\,\mathrm{MHz}$, i.e., similar to the trap size and the axial trap frequency in the example above.

In conclusion there are several good reasons on the list to make ω_z as large as possible, but there are upper limits given by the desired Lamb-Dicke parameter, the need for individual addressing and indirectly by the size of the trap, for which the factor of r_0^{-4} in the patch-potential heating rate is particularly severe.

With this in mind, $\omega_z \sim 2\pi \times 1\,\mathrm{MHz}$ seems to be a good compromise, since the resolved-sideband limit can be reached, sideband cooling works efficiently (Chap. 3) and it gives a reasonable value for the Lamb-Dicke parameter (~ 0.2). According to Eq. (7.2.2) and the discussion following it, a reasonable characteristic trap size would be $r_0 \lesssim 1\,\mathrm{mm}$ for this choice of axial trap frequency. At least in the Innsbruck experiments, the heating rate for a trap of this size is roughly 1 phonon per 100 ms [34, 37], which seems to be acceptable.

7.2.2 Electrode shape and dimensions

Apart from the above considerations, the experience gained from construction of other linear Paul traps in our group [119] has naturally played an important role for the design of the trap presented here. However, since this trap is smaller than the other traps ($r_0 = 1.75\,\mathrm{mm}$ and $r_0 = 3.50\,\mathrm{mm}$ have been used [120]), some changes of the design have been necessary.

In the other traps, the electrodes are cylindric with a diameter around $2.3r_0$, since this leads to a harmonic radial potential to a very good approximation [121]. For the present small trap, thin plates were chosen as electrodes in order to have a better optical access to the trap center than it would be the case with cylindrical electrodes of diameter $2.3r_0$. Using plate electrodes, the potential can still be made harmonic to a good approximation, as shown by the numerical calculations presented below.

In the previously constructed traps, all four electrodes are sectioned into three pieces. RF-voltages are applied to all four electrodes [$+U_{RF}\cos(\Omega_{RF}t)/2$ applied to two diagonally opposite electrodes and $-U_{RF}\cos(\Omega_{RF}t)/2$ applied to the other two electrodes]. DC-voltages can be applied to all twelve electrode pieces, with the endcap voltage being applied to the eight end-pieces. The RF-voltage and the DC-voltage can be adjusted on all twelve electrode pieces, which gives the possibility of adjusting the equilibrium position of the trapped ions as well as the shape of the potential. In an attempt to carry these possibilities along to the new trap, it was therefore designed and build with all four electrodes sectioned into three parts, as it can be seen from Fig. 7.4(b) below. The voltages are, however, effectively applied as in Fig. 7.1. It turned out that with the higher RF-frequency used for the present trap [3], the RF-voltage adjustment

[3] Previous traps: $\Omega_{RF}/2\pi \sim 5\,\mathrm{MHz}$.

on the individual electrode pieces was hampered by a significant 'cross-talk' between them, meaning that when the RF-voltage was supposed to be changed on a single electrode, the other electrode voltages were essentially changed by the same amount. This 'cross-talk' has been attributed to stray capacitance and/or inductance between the electrodes, between wires connected to the electrodes and the surroundings, and the fact that electronic components are non-ideal at high frequencies. Eventually, it was therefore decided to reduce the effective number of electrode pieces by applying the RF-voltage only to six diagonally opposite electrode pieces, with the electrode pieces being shortcut three by three. Consequently, the endcap voltage can only be applied to four electrode pieces. This reduction of the effective number of electrode pieces diminishes the possibilities of cross-talk at the cost of a reduced flexibility. The remaining adjustment possibilities and suppression of noise originating from the RF-voltage will be discussed in more detail in Chap. 8. The mechanical construction of the trap will be described below, after an account of the numerical calculations for determining the dimensions of the electrodes.

Numerical calculations of the trapping potential

Under the condition that r_0 should be around 1 mm or less and that the electrodes should be thin plates (thickness $< r_0$), the trap dimensions was determined from numerical calculations of the trapping potential with the goals of minimizing anharmonic terms in the potential and minimizing the loss factor L. First the 2D electrode configuration in the radial plane, i.e., the parameters r_0, the electrode thickness and the electrode length was determined. Following that, the 3D electrode configuration, i.e., the width and the sectioning of the electrodes, was determined. For a given electrode configuration, the static potential due to voltages applied to the electrodes was calculated using the program 'Simion', which solves the Laplace equation on a grid of points. The spatial resolution of the grid was 5 μm for 2D-calculations and 42 μm for 3D-calculations.

For the configuration in the radial plane, we chose a distance between the electrodes of $r_0 \approx 0.75$ mm, as a compromise between having a small trap (not too large voltages) and good access to the central region of the trap. The electrodes are chosen to be much longer than r_0, such that their exact length does not influence the potential in the trap center. Thus, for the configuration in the radial plane the only free parameter left is the thickness of the electrodes, which hence should be optimized with respect to minimization of the anharmonic terms and L. To this end, the static potential in the radial plane, $\Phi(x, y)$, was calculated, when a voltage, U_{RF}, was applied to two diagonally opposite electrodes and the other two electrodes were on ground. $r_0 = 0.71$ mm was used. Then the potential along the x-axis (by symmetry equivalent to the y-axis) was fitted to the even terms, $C_{2i}x^{2i}$ $(i = 0 - 4)$, of an eight order polynomial. From this fit, the loss factor $L = U_{RF}/(2r_0^2 C_2)$ and the anharmonicity of the potential along the x-axis, defined as [112]

$$f_x(x) = \frac{\Phi(x, y = 0) - C_0 - C_2 x^2}{C_2 x^2} \tag{7.2.3}$$

could be determined. For values of x, which are relevant for a cold ion-string, we have $f_x(x) \approx C_4 x^2/C_2$. Calculations were made for three different values of the electrode thickness: 0.15 mm, 0.25 mm and 0.35 mm. The obtained values of $C_4/C_2 \approx f_x(x)/x^2$ and L are presented in Table 7.1, showing that a thickness of 0.25 mm or 0.35 mm is most

Thickness[mm]	L	C_4/C_2
0.15	1.31	$1.7 \cdot 10^{-5}$
0.25	1.23	$6.3 \cdot 10^{-6}$
0.35	1.18	$7.1 \cdot 10^{-6}$

Table 7.1: The loss factor L and $C_4/C_2 \approx f_x(x)/x^2$ (x in units of the spatial resolution of 5 μm) for three different values of the electrode thickness.

favorable. Since there is no significant difference between the two, 0.25 mm thickness was chosen, since various metals are available in this thickness as a standard.

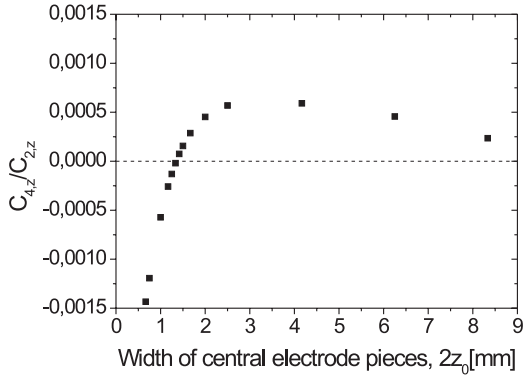

Figure 7.3: $C_{4,z}/C_{2,z} \approx f_z(z)/z^2$ (z in units of the spatial resolution of 42 μm) vs. width of the central electrode pieces. The zero crossing is around $2z_0 = 1.35$ mm.

The sectioning of the electrodes was determined from 3D-calculations of the potential. The eight end-pieces are chosen so wide that their exact width is irrelevant for the potential near the trap center. The spacing between the central electrode pieces and the end-pieces was fixed to 0.12 mm in the calculations and the distance between diagonally opposite electrodes was $2r_0 = 1.50$ mm, almost as above. Thus, the width of the four central electrode pieces, $2z_0$, is the only free parameter left. This width was optimized with respect to the anharmonicity along the z-axis, $f_z(z)$, defined analogously to $f_x(x)$. Once again, the anharmonicity is essentially given by $C_{4,z}z^2/C_{2,z}$ for all relevant values of z, where $C_{2,z}$ and $C_{4,z}$ are the coefficients of the second and the fourth order term, respectively, in the potential along the z–axis. The values obtained for $C_{4,z}/C_{2,z}$, with z in units of the spatial resolution of 42 μm, are shown in Fig. 7.3 for different values of $2z_0$. We observe that the anharmonicity, or at least the leading anharmonic term, is zero around a width of $2z_0 = 1.35$ mm and approaches zero at large values of $2z_0$. A width of $2z_0 \approx 1.35$ mm was chosen, since the alternative of rather wide central electrode pieces ($\gtrsim 10$ mm) would require large endcap voltages.

Numerical calculations using $r_0 = 0.75$ mm, $2z_0 = 1.33$ mm, an electrode thickness of 0.25 mm and a spacing between the central electrode pieces and the end-pieces of 0.12 mm yields the following trap parameters for a single $^{40}Ca^+$ ion in the trap:

$$\omega_z = 2\pi \times 177\,\mathrm{kHz} \times \sqrt{U_{end}[\mathrm{V}]} \tag{7.2.4}$$

$$a_z = -0.0627 \times U_{end}[\mathrm{V}] \times \left(\frac{\Omega_{RF}[\mathrm{MHz}]}{2\pi}\right)^{-2} \tag{7.2.5}$$

$$a = 0.367 \times U_a[\mathrm{V}] \times \left(\frac{\Omega_{RF}[\mathrm{MHz}]}{2\pi}\right)^{-2} \tag{7.2.6}$$

$$q = 0.184 \times U_{RF}[\mathrm{V}] \times \left(\frac{\Omega_{RF}[\mathrm{MHz}]}{2\pi}\right)^{-2} \tag{7.2.7}$$

$$\chi = 0.269 \tag{7.2.8}$$

7.2.3 Trap construction

Pictures of the trap are shown in Fig. 7.4. The electrodes are made of molybdenum, which is a suitable material, since it has a large conductivity ($\sim 1/3$ of the conductivity of copper), is non-magnetic and sufficiently stiff that the thin plates do not bend. The electrodes were cut and polished [4] in the chemistry-lab at the institute, to final dimensions (thickness×width×length) of $(0.25 \pm 0.01)\,\mathrm{mm} \times (5.0 \pm 0.1)\,\mathrm{mm} \times (20.0 \pm 0.3)\,\mathrm{mm}$ for the end electrode pieces and $(0.25 \pm 0.01)\,\mathrm{mm} \times (1.30 \pm 0.01)\,\mathrm{mm} \times (20.0 \pm 0.3)\,\mathrm{mm}$ for the central electrode pieces. The distance between diagonally opposite electrodes is $2r_0 = (1.44 \pm^{0.02}_{0.00})\,\mathrm{mm}$ and the spacing between the central electrode pieces and the end-pieces is $\left(0.10 \pm^{0.02}_{0.00}\right)$ mm. For technical reasons, the dimensions are not exactly the same as in the numerical calculations, but after a proper rescaling they are still 'optimal' within the spatial resolution of the calculations.

The electrodes are mounted in four slits in the Macor-block [5] seen in Fig. 7.4, and fixed using UHV-compatible, non-conducting glue [6]. The Macor-holder has a ∅6-hole for optical access along the trap axis and 3 mm wide slits for optical access perpendicular to the trap axis, both horizontally and vertically. The holder is fixed to a stainless steel mounting [can be seen in Fig. 7.4(b)], which in turn is fixed to a stainless steel base [7]. The base is mounted in the center of a vacuum chamber, which will be described in more detail in the next chapter. For feeding in voltages to the electrodes, short pieces of ∅0.25 tantalum wires are spot-welded onto the electrodes and connected either to ∅1 copper-wire or to electronic components, which will be described in the next chapter. The thin wire seen below the trap in Fig. 7.4(a) is a ∅0.2 tungsten-wire, which is placed immediately beneath the trap center. Serving as a glow lamp, it can mark the trap center, when adjusting an imaging system, which also is described in the next chapter. Since it never has been necessary to use the lamp for this purpose and it probably contaminates the electrodes when glowing, it could be left out in future traps of this type.

[4] Polished using a 1 μm diamond polishing paste.

[5] Macor® is a machinable glass-ceramic material, which is ultrahigh vacuum (UHV) compatible and non-conducting.

[6] Epotek H74F, two-component epoxy-glue.

[7] Since the mounting is close to the trap center, it is made of essentially non-magnetic stainless steel, grade 316, in contrast to the standard grade 304 used for the base.

(a) (b)

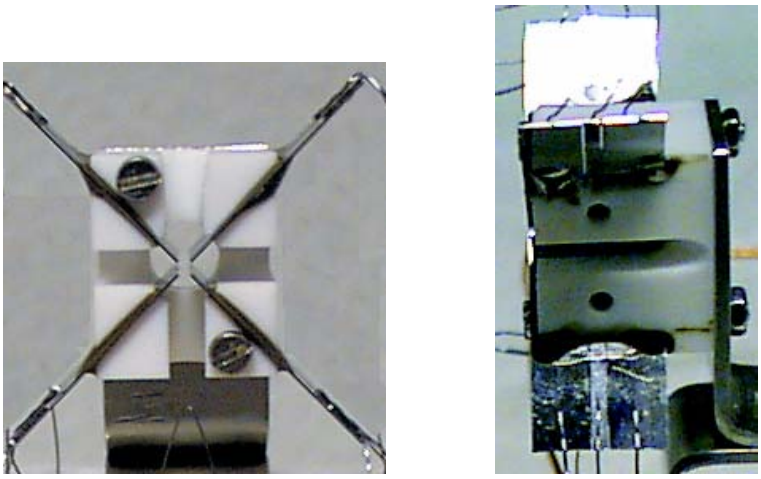

Figure 7.4: Pictures of the linear Paul trap. The thin metal plates are the molybdenum electrodes and the white block holding the electrodes is made of Macor. The precise trap dimensions are given in the text. (a) Front view, the Macor block is 15 mm wide. (b) Side view, the Macor block is 15 mm long.

Chapter 8

Experimental equipment and methods

In this chapter, we describe the experimental equipment and methods which have been used in the experiments described in Chap. 9 and Chap. 10, as well as equipment for controlling laser frequencies and making laser pulses (Sec. 8.5), which will be used for the future trapped-ion quantum logic experiments.

8.1 Vacuum chamber

The trap presented in the preceding chapter is mounted in the vacuum chamber shown in Fig. 8.1. The vacuum chamber is made of stainless steel and has an inner diameter of 30 cm. It is mounted in a hole in an optical table, from here on referred to as the trap table. An ion pump and a sublimation pump are permanently connected to the vacuum chamber and a turbo molecular pump can be connected via a roughing valve [1]. To reach ultrahigh vacuum (UHV) conditions the turbo pump is used for initial evacuation during a bakeout of the system to about 150°C lasting two to three days. This brings the chamber pressure down to the working pressure of the ion pump and by lowering the chamber temperature to room temperature and using the ion pump and the sublimation pump a chamber pressure of roughly $4 \cdot 10^{-11}$ Torr can eventually be obtained. The pressure is monitored by an ion gauge [2] and the restgas content in the chamber can be determined using a restgas-analyzer (RGA) [3].

In the vacuum chamber, a plate with threaded holes is mounted, which enables easy mounting of various parts in the chamber. The following parts are mounted in connection with the vacuum chamber:

- The **trap** is mounted on a stainless steel base in the center of the vacuum chamber. The tantalum wires, which are spot-welded onto the electrodes, are connected either to ∅1 copper-wire or to a resistor and a capacitor as illustrated

[1] The ion pump is a Varian VacIon Plus 300 Starcell pump (240 L/s) with a Midivac 929-5002 controller; the sublimation pump is constructed at the institute; the turbo pump is a Leybold Trivac pump.

[2] A Bayard-Alpert gauge, model AIG17G from Arun Microelectronics Ltd..

[3] Spectra restgas analyzer with LM61 satellite, LM502 analyzer and LM9 RF-head.

in Fig. 8.2(a) below. In order to avoid mechanical stress on the tantalum wires, the copper-wires/resistors are fixed in in-line connectors mounted in two Macor-blocks. The in-line connectors are connected by ∅1 copper-wire to the pins of a vacuum feedthrough [4]. Two of these wires carry the RF-voltage and they are shielded by grounded copper stockings.

- A pair of **coils**, for creating a Zeeman-splitting of the ground state sublevels of the $^{40}Ca^{+}$ ion, are mounted on either side of the trap, parallel to the trap axis. The coils, which are described in more detail below, are connected to ∅2.5 copper-wire (thick wire, for good heat-transport and low resistance), which in turn are connected to the pins of a high-current vacuum feedthrough [5].

- Two **ovens** for producing an effusive beam of calcium and magnesium (not used in this work) atoms, from which ions are produced as described in Sec. 8.6 and loaded into the trap. Each oven consists of a hollow graphite cylinder surrounded by a tungsten-wire wound as a coil. These parts are mounted in a hollow ceramic cylinder (for thermal and electric isolation) which in turn is mounted in a stainless steel housing. The graphite cylinder contains calcium (or magnesium) in metallic form and when heated, by passing a current through the tungsten-wire, an effusive atomic calcium beam passes through a hole and propagates towards the trap center. The oven temperature can be monitored by a thermosensor. The Ca-oven is normally operated at 470°C.

- An **aperture** and several **skimmers** made of stainless steel plates, which collimates the atomic beam(s) from the oven(s).

- An **oven shutter**, which can block the atomic beam(s). It consists of a stainless steel plate mounted on an axle, which can be rotated from outside the vacuum chamber.

- A small piece of an **optical fiber** of 125 μm diameter which can be placed in the trap center using a translation stage. When laser light impinges upon the fiber, it can be observed by using the imaging system described in Sec. 8.7. This is useful for calibrating the magnification of the imaging system as well as for a crude alignment of the various laser beams.

- An **electron gun** (not used in this work) enables ion production by electron impact ionization of the calcium or the magnesium atoms in the atomic beams. The electron beam can be steered through the trap center by two sets of **deflection plates**.

- Six **viewports** (anti-reflection coated fused silica windows) allow for laser access parallel and perpendicular to the trap axis as well as in a 45° angle. In a top flange (not shown in Fig. 8.1) another window is mounted, through which the ion fluorescence and scattered light from the fiber can be viewed by the imaging system. These windows can, at the very most, withstand a temperature of 200°C, thus, keeping a reasonable safety margin, the above-mentioned bakeout temperature of the vacuum system is limited to about 150°C.

[4] Caburn-MDC HV3-10Q-20-C40.
[5] Caburn-MDC HV5-25C-6-C40.

- A **Variable Leak Valve** [6] is mounted on a flange for letting various gasses into the vacuum chamber via a copper tube (not used in this work).

As indicated above, some parts have not been used for the present work; these parts were mounted in connection with previous experiments.

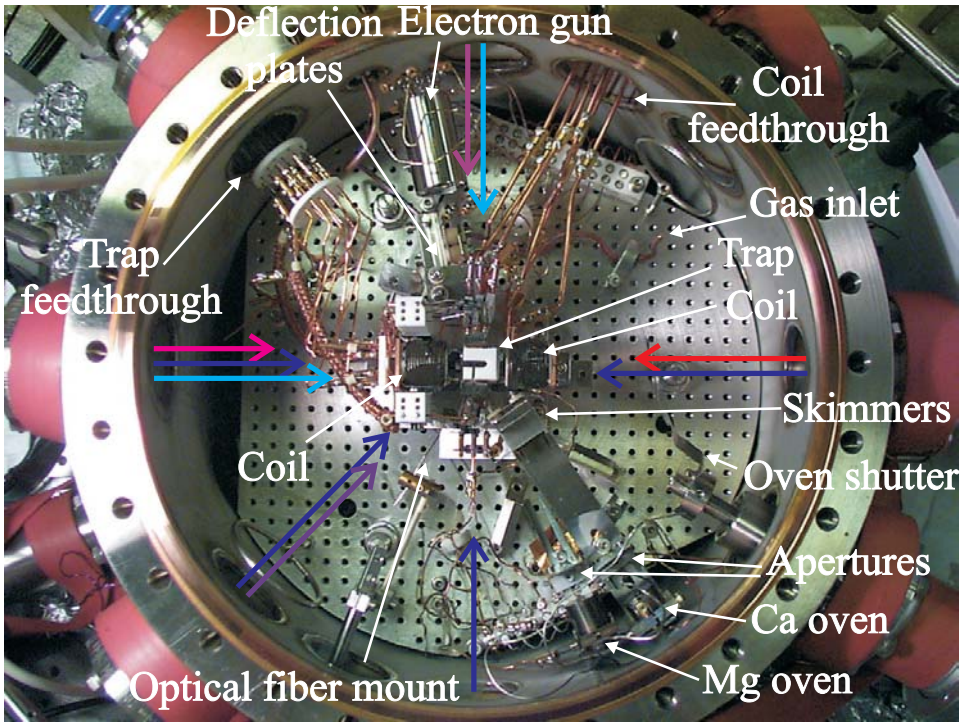

Figure 8.1: Overview of the vacuum chamber. The coloured arrows indicate laser beams; the colour coding is the same as in Fig. 8.5 below. For a length scale, we note that the distance between nearest neighbour holes in the base plate is 1 cm.

8.2 Trap voltage supplies

Two voltage supplies are used for operating the trap, one RF-supply, which generates the high-voltage RF-signal, and one DC-supply, which delivers DC-voltages to the effectively eight electrode pieces. These supplies have been constructed in the electronics department at the institute. Referring to Fig. 7.1, the two electrodes, to which the RF-voltage is applied, are named the RF-electrodes in the following and the other electrodes, to which only DC-voltages are applied, are named the DC-electrodes. Apart from the voltages indicated in Fig. 7.1, DC-voltages for adjusting the equilibrium position of captured ions can be applied to all electrodes.

The DC-voltage on a DC-electrode is equal to $U_{DC} = U_a + U_{adj}$ ($+U_{end}$ for endcap-electrodes), where U_{adj} is the adjustment voltage on the considered electrode. U_{DC} is

[6] Brechtel Manufacturing Inc..

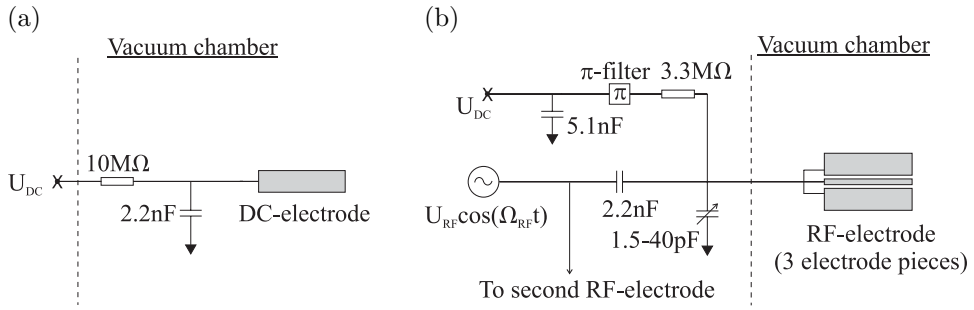

Figure 8.2: (a) In-coupling of DC-voltage to a DC-electrode. $U_{DC} = U_a + U_{adj}$ ($+U_{end}$ for endcap-electrodes). (b) In-coupling of RF- and DC-voltage to an RF-electrode.

applied as shown in Fig. 8.2(a). The capacitor and the resistor ensures that any RF-noise picked up between the DC-supply output and the resistor is strongly suppressed at the electrode. Therefore, the resistor and the capacitor are mounted as close to the electrode as practically feasible *inside* the vacuum chamber. The resistor is rated as UHV-compatible and the capacitor is a porcelain (high-frequency, high-voltage) capacitor [7], which proved to be UHV-compatible. The two components are soldered together using UHV-compatible solder wire [8] and connected to the electrodes via the above-mentioned tantalum wires.

For each of the RF-electrodes (consisting of three electrode pieces) the RF-voltage and a DC adjustment voltage is combined as shown in Fig. 8.2(b), ensuring that the RF-voltage is heavily damped at the output of the DC-supply [9]. The adjustable capacitor (1.5-40 pF) enables adjustment of the RF-voltage on the electrode but can also be used for adjustment of the RF-frequency as discussed below.

8.2.1 RF-supplies

In the past years two types of RF-supplies have been used with the present trap [10].

The first RF-supply which was used is a self-oscillating source [122]. The main components are two radio tubes [11], where the anode of each tube is connected to the cathode of the other. The anode-anode voltage can be brought to oscillate by feeding a sufficiently large DC-voltage to the anodes (through a coil), thus providing us an RF-voltage, which in turn is coupled inductively to the trap. The oscillation frequency depends on the load of the system, which mainly is presented by the capacitance and inductance of the trap, the cables/wires connected to the trap and the two adjustment capacitors [1.5-40 pF, only one is shown in Fig. 8.2(b)]. Using the two adjustable capacitors, the oscillation frequency can be varied roughly over the range 14-18 MHz [12].

[7] Temex 102CLE222JP.

[8] Johnson-Matthey metal joining, LM10A.

[9] Some of the components are non-standard high-frequency, high-voltage components. 2.2 nF: Temex 102CLE222JP. 5.1 nF: American Technical Ceramics, 100E512KW 500X. 1.5-40 pF: Voltronics corporation, AP40HV/1500 V.

[10] At this point extra credit should be given to people in the electronics department, who have worked hard to solve the non-trivial task of generating an RF-signal around 18 MHz with ~ 1 kV amplitude.

[11] `http://tdsl.duncanamps.com`, model 6146.

[12] In fact the system is bi-stable, meaning that under extreme conditions it can be brought to oscillate

The amplitude of the RF-voltage is controlled by the DC-voltage fed to the anodes and is limited to approximately 1 kV amplitude. Higher harmonics in the output are suppressed by at least 30dB, with third and fourth overtone being the most prominent ones. The RF-voltage output can be monitored via a calibrated signal from a pick-up coil. This RF-supply was used in initial tests of the trap and in some of the experiments described in the next chapter. It has, however, been discarded for now due to the fact that the RF-frequency is set by the load and not an external frequency source, as for the supplies described below. Since the load is temperature dependent, this means that after a change of the RF-voltage, which changes the equilibrium temperature of the system, the RF-frequency and hence the radial trap frequencies can drift. On one occasion we observed, that after having changed U_{RF} from 300 V to 500 V, one of the radial trap frequencies dropped [13] by 13 kHz before settling within 1-2 kHz of a new equilibrium value after 25 minutes. The RF-frequency actually settled faster than the observed radial trap frequency, which means that the amplitude of the RF-voltage, not unexpectedly, also was drifting. Although drifts of the radial trap frequencies on the level of 10 kHz may not be very critical (the power broadened linewidth of the Raman transition is 10 kHz or more in sideband cooling), it is an unsatisfactory situation that the radial trap frequencies drift, since they are the most important trap parameters for sideband cooling of the radial motion.

The currently used type of supply is a fixed-frequency supply. A sinusoidal signal from a function generator [14] is amplified [15] and coupled inductively to the trap electrodes using a ferrite core with a single winding on the primary side and 10-15 windings on the secondary side, depending on the desired RF-frequency. The windings, the ion trap and the adjustable capacitors in Fig. 8.2 constitute an LCR resonant circuit and the trap is operated at the resonance frequency of this circuit. Naturally, the resonance frequency of the LCR-circuit also varies with temperature, which will lead to a variation in the output-voltage if the RF-frequency is kept fixed, however, the problem seems to be smaller than with the self-oscillating source. The output-voltage is measured using a capacitive voltage-divider on the secondary side, which provides a monitoring signal (varies between 1:100 and 1:125 of the output voltage for the different supplies). For reasons discussed in Chap. 9, this type of supply has been used in the following three different versions having different resonance frequencies of the LCR-circuit.

1. Supply with resonance frequency adjustable over the range $14.0 - 19.4$ MHz, usually operated near 18.0 MHz for comparison with the self-oscillating supply.

2. Same supply as number 1, but with a resonance frequency in the range $10.4 - 14.5$ MHz. Usually operated near 11.0 MHz for comparison to an early version of the same supply and for reasons discussed in the next chapter.

3. An RF-supply constructed for the larger linear Paul traps used in our group, operated at 5.6 MHz.

around 100 MHz, however, with a rather small amplitude.

[13] Measurements of trap frequencies are described in detail in Chap. 9.

[14] Hewlett-Packard 8656B signal generator 0.1-990 MHz.

[15] Using either the 100 W amplifier unit in an Intraaction Frequency Synthesizer (VFE-30100A5) or a 4 W amplifier, 4W1000, from Amplifier Research.

Control #	Electrode #	Purpose	Voltage [V]
1	4,6,7,9	Endcap voltage	0 ... 100
2	4,5,6,7,8,9	a-parameter	−10 ... 10
3	4,7	Axial equilibrium position	−10 ... 10
4	6,9	Axial equilibrium position	−10 ... 10
5	4,5,6	Radial equilibrium position, x-axis	−10 ... 10
6	2	Radial equilibrium position, y-axis	−10 ... 10

Table 8.1: Overview of the control buttons on the DC-voltage control unit.

8.2.2 DC-supply

The necessary DC-voltages, U_{end}, U_a and U_{adj}, are provided by a DC control unit. The numbered outputs of this unit are connected to the electrodes as shown in Fig. 8.3 and controlled in six groups as summarized in Table 8.1. As the 'Purpose' column in the table indicates, the voltage on each group of electrodes controls either a trap parameter (a or ω_z) or the equilibrium position of the ions along a given axis.

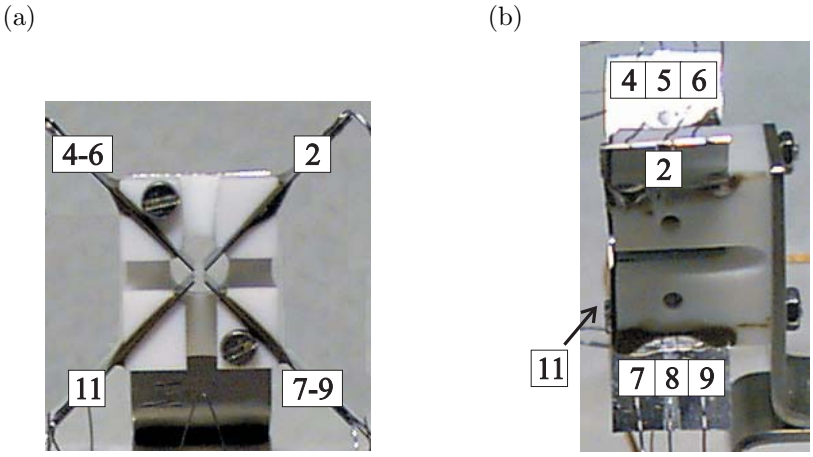

Figure 8.3: Overview of the electrode numbering. Electrodes 2 and 11 are RF-electrodes and electrodes 4-9 are DC-electrodes. (a) Front view. (b) Side view.

8.3 Magnetic field coils

As discussed in Chap. 3 (see particularly Fig. 3.8) a Zeeman-splitting of the ground state sublevels in $^{40}Ca^{+}$, which is much larger than the trap frequencies, is necessary. We will aim for a splitting of $2\pi \times 15\,\mathrm{MHz}$, which requires a magnetic field of 5.4 Gauss (see App. B). The coils for producing this field are the ones mentioned above, which are placed inside the vacuum chamber for two reasons. First, to avoid using large currents it is advantageous to place the coils close to the trap. Second, to have the possibility of quickly switching on and off the magnetic field, the coils should not be placed outside

the chamber, since this would require large coils (large inductance) and eddy currents would be induced, e.g., in the vacuum chamber. The coils are shown in Fig. 8.4. Since they have to be UHV-compatible, they are made of unisolated ∅1 copper-wire wound on a Macor-cylinder with grooves which keep the windings separated. The coils are mounted symmetrically around the trap center (see Fig. 8.1) such that an approximately homogenous magnetic field parallel to the trap axis can be produced. A ∅6 hole in each Macor-cylinder allows for passage of lasers beams parallel to the trap axis.

When a current I pass through the coils, the magnetic field strength B in the trap center is

$$B[\text{Gauss}] = 1.2(1) \cdot I[\text{A}]. \tag{8.3.1}$$

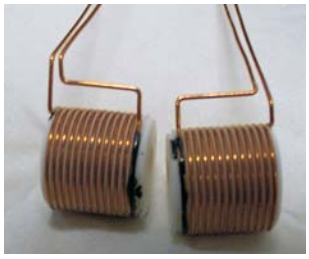

Figure 8.4: The magnetic field coils. The coils are wound on grooved Macor-cylinders of 21 mm length. The inner diameter of the 13 windings is 20 mm. A ∅6 hole in each Macor-cylinder allows for passage of laser beams.

The current is supplied by a stable current-controlled power-supply[16]. The magnetic field can be switched quickly on and off using a fast current-switch constructed at the institute, which can switch the current from the supply between going through the coils and a series-connected 1Ω high-power dummy-resistor or through another 1Ω high-power resistor. The current can be switched on to within 1 permille of the supplied current in approximately 200 μs, which is limited by the settling time of the supply. When switching off the current, it drops approximately exponentially with a time constant of $\sim 5\,\mu$s, consistent with L/R, where L is the inductance and R is the resistance of the coils and the dummy-resistor, respectively .

Since the coils are placed inside the vacuum chamber, the heat deposited in the coils can only be removed through the wires themselves or via blackbody-radiation. This can give rise to an elevated equilibrium temperature of the coils, which can lead to an increase in the chamber pressure. To reduce this problem, the coils have been smeared in glue [17], which improves the heat-conductance between the windings. The coils have been tested under UHV-conditions to 6 A with no observable increase in the chamber pressure. At a later stage of the experiments it might become relevant with a Zeeman-splitting of $2\pi \times 30$ MHz, which would require a current of 9 A. It can be estimated that the temperature of the coils will increase by about 40 K in this case, which would be below the bakeout temperature and hence it should not increase the chamber pressure.

[16]Toellner, TOE8851-16, 20 A. Stability within 8 hours: 0.1%. Residual ripple: 500 μA (rms). Relative temperature sensitivity: $10^{-4}/K$.

[17]EPOTEK H74F, also used for gluing the trap electrodes to the Macor block.

In order to compensate for earth-fields and stray magnetic fields, five coils are mounted outside the vacuum chamber, which enables compensation in all three spatial dimensions. Two sets of coils are mounted pairwise symmetric around the trap center, providing relatively homogenous compensation fields in the horizontal plane, respectively parallel and perpendicular to the trap axis. Another coil mounted above the vacuum chamber (no counterpart below the chamber) can provide a vertical compensation field. The power supplies are identical to the one used for the Zeeman coils.

Finally, a coil mounted close to the chamber can provide a vertically directed magnetic field in order to define a vertical quantization axis for the ions (see Sec. 3.1.).

8.4 Laser light sources for Ca^+ ions

The laser systems providing light at 397 nm, 850 nm, 854 nm and 866 nm are placed on two separate optical tables. Light from these lasers are brought to the trap table through polarization-maintaining optical fibers. Alternatively, the 397 nm light is brought to the trap table via mirrors through air.

8.4.1 397 nm sources

For sideband cooling, quantum logic operations (Raman transition) and Doppler cooling, 397 nm light is provided by a frequency-doubled Titanium:Sapphire (Ti:Sa) laser [18]. The Ti:Sa laser is normally pumped by 6 W of optical power at 532 nm from a Coherent Verdi V8 laser, which usually results in 400-500 mW of 794 nm light from the Ti:Sa laser. This light is frequency-doubled in a 12 mm long LBO crystal placed in an external bow-tie cavity, which is locked using a Hänsch-Couillaud lock [123, 124], typically yielding 25-35 mW of 397 nm blue light [19]. The blue light is passed through a series of cylindrical and spherical lenses in order to obtain an approximately Gaussian, collimated beam. The light can be transported to the trap table through air with negligible losses or through an optical fiber with 70-75% incoupling/transmission losses resulting in ~ 8 mW available at the trap table. The advantage of using the fiber instead of the air-beam is the good pointing stability and the relatively well-defined spatial mode after the fiber. The drawback is the power loss and non-perfect polarization maintenance in the fiber.

The frequency of the Ti:Sa laser has until recently been locked to a passively temperature-stabilized commercial cavity [20], but is now locked to a home-built actively temperature-stabilized cavity using a Pound-Drever-Hall lock [71, 125]. A typical long-term frequency drift is 1 MHz at 794 nm over one hour [71].

In order to stabilize the output power from the frequency doubling cavity, a power stabilization system based on an acoustooptic modulator (AOM) has recently been build up [126]. The undeflected zeroth diffraction order from the AOM is send to the trap table, with the power kept constant to a chosen level by feedback-controlled deflection of (surplus) power out of the zeroth order beam. The system provides a power-stability at the level of a few percent from DC to 5 kHz, which particularly is an improvement

[18] Coherent 899 ring laser.

[19] With a mode matched input beam and a new crystal, 150 mW blue light at 500 mW input power has been obtained [123].

[20] From Coherent.

for the long-term stability of the output from the doubling cavity. Above 5 kHz there is only little noise in the output from the doubling cavity, although one should be aware of noise somewhere in the range 20-30 kHz generated by the cavity-lock itself, which can be removed by adjusting the feedback voltage in the cavity-lock. For the present experiment, this power-stabilization system may in the future be complemented, or replaced, by a cavity placed on the trap table with the cavity length being locked to keep the transmitted power constant. This may seem superfluous, but the cavity has the additional advantage of providing a well-defined spatial mode and direction of the transmitted beam, when the direction of the input beam is properly optimized. This would render the optical fiber superfluous.

The wavelength of the Ti:Sa laser beam can be measured down to seven digits relative precision using a wave-meter. Alternatively, the resonance frequency of the $^2S_{1/2}$–$^2P_{1/2}$ transition can be found by optogalvanic spectroscopy using a hollow-cathode discharge lamp [127, 128].

In the lab, another laser source at 397 nm is available, namely a home built diode laser system [21] capable of delivering about 5 mW of 397 nm light. Currently, it is, however, not planned to use this laser in connection with the project presented here.

8.4.2 Infrared sources

The three infrared transitions in the $^{40}Ca^+$ ion, near 850 nm, 854 nm and 866 nm, are all covered by diode lasers built from anti-reflection (AR)-coated laser diodes [22], which provides tunability over a broad wavelength range. Two of the lasers (850 nm and 866 nm) are entirely home built and the third one (854 nm) is partly home built, in that the AR-coated diode has replaced the diode in a commercial diode laser [23]. In each of the home-built lasers, the laser-cavity is constituted by the back-side of the laser diode and an external grating (1800 lines/mm) mounted in the Littrow configuration. The laser light is out-coupled via the grating and send through a Faraday isolator and a set of anamorphic prisms; the latter in order to make the elliptically shaped beam from the diode laser circular. The laser light is then coupled into an optical fiber and brought to the trap table (60-80% transmitted).

The frequency of the 850 nm and the 854 nm lasers can be locked to the same actively temperature-stabilized cavity, identical to the one used for the Ti:Sa laser. Thus, the relative drift of the two laser frequencies, which is the important quantity for STIRAP, is much smaller than the drift of the cavity resonance (~ 1 MHz/hour). The 866 nm laser can be frequency-locked to another actively temperature-stabilized cavity, also identical to the one used for the Ti:Sa laser.

The wave-meter and optogalvanic spectroscopy can also be used at the infrared wavelengths of these three lasers.

8.5 Laser light control

To implement the sideband-cooling scheme, the STIRAP detection scheme and to perform quantum logic operations, the frequency and the intensity of the involved laser

[21] Laser diode from the Nichia Corporation.
[22] From the Ferdinand-Braun Institute, Berlin.
[23] SDL-TC10.

beams must be accurately controlled on the timescales relevant for these processes. Furthermore, the phase-difference between the Raman beams has to be controlled (see Sec. 5.3).

The frequency should first of all be controlled to better than 20 kHz or so for efficient sideband cooling (see Fig. 3.12) and for reliably performing gate operations. Moreover, it should be possible to change the frequency-difference between the Raman beams for sideband cooling of the various motional modes and for gate operations on the carrier and the red and blue sidebands. The fastest frequency changes needed are on the timescale of the shortest frequently used pulses, i.e., carrier $\pi/2$-pulses, for which a reasonable duration would be 50 μs (much larger than $\pi/\omega_z \sim 0.5\,\mu$s, see Chap. 5). With respect to fast control of the intensity (pulse shaping), the duration of the $\pi/2$ carrier pulses sets the most stringent requirements for the Raman transition. Furthermore, it is required that all the STIRAP pulses of duration 5–10 μs are smooth.

The laser frequencies can be changed and hence controlled by exploiting the frequency shift of light deflected by AOM's. Likewise, pulse-shaping can be done using the deflected light from AOM's, since the amount of deflected power depends on the RF-power applied to the AOM. The phase-difference between the Raman beams can be controlled using an electrooptic modulator (EOM) inserted in one of the Raman beams.

Analog and digital control signals to the AOM's and the EOM's will be provided by four boards from National Instruments [24], which also will be used for data acquisition, with everything being controlled by Labview [25]-based programs. One board (PCI-DIO-32-HS) will control the timing, providing up to $16 \cdot 10^6$ updates of 16 digital output channels, e.g., at a rate of 100 kHz. For the STIRAP pulses, a much higher resolution is needed and therefore the control voltages for creating these pulses are generated using a 4-channel 40 MHz arbitrary waveform generator [26].

The entire setup involves nine AOM's and two EOM's, for which details are given below. An overview of the setup on the trap table is given in Fig. 8.5, of the involved AOM's and EOM's in Table 8.2 and of the frequency shifts from the many AOM's in the blue beamline in Fig. 8.6. At present, the AOM's numbered 1-6 below and the EOM numbered 1 have not yet been set up.

8.5.1 397 nm sources

At the trap table, light from the frequency-doubled Ti:Sa laser is split in frequency as shown in Fig. 8.6 and spatially as shown in Fig. 8.5 [27].

Considering the light for the Raman transition first, the -1. diffraction order from AOM1 provides light at a large detuning with respect to the $^2S_{1/2}$–$^2P_{1/2}$ transition frequency. AOM2 enables pulse-shaping and AOM3 and AOM4 controls the frequency difference between the Raman beams. The 15 MHz difference between the center-frequencies for AOM3 and AOM4 corresponds to the projected Zeeman-splitting. From AOM2, AOM3 and AOM4, the -1. diffraction order is used in order to get the largest possible detuning of the Raman beams (as opposed to using the $+1$. diffraction order). For simplicity, the AOM's are intended to be used in single-pass, but an even larger de-

[24] National Instruments PCI-6704, PCI-6713, PCI-6071E, PCI-6533 (PCI-DIO-32-HS).

[25] National Instruments.

[26] Thurlby Thandar Instruments TGA1244.

[27] In Fig. 8.5 blue light is brought to the trap table through the fiber, but the 'air-beam' can be used just as well.

Device	Type	Purpose
AOM1	Brimrose TEF-600-100-.397	Raman, detuning
AOM2	Brimrose TEF-80-20-.397	Raman, pulse-shaping
AOM3	Brimrose TEF-225-50-.397	Raman, frequency control
AOM4	Brimrose TEF-240-50-.397	Raman, frequency control
AOM5	Intraaction ASM-702B8	STIRAP-pulse/frequency shift
AOM6	Intraaction ASM-702B8	Frequency shift
AOM7	Intraaction AOM-40N	STIRAP-pulse
AOM8	Intraaction AOM-40N	STIRAP-pulse
AOM9	Brimrose TEF-80-10-.866	STIRAP-pulse
EOM1	Linos LM 0202 Phas VIS 0.1W	Raman, phase control
EOM2	Linos LM 0202 IR 0.1W	Repumping, polarization rotation

Table 8.2: Overview of AOM's and EOM's involved in the setup in Fig. 8.5.

tuning can be obtained if some, or all of them, are used in double-pass. For AOM3 and AOM4, this would also cancel a small change in deflection angle which occurs whenever the frequency is changed. For doing this, a Zeeman-splitting of about $2\pi \times 30\,\mathrm{MHz}$ would be needed.

For all processes which are near-resonant with the ${}^2S_{1/2}{}^-{}^2P_{1/2}$ transition, i.e., Doppler-cooling, STIRAP, pumping in the sideband-cooling scheme and optical pumping to one of the sublevels of the ground state, the zeroth diffraction order from AOM1 is used. The STIRAP-pulse needed at 397 nm is made using AOM5. AOM6 is necessary for shifting the light into resonance (or close to) with the ${}^2S_{1/2}{}^-{}^2P_{1/2}$ transition.

The drivers for AOM1, AOM2, AOM 5 and AOM 6 are standard fixed-frequency drivers from Brimrose. The drivers for AOM3 and AOM4 have been developed at the institute. They are based on a direct digital synthesizer [28], which can generate a frequency in the range $200 - 265\,\mathrm{MHz}$ from a 400 MHz reference signal. The width of the reference signal sets the width of the output signal, which is about 20 kHz (full width at -40 dB). Up to 1024 frequencies can be defined in a table, whose entries can be addressed by a digital or an analog signal. Frequencies can be scanned by scanning through the entries in the table in various modes at a max. frequency of 10 kHz. A faster scan rate can be obtained by employing internal ramp-functions of the synthesizer.

Changes of the phase-difference between the Raman beams will be made by EOM1. The voltage supply for this EOM is a fast linear amplifier constructed at the institute, which can switch from zero voltage to the EOM half-wave voltage of 150 V (within 1%) in $\sim 2\,\mu$s. In Fig. 8.5 the two beam paths from the polarizing beamsplitter after AOM2 to the trap center are made equally long, with the purpose of cancelling some drifts of the phase-difference between the Raman-beams. For example drifts due to thermal expansion of the trap table, which would lead to a change in the beam path lengths.

8.5.2 Infrared sources

STIRAP pulses at 850 nm, 854 nm and 866 nm are produced using AOM7, AOM8 and AOM9, respectively. The AOM-drivers are standard fixed-frequency drivers from the

[28] AD9954 from Analog Devices.

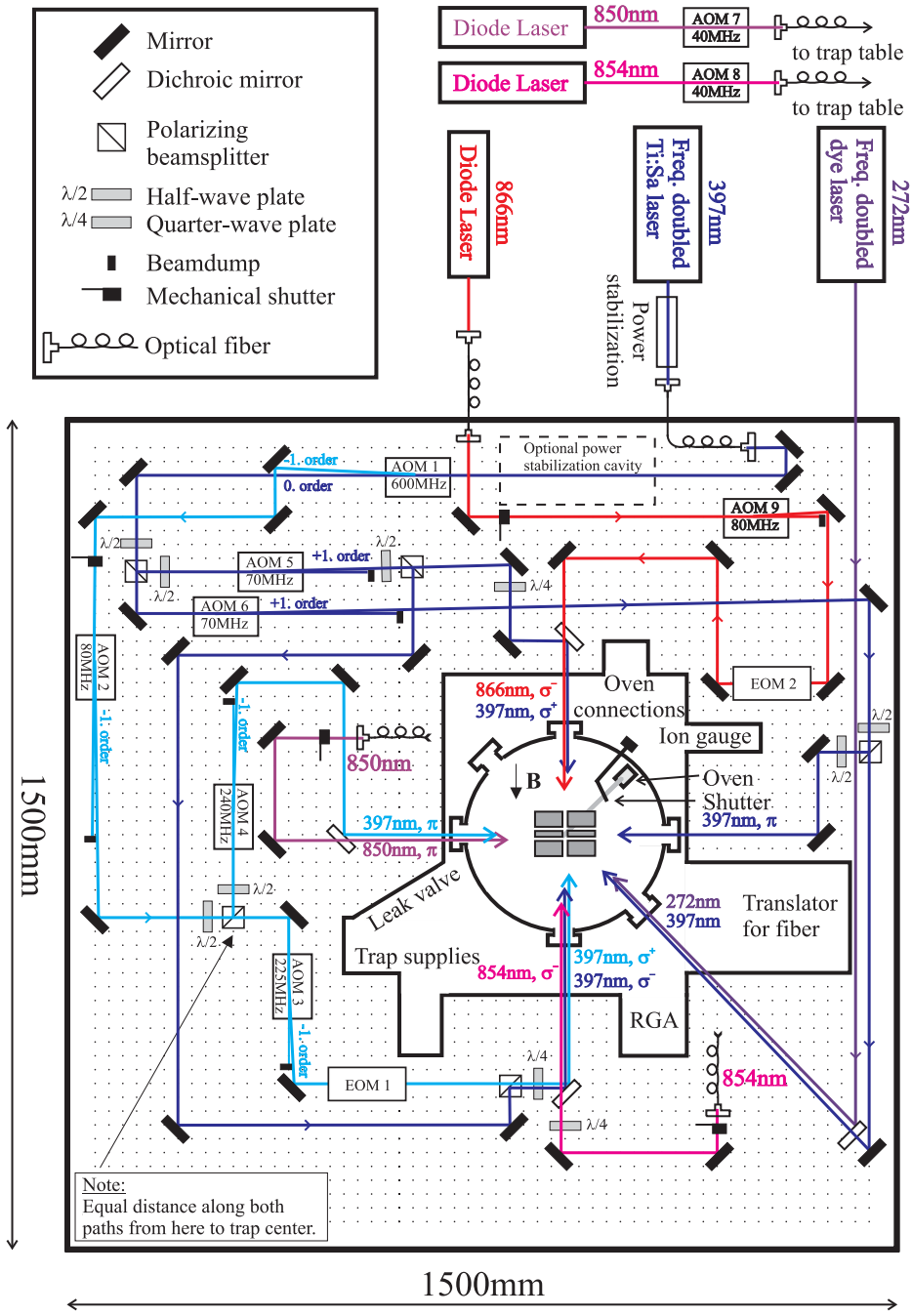

Figure 8.5: Setup of optical components on the trap table with signatures given in the upper left box. See text for details. The white space around the chamber is occupied by compensation coils and other parts as indicated on the drawing. Dots indicate threaded holes with a distance of 2.5 cm between nearest neighbours. The entire drawing is rotated 90° counter-clockwise with respect to the picture in Fig. 8.1.

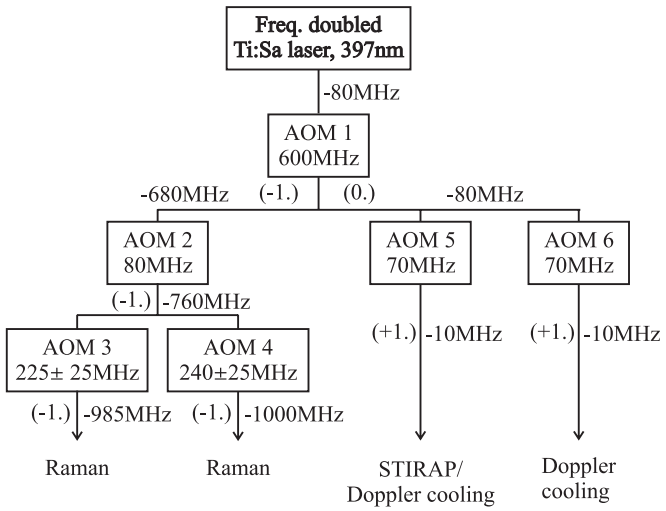

Figure 8.6: Schematic overview of the AOM's and approximate frequencies along the blue beamline given as the detuning with respect to the resonance frequency of the $^2S_{1/2}$–$^2P_{1/2}$ transition. The numbers in parentheses indicate the used diffraction order.

manufacturer of the AOM's (see Table 8.2).

As mentioned in Sec. 3.1, the efficiency of repumping from the $^2D_{3/2}$ state to the $^2P_{1/2}$ state is reduced, when the applied magnetic bias field is small, which it should be to avoid a large Zeeman-splitting. In this case, the repumping efficiency can be improved by quickly rotating the polarization of the repumper light, which is done using EOM2 with an applied sinusoidal voltage of $\sim 4\,\mathrm{MHz}$ frequency and $\sim 300\,\mathrm{V}$ peak-peak amplitude (the half-wave voltage of the EOM). The voltage supply, which is constructed at the institute, is able to switch 'on' in $\sim 40\,\mu\mathrm{s}$ and 'off' in $\sim 2\,\mu\mathrm{s}$ within 1% of the peak-peak voltage and zero, respectively. A preliminary test has shown that Doppler cooling works well using polarization rotation of the repumper light.

8.6 Ion production

For loading ions into the trap, ions are produced in or near the trap center by ionization of atoms in the atomic beam from the calcium oven. Previously, ions have been produced by electron impact ionization using the electron gun, however, this method has not been used for the present work. Instead, a resonance-enhanced two-photon ionization technique developed within the last few years has been used [129], [IV]. In contrast to electron impact ionization, this technique is very clean, meaning that no background gas atoms or molecules are ionized and no doubly-charged calcium ions are produced. Furthermore, the trap electrodes are not charged by electrons, as it often would be the case if the electron gun was used.

In our scheme for resonance-enhanced two-photon ionization illustrated in Fig. 8.7, calcium atoms are ionized using 272 nm light from a frequency-doubled dye laser described below. From the $4s^2\,^1S_0$ ground state, the atoms are resonantly excited to the

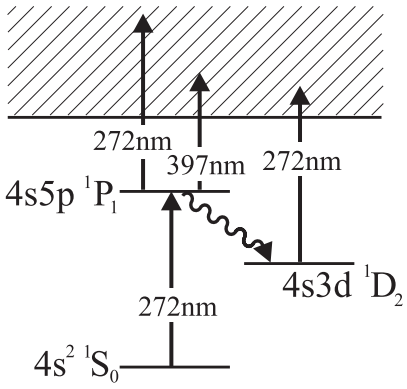

Figure 8.7: Resonance enhanced two-photon ionization of neutral calcium. The hatched area indicates the continuum. Further details are given in the text.

$4s5p\,^1P_1$ state, from which they can be ionized by absorption of another 272 nm photon or a 397 nm photon from the laser cooling light. Alternatively, the atoms can decay to the $4s3d\,^1D_2$ state, from which they can be ionized by absorption of a 272 nm photon. Light at 272 nm is produced by frequency doubling of 544 nm light from a dye laser [29] pumped by an Argon-ion laser [30]. Frequency doubling takes place in a 7 mm long BBO crystal placed in an external bow-tie cavity, which is locked using a Hänsch-Couillaud lock [124, 130]. The light is brought to the trap table through air and focussed to a beam waist of approximately 100 μm in the trap center. With this waist, a few mW of 272 nm light, which easily can be produced, is sufficient for producing the needed number of ions.

The spectral linewidth of the 272 nm light is sufficiently small, that we can load all the naturally abundant isotopes of calcium (see App. B) selectively and resolve the hyperfine structure of the $4s5p\,^1P_1$ state in the ^{43}Ca isotope. This was recently exploited to measure the isotope shifts of the $4s^2\,^1S_0$–$4s5p\,^1P_1$ transition in neutral calcium and the hyperfine splitting of the $4s5p\,^1P_1$ state in ^{43}Ca [IV].

8.7 Imaging system

The imaging system used for observing the 397 nm fluorescence light from the ions, as well as scattered light from the optical fiber, is placed above the trap, as illustrated in Fig. 8.8. A Nikon objective lens for MM40/60 measuring microscopes (10x magnification, f-number ~ 1.7) placed about 5 cm above the trap center collects the fluorescence/scattered light, which subsequently is amplified by an image intensifier and imaged onto a CCD-camera, resulting in an all over magnification of about 20 for the entire imaging system [31]. The image-intensifier consists of a photo-cathode, a pair of micro-channel plates and a phosphor screen. When photons impinge on the photocathode, electrons are produced, which are accelerated through the microchannel plates and

[29] Coherent CR-699 ring laser. Laser dye: Pyrromethene 556.

[30] Spectra Physics Beamlok laser, 20 W.

[31] The image intensifier is from Proxitronic, model BV 2581 BY-V 1N. The CCD-camera is a SensiCam system from PCO.

hence multiplied. When the electrons hit the phosphor screen, light is produced, which is imaged onto the CCD-chip. The CCD-images are digital images with 12 bit resolution, which can be viewed on a personal computer while they (optionally) are recorded to the RAM of the computer. The image-intensifier as well as the CCD-chip has a linear response to the intensity of the incoming light.

The image intensifier can be gated by quickly switching on and off the acceleration voltage for the microchannel plates. Gating is possible in two modes: a 'normal' mode, where the opening time of the image intensifier is adjustable down to approximately 40 ns (max. gating frequency 5 MHz) and a 'needle' mode, where the opening time of the image intensifier is fixed to about 20 ns (max. gating frequency 2 MHz). The acceleration voltage can be measured via a monitoring output (approximately 1:100 of the acceleration voltage).

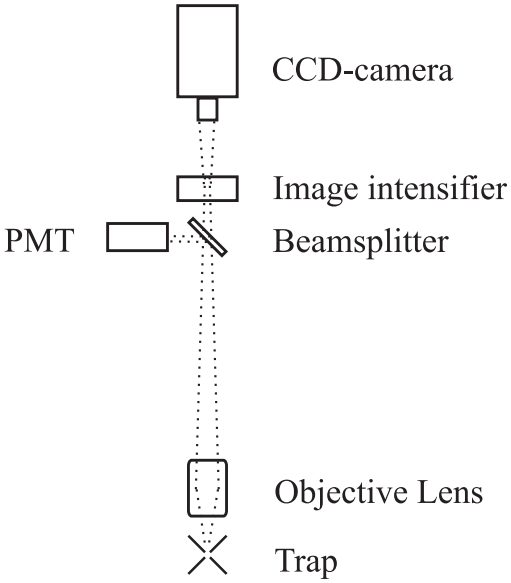

Figure 8.8: Schematic drawing of the imaging system. PMT: Photo-multiplier tube.

The CCD-images provide spatially resolved images of the ions as well as a measure of the ion fluorescence. The ion fluorescence can additionally be counted using a recently installed photo-multiplier tube [32], for which light is tapped off by a (removable) 1 mm thick 50/50 beamsplitter inserted between the objective lens and the image intensifier.

[32] Hamamatsu H5783P-06.

Chapter 9

Trap characterization and ion mass measurements

In sideband cooling and trapped-ion quantum logic experiments, the axial and radial trap frequencies play an important role, as described in previous chapters. Thus, it is an important step towards such experiments to measure the trap frequencies and determine experimentally how they behave as a function of various parameters, i.e., to characterize the trap. In this chapter we present the results of a series of experiments initiated with the goal of characterizing the trap by measuring the trap parameters introduced in Chap. 7. Some of the results were quite unexpected, which has led us to perform a rather extensive series of measurements. The trap characterization experiments and the interpretation of the results are described in Sec. 9.1. To conclude the trap characterization, a brief discussion of micromotion and patch potential problems is given in Sec. 9.2.

The technique used for measuring the trap parameters is applicable for measuring ion masses, allowing a clear distinction between ions with different atomic masses. Using a refined technique, it should even be possible to discriminate between ions with the same number of nucleons, which only differ in mass due to their different nuclear binding energies. Since this would be a valuable tool for an ongoing research project in our group concerning molecular ions, these possibilities for mass measurements have been investigated. The theory for the mass measurements and preliminary experimental results are presented in Sec. 9.3.

9.1 Measuring the trap parameters

In order to characterize the trap, we have measured the characteristic axial and radial trap oscillation frequencies of an ion, while systematically varying the RF-voltage or the applied DC-voltages. Assuming that the 3-dimensional trap potential is harmonic, such that a single laser cooled ion behaves as a classical damped harmonic oscillator (but a very expensive one!), an axial or radial trap frequency can be measured by determining the frequency at which a sinusoidally varying force resonantly excites the oscillatory motion of the ion.

9.1.1 Experimental setup

The experimental setup is in principle as described in Chap. 8, particularly as illustrated in Fig. 8.5, although the equipment for STIRAP and for the Raman transitions was not used. A single ion (or several ions) is (are) loaded into the trap using the photoionization technique described in Chap. 8 and Doppler laser cooled by the blue 397 nm and the red 866 nm cooling lasers focussed to waist sizes of $\sim 100\,\mu$m and $\sim 200\,\mu$m, respectively, in the trap center. Three blue cooling beams were used, two beams counter-propagating parallel to the trap axis and one beam propagating perpendicular to the trap axis, thus allowing cooling of the axial as well as the radial degrees of freedom and balancing of the radiation pressure forces along the trap axis. The ions were viewed using the CCD-camera, typically with 50-100 ms exposure time for each image.

A sinusoidally varying force for exciting the ion motion was obtained in two different ways. Either by applying a (small) oscillating voltage to the trap electrodes, which excites the ions due to the resulting oscillating Coulomb force [131], or by intensity-modulation of the laser cooling light, leading to a modulation of the laser cooling force, which enables motional excitation of the ions. In the following these methods are named voltage-modulation and intensity-modulation, respectively. Intensity-modulation is in a sense more 'clean' than voltage-modulation, since no voltages are added to those necessary for trapping ions and hence the trap potential is not perturbed. As discussed below, intensity-modulation is, however, only suitable for measuring the axial trap frequencies. In contrast, voltage-modulation can be used for measuring both axial and radial trap frequencies. As we shall see below, measurements of the axial trap frequencies fortunately yield identical results within the experimental uncertainty for the two methods.

Voltage-modulation

The modulation voltage is applied to an electrode as shown in Fig. 9.1. A voltage of the form $V_0 \cos(\omega_{mod} t)$ (in the following named the input modulation voltage) is fed to the DC-input of one of the in-coupling circuits (to a DC- or an RF-electrode) shown in Fig. 8.2. Since the in-coupling circuits are designed with the purpose of damping RF-signals from the electrode side at the DC-input, only a small fraction of the input modulation voltage reaches the electrode from the DC-input. This fraction is the actual modulation voltage, $V_{mod} \cos(\omega_{mod} t)$. The amplitude V_{mod} depends on ω_{mod} and the damping effect of the in-coupling circuit, which is different for the RF- and DC-electrode in-coupling circuits (see Fig. 8.2). The DC-voltage, U_{DC}, applied to an electrode (see Fig. 8.2) is added to the input modulation voltage as shown in Fig. 9.1 and fed to the electrode as usual.

For studying the motion of an ion along a specific trap axis, the modulation voltage is applied to a corresponding set of electrodes. For the axial motion (z-axis, trap frequency ω_z) the modulation voltage is applied to the endcap-electrodes 4 and 7 in Fig. 8.3. For the radial motion along the diagonal between the DC-electrodes (x-axis, trap frequency ω_x), a modulation voltage is applied to the DC-electrodes 4-5-6. For the radial motion along the diagonal between the RF-electrodes (y-axis, trap frequency ω_y), a modulation voltage is applied to the RF-electrode numbered 11.

Images showing an unexcited ion and an ion which is motionally excited along the trap axis are shown in Fig. 9.2(a). V_0, the power and the detuning of the cooling laser beams, particularly the blue axial beams, have been adjusted to control the amplitude

of the motionally excited ions motion. The degree of excitation can be quantified

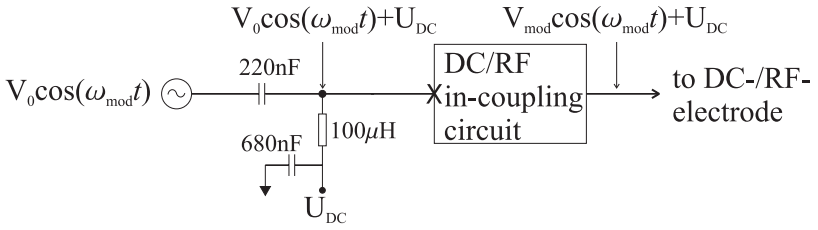

Figure 9.1: Incoupling of modulation voltage to an electrode. The input modulation voltage $V_0 \cos(\omega_{mod} t)$ is added to the DC-voltage, U_{DC}, supplied by the DC control unit described in Chap. 8 and fed to the DC-input of one of the in-coupling circuits shown in Fig. 8.2. The DC-input is marked by a cross on this figure and in Fig. 8.2. The resulting modulation voltage on the electrode is $V_{mod} \cos(\omega_{mod} t)$. No RF-voltage is indicated on this figure.

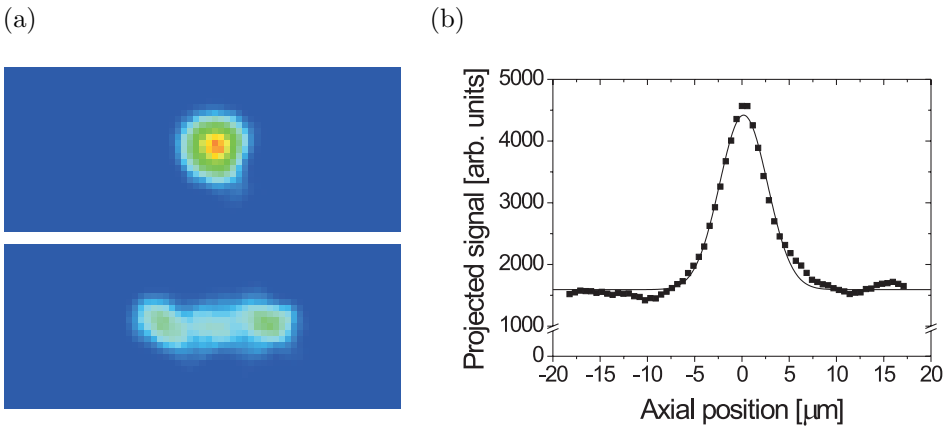

Figure 9.2: (a) Top: An unexcited, Doppler laser cooled $^{40}Ca^{+}$ ion. Bottom: The same ion excited along the trap axis (horizontal) using voltage-modulation. The width of the pictures corresponds to a distance of 47 μm in the trap center. (b) Projection of the signal from the unexcited ion onto the trap axis. The curve is a fit to a Gaussian distribution. The full-width at half-maximum (FWHM) is 6.0 μm.

by projecting the signal from the ion onto the z-axis [horizontal in Fig. 9.2(a)], i.e., to sum the pixel values in each vertical column of pixels. For the unexcited ion in Fig. 9.2(a), the distribution of the projected signal is approximately Gaussian, as shown in Fig. 9.2(b), where the full-width at half-maximum (FWHM) in this example is 6.0 μm. For measuring the degree of excitation versus modulation frequency, a whole sequence of images is recorded while synchronously sweeping the modulation frequency over a frequency range of interest. By projecting the signal from the ion onto the z-axis for each image, the projected signal as a function of axial position z and modulation frequency ω_{mod} is obtained. The function describing this projected signal is called the

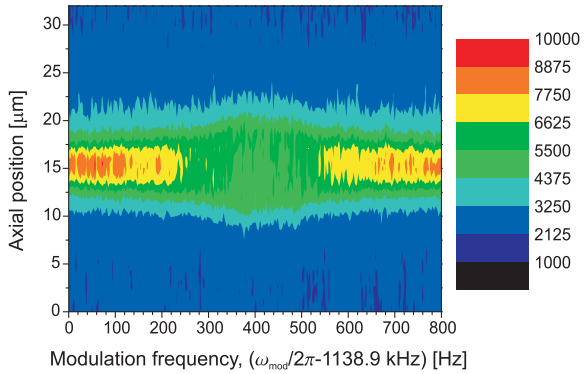

Figure 9.3: Contour plot of $S_P(\omega_{mod}, z)$ for a scan of the modulation frequency across a frequency range containing the axial trap frequency ω_z.

projected signal function and denoted by $S_P(\omega_{mod}, z)$ in the following. An example of a contour plot of $S_P(\omega_{mod}, z)$ near a resonance of the axial motion is shown in Fig. 9.3, clearly showing a resonant structure, which will be discussed in more detail below. Experimental details of recording such image sequences and obtaining the projected signal function are discussed in connection with the mass measurements described in Sec. 9.3.

Intensity-modulation

Intensity-modulation was only used for excitation of the axial motion (for reasons discussed below). One of the blue cooling laser beams propagating parallel to the trap axis was intensity-modulated using an EOM followed by a polarizer. By applying a variable voltage to the EOM, the polarization of the light passing through the EOM and hence the amount of light transmitted by the polarizer can be varied. Using a pulse-amplifier [1], a square wave intensity-modulation at frequencies ranging from DC to roughly 1.3 MHz could be generated. The low and high intensity level in the modulated signal was usually adjusted to minimum and maximum transmission, respectively, in order to obtain maximal modulation. The fraction of a modulation-period where the intensity level is high could be varied from zero to one.

Since fluorescence light from an ion only is emitted when laser cooling light is applied, the intensity-modulated cooling light effectively acts a strobed light source. If the intensity-modulated cooling beam is the main source of blue cooling light, a scan across a resonance therefore looks quite different from Fig. 9.3. Examples of this and further details follow below in the section on mass measurements.

[1] Pulse amplifier with similar properties as the Linos LAV 400 analog amplifier, amplifying the signal from a Hewlett-Packard 33120A function generator.

9.1.2 Theory: The driven damped harmonic oscillator

To give a quantitative description of the motional excitation, it is natural to consider a classical driven, damped harmonic oscillator. We consider the one dimensional case, which describes the axial motion or the radial motion along one principal axis if micromotion is neglected. Assuming the laser cooling force is linear in the ion-velocity, the equation of motion for a single ion is

$$\ddot{z} + \gamma\dot{z} + \omega_z^2 z = \frac{F_{mod}}{m}\cos(\omega_{mod}t), \tag{9.1.1}$$

where the position coordinate is denoted by z, dots denote time derivatives, m is the ion mass, F_{mod} and ω_{mod} are the amplitude and the frequency of the modulation force, respectively, and $\gamma = \alpha/m$, where α is the friction coefficient of the laser cooling force defined in Eq. (3.1.4). For the square wave intensity-modulation, it is assumed that the frequency of a single component in its Fourier-series is close to the resonance frequency ω_z such that the modulation force to a good approximation can be described by a single sinusoidally varying component. As mentioned, the validity of the above equation is limited to the regime where the damping force is linear in the ion velocity, which for the $^2S_{1/2}{}^-{}^2P_{1/2}$ transition in $^{40}Ca^+$ is the case when $\dot{z} = v_z \ll \Gamma_{1/2}/k_{1/2} = 8\,\mathrm{m/s}$ ($k_{1/2}$ is the wave-number for the transition). For a trap frequency of $\omega_z = 2\pi \times 1\,\mathrm{MHz}$, the maximum ion speed is about 60 m/s for an excursion from the equilibrium position of only $1\,\mu$m, which actually is less than a typical excitation amplitude. Having stated this warning, we will for simplicity assume that Eq. (9.1.1) is valid, or at least that it describes the motional excitation well. The steady-state solution, $z_{ion}(\omega_{mod,t})$, to Eq. (9.1.1) is [132]

$$z_{ion}(\omega_{mod}, t) = \frac{F_{mod}}{m\sqrt{(\omega_{mod}^2 - \omega_z^2)^2 + \gamma^2\omega_{mod}^2}}\cos(\omega_{mod}t + \varphi) \equiv z_0(\omega_{mod})\cos(\omega_{mod}t + \varphi), \tag{9.1.2}$$

where

$$\tan(\varphi) = \frac{\gamma\omega_{mod}}{\omega_{mod}^2 - \omega_z^2}. \tag{9.1.3}$$

The amplitude $z_0(\omega_{mod})$ is maximal at $\omega_{mod} = \sqrt{\omega_z^2 - \gamma^2/2} \equiv \omega_{max}$, which is close to ω_z, since for the $^2S_{1/2}{}^-{}^2P_{1/2}$ transition in $^{40}Ca^+$, γ is much smaller than typical trap frequencies [according to Eq. (3.1.5) $\gamma < 2\pi \times 32\,\mathrm{kHz}$]. In the trap characterization measurements presented below, ω_{max} has been used for the axial and radial trap frequencies, since it is relatively simple to determine manually, i.e., by manually scanning the modulation frequency across the resonance and estimating the modulation frequency where the amplitude is maximal. If Eq. (9.1.1) is invalid, due to a large ion velocity outside the linear regime of the laser cooling force and/or if micromotion is present, we will in practice also find a trap frequency close to the real resonance frequency [133]. Typically, ω_{max} can be determined with an uncertainty of a few hundred Hz for the axial motion and about 1 kHz for the radial motion.

9.1.3 Axial trap frequencies

As a first investigation of the trap properties, we measured the axial trap frequency ω_z versus the endcap voltage U_{end}, using ω_{max} for ω_z. A typical data set (obtained using

intensity-modulation) is plotted in Fig. 9.4. Error bars are smaller than the size of the squares in Fig. 9.4. A fit to the expected square root dependence [see Eq. (7.1.9)] with an offset of the endcap voltage included, yields $\omega_z/2\pi = 180.36(5)\,\mathrm{kHz}\sqrt{U_{end}[\mathrm{V}] - 0.251(11)}$. The front factor of about 180 kHz is in good agreement with the factor of 177 kHz expected from numerical calculations of the trapping potential [see Eq. (7.2.4)]. The small deviation of about 2% can be explained by the fact that the actual width of the center electrode pieces ($2z_0$) is about 2% smaller than the value used for $2z_0$ in the simulations and recalling that ω_z is proportional to $(2z_0)^{-1}$ [see Eq. (7.1.9)]. Note that axial trap frequencies larger than 1 MHz, which we probably need for successfully performing sideband cooling and quantum logic experiments, have been obtained.

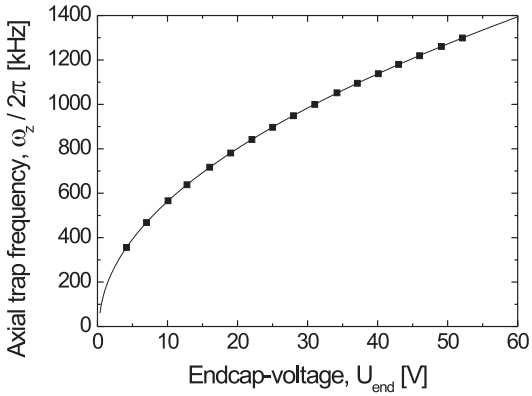

Figure 9.4: Measurement of ω_z vs. U_{end}. The solid line is a fit to the data points yielding $\omega_z/2\pi = 180.36(5)\,\mathrm{kHz}\sqrt{U_{end}[\mathrm{V}] - 0.251(11)}$.

To check whether the two excitation methods yield consistent results and hence to check indirectly if any of the methods affect the measured axial oscillation frequency, ω_z vs. U_{end} was measured using both excitation methods. At each value of U_{end}, ω_z was measured for both methods before changing to a new value of U_{end}. The results are plotted in Fig. 9.5(a), from which we observe that the two methods agree fairly well. More quantitatively, fits to the two data sets yield $\omega_z/2\pi = 180.54(5)\,\mathrm{kHz}\sqrt{U_{end}[\mathrm{V}] - 0.265(12)}$ and $\omega_z/2\pi = 180.55(4)\,\mathrm{kHz}\sqrt{U_{end}[\mathrm{V}] - 0.272(10)}$ for voltage-modulation and intensity-modulation, respectively, showing a very good agreement between the two methods. Measurements of ω_z vs. U_{end} have been performed on different days, using one or the other excitation method, different RF-supplies and RF-voltages, always with the front factor being between 180.1 kHz and 180.6 kHz. This variation is much smaller than our level of sensitivity for resolved sideband Raman transitions which, amongst other things, is set by the width of the AOM-drivers for AOM3 and AOM4 (~ 20 kHz, see Chap. 8).

According to the discussion of the axial motional modes in a harmonic potential given in Chap. 2, the center-of-mass mode oscillation frequency of two ions is expected to be equal to the axial oscillation frequency of a single ion. However, if the trap potential contains axial anharmonicities, this is not necessarily the case. To investigate this, a measurement of ω_z vs. U_{end} was performed with one and two $^{40}Ca^+$ ions in the trap. To avoid repeated emptying/loading of the trap, measurements of ω_z vs. U_{end}

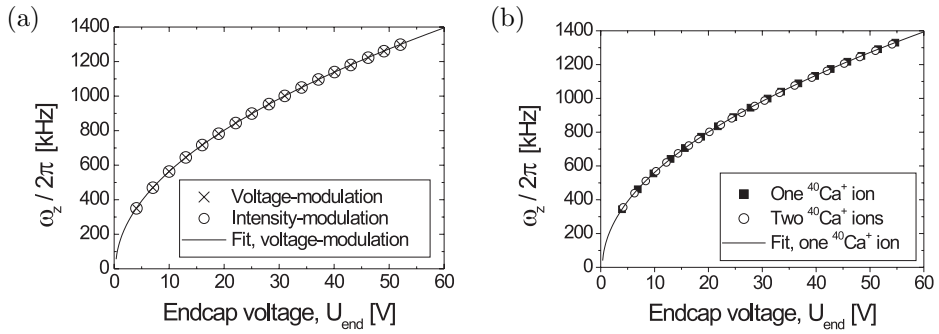

Figure 9.5: (a) Measurement of ω_z vs. U_{end} using voltage-modulation and intensity-modulation. Fits to the data yields $\omega_z/2\pi = 180.54(5)\,\mathrm{kHz}\sqrt{U_{end}[\mathrm{V}] - 0.265(12)}$ (voltage-modulation, shown as solid curve) and $\omega_z/2\pi = 180.55(4)\,\mathrm{kHz} \times \sqrt{U_{end}[\mathrm{V}] - 0.272(10)}$ (intensity-modulation, not shown). (b) ω_z vs. U_{end} for one and two $^{40}Ca^{+}$ ions. Fits to the data yields $\omega_z/2\pi = 180.41(4)\,\mathrm{kHz}\sqrt{U_{end}[\mathrm{V}] - 0.312(10)}$ (one ion, shown as solid curve) and $\omega_z/2\pi = 179.98(5)\,\mathrm{kHz}\sqrt{U_{end}[\mathrm{V}] - 0.301(11)}$ (two ions, not shown).

was done for one ion first and then for two ions. The results are shown in Fig. 9.5(b) and fits to the two data sets yield $\omega_z/2\pi = 180.41(4)\,\mathrm{kHz}\sqrt{U_{end}[\mathrm{V}] - 0.312(10)}$ and $\omega_z/2\pi = 179.98(5)\,\mathrm{kHz}\sqrt{U_{end}[\mathrm{V}] - 0.301(11)}$ for one and two ions, respectively, showing a deviation between the front-factors of a few permille. In another experiment, where the axial oscillation frequency/center-of-mass mode frequency was measured for one to eight ions (see Fig. 9.6) by loading ions while keeping the trap parameters fixed, the measured trap frequencies were 437.8(1) kHz for the single ion and 437.7(1) kHz for two to eight ions, thus showing a much better agreement than for the results in Fig. 9.5(b). The measurement with one to eight ions is expected to be the most accurate, since the trap parameters were held fixed. In any case, the frequency differences are much smaller than our resolution for resolved sideband Raman transitions.

In conclusion, the axial trap frequencies behave as we expect, they are stable and predictable to better than our sensitivity for resolved sideband Raman transitions and we have measured axial trap frequencies above 1 MHz, which is important for future sideband cooling and quantum logic experiments.

9.1.4 Radial trap frequencies

The radial trap frequencies are important for sideband cooling of the radial motion. Due to the dynamical confinement in the radial plane, the dynamics of the radial motion is more complex than for the axial motion, and the radial trap frequencies depend on several independent variable parameters, q, a and a_z, with respect to which the trap should be characterized.

The radial trap frequencies were measured by determing ω_{max} manually for the motion along the x-axis as well as the y-axis, using voltage-modulation to excite the ions. Although this method is identical to the one used for measuring axial trap frequencies, it is in practice more difficult to employ. It appears that when the modulation frequency is near-resonant with one of the radial motional modes, the oscillation am-

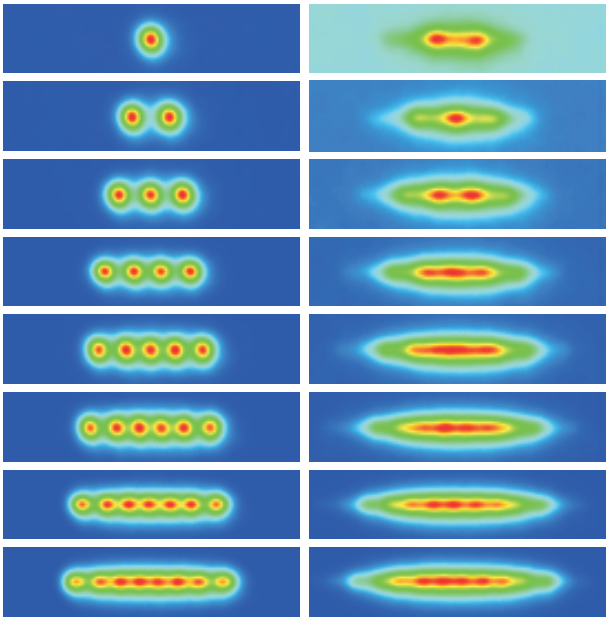

Figure 9.6: Pictures of one to eight ions on a string at identical trap parameters. Left: Unexcited ions. Right: The axial motion is excited. The width of the pictures corresponds to a distance of 75 μm. The pictures are produced from the average of the pixel values of 100 individual CCD-images recorded with 100 ms exposure time.

plitude depends very critically on the modulation force as well as the detuning and the power of the cooling lasers, meaning that the amplitude easily can become as large as shown by the rightmost picture in Fig. 9.7 or even larger than that, in which case the ion essentially is invisible on the CCD-images. The criticality of these parameters mainly has its origin in the fact that when the ion is excited, micromotion becomes very significant, which leads to large velocities and hence inefficient Doppler laser cooling. Since the motion is driven, the ion is never significantly slowed down by the Doppler cooling, which therefore remains inefficient [134]. For the same reason, excitation by intensity-modulation of the laser cooling light is problematic, which is the reason for measuring the radial trap frequencies using voltage-modulation. When the amplitude of the modulation voltage and the cooling laser parameters were adjusted such that the ions oscillation amplitude was reasonably controllable, we could as mentioned determine ω_{max} approximately within 1 kHz, which is around 1 permille of a typical radial frequency and sufficiently accurate for determining the relevant trap parameters to a good precision.

The first measurements of radial trap frequencies were performed using the self-oscillating RF-supply operated approximately at 18 MHz. The results were quite unexpected, showing indications of what we now believe is a complex non-linear dynamics. At first we suspected, however, that the self-oscillation principle of the RF-supply could be the cause of the strange results. This possibility was, however, ruled out by measurements using the fixed-frequency 18 MHz supply (supply number 1 in Chap. 8) which yielded similar results as for the self-oscillating supply. Further measurements using

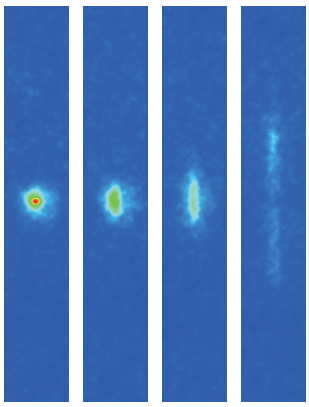

Figure 9.7: Different amplitudes of the radial motion of a single $^{40}Ca^{+}$ ion around a frequency of 2420 kHz. On the leftmost picture the ion is unexcited. The height of the pictures corresponds to a distance of 175 μm. Note: The images do not to show a variation with respect to a specific parameter, they are only meant to illustrate the different, sometimes very large, amplitudes.

supplies number 2 and 3 (see Chap. 8) at the lower RF-frequencies of 11 MHz and 5.6 MHz yielded results, which are explainable by a model which extends the theory presented in Chap. 7. The results of a series of measurements at 11MHz RF-frequency and an explanation of the results are presented in the following. Subsequently, the results at 18 MHz are described and a qualitative explanation for the observations at this RF-frequency is given.

Measurements for $\Omega_{\mathbf{RF}} = 2\pi \times 11.05\,\mathbf{MHz}$

For the measurements obtained with the trap operated near an RF-frequency of 11 MHz, we first consider measurements of the radial trap frequencies ω_x and ω_y vs. the amplitude of the RF-voltage, U_{RF}. Instead of plotting ω_x and ω_y, we plot in Fig. 9.8 the quantity $(2/\Omega_{RF})\sqrt{\omega_x^2 + \omega_y^2 + \omega_z^2}$, which according to the theory presented in Chap. 7 is equal to the q-parameter. For the model presented below, the plotted quantity is still equal to q. As seen from Fig. 9.8, q is proportional to U_{RF} as expected, however, the proportionality factor deviates significantly from the results of the numerical calculations [2]. This deviation is probably due to a difference between the actual voltage on the trap electrodes and the RF-voltage at the output of the RF-supply, where the RF-voltage is measured. Such a difference could, e.g., occur due to the influence of stray capacitances and inductances. Additionally, there is roughly a 10% uncertainty on the calibration of the monitoring signal used for measuring the RF-voltage. From the measurements discussed in the following, we shall argue that a difference between the measured RF-voltage and the actual voltage most likely is present and introduce a recalibrated value of U_{RF}, which brings the measured values of q (Fig. 9.8) and the numerically calculated values in good agreement.

[2] Using the more accurate expression $q = \sqrt{[2\sin(\pi\omega_x/\Omega_{RF})/\pi]^2 + [2\sin(\pi\omega_y/\Omega_{RF})/\pi]^2 + (\omega_z/\Omega_{RF})^2}$ does not change this conclusion [135].

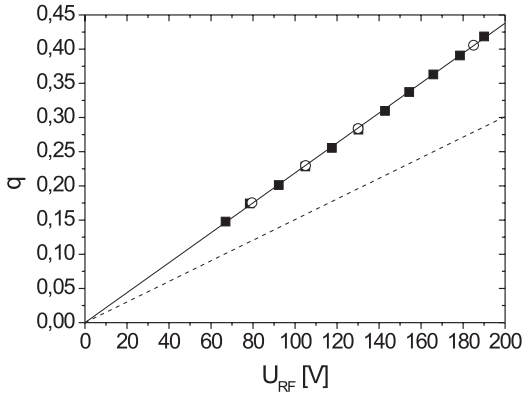

Figure 9.8: q vs. U_{RF}, obtained from measurements of ω_x and ω_y as discussed in the text (solid squares). A fit (solid line) to the data yields $q = 0.00219(1)U_{RF}$. The four data points represented as circles have been obtained from the data in Figs. 9.9 and 9.10 as discussed in the text. A constant has been subtracted from the originally recorded values of U_{RF} to correct for a voltage offset on a 'measure function' on the digital oscilloscope which was used. The dashed line represents the expectation from the numerical calculations of the trapping potential, see Eq. (7.2.7).

The measurements to be considered are measurements of the radial trap frequencies versus U_a, at four different values of U_{RF} with constant ω_z. The data are presented in Figs. 9.9 and 9.10 (the designation $\omega_\pm$ and the curves are explained below). These results were at first surprising since the radial trap frequencies were expected to be *equal* when $a - \chi a_z = 0$ [see Eqs. (7.1.13) and (7.1.14)], i.e., at a small negative value of U_a. Instead, we observe two branches of trap frequencies with a minimum frequency splitting of some tens of kHz. All data points are recorded with a modulation-voltage applied to the DC-electrodes numbered 4-5-6 in Fig. 8.3. For the upper branch, it was qualitatively observed that only a small modulation voltage was required to excite the radial motion at large positive values of U_a, while the required modulation voltage gradually became larger as U_a was decreased, until we eventually were unable to excite the radial motion. Similarly for the lower branch, a small modulation voltage was required at negative values of U_a and a large one was required at positive values of U_a. Near $U_a = 0\,\mathrm{V}$ the radial motion could be excited by an approximately equally large modulation voltage for the two branches.

With modulation on an RF-electrode (number 11 in Fig. 8.3) it was generally hard to excite the radial motion due to a strong damping of the input modulation voltage through the in-coupling circuit. It was checked that the points which are 'missing' at large positive (negative) values of U_a on the lower (upper) branch could not be detected by applying modulation on an RF-electrode.

The fact that we observe a splitting between the two branches, instead of a crossing, hints that the radial potential contains a term which couples the two radial modes. Such a term could for example be present due to misalignments of the trap electrodes or due to patch potentials.

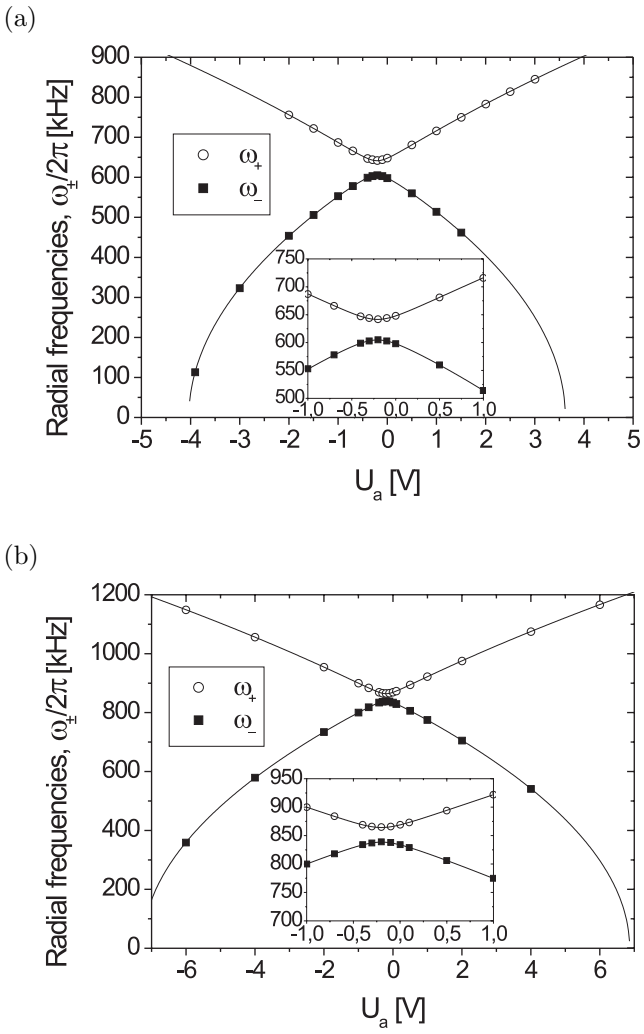

Figure 9.9: Radial trap frequencies vs. U_a at $\Omega_{RF}/2\pi = 11.05\,\mathrm{MHz}$ and $\omega_z/2\pi = 403\,\mathrm{kHz}$. (a) $U_{RF} = 79.5\,\mathrm{V}$. (b) $U_{RF} = 109\,\mathrm{V}$.

Coupling term model To describe such effects, we assume that the radial potential contains a constant term of the form

$$\Phi_c(x, y, t) = -U_c \frac{xy}{2Lr_0^2}, \tag{9.1.4}$$

which is the coupling term of the lowest possible order in x and y. U_c is a voltage describing the strength of the coupling term [3]. The model will be named the 'coupling term model' or CT-model for short. In the following, the radial oscillation frequencies and principal axes of oscillation following from the addition of the coupling term are

[3] In Ref. [136] a coupling term due to the magnetic field in a combined linear Paul trap/Penning trap was considered.

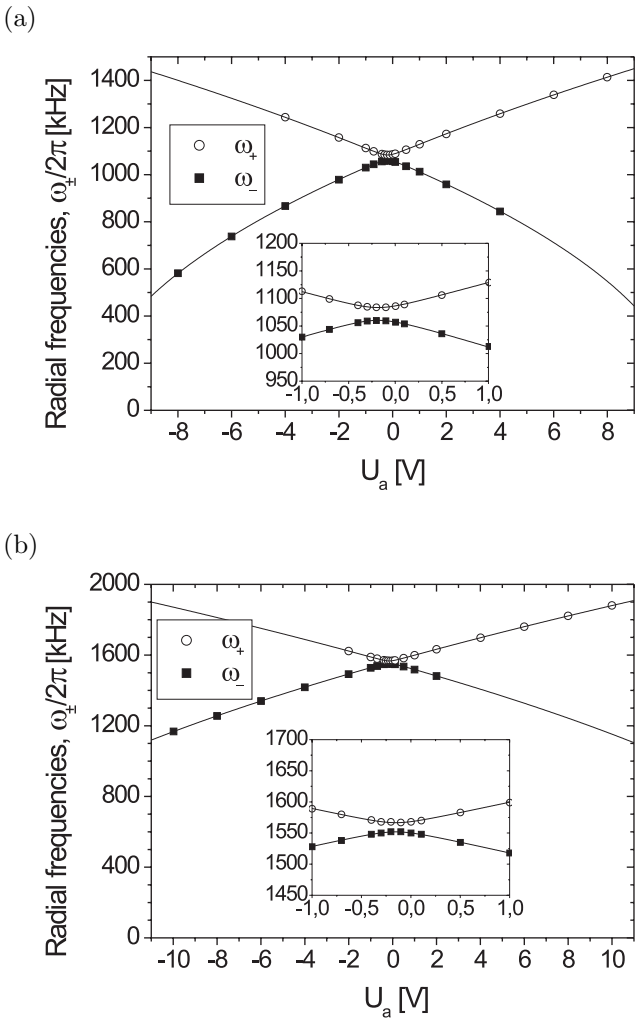

Figure 9.10: Same as Fig. 9.9, but with $U_{RF} = 130\,\mathrm{V}$ (a) and $U_{RF} = 185\,\mathrm{V}$ (b).

derived.

The coupling term immediately gives rise to a coupled set of Mathieu equations:

$$\frac{\partial^2}{\partial\tau^2}\begin{pmatrix}x\\y\end{pmatrix} = \begin{bmatrix}-a - a_z(1-\chi) + 2q\cos(2\tau) & qU_c/U_{RF}\\ qU_c/U_{RF} & a - a_z(1+\chi) - 2q\cos(2\tau)\end{bmatrix}\begin{pmatrix}x\\y\end{pmatrix}. \quad (9.1.5)$$

To solve them, we make the Ansatz that $x(\tau) = \tilde{x}(\tau)[1 - q\cos(2\tau)/2]$ and $y(\tau) = \tilde{y}(\tau)[1+q\cos(2\tau)/2]$ in analogy with Eqs. (7.1.5) and (7.1.6). Inserting these expressions in Eq. (9.1.5) and averaging over an RF-period, i.e., $\cos^2(2\tau)$ is replaced by $1/2$ and terms proportional to $\cos(2\tau)$ drop out, a set of coupled differential equations for the supposedly slowly varying functions $\tilde{x}(\tau)$ and $\tilde{y}(\tau)$ can be obtained:

$$\frac{\partial^2}{\partial\tau^2}\begin{pmatrix}\tilde{x}\\\tilde{y}\end{pmatrix} = \begin{bmatrix}-a - a_z(1-\chi) - q^2/2 & qU_c/U_{RF}\\ qU_c/U_{RF} & a - a_z(1+\chi) - q^2/2\end{bmatrix}\begin{pmatrix}\tilde{x}\\\tilde{y}\end{pmatrix}. \quad (9.1.6)$$

U_{RF} [V]	$U_{RF,recal}$[V]	q	g	χ	$U_{c,recal}$ [V]
79.5	105	0.17545(2)	0.00332(< 1)	0.257(2)	0.45
105	138	0.22982(2)	0.00336(< 1)	0.252(2)	0.43
130	172	0.28392(2)	0.00340(< 1)	0.235(3)	0.49
185	245	0.40573(2)	0.00356(< 1)	0.202(4)	0.46
Chap. 7:			0.00301	0.269	

Table 9.1: Fitting parameters and derived values from the measurements of radial frequencies vs. U_a presented in Figs. 9.9 and 9.10. The bottom line is the predictions from Chap. 7.

The eigenvalues $\lambda_\pm$ of the matrix on the r.h.s. are

$$\lambda_\pm = -\left(\frac{q^2}{2} \pm a' + a_z\right), \tag{9.1.7}$$

where

$$a' = \sqrt{(a - \chi a_z)^2 + (qU_c/U_{RF})^2}, \tag{9.1.8}$$

which corresponds to secular oscillation frequencies

$$\omega_\pm = \frac{1}{2}\sqrt{\frac{q^2}{2} \pm a' + a_z}\,\Omega_{RF} \tag{9.1.9}$$

of a harmonic motion along the principal axes given by the eigenvectors corresponding to the eigenvalues $\lambda_\pm$. These principal axes will be discussed below. When $U_c = 0$, the eigenfrequencies ω_+ and ω_- reduce to ω_x and ω_y, respectively, as given by Eqs. (7.1.13) and (7.1.14).

The curves in Figs. 9.9 and 9.10 are fits of the data points on the upper and lower branches to the expressions for ω_+ and ω_-, respectively, using q, χ, $\alpha = U_c/U_{RF}$ and $g = a/U_a = 4Q/(mLr_0^2\Omega_{RF}^2)$ as fitting parameters in a common fit to the two branches. a_z is fixed by a direct measurement of $\omega_z = 2\pi \times 403\,\mathrm{kHz}$ and $\Omega_{RF} = 2\pi \times 11.05\,\mathrm{MHz}$. Clearly, the data points are fitted very well by this model. The values found for q, χ and g are summarized in Table 9.1 together with the quantities $U_{RF,recal}$ and $U_{c,recal}$ discussed below. The fitted values of the constants g and χ are reasonably consistent at the two lowest q-values. At larger q-values, g increases and χ decreases, which probably can be ascribed to the fact that Eqs. (7.1.5) and (7.1.6), on which the Ansatz for $x(\tau)$ and $y(\tau)$ was based, only are valid for $q, a \ll 1$. At low q-values, g and χ deviate roughly by 10% and 5%, respectively, from the numerical calculations in Chap. 7. For g, the deviation can essentially be explained by the fact that the real value of r_0 is about 4% smaller than the value used in the numerical calculations, thus leading to a value of g which is about 8% larger than the numerically calculated value, since g is proportional to r_0^{-2}. χ depends on z_0 as well as r_0. The deviation of about 5% between the measured and the numerically calculated value seems reasonable, since it is comparable to the deviation found for ω_z/U_{end} (2%, z_0-dependent deviation) and the deviation found for g (10%, r_0-dependent deviation). Note also that the fitted value of χ would be affected by an offset in U_a.

The values listed for q in Table 9.1 are plotted as circles in Fig. 9.8, which shows consistency with the q vs. U_{RF} data.

Now, returning to the large discrepancy between the q vs. U_{RF} data and our expectations, we note that *by definition of* q *and* a, we have that $g = a/U_a = 2q/U_{RF}$. From the q vs. U_{RF} data (Fig. 9.8), we find $2q/U_{RF} = 0.00438$, clearly inconsistent with the values of g in Table 9.1. To remove this inconsistency, recall first that a difference between the actual voltage on the electrodes and the measured voltage, U_{RF}, is likely. Furthermore, the CT-model fits the $\omega_\pm$ vs. U_a data very well and yields values of the U_{RF}-independent parameters g and χ, which are in good agreement with the numerically calculated values, when we take the small differences between the simulated and the real trap dimensions into account. Therefore, we choose to believe in the value for g obtained from the $\omega_\pm$ vs. U_a data (we take $g = 0.00332$, obtained at the lowest value of q in Table 9.1) and introduce a recalibrated value, $U_{RF,recal} = 1.32U_{RF}$, for the RF-voltage, which fulfills $g = 2q/U_{RF,recal}$. Below, we shall check against other data if $U_{RF,recal}$ is, or could be, the actual amplitude of the RF-voltage on the trap electrodes. We note that for the driver at 5.6 MHz, we find that a correction of about 10% of the RF-voltage is needed to obtain consistency between measurements of q vs. U_{RF} and $\omega_\pm$ vs. U_a (a lower and an upper branch of radial trap frequencies are also observed in this case).

In the fits in Figs. 9.9 and 9.10, the coupling term strength U_c was fitted through the parameter $\alpha = U_c/U_{RF}$, and hence we should also use recalibrated values $U_{c,recal} = \alpha U_{RF,recal}$ for the coupling strength, which are given in the rightmost column of Table 9.1. If the coupling term is due to patch potentials, the value of $U_{c,recal}$ need not be constant, although we would expect this for the data in Figs. 9.9 and 9.10, since they were recorded successively on the same day. Indeed, the values listed in Table 9.1 are all close to a constant value of 0.45 V [4]. To see if patch potentials could be a reasonable explanation for the coupling term, it is relevant to consider the patch potential (or contact potential [118]) arising when calcium is deposited on the molybdenum electrodes, because calcium *is* probably being deposited on the electrodes as discussed in Sec. 9.2 below. The patch potential is equal to the difference in the work function of calcium and molybdenum divided by the electron charge [118], which equals ~ 1.7 V [137]. Since this is only 3-4 times larger than $U_{c,recal}$, which describes the strength of the coupling term rather than the patch potential on an electrode, patch potentials could be a reasonable explanation for the presence of the coupling term.

Further measurements and checks of the CT-model Having determined all relevant trap parameters, we can check the recalibration of the RF-voltage as well as the CT-model against additional measurements. From now on, we will use the values $g = 0.00332$ and $\chi = 0.257$ (lowest q-value in Table 9.1), the recalibrated RF-voltage $U_{RF,recal}$ and assume $U_{c,recal} = 0.45$ V constant. We consider first measurements of $\omega_\pm$ versus ω_z with $U_{RF,recal} = 172$ V ($q = gU_{RF,recal}/2 = 0.286$) and $a \approx 0$. The data are presented in Fig. 9.11. Making a common fit of the data to $\omega_\pm$ given by Eq. (9.1.9) with q as the only free parameter, the fits represented by the curves in Fig. 9.11 are obtained, yielding $q = 0.28274(1)$. This value of q agrees with the expected q-value roughly within 1%, which is more than acceptable, taking the uncertainty of g and

[4] For a data set recorded at $\Omega_{RF}/2\pi = 5.6$ MHz, two weeks earlier than those considered here, a coupling voltage of 0.55 V was found.

$U_{RF,recal}$ into account. In Fig 9.11, slight deviations between the data points and the fit are seen at small and large values of ω_z, which, however, also are present if all fitting parameters are free.

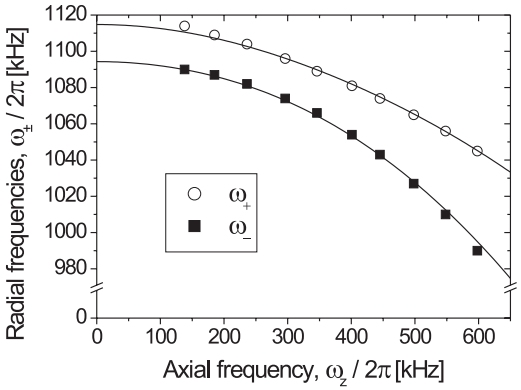

Figure 9.11: $\omega_\pm$ vs. ω_z at $\Omega_{RF}/2\pi = 11.05\,\mathrm{MHz}$, $U_{RF,recal} = 172\,\mathrm{V}$ and $a \approx 0$. A fit (solid curves) to Eq. (9.1.9) with these values and $U_{c,recal} = 0.45\,\mathrm{V}$ fixed, yields $q = 0.28274(1)$.

To provide a further check of the CT-model, we shall consider one last data set, representing measurements of the minimum splitting, $\Delta\omega$, between the two branches for different values of $U_{RF,recal}$. The splitting is found from measurements of $\omega_\pm$ at a few values of U_a near $a - \chi a_z = 0$ where the splitting is minimal, i.e., not over a large range as in Figs. 9.9 and 9.10. The measured minimum splittings are presented in Fig. 9.12 of which four of the data points are derived from the data in Figs. 9.9 and 9.10. The CT-model predicts a minimum splitting of

$$\Delta\omega = \omega_+ - \omega_-\big|_{a-\chi a_z=0} \approx \frac{qU_{c,recal}/U_{RF,recal}}{\sqrt{2q^2+4a_z}}\,\Omega_{RF}, \tag{9.1.10}$$

when $U_{c,recal}/U_{RF,recal} \ll 1$, which indeed is the case. The curve in Fig. 9.12 is plotted according to Eq. (9.1.10), with $U_{c,recal} = 0.45\,\mathrm{V}$, $q/U_{RF,recal} = g/2 = 0.00166$ and a_z derived from $\omega_z = 2\pi \times 403\,\mathrm{kHz}$, and $\Omega_{RF} = 2\pi \times 11.05\,\mathrm{MHz}$ and shows a reasonable agreement with the data, thus giving further support to the CT-model.

Finally, we shall discuss our observation that the modulation voltage required to excite the radial motion varies with U_a for the two branches. If there was no coupling term, we would have two motional modes with principal axis directed along the x-axis and the y-axis, i.e., from the trap center and towards the DC-electrodes and the RF-electrodes, respectively. For the coupling-term model, the principal axes are defined by eigenvectors $\boldsymbol{v}_\pm$ corresponding to the eigenvalues $\lambda_\pm$ of the matrix on the r.h.s. of Eq. (9.1.6). A set of eigenvectors is

$$\boldsymbol{v}_+ = \begin{pmatrix} a' + a - \chi a_z \\ -qU_c/U_{RF} \end{pmatrix} \quad \text{and} \quad \boldsymbol{v}_- = \begin{pmatrix} a' - a + \chi a_z \\ qU_c/U_{RF} \end{pmatrix}, \tag{9.1.11}$$

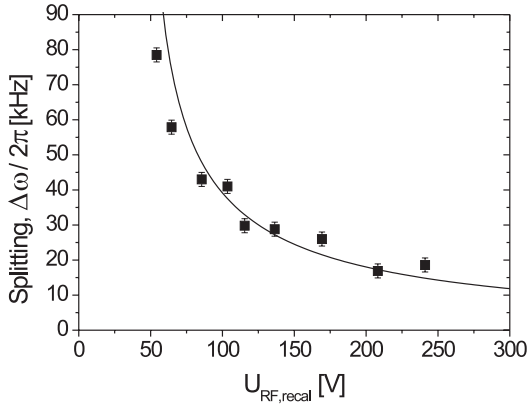

Figure 9.12: Measured minimum splitting between the upper and lower branch of radial trap frequencies. $\Omega_{RF}/2\pi = 11.05\,\mathrm{MHz}$ and $\omega_z/2\pi = 403\,\mathrm{kHz}$. The error bars represent an estimated uncertainty of 2 kHz on the measured splitting. The curve is plotted according to Eq. (9.1.10) using the parameters given in the text.

which in general are non-parallel to the x- and the y-axis. The angles from the x-axis to the eigenvectors $\boldsymbol{v}_+$ and $\boldsymbol{v}_-$ are denoted by θ_+ and θ_-, respectively, and plotted in Fig. 9.13, showing that the eigenvectors rotate as a is varied. This explains the way the required modulation voltage varies with U_a for the two branches, since at large negative a-values, where $\boldsymbol{v}_-$ ($\boldsymbol{v}_+$) is parallel (perpendicular) to the x-axis, the coupling to the corresponding radial mode is large (small) using modulation on the DC-electrodes and therefore only a small (large) modulation voltage is needed to excite the mode. As the a-parameter is increased to large positive values, the eigenvectors complete a 90° rotation, thus decreasing (increasing) the coupling between the modulation force and the motional modes corresponding to the lower (upper) branch.

In practice this is very important for our sideband-cooling scheme. Since we want to cool both radial modes, they should be coupled to at least one of the Raman beams, i.e., a principal axis should not be perpendicular to the propagation directions of both Raman beams. In our setup this will, however, be the case near $a - \chi a_z = 0$ for one of the modes and hence we need to apply a bias voltage U_a when doing sideband cooling.

Conclusion In conclusion, we have observed that the behaviour of the radial modes differs significantly from the predictions based on the theory presented in Chap. 7. By introducing a coupling term in the radial potential, which physically can be justified by patch potentials or small misalignments of the electrodes, the measurements can be explained very well. Within the CT-model, good agreement with the numerical calculations from Chap. 7 was found, although the RF-voltage had to be recalibrated by a rather large (but qualitatively explainable) amount. The deviation from the standard theory from Chap. 7 underlines the importance of this experimental characterization.

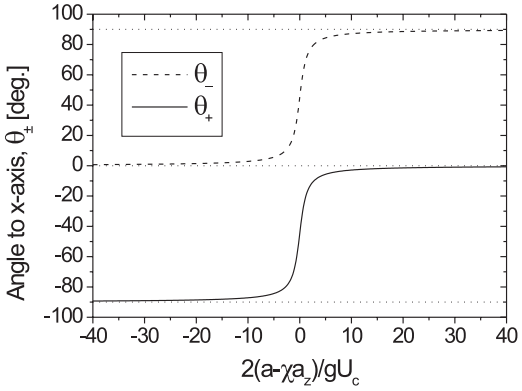

Figure 9.13: Angles between the x-axis and the principal axes given by the eigenvectors in Eq. (9.1.11). The range of the parameter $2(a - \chi a_z)/gU_c$, over which the angles are plotted, corresponds roughly to U_a being in the experimentally relevant range $[-10\,\mathrm{V}, 10\,\mathrm{V}]$. Dotted lines indicate the asymptotic limits of $0°$ and $\pm 90°$.

Measurements for $\Omega_{\mathbf{RF}} = \mathbf{2}\pi \times \mathbf{18.06\,MHz}$

Measurements of the radial frequencies with the trap being operated at $\Omega_{RF}/2\pi \approx 18\,\mathrm{MHz}$, either using the self-oscillating supply or fixed frequency supply number 1 (see Chap. 8), are performed in the same way as the measurements at 11 MHz RF-frequency. The results are, however, quite different. Instead of observing two distinct resonance frequencies for the radial motion, we observe two frequency bands within which the radial motion can be excited. To illustrate such a frequency band, we plot in Fig. 9.14 the amplitude V_0 of the input modulation voltage (see Fig. 9.1), which is found to be required to excite the radial motion when the modulation frequency is varied across the considered frequency band. The band edges are quite sharp, which therefore easily can be identified within a few kHz. At, or near, each edge a 'dip' is observed, indicated by arrows, where only a relatively small modulation voltage is required to excite the radial motion and where the oscillation amplitude of the ion easily becomes very large. Between these dips the radial motion can be excited at all frequencies using modulation voltages at a similar level, except between 1225 kHz and 1250 kHz where a somewhat larger modulation voltage is required to excite the radial motion. Such an increase in required modulation voltage near the center of a band has only been observed in cases where $a \approx 0$.

In Fig. 9.15(a), the results of a measurement of the radial frequencies vs. U_a is plotted. For each value of U_a, the points indicate the frequencies of the dips, which define the edges of the bands. These frequencies are named the edge frequencies in the following. The two branches are designated RF-electrode and DC-electrodes, respectively, meaning that for the branch designated RF-electrode (DC-electrodes), the voltage V_0 required to excite the radial motion with modulation on the RF-electrode (DC-electrodes) was smaller than for the other branch, indicating that the principal axis corresponding to the branch named RF-electrode (DC-electrodes) to some extent is aligned with the axis from the trap center to the RF-electrode (DC-electrodes), i.e.,

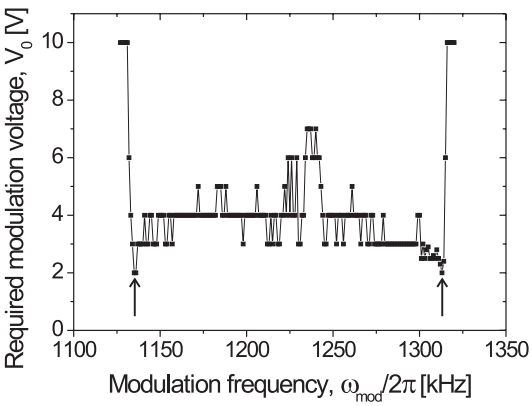

Figure 9.14: Input modulation voltage V_0 (applied to DC-electrodes 4-5-6) required to excite the radial motion within one of the frequency bands described in the text. The data points have an uncertainty of $\pm 1\,\mathrm{V}$, except those at modulation frequencies between 1300 kHz and 1315 kHz (near the rightmost arrow), which have an uncertainty of $\pm 0.1\,\mathrm{V}$. Points at $V_0 = 10\,\mathrm{V}$ means that the radial motion could not be excited with the available modulation voltage. Note the increase in required modulation voltage between 1225 kHz and 1250 kHz. The arrows indicate the 'dips' discussed in the text. The trap was operated with the self-oscillating 18 MHz RF-supply, $U_{RF} = 260\,\mathrm{V}$, $\Omega_{RF}/2\pi = 18.06\,\mathrm{MHz}$, $\omega_z/2\pi = 457\,\mathrm{kHz}$ and $a \approx 0$. Modulation on an RF-electrode yields a frequency band between 1100 kHz and 1375 kHz, also with an increase in required modulation voltage roughly between 1225 kHz and 1250 kHz.

the y-axis (x-axis). Near $U_a = 0\,\mathrm{V}$, the excitation strength was roughly independent of which set of electrodes the modulation was applied to, and here designations are given to fit the overall behaviour of the two branches.

The explanation given in the following for the variation of the frequency bands with U_a, as well as with other parameters, falls in two parts. First, we consider only the center frequencies of the bands, i.e., the average values of the edge frequencies for each band, and show that they can be described in terms of the CT-model, which indicates that the center frequencies are the 'true' radial trap frequencies. Second, a possible explanation for the observation of frequency bands centered around a 'true' radial trap frequency will be given.

Center frequencies The center frequencies of the bands in Fig. 9.15(a) (crosses) was fitted to the expressions for $\omega_\pm$ given in Eq. (9.1.9), with the lower (upper) branch in the CT-model describing the center frequencies of the DC(RF)-electrode branch for negative U_a and the RF(DC)-electrode branch for positive U_a. When $U_a \approx 0\,\mathrm{V}$ it is hard to tell if the data points belong to the upper or lower branch and therefore the points near $a = 0$ indicated by arrows in Fig. 9.15(a) and the neighbouring points were not included in the fit. g, which determines the main variation of the radial frequencies with U_a, was kept fixed to $g = 0.00332(11.05/18.06)^2 = 0.00124$, i.e., the

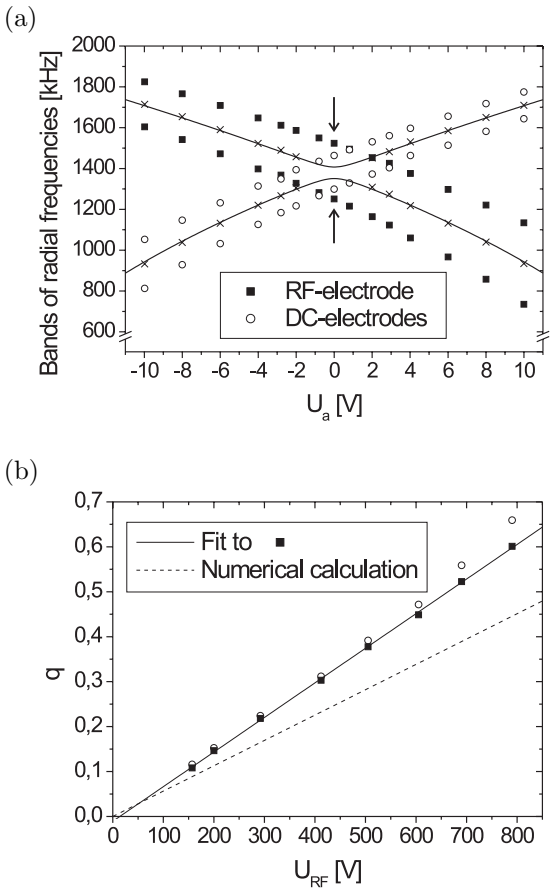

Figure 9.15: (a) Radial frequencies vs. U_a measured at $U_{RF} = 292\,\mathrm{V}$, $\Omega_{RF}/2\pi = 18.06\,\mathrm{MHz}$ and $\omega_z/2\pi = 446\,\mathrm{kHz}$. The designation RF(DC)-electrode(s) is explained in the text. The center of the bands (crosses) are fitted using Eq. (9.1.9) as explained in the text. (b) q vs. U_{RF} measured at $\Omega_{RF}/2\pi = 18.06\,\mathrm{MHz}$. Circles are plotted according to the coupling-term model. Solid squares are plotted according to Eq. (9.1.12) and fitted to a straight line (solid line). The dashed line represents the expectation from Eq. (7.2.7).

value derived from the measurements near 11 MHz RF-frequency, scaled by Ω_{RF}^{-2}. ω_z and Ω_{RF} are also fixed, but q, χ and α are free parameters in the fit. The considered center frequencies are clearly well fitted by this model. The fit yields a value of $q = 0.2216(2)$ (at $U_{RF} = 292\,\mathrm{V}$), which is consistent with measurements of q vs. U_{RF} presented in Fig. 9.15(b), which will be discussed below.

Looking very carefully at Fig. 9.15(a), it can be noted that for the four data points between the arrows, the average of the lower edge frequency of the RF-electrode band and the upper edge frequency of the DC-electrode band falls onto the lower branch of the fitted curves. Likewise, the average of the upper edge frequency of the RF-electrode band and the lower edge frequency of the DC-electrode band falls onto the upper branch.

This mixing of the DC- and the RF-electrode band could indicate that each of these frequency pairs comprises the edge frequencies of a frequency band, where the principal axis of the corresponding radial motional mode has a component along the x-axis as well as the y-axis. This would be in accordance with the rotation of the principal axes predicted by the CT-model [see Eq. (9.1.11) and Fig. 9.13].

Carrying this pairing over to the data for which the DC-electrode band is shown in Fig. 9.14 [5], we find that the lower and upper branch frequencies are approximately 1205 kHz and 1255 kHz, respectively. The small range of frequencies near the center of the band, where an increase in the required modulation voltage is observed, is roughly the same for the DC-electrode band and the RF-electrode band and falls in between the lower and the upper branch frequencies. We have not systematically recorded data as in Fig. 9.14, but on two other occasions [6] we have found a similar range, where the required modulation voltage increases near the center of both the DC-electrode band and the RF-electrode band, and on both occasions the range fell in between the lower and the upper branch. A partial explanation for observing such ranges could be the following: According to the CT-model, the principal axes are at an angle of about 45° with respect to the x- and y-axis near $a - \chi a_z = 0$. If a modulation voltage acting along the x-axis is applied, both radial motional modes can be excited. When the modulation frequency ω_{mod} fulfills $\omega_- < \omega_{mod} < \omega_+$, the modulation force is out of phase with the mode at frequency ω_- and in phase with the mode at frequency ω_+, which means that the resulting motion is perpendicular to the x-axis. In this situation it is apparently difficult to excite the motion, even though the principal axes of motion are non-perpendicular to the x-axis. Similar considerations hold for a modulation force along the y-axis.

Measurements of the radial trap frequencies versus U_{RF} yields two bands at each value of U_{RF} from which the q-parameter can be extracted as shown in Fig. 9.15(b) and explained in the following. Since the measurements were performed near $a = 0$, it is once again hard to determine if the bands belong to the upper or lower branch of the CT-model. Instead we assume that the average of the center frequencies of the two bands (denoted $\overline{\omega}$) is equal to $(\omega_+ + \omega_-)/2$, such that we according to the CT-model have $q = (2/\Omega_{RF})\sqrt{2\overline{\omega}^2 + \omega_z^2}$, when $a'/q^2 \ll 1$. Using this relation, q has been plotted versus U_{RF} in Fig. 9.15(b) (circles). For large q, where the CT-model is expected to be invalid, the points do not fall onto a straight line. This can be remedied by using the more accurate expression [135]

$$\begin{aligned} q =& \sqrt{[2\sin(\pi\omega_+/\Omega_{RF})/\pi]^2 + [2\sin(\pi\omega_-/\Omega_{RF})/\pi]^2 + (\omega_z/\Omega_{RF})^2} \\ \approx& \sqrt{2[2\sin(\pi\overline{\omega}/\Omega_{RF})/\pi]^2 + (\omega_z/\Omega_{RF})^2}, \end{aligned} \tag{9.1.12}$$

for which the corresponding points are plotted as solid squares in Fig. 9.15(b), showing that they fall nicely onto a straight line. The dashed line in Fig. 9.15(b) illustrates our expectation from the numerical calculations, which once again deviates significantly from the measured q-values, probably due to the same reasons as discussed above for the measurements near 11 MHz RF-frequency.

Finally, for measurements of the radial trap frequencies vs. ω_z, it is also found that the center frequency of the RF- and DC-electrode bands are well described by the

[5] Note: The data in Fig. 9.14 and Fig. 9.15(a) are not directly comparable, since they are recorded at different RF- and endcap voltages.

[6] Where the trap actually was operated at $\Omega_{RF}/2\pi = 14.56$ MHz and $\Omega_{RF}/2\pi = 19.47$ MHz.

CT-model.

Thus, concerning the center frequencies of the bands, we can conclude that they are well described by the CT-model. A possible explanation for the observation of frequency bands, instead of distinct resonance frequencies is given in the following.

Frequency bands It is well-known that under certain circumstances the dynamics of single ions (or several ions) in Paul traps cannot be described as simply as we did in Chap. 7 or with the CT-model. For example, non-linear resonances and instabilities in anharmonic traps [138, 139] or quadrupole mass-filters [140] have been studied, and it is known that the presence of a laser cooling force can play an important role for the stability/instability of a trapped ion [135, 141, 142]. The latter takes us back to Eq. (9.1.1) for the driven damped harmonic oscillator, where we assumed that the damping force was linear in the ion velocity which, however, not necessarily is the case when we consider large oscillation amplitudes and/or take micromotion into account. In continuation of the present experiments, a theoretical study has been undertaken by Jens Lykke Sørensen [133], who models the radial motion of a single ion by a driven harmonic oscillator, taking micromotion and the full velocity dependence of the Doppler laser cooling force for a two-level ion into account. Under certain conditions it is predicted that the ions motion is bi-stable. For modulation frequencies near the harmonic oscillator resonance frequency and when the modulation force is below a certain level, there are three trajectories of motion which can be characterized as follows. #1: A small-amplitude trajectory, which roughly follows the predictions for a linear damping force. #2: A large-amplitude trajectory, which exists when the modulation frequency is within a certain frequency range centered around the resonance frequency. #3: A trajectory, where the amplitude approaches infinity when the modulation frequency approaches the resonance frequency, i.e., the ion will be lost from the trap. Trajectory #2 seems to explain our observations that the ion can be excited within a frequency band without being lost from the trap and that the center of the band could correspond to a normal radial trap frequency. At the boundaries of the predicted band, a continuous transition from trajectory #2 to trajectory number #3 can take place, which explains the observed dips in required modulation voltage. At frequencies well within the predicted band, only a discontinuous transition to trajectory #3 can take place, which (most of the times!) are avoided in the experiment by adjusting the modulation voltage. The width of the predicted bands is at most around 50 kHz, while the experimentally observed bands typically are hundreds of kHz wide, as it can be seen from Figs. 9.14 and 9.15(a). Although this discrepancy is yet to be resolved, a large part of our observations seems to be explained, at least qualitatively, when the velocity-dependence of the Doppler laser cooling force as well as micromotion is taken into account. The model is still being developed and we shall therefore not go into further details here. The above-mentioned non-linearities and instabilities in anharmonic trap potentials or the intricate internal dynamics of a three-level ion [141] may also have a role to play for a full theoretical explanation.

Further experimental studies are needed to understand why we observe frequency bands when the trap is operated at 18 MHz RF-frequency and not at 11 MHz RF-frequency. So far, frequency bands have been observed with the trap being operated at RF-frequencies of 14.56 MHz and 19.47 MHz. A reasonable explanation for observing frequency bands at high RF-frequencies ($\geq$ 14.56 MHz) and not at lower RF-frequencies ($\leq$ 11.05 MHz) could be the larger ion velocities which are obtained at larger RF-

frequencies due to micromotion, since by taking the full velocity dependence of the Doppler laser cooling force (which is relevant for large velocities) and micromotion into account, trajectories of motion are predicted, which can be interpreted as giving rise to the observed frequency bands.

If this explanation is correct, the frequency bands appear only as an effect of motionally exciting the ions. In this case, the good understanding of the measurements at 11 MHz shows that the properties of the trap are well understood.

9.2 Micromotion

To conclude the work on characterization of the trap, we shall in this section briefly discuss micromotion, the problems it implies and how to observe and reduce micromotion. For a more detailed discussion, we refer to Ref. [134].

When the RF-field used for confinement in the radial plane has a non-zero amplitude at the position of an ion, micromotion at the RF-frequency Ω_{RF} will be superposed on the ions secular motion. For a perfectly symmetric linear Paul trap, there is no RF-field on the trap axis, and hence for an ion-string with equilibrium position on the trap axis, micromotion only occurs as a result of the secular motion [see Eqs. (7.1.5) and (7.1.6)], which for well-localized laser-cooled ions has a small amplitude. In reality there are, however, other reasons for micromotion to be present. For example: (i) If the trap is (slightly) asymmetric there need not be a straight line with zero RF-field and there can even be micromotion along the trap axis. (ii) Due to unwanted DC electric fields, the equilibrium position of an ion-string is not necessarily on a line with zero RF-field (if such a line exists at all). (iii) A phase difference between the RF-voltages on two diagonally opposite electrodes will lead to micromotion [134]. A phase difference can, e.g., occur if the wires from the RF-supply to the electrodes are of different length [7] or if the impedance of the electrodes is different.

Micromotion due to (iii) can to a small extent be compensated using the adjustable capacitors (see Fig. 8.2). The effects of (i) and (ii) can at least partly be compensated by adjusting the equilibrium position of the ions to a position where the amplitude of the RF-field is minimal. This is normally done by adjusting the DC adjustment-voltages (controls #5 and #6 in Table 8.1) such that the equilibrium position of the ions does not change when the strength of the radially confining potential is varied. Unfortunately, this adjustment cannot be done once and for all; readjustments are needed from time to time because of changing patch potentials.

Since patch potentials also were used as a common explanation for many effects in the previous section, it should be pointed out that we believe we do see effects of changing patch potentials. The patch potentials are due to calcium being deposited on the electrodes, and changes can be observed as a change in the equilibrium position of the ions, when the oven has been on and the oven shutter open for a while (such electrode contamination was also reported in Refs. [105, 143]). Mostly, it is just a minor change, but a few times where the oven shutter by mistake was left open for an extended period of time, it was subsequently hard to trap ions. By leaving the trap alone for

[7] For the present trap, the difference is below 1 permille of the RF-wavelength for RF-frequencies up to 20 MHz, and hence micromotion due to a phase difference is reduced by a similar factor (see Ref. [134]).

1/2–1 hour (a shorter period may be sufficient), ions could normally be trapped again, perhaps due to some redistribution of the patch potentials.

The main unwanted effect of micromotion is a modification of the absorption spectrum of an ion [8]. In Chap. 2, we considered the absorption spectrum for an ion at rest at the position $\boldsymbol{r}$ interacting with a travelling-wave electric field. In the presence of micromotion with amplitude A, in a direction given by a unit vector $\hat{\boldsymbol{r}}_m$ in the radial plane, $\boldsymbol{r}$ should be replaced by $\boldsymbol{r} + A\cos(\Omega_{RF}t)\hat{\boldsymbol{r}}_m$ in Eq. (2.1.4), assuming for simplicity that the micromotion is in phase with the RF-field. In this case the electric field becomes [134]

$$\boldsymbol{E}(\boldsymbol{r},t) = E_0\hat{\boldsymbol{\epsilon}} \sum_{n=-\infty}^{\infty} J_n(A\boldsymbol{k}\cdot\hat{\boldsymbol{r}}_m)\cos[\boldsymbol{k}\cdot\boldsymbol{r} - (\omega_L - n\Omega_{RF})t + \phi + n\pi/2], \qquad (9.2.1)$$

where J_n is the Bessel-function of n'th order. This means that the ion 'sees' a laser with carrier frequency ω_L and sidebands at integer multiples of the RF-frequency above and below the carrier frequency. For Doppler cooling in $^{40}Ca^+$, where $\Omega_{RF} \lesssim \Gamma_{1/2}$ in our case, this leads to a broadening of the $^2S_{1/2}$–$^2P_{1/2}$ transition (with some structure) and a decrease of the carrier strength due to the factor $J_0(A\boldsymbol{k}\cdot\hat{\boldsymbol{r}}_m)$. For the Raman transition, where Ω_{RF} is larger than the effective linewidth of the transition, distinguishable sidebands will occur [134].

For Doppler cooling, micromotion gives rise to a modulation of the ions velocity and hence of the Doppler cooling force [see Eq. (3.1.2)] as well as the amount of fluorescence light emitted by the ion. Micromotion can be detected by measuring the variation of the fluorescence level with the RF-phase, which can be accomplished by collecting fluorescence light only in time windows of width $\Delta t \ll 1/\Omega_{RF}$ (by gating the image-intensifier), phase-locked to the RF-voltage, and varying the relative phase between the time windows and the RF-voltage. More details are given below, where essentially the same technique was used for the mass measurements.

We have done some very preliminary experiments looking for axial micromotion, which was observed and reduced to some extent. After reduction, the fluorescence signal was characterized by a constant level, overlayed with a sinusoidal variation at the RF-frequency, with amplitude $\lesssim 3\%$ of the constant fluorescence level, which translates into a maximal Doppler-shift of $\lesssim 0.6\,\mathrm{MHz}$ ($\lesssim 3\%$ of $\Gamma_{1/2}/2\pi$) [134]. This may not be critical for STIRAP, but in order to demonstrate sideband cooling it is probably necessary to reduce axial as well as radial micromotion below this level.

9.3 Ion mass measurements

The work on mass measurements presented in this section is a spin-off from the trap characterization measurements. It is motivated by an ongoing research project, which aims at studying laser cooling of the rotational degrees of freedom of sympathetically cooled molecular ions [144] as well as studying chemical reactions with laser cooled or sympathetically cooled ions [145][II, V]. For these studies, identification of a sympathetically cooled ion by a precise and non-destructive mass measurement will be a valuable tool. To demonstrate the usefulness of this tool, there are two natural goals, which require different levels of precision to achieve. The first goal is to discriminate

[8] The effects of micromotion can also be *exploited* for entanglement of two trapped ions [16].

between ions with different atomic masses, which only requires a precision better than one percent or so. The second goal is to discriminate between ions which have the same number of nucleons, but differ in mass due to a difference in nuclear binding energy, e.g., $^{25}Mg^+$ and $^{24}MgH^+$, for which the relative mass difference is $2.8 \cdot 10^{-4}$ [146]. MgH^+ is relevant for laser cooling of the rotational degrees of freedom of molecules [144].

9.3.1 Theory

In Chap. 7 we saw that the axial trap frequency of an ion is proportional to the square root of its charge-to-mass ratio [see Eq. (7.1.9)]. Thus, precise measurements of the axial trap frequencies for two different ion species, trapped at identical trap parameters, immediately yields a precise relative measurement of their charge-to-mass ratio or, specifying to singly-charged ions in the following, of their relative mass. The technique for measuring axial trap frequencies, which was demonstrated above, requires a laser-cooled ion species. Since only a few ion species can be Doppler laser-cooled as simply as, e.g., $^{40}Ca^+$, it seems at first sight not to be a very general method. However, by using one laser-cooled ion and one other ion, which is sympathetically cooled by the laser-cooled ion [94], the method can be applied to all ions, including molecular ions, which can be trapped simultaneously with the laser-cooled ion [145]. The pictures in Fig. 9.16 show two $^{40}Ca^+$ ions and a single $^{40}Ca^+$ ion trapped together with a sympathetically cooled ion. Although the sympathetically cooled ion cannot be seen in the bottom picture, since it is not Doppler laser-cooled, it is nevertheless certain that there are two and only two singly-charged ions in the trap, since otherwise the equilibrium position of the $^{40}Ca^+$ ion would have been different from the equilibrium positions of the two $^{40}Ca^+$ ions in the upper picture. The mass of the sympathetically cooled ion can be deduced from a measurement of the mass-dependent trap oscillation frequencies for both two-ion strings, with the measured trap frequency for the $^{40}Ca^+$–$^{40}Ca^+$ two-ion string serving as a reference.

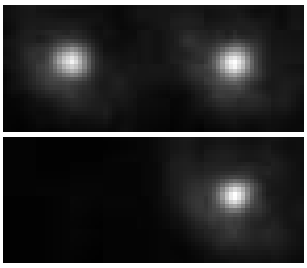

Figure 9.16: Top: Two Doppler laser-cooled $^{40}Ca^+$ ions. Bottom: A single Doppler laser-cooled $^{40}Ca^+$ ion trapped together with a sympathetically cooled ion ($^{42}Ca^+$).

For two identical ions, we know from Sec. 2.2.2 that there are two axial eigenmodes at oscillation frequencies ω_z and $\sqrt{3}\omega_z$, respectively, where ω_z is the oscillation frequency for a single ion. The mode frequencies for two ions with a different mass are derived in the following, where we consider the case of one laser-cooled and one sympathetically cooled ion, and therefore take into account that the laser-cooled ion can be subject to a net light-pressure force. We consider two singly-charged ions, Ion 1 and Ion 2, with masses m_1 and m_2 and position coordinates z_1 and z_2 ($z_2 > 0 > z_1$), respectively,

confined in the axial harmonic potential of a linear Paul trap. Ion 1 is assumed to be subject to a constant light pressure force, F_{light}, which is positive for a laser beam propagating in the direction of positive z. The position-dependent part of the potential energy is

$$U(z_1, z_2) = \frac{1}{2}m_1\omega_1^2 z_1^2 + \frac{1}{2}m_2\omega_2^2 z_2^2 + \frac{e^2}{4\pi\varepsilon_0(z_2 - z_1)} - F_{light}z_1, \tag{9.3.1}$$

where ω_i $(i = 1, 2)$ is the trap frequency for a single trapped ion with mass m_i. Since the axial trap potential is independent of the ion masses, we have that

$$\frac{\omega_1^2}{\omega_2^2} = \frac{m_2}{m_1} \equiv \mu. \tag{9.3.2}$$

The presence of the light-force gives rise to a change in equilibrium positions as compared to the situation in Sec. 2.2.2. Writing the equilibrium distance as $\Delta z + \delta z$, where

$$\Delta z \equiv \left(\frac{e^2}{2\pi\varepsilon_0 m_1\omega_1^2}\right)^{1/3} \tag{9.3.3}$$

is the equilibrium distance in the absence of the light-force, and assuming $\delta z/\Delta z \ll 1$, we find to first order in $\delta z/\Delta z$ that the new equilibrium positions are

$$z_{1,eq} = -\Delta z/2 - 2\delta z \quad \text{and} \quad z_{2,eq} = \Delta z/2 - \delta z, \tag{9.3.4}$$

where

$$\delta z = -\frac{F_{light}}{3m_1\omega_1^2}. \tag{9.3.5}$$

In the following we will continue keeping only terms of first order in $\delta z/\Delta z$ and justify below that $\delta z/\Delta z \ll 1$. Following Refs. [25, 91], we write $z_i = z_{i,eq} + q_i$ $(i = 1, 2)$, where q_i is the deviation from the equilibrium position $z_{i,eq}$. For sufficiently small q_i, the Lagrangian for the coupled motion of the ions can be written as

$$L = \frac{1}{2}m_1\dot{q}_1^2 + \frac{1}{2}m_2\dot{q}_2^2 - \frac{1}{2}m_1\omega_1^2\sum_{m,n=1}^{2} q_m q_n A_{mn}, \tag{9.3.6}$$

where

$$A_{mn} = \frac{1}{m_1\omega_1^2}\frac{\partial^2 U}{\partial z_m \partial z_n}(z_{1,eq}, z_{2,eq}). \tag{9.3.7}$$

The coefficients A_{mn} are (in matrix form)

$$\underline{\underline{A}} = \begin{bmatrix} 2 - 3\delta z/\Delta z & -(1 - 3\delta z/\Delta z) \\ -(1 - 3\delta z/\Delta z) & (2 - 3\delta z/\Delta z) \end{bmatrix}. \tag{9.3.8}$$

Introducing normalized coordinates $\tilde{q}_1 = q_1$ and $\tilde{q}_2 = q_2/\sqrt{\mu}$, the Lagrangian can be rewritten as follows

$$L = \frac{m_1}{2}\left(\dot{\tilde{q}}_1^2 + \dot{\tilde{q}}_2^2 - \omega_1^2\sum_{m,n=1}^{2}\tilde{q}_m\tilde{q}_n\tilde{A}_{mn}\right), \tag{9.3.9}$$

where

$$\underline{\underline{\tilde{A}}} = \begin{bmatrix} 2 - 3\delta z/\Delta z & -(1 - 3\delta z/\Delta z)/\sqrt{\mu} \\ -(1 - 3\delta z/\Delta z)/\sqrt{\mu} & (2 - 3\delta z/\Delta z)/\mu \end{bmatrix}. \tag{9.3.10}$$

The eigenvalues $\tilde{\lambda}_\pm$ of $\underline{\underline{\tilde{A}}}$ are

$$\begin{aligned} \tilde{\lambda}_\pm &= \left(1 + \frac{1}{\mu}\right)\left(1 - \frac{3\delta z}{2\Delta z}\right) \pm \sqrt{1 - \frac{1}{\mu} + \frac{1}{\mu^2} - 3\frac{\delta z}{\Delta z}(1 + \frac{1}{\mu^2})} \\ &\approx 1 + \frac{1}{\mu} \pm \sqrt{1 - \frac{1}{\mu} + \frac{1}{\mu^2}} - \frac{3}{2}\frac{\delta z}{\Delta z}\left(1 + \frac{1}{\mu} \pm \frac{1 + 1/\mu^2}{\sqrt{1 - 1/\mu + 1/\mu^2}}\right), \end{aligned} \tag{9.3.11}$$

which yields the new motional mode frequencies $\omega_{COM} = \sqrt{\tilde{\lambda}_-}\omega_1$ and $\omega_{br} = \sqrt{\tilde{\lambda}_+}\omega_1$, where ω_{COM} and ω_{br} are equal to the center-of-mass mode frequency ω_z and the breathing mode frequency $\sqrt{3}\omega_z$, respectively, in the limit where $\delta z = 0$ and $\mu = 1$.

The δz-dependent shift of the mode frequencies, which is due to the light-force, is in the following called the light-force shift. To estimate its magnitude, we note that for the ${}^2S_{1/2}{}^-{}^2P_{1/2}$ transition in ${}^{40}Ca^+$, the light-force is at most $\hbar k_{1/2}\Gamma_{1/2}/2$ (see Sec. 3.1), which implies that

$$\frac{\delta z}{\Delta z} < \hbar k_{1/2}\Gamma_{1/2}\left(\frac{\pi\epsilon_0}{108e^2m_1^2\omega_1^4}\right)^{1/3} = 5.3 \times 10^{-2} \tag{9.3.12}$$

for $m_1 = 40\,\mathrm{AMU}$ and $\omega_1/2\pi = 100\,\mathrm{kHz}$. This justifies the assumption $\delta z/\Delta z \ll 1$. In practice $\delta z/\Delta z$ can be made smaller than this limit by driving the ${}^2S_{1/2}{}^-{}^2P_{1/2}$ transition below saturation and by using two counter-propagating beams to reduce the net light-force.

The relative mass obtained from the light-force independent term in Eq. (9.3.11) is

$$\mu = \frac{1 - 2(\tilde{\lambda}_\pm - 1)}{1 - (\tilde{\lambda}_\pm - 1)^2}. \tag{9.3.13}$$

For the center-of-mass mode [inserting $\tilde{\lambda}_-$ in Eq. (9.3.13)], it is a very good approximation to neglect the light-force shift, since the light-force dependent term in Eq. (9.3.11) is proportional to

$$1 + \frac{1}{\mu} - \frac{1 + 1/\mu^2}{\sqrt{1 - 1/\mu + 1/\mu^2}}, \tag{9.3.14}$$

which, e.g., for $\mu = 1.1$ equals 2.1×10^{-3}. Thus, for mass measurements which require a precision on the percent level (relevant for discriminating between ions with different atomic masses), we can, at least for the center-of-mass mode, safely neglect the light-force shift. However, if the mode frequency, ω_{COM}, is determined as the modulation frequency where the amplitude of the excited motion is maximal (ω_{max}), the measured frequency will deviate from ω_{COM} by an amount which depends on the laser cooling force through γ. This γ-dependent shift of the mode frequency is normally negligible on the 10^{-2} level and hence the relatively simple technique used for the trap characterization

measurements, where ω_{max} is determined manually, is sufficient to achieve the goal of discriminating between ions with a different atomic mass.

To achieve the goal of discriminating between ions with the same nucleon number but with different nuclear binding energies, which requires measuring relative mass differences at about the 10^{-4} level, we have to avoid the γ-dependent shift and in general also to take the light-force shift into account. Noting that the sign of the light-force shift depends on the sign of F_{light} or, equivalently, the position of the sympathetically cooled ion with respect to the laser cooled ion (left or right in Fig. 9.16, bottom), the light-force shift can be cancelled to first order by taking the average of two mode frequencies measured for the two possible relative positions of the two ions (if the net light-force is constant). To account for the γ-dependent shift, one might consider correcting ω_{max}, which, however, is hard to do precisely. Instead, the γ-dependent shift of the measured mode-frequency can be avoided by measuring the relative phase φ between the modulation force and the ion motion versus modulation frequency. A technique for doing this is described for one ion in the following and generalized to two ions below.

By rewriting the solution in Eq. (9.1.2) as

$$z_0(\omega_{mod})\cos(\omega_{mod}t+\varphi) = z_0(\omega_{mod})[\cos(\omega_{mod}t)\cos(\varphi) - \sin(\omega_{mod}t)\sin(\varphi)], \quad (9.3.15)$$

it is clear that the motion of a single ion is composed of a component in phase with the driving force (the cosine term) and an out-of-phase component (the sine term). The amplitudes $z_0(\omega_{mod})\cos(\varphi)$ and $z_0(\omega_{mod})\sin(\varphi)$ of the two components are plotted in Fig. 9.17 for typical values of $\omega_z/2\pi = 100\,\text{kHz}$ and $\gamma/2\pi = 200\,\text{Hz}$, using Eq. (9.1.2) and [132]

$$\cos(\varphi) = \frac{\omega_z^2 - \omega_{mod}^2}{\sqrt{(\omega_{mod}^2 - \omega_z^2)^2 + \gamma^2\omega_{mod}^2}} \quad (9.3.16)$$

and

$$\sin(\varphi) = -\frac{\gamma\omega_{mod}}{\sqrt{(\omega_{mod}^2 - \omega_z^2)^2 + \gamma^2\omega_{mod}^2}}. \quad (9.3.17)$$

Since the amplitude of the in-phase component is zero at $\omega_{mod} = \omega_z$, a measurement of this component would enable a determination of ω_z, which is independent of γ, and in addition relatively precise since the zero-crossing is sharp (for small γ).

To see how the in-phase component can be measured, consider the projected signal function $S_P(\omega_{mod}, z)$ for a single ion obtained from a single CCD-image recorded during an exposure time T_{exp} at a constant modulation frequency ω_{mod}. In a small time interval dt around time t, the projected collected signal dS_P is

$$dS_P(\omega_{mod}, z, t) = dtS'_P f[z_{ion}(\omega_{mod}, t)], \quad (9.3.18)$$

where S'_P is a constant and the function f describes the shape of the projected signal from an ion at rest at the position $z_{ion}(\omega_{mod}, t)$. We will assume a Gaussian signal distribution having a characteristic width σ [$\sigma = FWHM/(2\sqrt{2\ln 2}) = 2.5\,\mu$m in Fig. 9.2(b)], i.e.,

$$f[z_{ion}(\omega_{mod}, t)] = e^{-[z - z_{ion}(\omega_{mod}, t)]^2/2\sigma^2}. \quad (9.3.19)$$

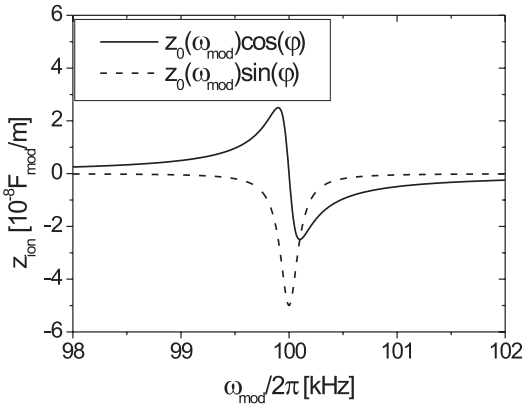

Figure 9.17: The amplitudes $z_0(\omega_{mod})\cos(\varphi)$ and $z_0(\omega_{mod})\sin(\varphi)$ of the two components in Eq. (9.3.15). $\omega_z/2\pi = 100\,\text{kHz}$ and $\gamma/2\pi = 200\,\text{Hz}$.

Note that f is periodic with the period of the modulation force, $2\pi/\omega_{mod}$, which we will assume to be much smaller than T_{exp}. Now, assume that fluorescence light only reaches the CCD-chip in time windows of width Δt, centered around all times t within the exposure time where $\omega_{mod}t = n\cdot 2\pi + \varphi_0$, where n is an integer and φ_0 is a constant phase. In this case, the integrated signal for a single frame is

$$S_P(\omega_{mod}, z) = S'_P \int_0^{T_{exp}} dt f[z_{ion}(\omega_{mod}, t)] \times \tag{9.3.20}$$
$$\sum_{n=1}^{N} \Theta[t - (n\cdot 2\pi/\omega_{mod} + \varphi_0/\omega_{mod} - \Delta t/2)] \times \Theta[n\cdot 2\pi/\omega_{mod} + \varphi_0/\omega_{mod} + \Delta t/2 - t],$$

where Θ is the Heaviside step-function, the product of step-functions defines a time-window and $N \approx \omega_{mod}T_{exp}/2\pi \gg 1$ is the number of time windows (the number of full modulation periods) within T_{exp}. For $\Delta t \ll 2\pi/\omega_{mod}$, we find

$$\begin{aligned} S_P(\omega_{mod}, z) =& S'_P T_{exp}\frac{\omega_{mod}\Delta t}{2\pi} f[z_{ion}(\omega_{mod}, \varphi_0/\omega_{mod})] \\ =& S'_P T_{exp}\frac{\omega_{mod}\Delta t}{2\pi} e^{-[z - z_0(\omega_{mod})\cos(\varphi_0+\varphi)]^2/(2\sigma^2)}, \end{aligned} \tag{9.3.21}$$

i.e., a Gaussian distribution centered at the position

$$z_0(\omega_{mod})\cos(\varphi_0 + \varphi) = z_0(\omega_{mod})[\cos(\varphi_0)\cos(\varphi) - \sin(\varphi_0)\sin(\varphi)]. \tag{9.3.22}$$

Thus, by choosing $\cos(\varphi_0) = 1$, the amplitude $z_0(\omega_{mod})\cos(\varphi)$ of the in-phase component can be selected. By recording an image sequence while scanning ω_{mod} slowly enough that it can be considered a continuous variable, the variation of the amplitude of the in-phase component with modulation frequency can be measured. For two $^{40}Ca^+$ ions, both emitting fluorescence light, the projected signal function is a sum of two functions of the form given in Eq. (9.3.21).

For two identical ions in the center-of-mass mode, the phase φ is the same as for a single ion. For two ions with a different mass, where only one of the ions is laser cooled, the relative phase, φ_1, between the laser cooled ion and the modulation force is given by a more complicated expression than φ (see derivation in App. A.3). Fortunately, $\cos(\varphi_1) = 0$ is fulfilled at $\omega_{mod} = \omega_{COM}$ (and $\omega_{mod} = \omega_{br}$) such that the approach described above also is valid for two different ions.

9.3.2 Experiment

The experiment presented here demonstrates the phase-sensitive technique described above, showing that the frequency where the amplitude of the in-phase component of motion is zero can be determined with a relative statistical uncertainty down to $\sim 2 \cdot 10^{-5}$. For a demonstration of relative mass measurements on the 10^{-4} level or better, it does, however, still remain to take care of the light-force shift and other systematic errors, and in that sense the present experiment is only preliminary. The experiment was performed using two ions as in the situation described theoretically above. The Doppler laser-cooled ions are $^{40}Ca^{+}$-ions and the sympathetically cooled ion is a singly-charged calcium ion, $^{A}Ca^{+}$, with nucleon number $A \neq 40$. Thus, rather than trying to measure small mass differences, we use a calcium isotope as a test mass. The $^{A}Ca^{+}$ ion is unaffected by the cooling lasers for the $^{40}Ca^{+}$ ion due to the isotope-shifts of the cooling transitions. The axial motion was excited by intensity-modulation, since it naturally selects the in-phase component (strobe light effect).

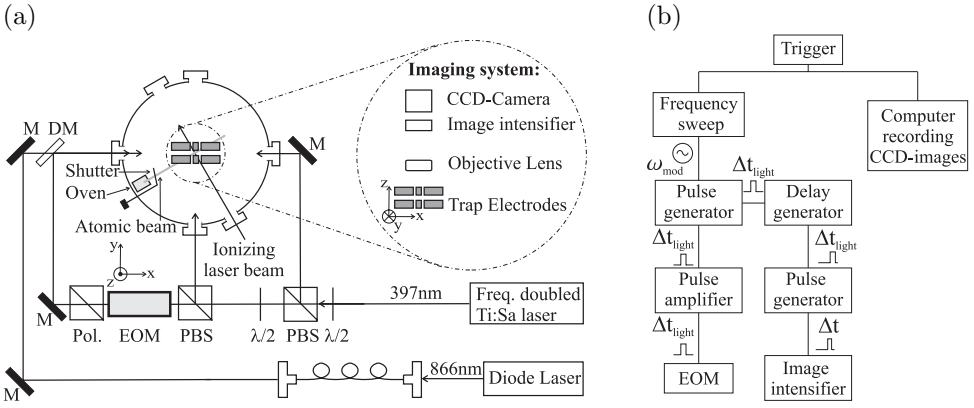

Figure 9.18: Experimental setup for mass measurements. (a) Ion trap, lasers and imaging system. M: mirror, DM: dichroic mirror, PBS: polarizing beamsplitter, $\lambda/2$: half-wave plate, Pol.: polarizer. The EOM and the polarizer are used for intensity modulation as described in Sec. 9.1.1. (b) Schematic overview of the setup for recording images while synchronously scanning the modulation frequency. Further details are given in the text.

The experimental setup is shown in Fig. 9.18. For this experiment, a linear Paul trap which is larger than the one presented in Chap. 7 was used, since it is less sensitive to patch potentials. This larger trap consists of four cylindrical electrodes (gold-coated stainless steel rods) arranged in a quadrupole configuration, where two diagonally op-

posite rods are separated by 7.00 mm. The rods are 8.00 mm in diameter, and each rod is sectioned into three parts, where the center piece is 5.40 mm long and the two end-pieces are 20.00 mm long. An RF-voltage is applied to two diagonally opposite rods and the same RF-voltage with the opposite phase is applied to the other two rods. The peak-peak amplitude of the RF-voltage was typically 500 V and the frequency was 3.894 MHz, which results in a radial trap frequency of $\omega_r \approx 2\pi \times 450\,\mathrm{kHz}$. The axially confining endcap voltage applied to the eight end-electrode pieces was chosen to about 4 V, yielding an axial trap frequency of $\omega_z \approx 2\pi \times 130\,\mathrm{kHz}$ for a Ca^+ ion. Additional DC-voltages can be applied to all twelve electrode pieces for adjustment of the equilibrium position of the ions. Otherwise, the imaging system is identical to the one described in Chap. 8, the vacuum chamber setup is equivalent to the one described in Chap. 8 and the laser sources are the same. Two $^{40}Ca^+$ ions was loaded into the trap using the isotope-selective photoionization technique described in Chap. 8. A $^{40}Ca^+$ ion and a $^{A}Ca^+$ ion was 'loaded' from two $^{40}Ca^+$ ions by keeping the oven shutter open until one of the $^{40}Ca^+$ ions was exchanged with a $^{A}Ca^+$ ion by a charge transfer process of the type [II,IV]

$$^{40}Ca^+ + {}^{A}Ca \longrightarrow {}^{40}Ca + {}^{A}Ca^+, \tag{9.3.23}$$

after which the oven shutter was closed. Laser cooling was done as in the trap characterization experiments described in Sec. 9.1, using two blue cooling beams counter-propagating parallel to the trap axis, one blue cooling beam propagating perpendicular to the trap axis and a red cooling beam propagating parallel to the trap axis.

One of the blue cooling beams propagating along the trap axis was intensity modulated, such that it was 'on' for a time Δt_{light} and 'off' (extinction to $< 1\%$ of the 'on' intensity level) for the rest of a modulation period of duration $2\pi/\omega_{mod}$. The modulation frequency ω_{mod} was defined by the frequency of a sinusoidal signal from the Thurlby Thandar Instruments (TTi) waveform generator mentioned in Chap. 8 [see Fig. 9.18(b)]. The modulation frequency could be scanned across a chosen frequency-interval of width $\Delta\omega_{mod}$ in a time T_{scan}. Although the in-phase component of the motion of the ions naturally is selected using intensity-modulation, fluorescence light can still be seen during the 'off'-periods, due to the unmodulated blue cooling beams. To exclude this light, the image-intensifier was gated at the modulation frequency, being open in a time window of width Δt. This time window was overlapped by the 'on'-periods of the intensity-modulated cooling beam ($\Delta t_{light} > \Delta t$) using a variable delay of the trigger-pulse for the image-intensifier [see Fig. 9.18(b)]. To ensure a well-defined correspondence between picture number and modulation frequency, a frequency-scan and recording of CCD-images was triggered by the same pulse.

In recording an image sequence for obtaining the projected signal function $S_P(\omega_{mod}, z)$, there are three important parameters: The amount of fluorescence collected per CCD-image ($\sim S'_P T_{exp} \omega_{mod} \Delta t/2\pi$), the frequency resolution (frequency/image) and the scan time T_{scan}. Δt was chosen as $\Delta t = 1.1\,\mu$s (with $\Delta t_{light} = 1.3\,\mu$s) for obtaining the largest possible signal, while still being able to observe the in-phase component, i.e., fulfilling the condition $\Delta t \ll 2\pi/\omega_{mod} \approx 2\pi/\omega_z \approx 7.7\,\mu$s. Having fixed $\omega_{mod}\Delta t/2\pi$, the exposure time of the CCD-chip, T_{exp}, was set between 100 ms and 150 ms. The exposure time and the read-out time of the CCD-chip defines the so-called frame-rate ν_{frame}, at which images are recorded, which is constant and ranged between 4.79 Hz and 9.20 Hz. The number of images recorded during a scan, N_{image}, was set as a trade-off between having a high frequency resolution ($\Delta\omega_{mod}/N_{image}$) and a low scan time

(N_{image}/ν_{frame}). The upper limit of the scan time is in practice set by the fact that the ions change places from time to time, either as a result of the motional excitation or due to collisions with background gas atoms or molecules. For this preliminary experiment, laser stability was not a problem on the timescale of a scan, however, to cancel the first-order light-force shift by averaging over measurements for the two different positions of the ions, laser stability is important and may be a practical limit to the scan time. In the present experiment, the frequency resolution ranged between 16 Hz/image and 2 Hz/image, using $N_{image} = 1024$, $\Delta\omega_{mod} = 2\,\text{kHz}$ and $T_{scan} = 163\,\text{s}$ for the highest resolution scans.

Having recorded a sequence of images and projecting the pixel values onto the z-axis, a projected signal function was obtained. Examples are shown in Fig. 9.19 for a $^{40}Ca^{+}$–$^{40}Ca^{+}$ and a $^{40}Ca^{+}$–$^{42}Ca^{+}$ two-ion string. The center-of-mass mode resonance

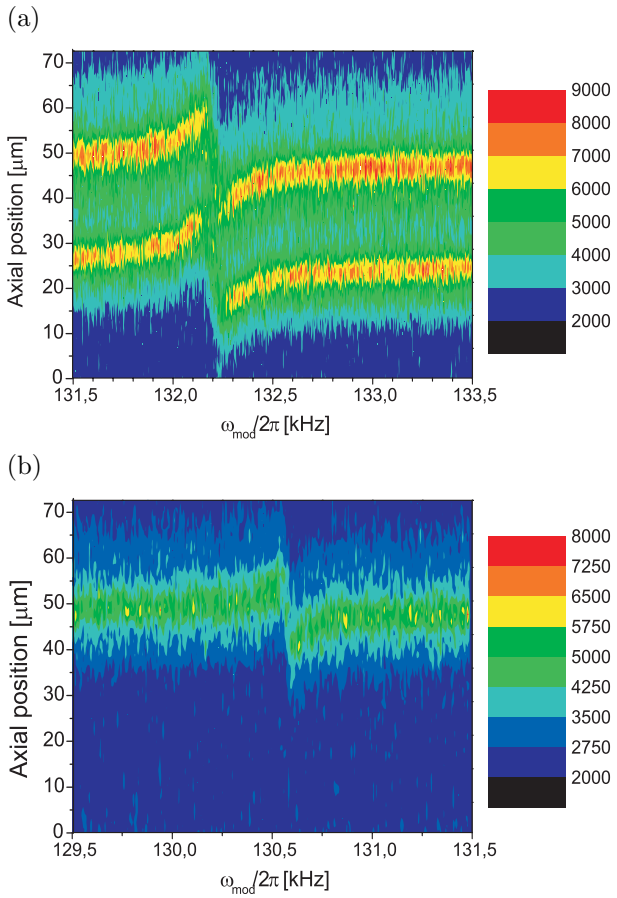

Figure 9.19: (a) Contour plot of the projected signal function for a scan across the center-of-mass mode resonance of a $^{40}Ca^{+}$–$^{40}Ca^{+}$ two-ion string. The resonance frequency is 132203 ± 2 Hz. The frequency resolution is 2 Hz/image. (b) Same as (a), but for a $^{40}Ca^{+}$–$^{42}Ca^{+}$ two-ion string. The resonance frequency is 130572 ± 13 Hz. The frequency resolution is 8 Hz/image.

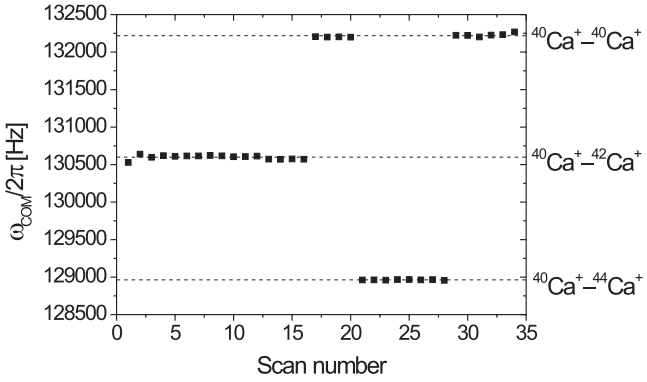

Figure 9.20: Measured center-of-mass mode frequencies at identical trap parameters for a $^{40}Ca^{+}$–$^{40}Ca^{+}$, a $^{40}Ca^{+}$–$^{42}Ca^{+}$ and a $^{40}Ca^{+}$–$^{44}Ca^{+}$ two-ion string. The average frequencies indicated by the dashed lines are 132218±7 Hz, 130599±7 Hz and 128963.5± 1.5 Hz, respectively.

frequencies of 132203 ± 2 Hz and 130572 ± 13 Hz for the $^{40}Ca^{+}$–$^{40}Ca^{+}$ and the $^{40}Ca^{+}$–$^{42}Ca^{+}$ two-ion string, respectively, are found from a fit to a function of the same form as Eq. (9.3.21) (or a sum of two such functions) with appropriate extra fitting parameters to account for a constant background signal and the equilibrium position(s) of the ion(s) [9]. The resonance frequencies can be determined with a relative statistical uncertainty below 10^{-4}, showing that with the phase-sensitive technique we can resolve relative mass differences at the level of interest (e.g., for discriminating between $^{25}Mg^{+}$ and $^{24}MgH^{+}$). This is the main result of this section. The actual resonance frequencies are subject to some systematic errors, which will be discussed below. Several scans of the type shown in Fig. 9.19 have been recorded, also for a $^{40}Ca^{+}$–$^{44}Ca^{+}$ two-ion string. The resonance frequencies found from all the scans are plotted in Fig. 9.20. Generally, the reproducibility is good, however, there are some apparently systematic jumps, particularly for the $^{40}Ca^{+}$–$^{42}Ca^{+}$ series.

From the average center-of-mass mode frequencies and Eq. (9.3.13), the measured relative mass $\mu_{A/40,meas}$ between a $^{A}Ca^{+}$ ion ($A = 42, 44$) and a $^{40}Ca^{+}$ ion can be extracted, yielding $\mu_{42/40,meas} = 1.0493(3)$ and $\mu_{44/40,meas} = 1.0998(2)$. This can be compared to the tabulated values [146] [10] of $\mu_{42/40,tab} = 1.049934$ and $\mu_{44/40,tab} = 1.099899$, which yields a relative deviation of $6 \cdot 10^{-4}$ and $4 \cdot 10^{-5}$, respectively. Due to the systematic errors of the order of 10^{-4} discussed below, these deviations should be taken with a grain of salt. On the other hand it is promising, that neither of the results shows a deviation very much larger than 10^{-4}.

[9] Strictly speaking, the expression for $\cos(\varphi_1)$ given in App. A.3 should be used for fitting of data for a $^{40}Ca^{+}$–$^{A}Ca^{+}$ two-ion string.

[10] Electron masses are taken into account, but electron binding energies can be neglected for Ca^{+} at the 10^{-4} level of precision.

Systematic errors

A number of systematic errors can originate from the correspondence between picture number and modulation frequency. Using a continuous scan as above, the frame-rate needs to be constant and precisely known. To ensure this, more care should be taken than in this preliminary experiment. The frame-rate was only known to three digits precision (this can easily be improved), which gives rise to a systematical uncertainty roughly equal to the relative uncertainty of the frame-rate times $\Delta\omega_{mod}/2$, which amounts to $\sim 5\,\mathrm{Hz}$, or $\sim 5 \cdot 10^{-5}$ times the resonance frequency. Furthermore, the frame-rate may be affected if the computer starts running other processes than recording images. For the $^{40}Ca^{+}$–$^{42}Ca^{+}$ two-ion string, we note that the measured frequencies shown in Fig. 9.20 roughly fall in two groups having a slight frequency difference. The higher lying frequencies were obtained at a low resolution of 16 Hz/image, while the last four frequencies in this series were recorded at a resolution of 8 Hz/image. Although a change of resolution should not shift the measured resonance frequency, there seems nevertheless to be a correlation, which could indicate some timing problems. Using the average of the last four points in the $^{40}Ca^{+}$–$^{42}Ca^{+}$ series to extract $\mu_{42/40,meas}$, the relative deviation from the tabulated value is in fact only $1.6 \cdot 10^{-4}$. On the other hand, the frequencies for the $^{40}Ca^{+}$–$^{44}Ca^{+}$ two-ion string, which yields a good agreement with the tabulated value, were also recorded at a resolution of 16 Hz/image. The reference $^{40}Ca^{+}$–$^{40}Ca^{+}$ frequencies were recorded with a resolution of 2-8 Hz/image. The safe way of avoiding all these possible errors would be to record one image at a fixed modulation frequency, step the modulation frequency, record another image and so on. This is not an immediate option with the TTi waveform generator, but with some programming it can be done.

Another systematic error is the light-force shift. In the experiment, the net light-pressure forces of the counter-propagating blue cooling beams were balanced to some extent, in order to control the amplitude of the motion of the excited ions, which means that $\delta z/\Delta z$ is somewhat lower than the limit given by Eq. (9.3.12). Together with the reduction of the light-force shift for the center-of-mass mode [see Eq. (9.3.14)], this means that the relative shift is below 10^{-4}. We were not able to see any systematic dependence on the position of the sympathetically cooled ion, which indicates that the light-force shift indeed is small. Since the blue cooling laser was not intensity-stabilized in this experiment, the light-force shift was not investigated any further.

Finally, in a more precise experiment, the expression for $\cos(\varphi_1)$ given in App. A.3 should be used for fitting the projected signal function for a $^{40}Ca^{+}$–$^{A}Ca^{+}$ two-ion string ($A \neq 40$).

Conclusion

In conclusion, we have demonstrated that with the phase-sensitive technique it is possible to resolve relative mass differences at the level of 10^{-4}. By addressing the systematic errors discussed above, it should be possible to measure relative mass differences at this level, which in most cases is sufficient to discriminate between ions with the same number of nucleons, only having a different mass due to their different nuclear binding energies, e.g., $^{25}Mg^{+}$ and $^{24}MgH^{+}$.

Chapter 10

Shelving in the metastable $3d\,^2D_{5/2}$ state

The internal state detection scheme described in Chap. 4 relies on state-selectively shelving the optically active electron in the $^2D_{5/2}$ state. Subsequent collection of fluorescence light determines if the electron has been shelved ('non-fluorescing' ion) or if it is cycling within the $^2S_{1/2}$–$^2P_{1/2}$–$^2D_{3/2}$ family of states ('fluorescing' ion).

To demonstrate shelving prior to any STIRAP experiments, and to do a realistic test of our ability to make an unequivocal distinction between non-fluorescing and fluorescing ions, we have performed shelving, as described in more detail below, by exciting ions from the $^2D_{3/2}$ state to the $^2P_{3/2}$ state, from where the ions can spontaneously decay to the $^2D_{5/2}$ state. A clear distinction between non-fluorescing and fluorescing ions could indeed be made, which has enabled a measurement of the lifetime of the (metastable) $^2D_{5/2}$ state.

The lifetime experiment, which also contains a demonstration of the shelving technique, is presented in Sec. 10.1. A discussion of the relevance of the lifetime experiment for the internal state detection scheme is given in Sec. 10.2, together with a short account of some further progress towards the first STIRAP experiments. The work concerning the lifetime measurement has been published in Ref.[III], to which Sec. 10.1 is closely linked.

10.1 Lifetime measurement of the $3d\,^2D_{5/2}$ state

Apart from being relevant for our own internal state detection scheme, the $^2D_{5/2}$ state and its lifetime are important for several other reasons. First of all, in the work by the Innsbruck group one of the qubit states is defined as one of the sublevels of the $^2D_{5/2}$ state [147]. For atomic structure calculations, the $^2D_{5/2}$ state is an important test case for the study of valence-core interactions and core-polarization effects [148]. Moreover, the long lifetime of the $^2D_{5/2}$ state implies a sub-Hz natural linewidth of the 729 nm electric quadrupole transition to the $^2S_{1/2}$ ground state, which makes this transition an attractive candidate for an optical frequency standard [149, 150]. Finally, in astronomy, the $^2D_{5/2}$ state has been used in a study of the β pictoris disk [151], and it is also used

in the study of so-called Seyfert 1 galaxies and T Tauri stars [152].

Therefore, the natural lifetime of the $^2D_{5/2}$ state has attracted much attention in recent years, which has given rise to a wealth of measurements [150, 153, 154, 155, 156, 157, 158, 159, 160] and theoretical calculations [148, 152, 161, 162, 163, 164, 165]. Unfortunately, these results are scattered over a rather broad range (see Fig. 1 in Ref. [153] for an overview). Among the experimental results, the lifetime found by Barton *et al.* [153], using the shelving technique on a single trapped and laser-cooled $^{40}Ca^+$ ion, has the smallest error bars, with an estimated lifetime of $\tau = 1168 \pm 7\,\text{ms}$.

Our measurement was performed using a string of five ions and resulted in a lifetime of $\tau = 1149 \pm 14(\text{stat.}) \pm 4(\text{sys.})\,\text{ms}$.

The experimental setup and the experimental procedure for the lifetime experiment are described in Sec. 10.1.1. In Sec. 10.1.2, we give a detailed account of the data analysis, including a description of the maximum likelihood method used for the statistical data analysis and a discussion of systematic errors with emphasis on radiation effects and collision effects. In Sec. 10.1.3, the estimated lifetime based on the measurements is given and discussed.

10.1.1 Experimental setup

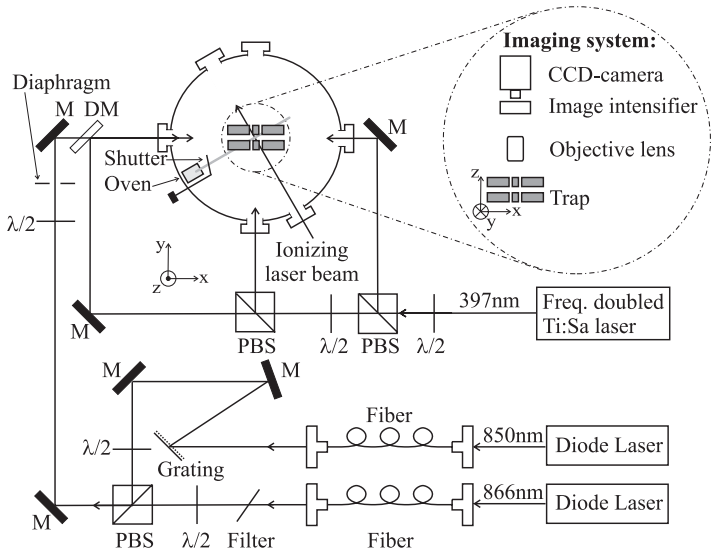

Figure 10.1: Experimental setup, see text for details. M: mirror, DM: dichroic mirror, PBS: polarizing beamsplitter, $\lambda/2$: half-wave plate.

A sketch of the experimental setup is shown in Fig. 10.1. The experiment was performed using the large linear Paul trap, which was used for the mass measurements. Cooling lasers and the imaging system are also the same, but the 850 nm diode laser has been added to the experimental setup. Also a long-pass filter and a grating and a diaphragm have been inserted in the diode laser beamlines for reasons discussed below. In this lifetime experiment, the peak-peak amplitude of the RF-voltage is 600 V and the frequency is 3.894 MHz, which results in a radial trap frequency of $\omega_r \approx 2\pi \cdot 550\,\text{kHz}$.

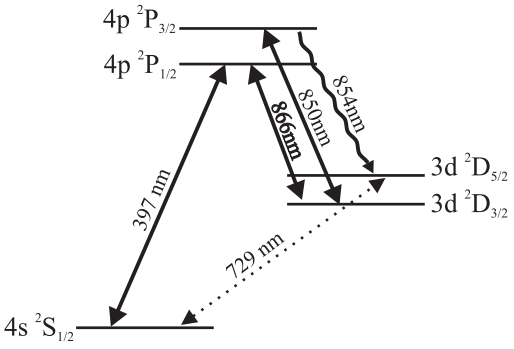

Figure 10.2: Relevant levels and transitions in $^{40}Ca^+$. Doppler laser cooling is performed with lasers at 397 nm and 866 nm. A laser at 850 nm excites the ion from the $3d\,^2D_{3/2}$ state to the $4p\,^2P_{3/2}$ state, from where it can decay to the $3d\,^2D_{5/2}$ state. The dashed line indicates the electric quadrupole transition by which the ion can decay from the $3d\,^2D_{5/2}$ state to the ground state.

The axially confining endcap voltage applied to all eight end electrodes is 580 mV, yielding an axial trap frequency $\omega_z \approx 2\pi \cdot 50\,\text{kHz}$. The ions were loaded into the trap using the photo-ionization technique described in Chap 8. During loading the oven was heated to 420° C, under which conditions the chamber pressure was $6.0 \cdot 10^{-11}$ Torr. After having loaded five ions and forced them onto a string by adjusting the trap parameters and applying Doppler laser-cooling in the usual way, the oven temperature was reduced, and the oven shutter was closed. During a one hour measuring session, the pressure dropped to about $3.6 \cdot 10^{-11}$ Torr. For recording fluorescence light emitted during the Doppler cooling process, the CCD-camera was operated with 50 ms exposure time and digital images were recorded at a frame-rate of 17.610 Hz. The optically active electron is shelved in the $^2D_{5/2}$ state by exciting ions from the $^2D_{3/2}$ state, where they occasionally end up during the Doppler cooling process, to the $^2P_{3/2}$ state using the diode laser at 850 nm (see Fig. 10.2). From the $^2P_{3/2}$ state the ions can spontaneously decay to the $^2D_{5/2}$ state, such that the optically active electron is shelved, and the fluorescence on the 397 nm transition is quenched. The time spent by the ion in the $^2D_{5/2}$ state before it decays back to the ground state, will in the following be called a *shelving period*. By continuously applying the two cooling lasers and the shelving laser at 850 nm, we obtain characteristic fluorescence signals like the one shown in Fig. 10.3.

10.1.2 Data analysis

Data reduction

The lifetime of the $^2D_{5/2}$ state can be estimated from the distribution of the shelving periods, since we expect it to be exponential with a time constant equal to the lifetime τ.

The duration of a shelving period can be determined by dividing the number of consecutive frames, where an ion is shelved, by the frame-rate of the CCD-camera. Our

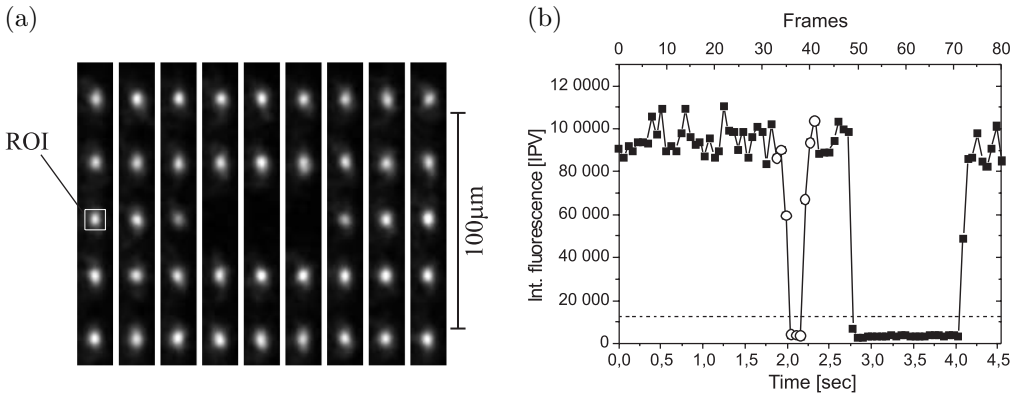

Figure 10.3: (a) A sequence of CCD-images including a shelving event for the central ion (see colour version of this figure on the front page). The white square indicates the 'region of interest' (ROI) within which the fluorescence is integrated to obtain the signal shown in (b). (b) Fluorescence signal from the central ion for an image sequence containing the nine images above. The data points corresponding to the nine images are indicated by open circles. The dashed line indicates the threshold level discussed in the text.

raw data are digital images of five ions, as shown in Fig. 10.3(a), and the main data set consists of ~ 200000 such images taken in three one hour experimental runs. The details of obtaining the distribution of the shelving periods from these images are described below.

From the images in Fig. 10.3(a), it is evident that the ions are spatially well resolved, and that a 'region of interest' (ROI) around each ion can be defined. The ROI is 13 x 13 pixels, corresponding to a region of $9.5\,\mu$m x $9.5\,\mu$m in the trap region. In order to establish a fluorescence data point which reflects the real ion fluorescence rate within a given image frame, we simply integrate the pixel values within the ROI. This is a valid measure, since the image intensifier and the CCD-chip have a linear response to the fluorescence collected by the objective lens. In the following the ion fluorescence will be given in integrated pixel values (IPV).

As shown in Fig. 10.4, the distribution of the fluorescence data points from a single ion is characterized by a rather sharp peak at a low fluorescence level and a Gaussian distribution of data points around a level of ~ 90000 IPV, originating from cases where the ion is scattering 397 nm light during a whole frame. In the following we define the fluorescing level as the center of the Gaussian distribution. The standard deviation of the Gaussian distribution is $\sigma \sim 7500$ IPV, which is mainly set by image-intensifier noise, but also by laser intensity and frequency drifts during the experimental run, and by the finite ion temperature. The peak at the low fluorescence level, or the background level, is due to data points originating from cases where the ion is shelved during a whole frame.

In order to establish a distribution of the shelving periods, we need to introduce a threshold level to discriminate between fluorescence data points corresponding to frames where the ion is fluorescing (above the threshold level) or shelved (below the threshold level). From the distribution of fluorescence data points in Fig. 10.4, it is evident

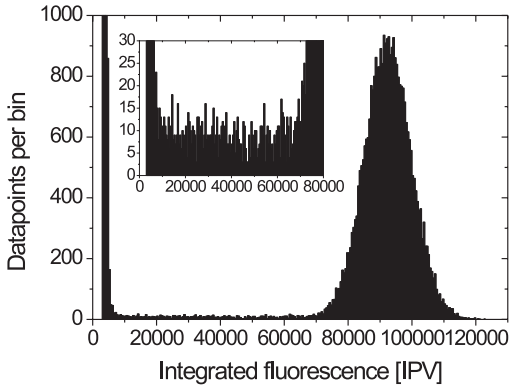

Figure 10.4: Distribution of data points from a single ion, binned in intervals of 500 IPV. The maximum of the narrow background peak near 4000 IPV is not shown but has a value of 8000. From the Gaussian distribution around 90 000 IPV with a width of $\sigma \sim 7500$ IPV, we can define a fluorescing level as the center of this distribution. The inset shows the intermediate points between 0 IPV and 80 000 IPV.

that we can choose a threshold level which can be used to unambiguously distinguish between the background level and the fluorescing level of an ion, as we also need for the internal state detection scheme. The specific choice of threshold level is discussed in the following.

From the inset of Fig. 10.4, it can be seen that the distribution of fluorescence data points contains some points with a value of the integrated fluorescence between the background level and the fluorescing level. These intermediate data points arise from images where the ion is only fluorescing during a fraction of the exposure time of the CCD-chip. This occurs naturally when an ion is shelved or decays to the ground state during the exposure of a single frame. Since a particular choice of threshold level decides whether an intermediate data point is counted as belonging to a shelving period or not, it affects the precise distribution of the shelving periods. Fortunately, the choice of another threshold level on average only adds a constant amount to all the shelving periods, and therefore the decay rate extracted from their distribution is not influenced by the choice of threshold level. This fact allows us to choose a threshold level in a broad range between the background level and the fluorescing level.

Unfortunately, intermediate fluorescence data points also occur in the following three situations: (i) shelving followed by fast decay to the ground state, (ii) decay to the ground state followed by fast re-shelving, (iii) a shelved and an unshelved ion change places, e.g., due to a weak collision with a background gas atom or molecule or due to the finite temperature of the ions. Examples of these events, all taking place within one or two camera frames, are shown in Fig 10.5(a)-(c). Hence, before we choose the threshold level to be used for extracting the distribution of shelving periods, we have to consider these three types of events in some detail.

(i) When an ion is shelved at a certain instant of a frame and decays back to the ground state within that same frame or the next, then the signal does not necessarily

fall *below* the threshold level, as the example in Fig. 10.5(a) shows. Hence these events may not even be counted as shelving events. In the data analysis we simply account for such events by discarding all periods with a duration of one or two frames from the shelving period distribution. Since the distribution is expected to be exponential, we can subsequently displace the remaining distribution, so that periods originally having a duration of n frames ($n \geq 3$) are set to be periods with a duration of $n - 2$ frames.

(ii) If an ion decays and is quickly re-shelved, we cannot be confident that the signal rises *above* the threshold level, see Fig. 10.5(b), and thus two shelving periods can appear as one longer shelving period, which would artificially increase the extracted lifetime. Noting that such events require a *high* shelving rate, it is possible to exclude them on probability grounds. First, we set a low threshold level, $T = 0.1 \cdot (F - B) + B$, where F is the fluorescing level, and B is the background level, which means that only the very fastest re-shelving events do not rise above the threshold level. Second, we require that after a decay, which ends a shelving period, there must be twenty consecutive data points above the threshold level; otherwise it is not counted as a shelving period in the data analysis. This requirement is only likely to be fulfilled with a *low* shelving rate, thus reducing the risk of accepting shelving periods where a quick re-shelving event has happened. The probability for an event of decay and quick reshelving, with the signal not rising above the selected threshold level, followed by a decay and twenty consecutive data points above the threshold level, is below 2 permille regardless of the shelving rate. Hence this method gives *at most* a systematic error of -2 ms to the final result, and we will take the systematic error to be -1 ± 1 ms.

(iii) As mentioned, two ions may change place, e.g., due to a weak collision with a background gas atom or molecule. Fig. 10.5(c) shows how a shelved and an unshelved ion changing place, effectively cut one long shelving period into two shorter ones, which artificially shortens the extracted lifetime. Therefore, in such events we restore the position of the ions to obtain a single shelving event, as shown in Fig. 10.5(d). Positions are only restored if the value of the fluorescence data points for the two ions involved adds up to the fluorescing level F within $\pm 2\sigma$ of this level. We find about 200 such events in our main data set. Since statistically the fluorescence from the two ions does not add up to the fluorescing level within $\pm 2\sigma$ in all events, we estimate a systematic error to the lifetime of $+2$ ms. True events of one ion shelving and another decaying within the same fraction of a frame will, however, occur, and erroneously be corrected by this procedure. We estimate a systematic error of -10 ms due to the erroneously corrected events. All together the systematic error due to ions switching place is -8 ms, with an estimated uncertainty of ± 4 ms.

During data-taking it happened that the ions heated up, so the ion-string became unstable. Such events are clearly visible on the images of the ions and were cut out of the data set before performing the data reduction process described above. Likewise, periods where the lasers were adjusted or unstable are not considered in the further data analysis.

After the data reduction process described above and using a threshold level of $T = 0.1 \cdot (F - B) + B$, we extract a distribution of the shelving periods for each ion, binned in time intervals of $\Delta t = 56.786$ ms, which is the inverse of the frame-rate. The counts in equivalent bins for all the ions in the three experimental runs are then added to obtain a single distribution, from which a decay rate can be determined. This distribution is shown in a histogram in Fig. 10.6, with the bins shifted such that the histogram has its origin at time zero.

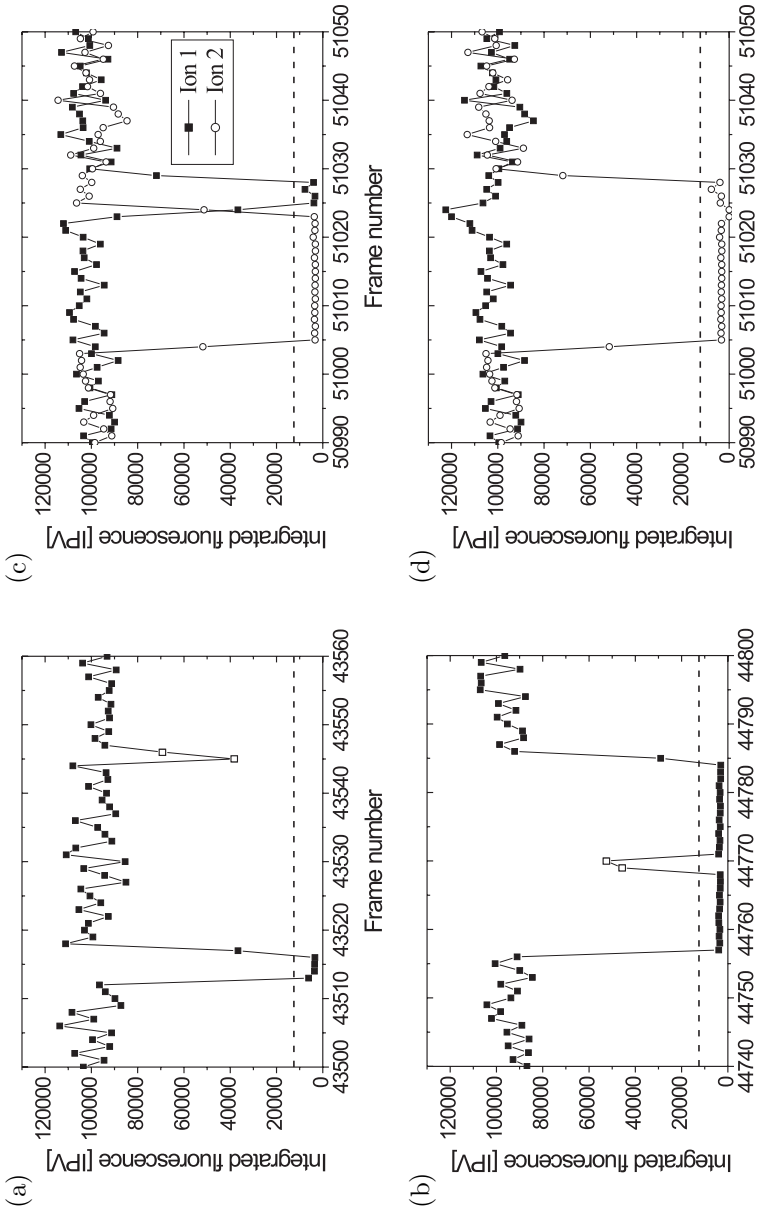

Figure 10.5: Examples of events which are problematic in connection with the data analysis. In all graphs the dashed line indicates the chosen threshold level of $\sim 12500\,\mathrm{IPV}$. (a) Shelving and fast decay; corresponding frames indicated by open squares. (b) Decay and fast re-shelving; corresponding frames indicated by open squares. Here the signal does rise above the threshold level, but for an even faster event this may not be the case. (c) A shelved and an unshelved ion change places. (d) The signals in (c) with the positions of the ions restored, i.e., the signals from Ion 1 and Ion 2 are interchanged after the crossing. At the frame where the two ions change places and the preceding frame, the fluorescence signal from Ion 1 and Ion 2 are given artificial values of $120\,000\,\mathrm{IPV}$ and $0\,\mathrm{IPV}$.

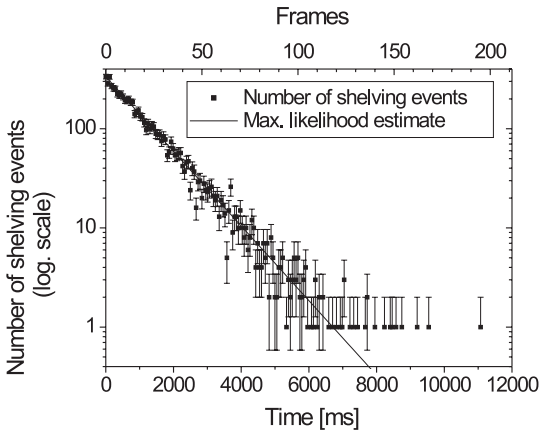

Figure 10.6: Histogram over the 6805 shelving events obtained after data reduction. Note that the number of shelving events is on a logarithmic scale. The error bars are the square root of the number of shelving events. The solid line is the maximum likelihood estimate of $\tau = 1154\,\mathrm{ms}$.

Statistical analysis

From the histogram in Fig. 10.6, we can infer the lifetime τ of the $^2D_{5/2}$ state by assuming an exponential distribution with a decay rate given by the inverse lifetime of the $^2D_{5/2}$ state. The histogram comprises 6805 shelving events with duration up to more than 11 s. Since, at large times, there are only a small number of events in the distribution, a least-squares-fitting method is inappropriate, and hence we employ a maximum likelihood estimate instead.

The probability p_i of falling into column i in the histogram, i.e., having a shelving period of duration t, which fulfills $t_i \leq t < t_{i+1}$, where $t_i = i\Delta t$, is

$$p_i = \int_{t_i}^{t_{i+1}} \frac{1}{\tau} e^{-t/\tau} dt = e^{-t_i/\tau} \left(1 - e^{-\Delta t/\tau}\right). \tag{10.1.1}$$

Mathematically, the p_i's define a proper probability distribution, since $\sum_{i=0}^{\infty} p_i = 1$. The sum starts at $i = 0$, corresponding to the origin of the distribution in the histogram. Since the sum extends to infinity, we must, in principle, be able to measure infinitely long shelving periods. In the case of real experiments, where one is only able to measure periods up to a finite duration, T_{max}, the p_i's should formally be renormalized by the factor $[1 - \exp(-T_{max}/\tau)]^{-1}$. In our case where $T_{max} \sim 1\,\mathrm{hour}$ and $\tau \sim 1\,\mathrm{s}$ we can, however, safely neglect this factor. In order to make the maximum likelihood estimate, we now introduce the likelihood function

$$L = N! \prod_{i=0}^{\infty} \frac{p_i^{n_i}}{n_i!}, \tag{10.1.2}$$

where n_i is the number of shelving events in the i'th column of the histogram, and $N = \sum_{i=0}^{\infty} n_i$ is the total number of shelving events. By maximizing L (or rather $\ln L$)

with respect to τ, we find

$$\tau = \frac{\Delta t}{\ln(\frac{\Delta t}{<t>}+1)}, \tag{10.1.3}$$

where $<t> = \sum n_i t_i/N$ is the mean duration of the shelving periods. The variance of the lifetime is [166]

$$\begin{aligned}\mathrm{Var}(\tau) = &-\left(\frac{\partial^2 \ln L}{\partial \tau^2}\bigg|_{\frac{\partial \ln L}{\partial \tau}=0}\right)^{-1} = \frac{\tau^4(e^{\Delta t/\tau}-1)^2}{N(\Delta t)^2 e^{\Delta t/\tau}} \\ =&\frac{\tau^2}{N}\left(1+\frac{1}{12}\left(\frac{\Delta t}{\tau}\right)^2+\mathcal{O}\left[\left(\frac{\Delta t}{\tau}\right)^4\right]\right).\end{aligned} \tag{10.1.4}$$

Using Eqs. (10.1.3) and (10.1.4), the lifetime and the statistical uncertainty can be determined solely from Δt, $< t >$ and N, and we find $\tau = 1154 \pm 14$ ms. The exponential distribution based on the maximum likelihood estimate is plotted as a solid line on top of the histogram in Fig. 10.6.

As a check of the efficiency and validity of our data reduction process, we have performed a test of goodness of fit [1]. To find the goodness of fit, we employ the so-called Kolmogorov test [167], which is based on the empirical distribution function (EDF). A general overview of EDF statistics can be found in Ref. [168], which also gives tables of significance levels appropriate for cases like ours, where the lifetime is estimated from the data set. We find from our data a value for the Kolmogorov test of 0.44, clearly below the 10% significance level value of 0.995, thus showing that the fit is good. We note for completeness that our data set is binned, whereas the values in Ref. [168] are for continuous data. However, since we have more than 100 channels this is not expected to play any significant role.

Radiation, collisions and other potential systematic effects

Apart from the systematic errors concerning the data reduction discussed above, there are a few other relevant systematic errors, which will be discussed in the following.

Radiation From the level scheme of Fig. 10.2, it is obvious that any radiation which couples the $^2D_{5/2}$ state to the $^2P_{3/2}$ state may deplete the $^2D_{5/2}$ state by excitation to the $^2P_{3/2}$ state followed by decay to the $^2S_{1/2}$ ground state or the $^2D_{3/2}$ state and result in a measured lifetime shorter than the natural lifetime. As a consequence, the occurrence of such radiation must be considered and, if possible, reduced. Blackbody radiation at the relevant transition wavelength is negligible at room temperature, as also discussed by Barton *et al.* [153]. Other 'thermal' sources such as the ion gauge, roomlight and computer screens were off during the measuring sessions, except for the screen where we watched the images of the ions. This screen was facing away from the vacuum chamber and is hence not expected to cause any problems. Another class of influencing light sources is the lasers used in the experiment. In particular the broad background of the emission spectrum of the 866 nm and the 850 nm diode lasers contains 854 nm light resonant with the $^2D_{5/2}$–$^2P_{3/2}$ transition. This radiation

[1] Kindly assisted by Karsten Riisager.

source was first recognized by Block *et al.* [154], and as noted by Barton *et al.* [153] the discrepancy between their own and many of the earlier measurements is possibly due to this previously unrecognized source of error. To reduce the level of 854 nm light from the diode lasers as much as possible, a long-pass filter was inserted in the 866 nm beamline and adjusted (by changing the angle of incidence) to 30% transmission at 866nm and $\lesssim 5 \cdot 10^{-4}$ at 854 nm, and a grating (1200 lines/mm) with a spectrally selective diaphragm (0.9 mm diameter, 1080 mm from the grating) was inserted in the 850 nm beamline. The filter, the grating and the diaphragm are shown in Fig. 10.1. The overall power of the lasers was reduced to ~ 18 nW and ~ 1.7 mW at the place of the ions, for the shelving laser and the repumping laser, respectively. The waist size of the beams was $670\,\mu\text{m} \times 700\,\mu\text{m}$ for the repumping laser and $360\,\mu\text{m} \times 430\,\mu\text{m}$ for the shelving laser.

In order to estimate the lifetime reduction due to radiation emitted from the diode lasers, we calculate the rate of de-shelving from the $^2D_{5/2}$ state, i.e., the excitation rate from the $^2D_{5/2}$ state to the $^2P_{3/2}$ state times $(1-b)$, where $b = 0.068$ is the branching ratio for decay from the $^2P_{3/2}$ state back to the $^2D_{5/2}$ state (see App. B).

First we consider de-shelving due to the repumping laser, which we split into two contributions, one from the off-resonant 866 nm radiation and one from the near-resonant background radiation around 854 nm. The de-shelving rate due to the 866 nm radiation was calculated by Barton *et. al.* [153] to $I_{866} \cdot 9.4 \cdot 10^{-5}\,\text{s}^{-1}/(\text{mWmm}^{-2})$, where I_{866} is the intensity of 866 nm radiation. With $I_{866} = 2.3\,\text{mWmm}^{-2}$ we find a de-shelving rate of $2.2 \cdot 10^{-4}\,\text{s}^{-1}$, yielding a lifetime reduction of 0.3 ms.

In order to calculate the excitation rate from the $^2D_{5/2}$ state to the $^2P_{3/2}$ state due to radiation near 854 nm, we first consider the rate at a given frequency ω_L, as expressed by Eq. (2) in Ref. [153]:

$$R_{12} = \frac{2J_2+1}{2J_1+1}\frac{\pi^2 c^3}{\hbar\omega_{12}^3} A_{21} \frac{I}{c} g(\omega_L - \omega_{12}), \tag{10.1.5}$$

where $J_1 = 5/2$ and $J_2 = 3/2$ are the total angular momenta of the involved levels, $\omega_{12} = 2\pi c/854.209\,\text{nm}$ (App. B) is the transition frequency, $A_{21} = 7.7 \cdot 10^6\,\text{s}^{-1}$ [153] the Einstein coefficient for spontaneous decay from the $^2P_{3/2}$ state to the $^2D_{5/2}$ state, I the intensity of the incoming radiation, and $g(\omega_L - \omega_{12})$ a normalized Lorentz-distribution. Assuming a flat background spectrum of the diode lasers, i.e., the intensity per frequency interval $\Delta I/\Delta\omega_L$ is constant, we can integrate Eq. (10.1.5) over frequency ω_L and find an excitation rate of

$$R = \frac{2J_2+1}{2J_1+1}\frac{\pi^2 c^2}{\hbar\omega_{12}^3} A_{21} \frac{\Delta I}{\Delta\omega_L}. \tag{10.1.6}$$

Using a diffraction grating we have measured $\Delta I/\Delta\omega_L \lesssim 0.19\,\text{nW}/(\text{mm}^2 \cdot \text{GHz})$ near 854 nm at the power used in the experiment, and we then find $R = 0.77\,\text{s}^{-1}$. Multiplying this rate by $1-b$ and the transmission of $5 \cdot 10^{-4}$ of the long-pass filter, we find a de-shelving rate of $3.6 \cdot 10^{-4}\,\text{s}^{-1}$, yielding a lifetime reduction of 0.5 ms.

As a check of this estimate, we performed an experiment, again with five ions, with the cooling lasers on but without the shelving laser. Even without the shelving laser the ions may be shelved due to radiation from the 866 nm repumping laser, which couples the $^2D_{3/2}$ state to the $^2P_{3/2}$ state. From the observed shelving rate, we can then find the excitation rate on the 850 nm $^2D_{3/2}$–$^2P_{3/2}$ transition and compare it to the

calculated excitation rate for the 854 nm $^2D_{5/2}$–$^2P_{3/2}$ transition, taking the different linestrengths into account. In this experiment the power of the 866 nm laser was 7.3 mW, the waist was as above, the long-pass filter was removed and the oven-shutter was open. In about 35 minutes we observed 12 shelving events, i.e., the observed shelving-rate is $5.8 \cdot 10^{-3}\,\mathrm{s}^{-1}$. Taking into account the number of ions, the population of the D-state ($\sim 1/3$, since both cooling transitions are saturated) and the branching ratio b, we find the excitation rate on the $^2D_{3/2}$–$^2P_{3/2}$ transition: $(3/5b) \cdot 5.8 \cdot 10^{-3}\,\mathrm{s}^{-1} = 5.1 \cdot 10^{-2}\,\mathrm{s}^{-1}$. By multiplying this number with the relative linestrength between the $^2D_{5/2}$–$^2P_{3/2}$ transition and the $^2D_{3/2}$–$^2P_{3/2}$ transition of 8.92 [25], we find an estimated value of $0.45\,\mathrm{s}^{-1}$ for the excitation rate on the $^2D_{5/2}$–$^2P_{3/2}$ transition, which should be compared to $R = 0.77\,\mathrm{s}^{-1}$ calculated above. The two numbers are not expected to be equal but only of the same order of magnitude, since the transition wavelengths are different, and the diode laser background is not necessarily equally strong near 850 nm and 854 nm. Also some of the shelving events may be due to collisions, as discussed below. Nevertheless, the numbers agree within a factor of 2 and our calculated estimate of the excitation rate, and hence the de-shelving rate seems to be reasonable.

Above we considered de-shelving due to the repumping laser. In exactly the same way we could consider de-shelving due to the shelving laser. However, since the intensity of the shelving laser is much lower than for the repumping laser, and the grating and the diaphragm strongly reduce the level of 854 nm light, the excitation rate is expected to be extremely small. To check this we performed additional lifetime measurements at three different power levels of the shelving laser, 18 nW, 193 nW and 2081 nW, yielding lifetimes of 1146 ± 24 ms, 1160 ± 29 ms and 1092 ± 27 ms, respectively. When using higher power, the laser was detuned from resonance to get a similar shelving rate in all experiments. In Fig. 10.7, the linear fit to the decay rates corresponding to the lifetimes shows that there is a weak dependence of the decay rate (or lifetime) on the 850 nm power. However, with only 18 nW the lifetime is only reduced by 0.5 ms. The results of the two low power measurements and the crossing at zero power are in agreement with the result obtained from our main data set. The measurement at 18 nW was in fact performed at the same shelving laser power as the measurements for the main data set.

All together, we include a systematic error of $+1 \pm 1$ ms in our final result due to de-shelving from the two diode lasers.

Collisions Another systematic effect which shortens the measured lifetime is collisions with background gas atoms and molecules. There are two relevant types of collisions: fine-structure changing (j-mixing) collisions and quenching collisions. In a j-mixing collision the internal state can change from the $^2D_{5/2}$ state to the $^2D_{3/2}$ state, or vice versa. In a quenching collision the internal state changes from the $^2D_{5/2}$ state to the $^2S_{1/2}$ ground state. Both types of collisions deplete the $^2D_{5/2}$ state and hence shorten the measured lifetime. j-mixing and quenching rate constants (Γ_j and Γ_Q) in the presence of different gases are given in Ref. [169] and references therein. Quite generally j-mixing collisions are found to be an order of magnitude stronger than quenching collisions. From a restgas analysis, we know that the restgas in our vacuum chamber is mainly composed of H_2 and gas of 28 atomic mass units, i.e., N_2 or CO. In the restgas analysis it was not possible to distinguish between N_2 and CO, since the chamber pressure was so low that the signal from the atomic constituents of these molecules could not be observed. Knoop *et al.* [169] found the following rate constants in units of $\mathrm{cm}^3\mathrm{s}^{-1}$ for collisions with H_2 and N_2: $\Gamma_j(H_2) = (3 \pm 2.2) \cdot 10^{-10}$, $\Gamma_Q(H_2) = (37 \pm 14) \cdot 10^{-12}$,

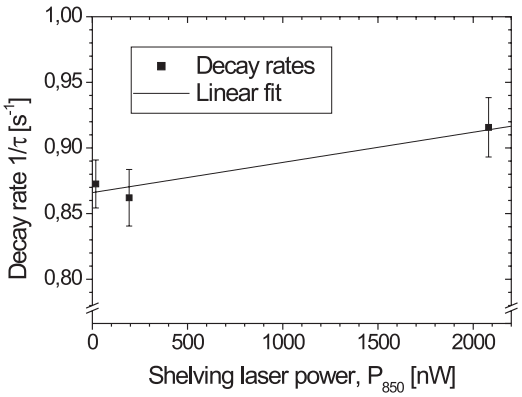

Figure 10.7: Decay rate measurements at three different power levels of the shelving laser. A weighted least-squares linear fit to the measured decay rates yields $1/\tau = 0.866(8)\,\mathrm{s}^{-1} + 0.023(7)\,\mathrm{s}^{-1}/\mathrm{nW} \cdot P_{850}$.

$\Gamma_j(\mathrm{N_2}) = (12.6 \pm 10) \cdot 10^{-10}$ and $\Gamma_Q(\mathrm{N_2}) = (170 \pm 20) \cdot 10^{-12}$. The measurements were performed on a cloud of relatively hot ions, as compared to the laser cooled ions considered in this paper. As noted in Ref. [169], other measurements of j-mixing with H_2 at different collision energies give similar results, so we may expect only a weak energy-dependence for the j-mixing collisions, and therefore we use the values given in Ref. [169]. On the other hand, higher quenching rates are expected at lower temperatures [169], but to our knowledge there are no measurements of that for Ca^+. Unfortunately, we are not aware of any similar measurements with CO, and in our estimate of the collision rate below, we therefore assume that the mass 28 restgas is N_2. The relatively large rate constants of N_2 found in Ref. [169] indicate that at least this assumption probably does not lead to a large underestimate of the collision induced de-shelving rate.

Assuming that the values given in Ref. [169] are applicable, we can estimate the collision-induced lifetime reduction. At a pressure of $5 \cdot 10^{-11}$ Torr, taking into account the sensitivity to different gases of the ion gauge and using the result of the restgas analysis, we find that the restgas is composed of $54\%H_2$ and $46\%N_2$, which yields a total collision induced de-shelving rate of $2.3 \cdot 10^{-3}\,\mathrm{s}^{-1}$, and a systematic error to the lifetime of $+3$ ms with an estimated uncertainty of ± 1 ms.

From the measurement of 12 shelving events in 35 minutes without the shelving laser on, described above, we can obtain an *upper limit* for the j-mixing collision rate if we assume that all the observed shelving events are due to j-mixing collisions inducing a transition from the $^2D_{3/2}$ state to the $^2D_{5/2}$ state (with rate γ_{35}). Again taking the number of ions and the population of the $^2D_{3/2}$ state into account, the collision induced shelving rate is $3.5 \cdot 10^{-3}\,\mathrm{s}^{-1}$. Since the oven shutter was open in that experiment, thus allowing collisions with neutral calcium atoms as well, we expect this number to be larger than under the conditions for the 'real' lifetime measurements. The transition rate, γ_{53}, for the $^2D_{5/2}$–$^2D_{3/2}$ de-shelving transition is expected to be given by $\gamma_{53} = 2\gamma_{35}/3$, owing to the principle of detailed balance, so the collision induced de-shelving rate is

$2.3 \cdot 10^{-3}\,\mathrm{s}^{-1}$. This is our upper limit for the j-mixing collision rate, which should be compared to our estimate above of the *total* collision-induced de-shelving rate, which is dominated by contributions from j-mixing collisions. Somewhat fortuitously, the numbers are equal, and hence our calculated estimate seems to be reasonable.

Other effects When observing shelving events from a string of ions, one might consider if there are any correlations in the decay of the individual ions from the $^2D_{5/2}$ state to the ground state, which could influence the measured lifetime. In the experiments by Block *et al.* [154] indications of correlated decays from the $^2D_{5/2}$ state were observed, manifested as an overrepresentation of events where several ions decay at the same time. A later detailed experiment by Donald *et al.* [160] showed, however, no such correlations. Apart from sudden bursts of 854 nm radiation, the only reasonable physical mechanism which could lead to correlations is so-called subradiant and superradiant spontaneous emission due to interference in the spontaneous decay of two or more ions [170]. In the simple case of two ions, superradiant and subradiant spontaneous emission is characterized by a relative change in the normal (single ion) decay rate of the order of $\pm \sin(kR)/kR$ (when $kR > 10$), where R is the ion-ion distance and $k = 2\pi/\lambda$ with $\lambda = 729\,\mathrm{nm}$ in our case [2]. For more ions the effect is of the same order of magnitude. In our case $1/kR \approx 6 \cdot 10^{-3}$ so just from this argument the effect is small, but not negligible. The interference effect, however, relies on creating and maintaining a superposition state of the form $|\pm\rangle = (|S_1 D_2\rangle \pm |D_1 S_2\rangle)/\sqrt{2}$, where S and D indicate the internal state, $^2S_{1/2}$ or $^2D_{5/2}$, and indices 1 and 2 relate to Ion 1 and Ion 2. In our experiment such a superposition state can only be created by a random process since the $^2D_{5/2}$ state is only populated through spontaneous emission, and consequently the relative phase between the states $|S_1 D_2\rangle$ and $|D_1 S_2\rangle$ is expected to be random. This fact would in itself average out the effect on the lifetime. In addition, if the superposition state is created, it is immediately (as compared to τ) destroyed since, from a quantum mechanical point of view, we are constantly measuring the internal state of the ions. So any superradiant or subradiant effect is in fact expected to be destroyed, and we do not expect any correlation in decays from the $^2D_{5/2}$ state. We have checked our data for correlated decays, and indeed a statistical analysis shows no evidence of correlations.

In Ref. [153] mixing of the $^2D_{5/2}$ state with the $^2P_{3/2}$ state due to static electric fields was considered and found to be negligible. For our trap we also find this effect to be negligible.

Finally, we note that the read-out time of the camera influences the measured duration of the shelving periods. As for the choice of threshold level, the read-out time has no effect on the measured decay rate and hence on the measured lifetime.

The total effect of systematic errors Above we have identified and evaluated systematic errors originating from the data analysis and from de-shelving due to radiation and collisions. An overview of the estimated errors and their uncertainties is given in Table 10.1.

The effects leading to the systematic errors can be modelled by extra decay rates

[2] In Ref. [170] a dipole transition is considered. For an electric quadrupole transition the relative change of the decay rate is of the same order of magnitude.

Effect	Systematic error [ms]
Quick re-shelving	-1 ± 1
Ions switching place	-8 ± 4
De-shelving, diode lasers	$+1 \pm 1$
De-shelving, collisions	$+3 \pm 1$
Total	-5 ± 4

Table 10.1: Overview of estimated systematic errors.

added to the natural decay rate:

$$\frac{1}{\tau_{meas}} = \frac{1}{\tau_{nat}} + \sum_i \gamma_i \tag{10.1.7}$$

or

$$\tau_{nat} \approx \tau_{meas} + \sum_i \tau_{meas}^2 \gamma_i, \tag{10.1.8}$$

where τ_{meas} is the measured lifetime as determined from the maximum likelihood estimate, τ_{nat} is the natural lifetime, and the γ_i's are the extra decay rates, which can attain both positive and negative values in this model. The systematic errors given in the text and Table I correspond to $\tau_{meas}^2\gamma_i$. Eq. (10.1.8) shows that the systematic errors should be added linearly, yielding -5 ms, and added to the result of the maximum likelihood estimate, giving a lifetime of 1149 ms. The uncertainties of the systematic errors are independent, and therefore they are added quadratically, yielding an uncertainty of ± 4 ms.

10.1.3 Result and conclusion

By correcting the maximum likelihood estimate with -5 ms, as described above, we find that our final result for the lifetime measurement is

$$\tau_{nat} = 1149 \pm 14(\text{stat.}) \pm 4(\text{sys.})\,\text{ms}. \tag{10.1.9}$$

The largest error is the statistical, but we do have a non-negligible systematic uncertainty, originating from the correction procedure when ions change places. The associated error, and hence the uncertainty, could be reduced by increasing our signal-to-noise ratio, which would narrow the time window where real events of simultaneous decay and shelving for two different ions could be taken for two ions changing place. The signal-to-noise ratio can be improved by frequency locking the Ti:Sa laser and power stabilizing the output from the doubling cavity as described in Chap. 8. This was, however, not implemented at the time when the experiment was performed. From Eq. (10.1.4) we see that the statistical uncertainty can only be reduced by a longer data acquisition time (increasing N), and not simply by increasing the frame-rate, since the second term in the expansion is already negligible in our case.

Our measurement was performed with a string of ions, unlike most other lifetime measurements using the shelving technique. In all single-ion experiments, one has to

Reference	Lifetime [ms]
This work	$1149 \pm 14 \pm 4$
Knoop *et al.*, 2003 [150]	1152 ± 23
Donald *et al.*, 2000 [160]	1177 ± 10
Barton *et al.*, 2000 [153]	1168 ± 7
Block *et al.*, 1999 [154]	1100 ± 18
Lidberg *et al.*, 1999 [155]	1090 ± 50

Table 10.2: Overview of recent experimental values for the lifetime of the $3d\,^2D_{5/2}$ state in the $^{40}Ca^+$ ion.

consider the fact that the ion may heat up, so the fluorescence level drops significantly, and the ion can appear to be shelved, although it is not. In our experiment with five ions on a string, we can detect and discard all events of this kind since if one ion or several ions heat up, we would see the remaining ions move or heat up as well. Moreover, with a string of ions, the shelved ions are sympathetically cooled by the unshelved ions, so the number of heating events are expected to be reduced using a string of ions, as compared to single ion experiments. The major drawback of using a string of ions is that ions may change places, which influences the measured lifetime if this is not taken care of in the data analysis, as demonstrated here.

In conclusion, we have measured the lifetime of the metastable $3d\,^2D_{5/2}$ state in the $^{40}Ca^+$ ion using the shelving technique on a string of five ions. Our result agrees roughly at the level of one standard deviation with the already mentioned result obtained by Barton *et al.* [153] and with the value reported in Ref. [150], which together with other recent results are presented in Table 10.2. On the level of two standard deviations, our result agrees with two other measurements where de-shelving due to diode lasers was taken into account [160, 154] and with the storage-ring measurement by Lidberg *et al.* [155] (see Table 10.2). Furthermore, our result agrees with two theoretical values [162, 163]. This newly obtained level of agreement should provide valuable input to future atomic structure calculations and astronomical studies. The importance of this result for our internal state detection scheme is discussed below.

10.2 Internal state detection revisited

From the lifetime experiment we learn two things, which are essential for the internal state detection scheme described in Chap. 4.

First, as already pointed out, it is absolutely necessary that we can tell with large certainty if the ion is fluorescing or shelved in the $^2D_{5/2}$ state. As Fig. 10.4 shows, this is clearly the case using a reasonably short exposure time of 50 ms.

Second, the measured lifetime is important for the efficiency of the detection scheme. If a relatively short lifetime had been measured, as compared to other measurements, this could indicate that we suffered from a significant depletion of the $^2D_{5/2}$ state, which would reduce the efficiency of the internal state detection scheme. As it turns out, our result is amongst the longest lifetimes measured, and as seen from Table 10.1 depletion due to radiation and collision effects is estimated to give rise only to a 4 ms lifetime reduction, which is less than 0.4% of the lifetime. This makes us confident

that depletion effects present no significant reduction of the efficiency of the internal state detection scheme. The small dependence on the laser power may even be further reduced using a recently purchased set of bandpass-filters instead of the longpass-filter, the grating and the diaphragm. Depletion effects should be independent of which trap is used, since the pressure is almost equal in the two vacuum chambers and the laser sources are the same.

STIRAP between the $^2D_{3/2}$ state and the $^2D_{5/2}$ state involves the 850 nm diode laser used here for shelving as well as the 854 nm diode laser. The latter diode laser has been tested; by shelving ions as above, it can clearly be seen that when the 854 nm laser is applied, fluorescence from the ions is regained due to excitation on the $^2D_{5/2}$–$^2P_{3/2}$ transition.

Moreover, the necessary STIRAP pulses can be created, which means that the first STIRAP experiments, which will be done on Doppler laser-cooled ions, are approaching. The first experiments will concern STIRAP from the $^2D_{3/2}$ state to the $^2D_{5/2}$ state, with the ion being initialized to the $^2D_{3/2}$ state by optical pumping (shutting off the 866 nm repumper laser, while leaving the blue cooling laser on). Successful transfer to the $^2D_{5/2}$ state will be detected using the same methods as for the lifetime experiment.

Next step will be experiments concerning the $^2S_{1/2}$– $^2D_{3/2}$ STIRAP process. After initialization in the ground state and transfer by STIRAP to the $^2D_{3/2}$ state, the $^2D_{3/2}$–$^2D_{5/2}$ STIRAP process will be applied. Subsequent fluorescence collection determines if the first STIRAP step was successful.

Chapter 11

Summary and outlook

In this thesis our work towards quantum logic experiments with trapped $^{40}Ca^{+}$ ions is presented.

A linear Paul trap has been specifically designed and constructed for quantum logic experiments and characterized in a series of measurements. The measured oscillation frequencies of ions in the trap are not explainable in terms of the standard theory for a linear Paul trap, but can be explained by including an additional term in the trapping potential. This deviation from the standard theory underlines the importance of our experimental characterization. Furthermore, it has been demonstrated that a refined version of the technique used for measuring the trap parameters should enable non-destructive ion mass measurements, at a level of precision which allows a discrimination between ions (atomic or molecular) having the same number of nucleons, but having different masses due to differences in their nuclear binding energy. The ability to make such a discrimination would be a valuable tool for other research projects within our group.

By demonstrating the so-called shelving technique, we have made the first step towards detection of the qubit state of an ion. Using the shelving technique we have furthermore measured the lifetime of the metastable $3d^2D_{5/2}$ state in the $^{40}Ca^{+}$ ion. This lifetime is interesting in several different areas of physics, however, the many measurements and calculations of the lifetime are scattered over a rather broad range spanning about 25% of the lifetime. Our result is in agreement with the most recent measured values at the level of 2%.

On the theoretical side, we have presented a study of the sideband-cooling scheme for cooling ions to their motional ground state in the trap. This is a crucial step towards quantum logic experiments and our study shows that ground state cooling is feasible using the envisaged scheme.

In addition, we have presented two theoretical proposals combining optical dipole potentials and dipole forces with trapped ions. In one proposal, we show that a high-fidelity two-ion quantum gate can be performed in less than $100\,\mu$s using realistic trap and laser parameters. It should be possible to apply this gate proposal in our own setup. In another proposal, we describe how individual and selective addressing of ions on a string can be obtained utilizing a position-dependent optical dipole potential. This proposal is also applicable in our own setup, but more attractive in other systems.

Currently, work in the laboratory is focussed on the first demonstration of stimulated Raman adiabatic passage (STIRAP) from the $3d\,^2D_{3/2}$ state to the $3d\,^2D_{5/2}$ state in the $^{40}Ca^+$ ion. This is one important step in our scheme for detection of the qubit state of a $^{40}Ca^+$ ion, and it will be our first experiment where the internal state of an ion is controlled in a coherent way. By combining this with a second STIRAP process, from the $4s\,^2S_{1/2}$ ground state to the $3d\,^2D_{3/2}$ state, it will be possible to detect the qubit state of an ion. This will enable a demonstration of Rabi-oscillations on the Raman transition between the two ground state sublevels of the $^{40}Ca^+$ ion, and prepare the way for sideband cooling and later quantum logic operations.

Appendix A

Derivations

A.1 Sideband cooling with second-order contributions to the rate equation

A.1.1 Solution to the second-order rate equation

Here we derive the solution given in Eq. (3.3.21), to the second-order rate equation in Eq. (3.3.20).

Starting from Eq. (3.3.20) and using $\overline{n^2} = 2\overline{n}^2 + \overline{n}$ valid for a thermal distribution (derived below), we find

$$\dot{\overline{n}} = -\underbrace{4\eta_{eg}^4(A_{--} - A_{++})}_{a}\overline{n}^2 - \underbrace{[\eta_{eg}^2(A_- - A_+) - 8\eta_{eg}^4 A_{++}]}_{b}\overline{n} \tag{A.1.1}$$

$$+ \underbrace{\eta_{eg}^2 A_+ + 4\eta_{eg}^4 A_{++}}_{c}, \tag{A.1.2}$$

which can be written as

$$\frac{d}{dt}\overline{n} = \frac{d}{dt}(\overline{n} + \frac{b}{2a}) = -a(\overline{n} + \frac{b}{2a})^2 + \frac{b^2}{4a} + c. \tag{A.1.3}$$

Solving this differential equation for $(\overline{n} + b/2a)$, by multiplying with dt and integrating the resulting equation, it is found that

$$\begin{aligned}\overline{n}(t) =& \frac{1}{a}\sqrt{b^2/4 + ac}\,\coth\left[\sqrt{b^2/4 + ac}\,(t + t_0)\right] - \frac{b}{2a} \\ \equiv& \frac{W^{(2)}}{2W'}\left\{\coth\left[W^{(2)}(t + t_0)/2\right] - 1\right\} + \overline{n}_{SS}^{(2)} \\ =& \frac{W^{(2)}}{W'}\left[e^{W^{(2)}(t+t_0)} - 1\right]^{-1} + \overline{n}_{SS}^{(2)}\end{aligned} \tag{A.1.4}$$

with W', $W^{(2)}$ and $\overline{n}_{SS}^{(2)}$ defined as in Eqs. (3.3.22)–(3.3.24) and t_0 a constant. From

the initial condition

$$\overline{n}_0 \equiv \overline{n}(t=0) = \frac{W^{(2)}}{W'}\left[e^{W^{(2)}t_0} - 1\right]^{-1} + \overline{n}^{(2)}_{SS}, \tag{A.1.5}$$

$e^{W^{(2)}t_0}$ can be determined and inserted into Eq. (A.1.4), which yields the solution stated in Eq. (3.3.21).

One way of establishing the relation $\overline{n^2} = 2\overline{n}^2 + \overline{n}$ is to take a small 'detour' around the two-photon correlation function for a single-mode light-field at zero delay [171]:

$$g^{(2)}(0) = \frac{< a^\dagger a^\dagger a a >}{< a^\dagger a >^2} = \frac{< a^\dagger (a a^\dagger - 1) a >}{< a^\dagger a >^2} = \frac{< n^2 - n >}{< n >^2}, \tag{A.1.6}$$

where, formally, a and $a^\dagger$ are harmonic oscillator annihilation and creation operators. For a thermal distribution $g^{(2)}(0) = 2$ [171], which immediately yields $\overline{n^2} = 2\overline{n}^2 + \overline{n}$ ($< n > \equiv \overline{n}$, $< n^2 > \equiv \overline{n^2}$) .

A.1.2 Derivation of Eqs. (3.3.26) and (3.3.27)

Here, Eqs. (3.3.26) and (3.3.27) are derived from Eqs. (3.3.22)–(3.3.24) using Eqs. (3.3.9), (3.3.17) and $\Omega, \Gamma \ll \omega_z$.

We start out by re-arranging Eq. (3.3.23) to get

$$W^{(2)} = W^{(1)}\sqrt{1 + 16\eta_{eg}^2 \frac{A_+ A_{--} - A_- A_{++}}{(A_- - A_+)^2} + 64\eta_{eg}^4 \frac{A_{++}A_{--}}{(A_- - A_+)^2}}. \tag{A.1.7}$$

Using Eqs. (3.3.9), (3.3.17) and $\Omega, \Gamma \ll \omega_z$, it can be found that

$$\frac{A_+ A_{--} - A_- A_{++}}{(A_- - A_+)^2} = \left(\frac{\Gamma}{2\omega_z}\right)^2 (\alpha^2 - \tilde{\alpha} - 1/9) \tag{A.1.8}$$

and

$$\frac{A_{++}A_{--}}{(A_- - A_+)^2} = \left(\frac{\Gamma}{2\omega_z}\right)^2 (\alpha\tilde{\alpha} + \alpha^2/4 + \alpha/9). \tag{A.1.9}$$

Inserting these expression into Eq. (A.1.7) and expanding to first order in $(\Gamma/\omega_z)^2$, Eq. (3.3.26) then follows.

In order to find $\overline{n}^{(2)}_{SS}$, we first calculate the second term in Eq. (3.3.24):

$$\frac{A_{++}}{A_{--} - A_{++}} = \left(\frac{\Gamma}{2\omega_z}\right)^2 [\tilde{\alpha}/\alpha + 1/4 + 1/(9\alpha)]. \tag{A.1.10}$$

By inserting this expression and Eq. (3.3.26) into Eq. (3.3.24), Eq. (3.3.27) follows immediately.

A.2 Displacements and phases in the geometric Controlled-Z gate

In this section the time-dependent displacements $\beta(t)$ and the phases $\phi(t)$ in the gate proposal of Sec. 6.2 are stated for the center-of-mass mode as well as the breathing mode. Using the definitions of the f-functions in Eq. (6.2.20) for the center-of-mass mode and carrying out the integral in Eq. (6.2.11) one arrives at the following expressions for the displacement

$$\beta_+(\downarrow\downarrow,t) = \beta_{0+} + \beta_{1+} \tag{A.2.1}$$
$$\beta_+(\downarrow\uparrow,t) = \beta_{0+} + \beta_{2+} \tag{A.2.2}$$
$$\beta_+(\uparrow\downarrow,t) = \beta_{0+} - \beta_{2+} \tag{A.2.3}$$
$$\beta_+(\uparrow\uparrow,t) = \beta_{0+} - \beta_{1+} \tag{A.2.4}$$

where

$$\beta_{0+} = -i\frac{f_{0+}}{\hbar\omega_z}(1-e^{-i\omega_z t}) \tag{A.2.5}$$
$$\beta_{1+} = \frac{f_{1+}}{2\hbar}\left(\frac{1-e^{-i(\omega_z+\Omega)t}}{\omega_z+\Omega} - \frac{1-e^{-i(\omega_z-\Omega)t}}{\omega_z-\Omega}\right) \tag{A.2.6}$$
$$\beta_{2+} = \frac{f_{2+}}{f_{1+}}\beta_{1+}. \tag{A.2.7}$$

At the end of the gate operation, where $t = T = 2\pi n/\omega_z$, the displacement is zero for all four combinations of qubit states, as requested. Inserting these expressions into Eq.(6.2.12) and carrying out the integral, it can be found that

$$\phi_+(\downarrow\downarrow,t) = \phi_{1+} + \phi_{2+} + \phi_{3+} + \phi_{4+} \tag{A.2.8}$$
$$\phi_+(\downarrow\uparrow,t) = \phi_{1+} + \phi_{5+} + \phi_{6+} + \phi_{7+} \tag{A.2.9}$$
$$\phi_+(\uparrow\downarrow,t) = \phi_{1+} - \phi_{5+} - \phi_{6+} + \phi_{7+} \tag{A.2.10}$$
$$\phi_+(\uparrow\uparrow,t) = \phi_{1+} - \phi_{2+} - \phi_{3+} + \phi_{4+}, \tag{A.2.11}$$

where

$$\phi_{1+} = \left(\frac{f_{0+}}{\hbar\omega_z}\right)^2 [\omega_z t - \sin(\omega_z t)] \tag{A.2.12}$$
$$\phi_{2+} = \frac{f_{0+}f_{1+}}{\hbar^2(\omega_z^2-\Omega^2)}\left[\frac{\Omega[\cos(\omega_z t)-1]}{\omega_z} - \frac{\omega_z[\cos(\Omega t)-1]}{\Omega}\right] \tag{A.2.13}$$
$$\phi_{3+} = \frac{f_{0+}f_{1+}}{(\hbar\omega_z)^2}\left[\frac{\omega_z\{1-\cos[(\omega_z-\Omega)t]\}}{2(\omega_z-\Omega)} - \frac{\omega_z\{1-\cos[(\omega_z+\Omega)t]\}}{2(\omega_z+\Omega)} - \frac{\omega_z[\cos(\Omega t)-1]}{\Omega}\right] \tag{A.2.14}$$
$$\phi_{4+} = \frac{f_{1+}^2}{(2\hbar)^2}\left[\frac{\sin[(\omega_z+\Omega)t] + \sin[(\omega_z-\Omega)t] - (\omega_z/\Omega)\sin(\Omega t) + 2\omega_z t}{\omega_z^2-\Omega^2}\right. \tag{A.2.15}$$
$$\left. - \frac{\sin[(\omega_z+\Omega)t]}{(\omega_z+\Omega)^2} - \frac{\sin[(\omega_z-\Omega)t]}{(\omega_z-\Omega)^2}\right]$$

and where $\phi_{5+} = (f_{2+}/f_{1+})\phi_{2+}$, $\phi_{6+} = (f_{2+}/f_{1+})\phi_{3+}$ and $\phi_{7+} = (f_{2+}/f_{1+})^2\phi_{4+}$.

For the breathing mode, the displacement and the phase can be found in exactly the same way as above, using the function f_- defined in Eq. (6.2.5) instead of f_+. To obtain the phases ϕ_- the following replacements should be made in Eqs. (A.2.8)-(A.2.15): $\phi_+ \to \phi_-$, $\phi_{i+} \to \phi_{i-}$ $(i = 1-7)$, $\omega_z \to \sqrt{3}\omega_z$ and $f_{j+} \to f_{j-}$ $(j = 0-2)$, where $f_{0-} = f_{0+}(\tilde{F}_2 - \tilde{F}_1)/[\sqrt[4]{3}(\tilde{F}_2 + \tilde{F}_1)]$ and f_{1-} and f_{2-} are defined in Eq. (6.2.32).

A.3 The coupled motion of two trapped ions

Here we consider the situation described in Sec. 9.3, with two singly-charged ions of different masses confined in the axial harmonic potential of a linear Paul trap, with one ion being subject to a constant light-pressure force, a damping laser-cooling force and a modulation force $F_{mod}\cos(\omega_{mod}t)$. From the coupled equations of motion for the two ions, the relative phase between the motion of the laser-cooled ion and the modulation force is derived. The derivation is valid to first order in $\delta z/\Delta z$.

Using the same notation as in Sec. 9.3, we have the following equations of motion:

$$\ddot{z}_1 + \gamma\dot{z}_1 + \omega_1^2 z_1 = -\frac{e^2}{4\pi\epsilon_0 m_1(z_2 - z_1)^2} + \frac{F_{light}}{m_1} + \frac{F_{mod}}{m_1}\cos(\omega_{mod}t) \tag{A.3.1}$$

$$\ddot{z}_2 + \omega_2^2 z_2 = \frac{e^2}{4\pi\epsilon_0 m_2(z_2 - z_1)^2}. \tag{A.3.2}$$

To solve them, we first expand the Coulomb force on Ion 2, $F_{Coul,2}$, around the equilibrium distance, $\Delta z + \delta z$, as follows

$$F_{Coul,2} = \frac{e^2}{4\pi\epsilon_0(z_2 - z_1)^2} \approx F_0 - F_1\frac{z_2 - z_1 - (\Delta z + \delta z)}{\Delta z} \tag{A.3.3}$$

where

$$F_0 = \frac{e^2}{4\pi\epsilon_0(\Delta z + \delta z)^2} \approx \frac{1}{2}m_1\omega_1^2\Delta z(1 - 2\delta z/\Delta z) \tag{A.3.4}$$

$$F_1 = \frac{2e^2\Delta z}{4\pi\epsilon_0(\Delta z + \delta z)^3} \approx m_1\omega_1^2\Delta z(1 - 3\delta z/\Delta z). \tag{A.3.5}$$

Inserting this linearized expression for the Coulomb force in the equation of motion for z_2, we find

$$z_1 = \frac{m_2\Delta z}{F_1}\ddot{z}_2 + \left(\frac{m_2\omega_2^2\Delta z}{F_1} + 1\right)z_2 - \frac{3}{2}(\Delta z + \delta z). \tag{A.3.6}$$

Inserting this expression for z_1 and its time derivatives in the equation of motion for z_1, we obtain after some calculations the following fourth order differential equation in z_2:

$$\begin{aligned}\dddot{\ddot{z}}_2 + \gamma\dddot{z}_2 + 2(\omega_1^2 + \omega_2^2)(1 - 3\delta z/2\Delta z)\ddot{z}_2 + 2\gamma\omega_2^2(1 - 3\delta z/2\Delta z)\dot{z}_2 + 3\omega_1^2\omega_2^2(1 - 2\delta z/\Delta z)z_2 \\ = 3\omega_1^2\omega_2^2\Delta z(1 - 4\delta z/\Delta z)/2 + \frac{\omega_2^2 F_{mod}}{m_1}(1 - 3\delta z/\Delta z)\cos(\omega_{mod}t).\end{aligned} \tag{A.3.7}$$

The first term on the r.h.s. is constant and can be removed by introducing $z = z_2 - z_{2,eq}$ [see Eq. (9.3.4)] and writing the differential equation in terms of z. Furthermore, putting the resulting differential equation on complex form, we obtain

$$\dddot{z} + \gamma\ddot{z} + 2(\omega_1^2 + \omega_2^2)(1 - 3\delta z/2\Delta z)\ddot{z} + 2\gamma\omega_2^2(1 - 3\delta z/2\Delta z)\dot{z} + 3\omega_1^2\omega_2^2(1 - 2\delta z/\Delta z)z$$
$$= \frac{\omega_2^2 F_{mod}}{m_1}(1 - 3\delta z/\Delta z)\exp(i\omega_{mod}t) \tag{A.3.8}$$

with z being a complex variable. Now, making the Ansatz $z = z_0\exp(i\omega_{mod}t)$, with z_0 complex, we find

$$\omega_{mod}^4 - i\gamma\omega_{mod}^3 - 2\omega_{mod}^2(\omega_1^2 + \omega_2^2)(1 - 3\delta z/2\Delta z) + 2i\gamma\omega_{mod}\omega_2^2(1 - 3\delta z/2\Delta z)$$
$$+ 3\omega_1^2\omega_2^2(1 - 2\delta z/\Delta z) = \frac{\omega_2^2 F_{mod}}{m_1}(1 - 3\delta z/\Delta z)z_0^{-1}. \tag{A.3.9}$$

Writing $z_0 = |z_0|e^{i\varphi_1}$, we then have that $z_2 = \mathrm{Re}[z] + z_{2,eq} = |z_0|\cos(\omega_{mod}t + \varphi_1) + z_{2,eq}$, where

$$\cos(\varphi_1) = \frac{\omega_{mod}^4 - 2\omega_{mod}^2(\omega_1^2 + \omega_2^2)(1 - 3\delta z/2\Delta z) + 3\omega_1^2\omega_2^2(1 - 2\delta z/\Delta z)}{N_0}, \tag{A.3.10}$$

and where N_0 is the norm of the l.h.s. of Eq. (A.3.9). From the expression for z_2, we could go back and find z_1 (the position of the observed laser cooled ion), but all we need to know is the phase relative to the phase of the driving force, which is the same as for z_2, i.e., φ_1. From Eqs. (A.3.10) and (9.3.2), it follows that $\cos(\varphi_1) = 0$ exactly at ω_{COM} and ω_{br} given in Eq. (9.3.11), thus showing that also in the case considered here, the mode-frequencies can be determined by picking out the amplitude of the in-phase component as described in Sec. 9.3.

Appendix B

The Ca^+ ion

B.1 Abundance of Ca-isotopes

The natural abundance of the stable isotopes of calcium is listed in Table B.1

Isotope	Abundance
40	96.941%
42	0.647%
43	0.135%
44	2.086%
46	0.004%
48	0.187%

Table B.1: Abundance of the stable isotopes of calcium [146].

B.2 Transitions in the $^{40}Ca^+$ ion

For the dipole-allowed transitions shown in Fig. 3.3, some relevant data are listed in Table B.2.

The coupling strength for dipole-allowed transitions between the various sub-levels is characterized by the values of Γ given in Table B.2 and the Clebsch-Gordan coefficients (see, e.g., Ref. [22] for a definition), which are listed in Tables B.3–B.5.

Transition	Wavelength [nm]	$\Gamma/2\pi$ [MHz]	Sat. intensity [mW/cm^2]
$^2S_{1/2}$-$^2P_{1/2}$	396.847	20.7	43.3
$^2S_{1/2}$-$^2P_{3/2}$	393.366	21.5	46.2
$^2D_{3/2}$-$^2P_{1/2}$	866.214	1.69	0.34
$^2D_{3/2}$-$^2P_{3/2}$	849.802	0.177	0.038
$^2D_{5/2}$-$^2P_{3/2}$	854.209	1.58	0.33

Table B.2: Data for dipole-allowed transitions in $^{40}Ca^+$, as shown in Fig. 3.3. Transition wavelengths are measured in air [25, 108]. $\Gamma/2\pi$ is the transition rate [25, 108]. Saturation intensities are calculated according to Eq. (2.1.30), using the relevant transition rate and transition frequency for Γ and ω_{eg}, respectively.

	$^2S_{1/2}(-1/2)$	$^2S_{1/2}(+1/2)$
$^2P_{1/2}(-1/2)$	$-\sqrt{1/3}$	$\sqrt{2/3}$
$^2P_{1/2}(+1/2)$	$-\sqrt{2/3}$	$\sqrt{1/3}$
$^2P_{3/2}(-3/2)$	1	-
$^2P_{3/2}(-1/2)$	$\sqrt{2/3}$	$\sqrt{1/3}$
$^2P_{3/2}(+1/2)$	$\sqrt{1/3}$	$\sqrt{2/3}$
$^2P_{3/2}(+3/2)$	-	1

Table B.3: Clebsch-Gordan coefficients for transitions between the $^2S_{1/2}$ state and the $^2P_{1/2}$ and $^2P_{3/2}$ states.

	$^2D_{3/2}(-3/2)$	$^2D_{3/2}(-1/2)$	$^2D_{3/2}(+1/2)$	$^2D_{3/2}(+3/2)$
$^2P_{1/2}(-1/2)$	$\sqrt{1/2}$	$-\sqrt{1/3}$	$\sqrt{1/6}$	-
$^2P_{1/2}(+1/2)$	-	$\sqrt{1/6}$	$-\sqrt{1/3}$	$\sqrt{1/2}$
$^2P_{3/2}(-3/2)$	$-\sqrt{3/5}$	$\sqrt{2/5}$	-	-
$^2P_{3/2}(-1/2)$	$-\sqrt{2/5}$	$-\sqrt{1/15}$	$\sqrt{8/15}$	-
$^2P_{3/2}(+1/2)$	-	$-\sqrt{8/15}$	$\sqrt{1/15}$	$\sqrt{2/5}$
$^2P_{3/2}(+3/2)$	-	-	$-\sqrt{2/5}$	$\sqrt{3/5}$

Table B.4: Clebsch-Gordan coefficients for transitions between the $^2D_{3/2}$ state and the $^2P_{1/2}$ and $^2P_{3/2}$ states.

	$^2P_{3/2}(-3/2)$	$^2P_{3/2}(-1/2)$	$^2P_{3/2}(+1/2)$	$^2P_{3/2}(+3/2)$
$^2D_{5/2}(-5/2)$	$\sqrt{2/3}$	-	-	-
$^2D_{5/2}(-3/2)$	$-\sqrt{4/15}$	$\sqrt{2/5}$	-	-
$^2D_{5/2}(-1/2)$	$\sqrt{1/15}$	$-\sqrt{2/5}$	$\sqrt{1/5}$	-
$^2D_{5/2}(+1/2)$	-	$\sqrt{1/5}$	$-\sqrt{2/5}$	$\sqrt{1/15}$
$^2D_{5/2}(+3/2)$	-	-	$\sqrt{2/5}$	$-\sqrt{4/15}$
$^2D_{5/2}(+5/2)$	-	-	-	$\sqrt{2/3}$

Table B.5: Clebsch-Gordan coefficients for transitions between the $^2D_{5/2}$ state and the $^2P_{3/2}$ state.

B.3 Zeeman-splitting in the $^{40}Ca^{+}$ ion

The Zeeman-splitting of the magnetic sublevels of $^{40}Ca^{+}$ is given by:

$$\Delta E_{Zeeman} = m_J g_J \mu_B B, \tag{B.3.1}$$

where m_J is the magnetic quantum number, μ_B is the Bohr magneton, B is the magnetic field strength and g_J is the Landé g-factor,

$$g_J = 1 + \frac{J(J+1) + S(S+1) - L(L+1)}{2J(J+1)}. \tag{B.3.2}$$

Values of g_J are listed in Table B.6 for the lowest lying states of the $^{40}Ca^{+}$ ion. For

State	g_J
$^2S_{1/2}$	2
$^2P_{1/2}$	2/3
$^2P_{3/2}$	4/3
$^2D_{3/2}$	4/5
$^2D_{5/2}$	6/5

Table B.6: Values of g_J for the lowest lying levels of the $^{40}Ca^{+}$ ion.

$B = 1\,\text{Gauss}$, the Zeeman-splitting of the ground-state sublevels is $2\pi \times 2.8\,\text{Mhz}$.

Appendix C

Sideband cooling – quantum Monte Carlo simulations

C.1 The simulation program

In the Monte Carlo simulation program, the coefficients in the wavefunction in Eq. (3.5.1) are evolved in time according to the Monte Carlo wavefunction method [59, 60]. This method contains two essential steps: a coherent evolution of the wavefunction and random decisions of the outcome of stochastic processes.

The simulation program is written in the C/C++ programming language. The coherent evolution of the wavefunction is performed according to Eqs. (3.5.6)–(3.5.8) in timesteps of duration $\Delta t = (2\Gamma_{1/2})^{-1}$, using the fourth order Runge-Kutta algorithm `rk4` from *Numerical Recipes in C* [172]. Using smaller or a little larger timesteps did not alter the results of the simulations significantly. Random decisions are made using random numbers uniformly distributed between 0 and 1 with 30 bit resolution, formed from the random numbers generated by two calls of the library function `rand()`. A stochastic process taking place with probability *dp*, is said to happen if a (30 bit) random number is less than *dp*.

In order to exploit the fact that the higher lying vibrational states become irrelevant, when population is driven towards the lowest lying vibrational states during sideband cooling, a dynamic cut-off was introduced in the program. This means that when it eventually occurs during the cooling process, that the population in the uppermost vibrational level $|n_{upper}\rangle$ is less than some number, ϵ, then the coefficients $C_i^{n_{upper}}$ are set to zero and left out of the calculation. The bottom three levels, where $n = 0 - 2$, cannot be removed by the dynamic cut-off. $\epsilon = 10^{-4}$ was used in all simulations and it was tested for each 1000 timesteps if the uppermost level could be removed. When cooling worked poorly, a simulation of 100 histories over 10^5 timesteps with 6 vibrational levels ($n_{max} = 5$) in the wavefunction, performed on a 500 MHz PC [1], typically lasted 17 hours, while if the cooling was very efficient, the dynamic cut-off could reduce the computation time to about 5 hours.

The individual steps in the simulation program are the following: First, the coeffi-

[1] More or less the standard at the time the simulations were made.

cients C_i^n ($n = 0 - n_{max}$) in the wavefunction are initialized to the values $C_2^n = 0$ and $C_1^n = C_3^n = \sqrt{\overline{n}_0^n/[2(\overline{n}_0+1)^{n+1}]}$. After initialization, the coefficients are normalized, such that $\sum_{i=1}^{3}\sum_{n=0}^{n_{max}} |C_i^n|^2 = 1$. Following that, the program runs through steps 1-6 below in a loop, typically for 10^5 timesteps.

1. The probability dp for a decay from $|2\rangle$ in a timestep Δt is calculated; $dp = \Gamma_{1/2}\Delta t \sum_n |C_2^n|^2$ is typically 10^{-4}.
2. The coefficients are evolved according to Eqs. (3.5.6)-(3.5.8) in a timestep Δt using `rk4` [172].
3. Based on the probability dp, calculated in step 1, it is randomly decided if a spontaneous decay from $|2\rangle$ takes place. If 'no', the program jumps to step 6. If 'yes', it continues to step 4.
4. A series of random decisions determines if the vibrational state changes in the decay.
   (a) A random decision decides if the decay goes to $|1\rangle$, which, depending on the choice of excited state, happens with probability 1/3 or 2/3, or if the decay goes to $|3\rangle$ instead.
   (b) The direction of the emitted photon is found randomly, with the probability for emission in a given direction governed by the distribution-function W for the radiation pattern, which depends on the choice of excited state [52]. See the definitions in Eq. (3.5.23).
   (c) Given the emission-direction, characterized by a wave-vector $\boldsymbol{k}_{decay}$, the Lamb-Dicke parameter $\eta_{decay} = \boldsymbol{k}_{decay} \cdot \boldsymbol{z}_0$ can be calculated and from that the probability for changing the vibrational state by $\Delta n = 0, \pm 1, \pm 2$. A random decision determines the change in the vibrational state.
5. The wavefunction is collapsed onto the internal state $|i\rangle$ ($i = 1, 3$) to which the decay happened, and the distribution over the vibrational levels is shifted by Δn, i.e., $C_i^n \mapsto C_i^{n+\Delta n}$ and $C_i^{n_{max}+\Delta n} = 0$ (if $\Delta n < 0$) or $C_i^{0+\Delta n} = 0$ (if $\Delta n > 0$).
6. The coefficients are normalized such that $\sum_{i=1}^{3}\sum_{n=0}^{n_{max}} |C_i^n|^2 = 1$.

C.2 Time evolution of coefficients

In this section the state $|2\rangle$ is adiabatically eliminated with respect to the Raman-transition and Eqs. (3.5.6)–(3.5.8) are derived.

The time-dependence of the coefficients C_i^n in the wavefunction $|\psi\rangle$ in Eq. (3.5.1) is governed by the time-dependent Schrödinger equation

$$i\hbar \frac{\partial |\psi\rangle}{\partial t} = H |\psi\rangle \tag{C.2.1}$$

or

$$i\hbar \sum_{i=1}^{3}\sum_{n=0}^{n_{max}} \dot{C}_i^n(t) |i,n\rangle = H \sum_{i=1}^{3}\sum_{n=0}^{n_{max}} C_i^n(t) |i,n\rangle , \tag{C.2.2}$$

where

$$H = H_{trap} + H_{ion} + H_{Raman} + H_{pump} \tag{C.2.3}$$

with the individual Hamiltonians defined in Eqs. (3.5.3)–(3.5.5). First we treat the case $H = H_{trap} + H_{ion} + H_{Raman}$ and then we consider H_{pump} separately.

Taking $H = H_{trap} + H_{ion} + H_{Raman}$ and following Ref. [173], it is useful to consider the time-dependence of the coefficients

$$B_i^n(t) = C_i^n(t) e^{iH_{ii}^{nn} t/\hbar}, \tag{C.2.4}$$

where

$$H_{ii}^{nn} = \langle i, n | \, H \, | i, n \rangle = E_i + n\hbar\omega_z. \tag{C.2.5}$$

From Eq. (C.2.2) it follows that the coefficients B_i^n evolve in time according to

$$\dot{B}_1^n(t) = -i\frac{\Omega_{12}^*}{2} e^{-i(\Delta+\omega_z)t} \sum_{n'} B_2^{n'}(t) e^{-i\omega_z(n'-n)t} U_{nn'}(-\eta_{12}) \tag{C.2.6}$$

$$\begin{aligned}\dot{B}_2^{n'}(t) = &-i\frac{\Omega_{12}}{2} e^{i(\Delta+\omega_z)t} \sum_{n} B_1^{n}(t) e^{i\omega_z(n'-n)t} U_{n'n}(\eta_{12}) \\ &-i\frac{\Omega_{32}}{2} e^{i(\Delta+\delta)t} \sum_{n''} B_3^{n''}(t) e^{i\omega_z(n'-n'')t} U_{n'n''}(\eta_{32})\end{aligned} \tag{C.2.7}$$

$$\dot{B}_3^{n''}(t) = -i\frac{\Omega_{32}^*}{2} e^{-i(\Delta+\delta)t} \sum_{n'} B_2^{n'}(t) e^{-i\omega_z(n'-n'')t} U_{n''n'}(-\eta_{32}), \tag{C.2.8}$$

where

$$\eta_{i2} = \boldsymbol{k}_{i2} \cdot \boldsymbol{z}_0, \qquad i = 1, 3. \tag{C.2.9}$$

Assuming that the coefficients B_1^n and $B_3^{n''}$ change on a timescale much longer than Δ^{-1}, we can integrate Eq. (C.2.7) with B_1^n and $B_3^{n''}$ constant. The expression obtained for $B_2^{n'}$ can then be inserted into Eqs. (C.2.6) and (C.2.8), which, under the assumption

$$\Delta \gg |\Omega_{12}|, \, |\Omega_{32}|, \, |\delta| \, , \, \omega_z, \tag{C.2.10}$$

yields

$$\dot{B}_1^n(t) = i\frac{|\Omega_{12}|^2}{4\Delta} B_1^n(t) + i\frac{\Omega_{12}^*\Omega_{32}}{4\Delta} e^{i(\delta-\omega_z)t} \sum_{n''} B_3^{n''}(t) e^{i\omega_z(n-n'')t} U_{nn''}(-\eta) \tag{C.2.11}$$

$$\dot{B}_3^{n''}(t) = i\frac{\Omega_{12}\Omega_{32}^*}{4\Delta} e^{-i(\delta-\omega_z)t} \sum_{n} B_1^{n}(t) e^{-i\omega_z(n-n'')t} U_{n''n}(\eta) + i\frac{|\Omega_{32}|^2}{4\Delta} B_3^{n''}(t), \tag{C.2.12}$$

where

$$\eta = \eta_{12} - \eta_{32}. \tag{C.2.13}$$

These solutions are consistent with the assumption that B_1^n and $B_3^{n''}$ change much slower than Δ^{-1}. From the definition in Eq. (C.2.4), it follows that the original coefficients C_i^n evolve as:

$$\dot{C}_1^n(t) = -i\left(n\omega_z - \frac{|\Omega_{12}|^2}{4\Delta}\right)C_1^n(t) + i\frac{\Omega^*_{Raman}}{4}e^{i\omega t}\sum_{n''}C_3^{n''}(t)U_{nn''}(-\eta) \tag{C.2.14}$$

$$\dot{C}_2^{n'}(t) = -i\left(\frac{E_2}{\hbar} + n'\omega_z\right)C_2^{n'}(t) \tag{C.2.15}$$

$$\dot{C}_3^{n''}(t) = -i\left(\frac{E_3}{\hbar} + n''\omega_z - \frac{|\Omega_{32}|^2}{4\Delta}\right)C_3^{n''}(t) + i\frac{\Omega_{Raman}}{4}e^{-i\omega t}\sum_{n}C_1^{n}(t)U_{n''n}(\eta), \tag{C.2.16}$$

where

$$\omega = \omega_{12} - \omega_{32}. \tag{C.2.17}$$

For the pumping transition, it immediately follows from the time-dependent Schrödinger equation with $H = H_{pump}$ that

$$\dot{C}_2^{n'}(t) = -i\Omega_{pump}e^{-i\omega_{pump}t}\sum_{n''}C_3^{n}(t)U_{n'n''}(\eta_{pump}) \tag{C.2.18}$$

$$\dot{C}_3^{n''}(t) = -i\Omega^*_{pump}e^{i\omega_{pump}t}\sum_{n'}C_2^{n'}(t)U_{n''n'}(-\eta_{pump}). \tag{C.2.19}$$

Now, combining Eqs. (C.2.18) and (C.2.19) with Eqs. (C.2.14)–(C.2.16), the full coherent time development of the coefficients are obtained. Following the Monte Carlo wavefunction method an extra term, $-\Gamma C_2^{n'}/2$, is added to $\dot{C}_2^{n'}$ to include spontaneous decay. The quickly oscillating terms $e^{\pm i\omega t}$ and $e^{\pm i\omega_{pump}t}$ can be removed by introducing the coefficients $\widetilde{C}_1^n = C_1^n e^{i\omega_z t}$, $\widetilde{C}_2^{n'} = C_2^{n'}e^{i(E_2/\hbar+\delta)t}$ and $\widetilde{C}_3^{n''} = C_3^{n''}e^{i(E_3/\hbar+\delta)t}$, which finally yields Eqs. (3.5.6)–(3.5.8).

Bibliography

[1] D. Leibfried, R. Blatt, C. Monroe, and D. Wineland, Rev. Mod. Phys. **75**, 281 (2003).

[2] P. W. Shor, SIAM J. Comput. **26**, 1484 (1997).

[3] L. K. Grover, Phys. Rev. Lett. **79**, 325 (1997).

[4] J. I. Cirac and P. Zoller, Phys. Rev. Lett. **74**, 4091 (1995).

[5] J. J. Bollinger, W. M. Itano, D. J. Wineland, and D. J. Heinzen, Phys. Rev. A **54**, R4649 (1996).

[6] Physics World, Special Issue on Quantum Information, 03/98.

[7] T. Laustsen, Ph.D. thesis, Department of Physics and Astronomy, University of Aarhus, Denmark, 2003.

[8] A. Einstein, B. Podolsky, and N. Rosen, Phys. Rev. **47**, 777 (1935).

[9] C. A. Sackett *et al.*, Nature **404**, 256 (2000).

[10] A. Aspect, J. Dalibard, and G. Roger, Phys. Rev. Lett. **49**, 1804 (1982).

[11] A. Rauschenbeutel *et al.*, Science **288**, 2024 (2000).

[12] B. Julsgaard, A. Kozhekin, and E. S. Polzik, Nature **413**, 400 (2001).

[13] F. Schmidt-Kaler *et al.*, Nature **422**, 408 (2003).

[14] D. Leibfried *et al.*, Nature **422**, 412 (2003).

[15] S. Gulde *et al.*, Nature **421**, 48 (2003).

[16] Q. A. Turchette *et al.*, Phys. Rev. Lett. **81**, 3631 (1998).

[17] M. A. Rowe *et al.*, Nature **409**, 791 (2001).

[18] M. A. Nielsen and I. L. Chuang, *Quantum Computation and Quantum Information* (Cambridge University Press, Cambridge, 2000).

[19] A. Steane, Appl. Phys. B. **64**, 623 (1997).

[20] H. J. Metcalf and P. van der Straten, *Laser Cooling and Trapping* (Springer-Verlag, New York, 1999).

[21] P. W. Milonni and J. H. Eberly, *Lasers* (John Wiley & Sons, New York, 1988).

[22] B. H. Bransden and C. J. Joachain, *Physics of Atoms and Molecules* (Longman Scientific & Technical, England, 1983).

[23] L. Allen and J. H. Eberly, *Optical resonance and two-level atoms* (Dover Publications, New York, 1975).

[24] D. Wineland *et al.*, J. Res. Natl. Inst. Stand. Technol. **103**, 259 (1998).

[25] D. James, Appl. Phys. B **66**, 181 (1998).

[26] The Nobel Foundation, Press release, `http://www.nobel.se`.

[27] T. Hänsch and A. Schawlow, Opt. Comm. **13**, 68 (1975).

[28] D. J. Wineland and H. Dehmelt, Bull. Am. Phys. Soc. **20**, 637 (1975).

[29] D.J.Wineland and W. M. Itano, Phys. Rev. A **20**, 1521 (1979).

[30] C. Cohen-Tannoudji, *Atomic motion in laser light* (Les Houches, Session LIII, editors J. Dalibard, J.-M- Raimond and J. Zinn-Justin, 1990).

[31] D. Reiss, A. Lindner, and R. Blatt, Phys. Rev. A **54**, 5133 (1996).

[32] I. Siemers *et al.*, Europhys. Lett. **18**, 139 (1992).

[33] D. Enzer *et al.*, Phys. Rev. Lett. **85**, 2466 (2000).

[34] H. Rohde *et al.*, J. Opt. B: Quantum Semiclass. Opt. **3**, S34 (2001).

[35] C. Monroe *et al.*, Phys. Rev. Lett. **75**, 4011 (1995).

[36] F. Diedrich, J. Bergquist, W. Itano, and D. J. Wineland, Phys. Rev. Lett. **62**, 403 (1989).

[37] C. Roos *et al.*, Phys. Rev. Lett. **83**, 4713 (1999).

[38] E. Peik *et al.*, Phys. Rev. A **60**, 439 (1999).

[39] B. E. King *et al.*, Phys. Rev. Lett. **81**, 1525 (1998).

[40] S. Hamann *et al.*, Phys. Rev. Lett. **80**, 4149 (1998).

[41] I. Bouchoule, M. Morinaga, C. Salomon, and D. S. Petrov, Phys. Rev. A **65**, 033402 (2002).

[42] V. Vuletic, C. Chin, A. J. Kerman, and S. Chu, Phys. Rev. Lett. **81**, 5768 (1998).

[43] H. Perrin *et al.*, Europhys. Lett. **46**, 141 (1999).

[44] G. Morigi, J. Eschner, and C. H. Keitel, Phys. Rev. Lett. **85**, 4458 (2000).

[45] C. F. Roos *et al.*, Phys. Rev. Lett. **85**, 5547 (2000).

[46] F. Schmidt-Kaler *et al.*, Appl. Phys. B **73**, 807 (2001).

[47] S. Stenholm, Rev. Mod. Phys. **58**, 699 (1986).

[48] J. Javanainen and S. Stenholm, Appl. Phys. **24**, 151 (1981).

[49] M. Lindberg and S. Stenholm, J. Phys. B: At. Mol. Phys. **17**, 3375 (1984).

[50] J. Javanainen, M. Lindberg, and S. Stenholm, J. Opt. Soc. Am. B **1**, 111 (1984).

[51] M. Lindberg, J. Phys. B: At. Mol. Phys. **17**, 2129 (1984).

[52] A. Corney, *Atomic and Laser Spectroscopy* (Clarendon Press, Oxford, 1977), chapter 5.2.2.

[53] R. Cline, J. Miller, M. Matthews, and D. Heinzen, Opt. Lett. **19**, 207 (1994).

[54] I. Marzoli, J. I. Cirac, R. Blatt, and P. Zoller, Phys. Rev. A **49**, 2771 (1994).

[55] M. Lindberg and J. Javanainen, J. Opt. Soc. Am. B **3**, 1008 (1986).

[56] D. Leibfried, private communication, 2000.

[57] J. I. Cirac, R. Blatt, P. Zoller, and W. Phillips, Phys. Rev. A **46**, 2668 (1992).

[58] H. Perrin, A. Kuhn, I. Bouchoule, and C. Salomon, Europhys. Lett. **42**, 395 (1998).

[59] K. Mølmer, Y. Castin, and J. Dalibard, J. Opt. Soc. Am. B **10**, 524 (1993).

[60] K. Mølmer and Y. Castin, Quantum Semiclass. Opt. **8**, 49 (1996).

[61] D. M. Meekhof *et al.*, Phys. Rev. Lett. **76**, 1796 (1996).

[62] K. Bergmann, H. Theuer, and B. W. Shore, Rev. Mod. Phys. **70**, 1003 (1998).

[63] H. Dehmelt, Bull. Am. Phys. Soc. **20**, 60 (1975).

[64] R. J. Hughes *et al.*, Fortschr. Phys. **46**, 329 (1998).

[65] D. M. Lucas *et al.*, Phil. Trans. R. Soc. Lond. A **361**, 1401 (2003).

[66] M. P. Fewell, B. W. Shore, and K. Bergmann, Aust. J. Phys. **50**, 281 (1997).

[67] U. Gaubatz, P. Rudecki, S. Schiemann, and K. Bergmann, J. Chem. Phys. **92**, 5363 (1990).

[68] M. Weitz, B. C. Young, and S. Chu, Phys. Rev. A **50**, 2438 (1994).

[69] G. G. Grigoryan and Y. T. Pashayan, Opt. Comm. **198**, 107 (2001).

[70] V. I. Romanenko and L. P. Yatsenko, Opt. Comm. **140**, 231 (1997).

[71] F. K. Jensen, Masters thesis, in preparation.

[72] B. W. Shore, J. Martin, M. P. Fewell, and K. Bergmann, Phys. Rev. A **52**, 566 (1995).

[73] J. Martin, B. W. Shore, and K. Bergmann, Phys. Rev. A **52**, 583 (1995).

[74] J. Martin, B. W. Shore, and K. Bergmann, Phys. Rev. A **54**, 1556 (1996).

[75] P. Marte, P. Zoller, and J. L. Hall, Phys. Rev. A **44**, R4118 (1991).

[76] L. S. Goldner *et al.*, Phys. Rev. Lett. **72**, 997 (1994).

[77] K. Mølmer and A. Sørensen, Phys. Rev. Lett. **82**, 1835 (1999).

[78] A. Sørensen and K. Mølmer, Phys. Rev. Lett. **82**, 1971 (1999).

[79] D. P. DiVincenzo, Phys. Rev. A **51**, 1015 (1995).

[80] A. M. Childs and I. L. Chuang, Phys. Rev. A **63**, 012306 (2000).

[81] A. Sørensen and K. Mølmer, Phys. Rev. A **62**, 022311 (2000).

[82] F. Mintert and C. Wunderlich, Phys. Rev. Lett. **87**, 257904 (2001).

[83] C. Wunderlich *et al.*, J. Phys. B: At. Mol. Opt. Phys. **36**, 1063 (2003).

[84] C. Monroe *et al.*, Phys. Rev. A **55**, R2489 (1997).

[85] B. DeMarco *et al.*, Phys. Rev. Lett. **89**, 267901 (2002).

[86] D. Jonathan, M. B. Plenio, and P. L. Knight, Phys. Rev. A **62**, 042307 (2000).

[87] J. Dalibard and C. Cohen-Tannoudji, J. Opt. Soc. Am. B **2**, 1707 (1985).

[88] D. Jonathan and M. B. Plenio, Phys. Rev. Lett. **87**, 127901 (2001).

[89] D. Kielpinski, C.Monroe, and D. Wineland, Nature **417**, 709 (2002).

[90] M. D. Barrett *et al.*, Phys. Rev. A **68**, 042302 (2003).

[91] D. Kielpinski *et al.*, Phys. Rev. A **61**, 032310 (2000).

[92] M. A. Rowe *et al.*, Quant. Inform. Comp. **2**, 257 (2002).

[93] B. B. Blinov *et al.*, Phys. Rev. A **65**, 040304(R) (2002).

[94] P. Bowe *et al.*, Phys. Rev. Lett. **82**, 2071 (1999).

[95] J. A. Jones, Phil. Trans. R. Soc. London ser. A **361**, 1429 (2003).

[96] D. Kielpinski *et al.*, Science **291**, 1013 (2001).

[97] A. M. Steane, Nature **399**, 124 (1999).

[98] A. M. Steane, Phys. Rev. A **68**, 042322 (2003).

[99] R. Grimm, M. Weidemüller, and Y. B. Ovchinnikov, Adv. At. Mol. Opt. Phys. **42**, 95 (2000).

[100] M. O. Scully and M. S. Zubairy, *Quantum Optics* (Cambridge University Press, Cambridge, 1997).

[101] P. Carruthers and M. M. Nieto, Am. J. Phys. **7**, 537 (1965).

[102] M. Sasura and A. M. Steane, Phys. Rev. A **67**, 062318 (2003).

[103] N. Schlosser, G. Reymons, I. Protsenko, and P. Grangier, Nature **411**, 1024 (2001).

[104] J. J. Garcia-Ripoll, P. Zoller, and J. I. Cirac, Phys. Rev. Lett. **91**, 157901 (2003).

[105] Q. A. Turchette *et al.*, Phys. Rev. A **61**, 063418 (2000).

[106] H. C. Nägerl *et al.*, Phys. Rev. A **60**, 145 (1999).

[107] D. Leibfried, Phys. Rev. A **60**, R3335 (1999).

[108] NIST Atomic Spectra Database, `http://physics.nist.gov`.

[109] C. E. Moore, *Atomic Energy Levels* (National Bureau of Standards, Washington, 1952), Vol. II.

[110] C. E. Moore, *Atomic Energy Levels* (National Bureau of Standards, Washington, 1958), Vol. III.

[111] A. Lindgård and S. Nielsen, Atomic Data and Nuclear Data Tables **19**, 533 (1977).

[112] C. A. Schrama, E. Peik, W. W. Smith, and H. Walther, Opt. Comm. **101**, 32 (1993).

[113] M. Abramowitz and I. A. Stegun, *Handbook of Mathematical Functions*, 9. ed. (Dover Publications, New York, 1965).

[114] A. Brøner, Masters thesis, Institute of Physics and Astronomy, University of Aarhus, 2000.

[115] P. Ghosh, *Ion Traps* (Clarendon Press, Oxford, 1995).

[116] M. Drewsen and A. Brøner, Phys. Rev. A **62**, 045401 (2000).

[117] S. K. Lamoreaux, Phys. Rev. A **56**, 4970 (1997).

[118] N. W. Ashcroft and N. D. Mermin, *Solid State Physics* (Saunders College Publishing, USA, 1976).

[119] K. Mølhave, Masters thesis, Institute of Physics and Astronomy, University of Aarhus, 2000.

[120] N. Kjærgaard, PhD Thesis, Institute of Physics and Astronomy, University of Aarhus, 2001.

[121] D. R. Denison, J. Vac. Sc. Tech. **8**, 266 (1971).

[122] R. Jones, D. Gerlich, and S. Anderson, Rev. Sci. Instrum. **68**, 3357 (1997).

[123] C. D. Bruun, Masters thesis, Institute of Physics and Astronomy, University of Aarhus, 1998.

[124] T. Hänsch and B. Couillaud, Opt. Comm. **35**, 441 (1980).

[125] R. W. P. Drever *et al.*, Appl. Phys. B. **31**, 97 (1983).

[126] P. Herskind, Intensity stabilization of a frequency doubled Ti:Sapphire laser, Bachelor project report, 2003.

[127] R. Ohmukai *et al.*, Jpn. J. Appl. Phys. **33**, 311 (1994).

[128] A. M. Thommesen, Master's thesis, Institute of Physics and Astronomy, University of Aarhus, Denmark, 2000.

[129] N. Kjærgaard *et al.*, Appl. Phys. B. **71**, 207 (2000).

[130] J. J. T. Lindballe, Masters thesis, Institute of Physics and Astronomy, University of Aarhus, 2003.

[131] H. C. Nägerl *et al.*, Appl. Phys B **66**, 603 (1998).

[132] D. Kleppner and R. J. Kolenkow, *An introduction to mechanics* (McGraw-Hill International Editions, Singapore, 1978).

[133] J. L. Sørensen, manuscript in preparation.

[134] D. J. Berkeland *et al.*, J. Appl. Phys. **83**, 5025 (1998).

[135] T. Hasegawa and K. Uehara, Appl. Phys. B. **61**, 159 (1995).

[136] T. Nakamura *et al.*, J. Appl. Phys. **89**, 2922 (2001).

[137] D. R. Lide, *Handbook of Chemistry and Physics*, 72 ed. (CRC press, Boca Raton, 1972).

[138] R. Alheit *et al.*, Appl. Phys. B. **61**, 277 (1995).

[139] P. H. Dawson and N. R. Whetten, Int. J. Mass. Spect. Ion Phys. **2**, 45 (1969).

[140] F. v. Busch and W. Paul, Z. Physik **164**, 588 (1961).

[141] J. Javanainen, in *Fundamentals of Laser Interactions*, edited by F. Ehlotzky (Lecture Notes in Physics vol. 229, Springer, Berlin, 1985).

[142] T. Sauter *et al.*, Europhys. Lett. **7**, 317 (1988).

[143] R. G. DeVoe and C. Kurtsiefer, Phys. Rev. A **65**, 063407 (2002).

[144] I. S. Vogelius, L. B. Madsen, and M. Drewsen, Phys. Rev. Lett. **89**, 173003 (2002).

[145] K. Mølhave and M. Drewsen, Phys. Rev. A **62**, 011401(R) (2000).

[146] P. Hodgson, E. Gadioli, and E. G. Erba, *Introductory Nuclear Physics* (Clarendon Press, Oxford, 1997).

[147] F. Schmidt-Kaler *et al.*, J. Phys. B: At. Mol. Opt. Phys. **36**, 623 (2003).

[148] E. Biémont and C. J. Zeippen, Comments At. Mol. Phys. **33**, 29 (1996).

[149] A. A. Madej and J. E. Bernard, in *Frequency Measurement and Control, Topics Appl. Phys.*, edited by A. N. Luiten (Springer Verlag, Berlin Heidelberg, 2001), Vol. 79, pp. 153–194.

[150] M. Knoop *et al.*, Eur. Phys. J. D, DOI:10.1140/epjd/e2004-00022-6 (2004).

[151] L. M. Hobbs *et al.*, Astrophys. J. **334**, L41 (1988).

[152] C. J. Zeippen, Astron. Astrophys. **229**, 248 (1990).

[153] P. A. Barton *et al.*, Phys. Rev. A **62**, 032503 (2000).

[154] M. Block, O. Rehm, P. Seibert, and G. Werth, Eur. Phys. J. D **7**, 461 (1999).

[155] J. Lidberg *et al.*, J. Phys. B: At. Mol. Opt. Phys. **32**, 757 (1999).

[156] G. Ritter and U. Eichmann, J. Phys. B: At. Mol. Opt. Phys. **30**, L141 (1997).

[157] T. Gudjons, B. Hilbert, P. Seibert, and G. Werth, Europhys. Lett. **33(8)**, 595 (1996).

[158] M. Knoop, M. Vedel, and F. Vedel, Phys. Rev. A **52**, 3763 (1995).

[159] F. Arbes *et al.*, Z. Phys. D. **29**, 159 (1994).

[160] C. J. S. Donald *et al.*, Europhys. Lett. **51**, 388 (2000).

[161] S.-S. Liaw, Phys. Rev. A **51**, R1723 (1995).

[162] T. Brage *et al.*, Phys. Scr. **48**, 533 (1993).

[163] N. Vaeck, M. Godefroid, and C. Froese Fischer, Phys. Rev. A **46**, 3704 (1992).

[164] C. Guet and W. R. Johnson, Phys. Rev. A **44**, 1531 (1991).

[165] M. A. Ali and Y.-K. Kim, Phys. Rev. A **38**, 3992 (1988).

[166] R. J. Barlow, *Statistics* (Wiley, New York, 1989).

[167] W. T. Eadie *et al.*, *Statistical methods in experimental physics* (North-Holland, Amsterdam, 1971).

[168] M. A. Stephens, in *Goodness-of-fit techniques* (Marcel Dekker, New York, 1986), p. 97, edited by R. B. D'Agostino and M. A. Stephens.

[169] M. Knoop, M. Vedel, and F. Vedel, Phys. Rev. A **58**, 264 (1998).

[170] R. G. DeVoe and R. G. Brewer, Phys. Rev. Lett. **76**, 2049 (1996).

[171] J. H. Eberly and P. W. Milonni, Encyclopedia of Physical Science and Technology **11**, 471 (1987).

[172] W. H. Press, S. A. Teukolsky, W. T. Vetterling, and B. P. Flannery, *Numerical Recipes in C*, 2nd ed. (Cambridge University Press, Cambridge, 1992).

[173] K. Moler, D. Weiss, M. Kasevich, and S. Chu, Phys. Rev. A **45**, 342 (1992).